Local and global Eulerian gyrokinetic simulations of microturbulence in realistic geometry with applications to the TCV Tokamak

Xavier Lapillonne

CRPP Association Euratom

ÉCOLE POLYTECHNIQUE FÉDÉRALE DE LAUSANNE

Abstract

In magnetically confined fusion devices, the energy and particle transport is significantly larger than expected from purely collisional processes. This degraded confinement mostly results from small-scale turbulence and prevents from reaching self-sustained burning plasma conditions in present day experiments. A better understanding of these nonlinear phenomena is therefore of key importance on the way towards controlled fusion. The small-scale microinstabilities and associated turbulence are investigated for Tokamak plasmas by means of numerical simulations in the frame of the gyrokinetic theory. This model describes the evolution of the particle distribution functions in phase space together with self-consistent electromagnetic fields, while neglecting the fast motion associated with the Larmor orbit of particles around the magnetic field lines.

In the course of this thesis work, substantial modifications to the existing Eulerian gyrokinetic code GENE have been carried out in collaboration with the Max-Planck-Institute für Plasmaphysik in Garching, Germany. The code has been extended from a local approximation, which only considers a reduced volume of a fusion plasma, to a global version which fully includes radial temperature and density profiles as well as radial magnetic equilibrium variations. To this end, the gyrokinetic equations have been formulated for general magnetic geometry, keeping radial variations of equilibrium quantities, and considering field aligned coordinates, suitable for their numerical implementation. The numerical treatment of the radial direction has been modified from a Fourier representation in the local approach to real space in the global code. This has in particular required to adapt the radial derivatives, the field solver, and to implement a real space dealiasing scheme for the treatment of the nonlinearity. A heat source was in addition introduced to allow for steady state global nonlinear simulations.

An important part of this work also focused on the description of the magnetic equilibrium. A circular concentric flux surface model as well as an interface with an MHD equilibrium code were implemented. A detailed investigation concerning the $s-\alpha$ model, previously used in local codes, was also carried out. It was shown that inconsistencies in this model had resulted in misinterpreted agreement between local and global results at large $\rho^* = \rho_s/a$ values, with ρ_s the Larmor radius and a the minor radius of the Tokamak. True convergence between local and global simulations was finally obtained by correct treatment of the geometry in both cases and considering the appropriate $\rho^* \to 0$ limit in the latter case.

The new global code was furthermore successfully tested and benchmarked against various other codes in the adiabatic electron limit in both the linear and nonlinear regime. A nonlinear ρ^* scan was in addition carried out showing convergence to the local results in the limit $\rho^* \to 0$ and also providing further insight on previous disagreements between two other global gyrokinetic codes concerning ρ^* convergence. Linear global simulations with kinetic electrons have shown consistent behavior with respect to local results.

Using the interface with the MHD equilibrium code, the effects of plasma shaping on Ion Temperature Gradient (ITG) instabilities were investigated by means of local simulations. A favorable influence of elongation and negative triangularity was observed. It was shown that these effects could be mostly accounted for by the modifications of the effective flux-surface averaged temperature gradient. Most importantly, a unique effective nonlinear critical temperature gradient could be determined for the different considered elongations and triangularities.

The local code was finally used to investigate particle and energy transport in the case of TCV discharges presenting an electron Internal Transport Barrier (eITB). It was shown that at the transition between ITG and Trapped Electron Mode (TEM) dominated turbulent regimes, the particle flux goes to zero. Interestingly, this effect could be well reproduced by a quasi-linear approach where all the different unstable wavenumbers are considered. The nonlinear simulations also revealed that a minimum of the electron heat diffusivity is observed at the transition between the TEM and ITG regimes. A strong dependence of this quantity was also noticed with respect to the density gradient. Quantitative comparisons with experimental results have shown that a reasonable agreement could only be reached in regions where the density gradient is small while the flux tube simulations seem to overestimate the heat transport if one accounts for gradient values in the center of the transport barrier. Some first nonlinear global simulations appear to indicate that finite ρ^* effects could potentially play an important role and thus reduce the heat diffusivity to realistic values.

Keywords: plasma, tokamak, fusion, turbulence, gyrokinetic, global, shaping, transport barrier

Version abrégée

Le transport de particules et d'énergie observé dans les machines à confinement magnétique pour la fusion est bien supérieur à celui attendu en considérant seulement les effets collisionels. Cette dégradation du confinement est le résultat de la turbulence agissant à petite échelle, qui empêche d'atteindre les conditions nécessaires à une réaction de fusion auto-entretenue dans les machines expérimentales actuelles. Une meilleure compréhension de ces phénomènes non-linéaires est par conséquent essentielle en vue d'une maitrise future de la fusion comme source d'énergie. Ces microinstabilités, et la turbulence qui leur est associée, sont étudiées dans les Tokamaks à l'aide de simulations numériques dans le cadre de la théorie gyrocinétique. Dans ce modèle, le plasma est décrit en termes des fonctions de distributions des particules dans l'espace de phase, ainsi que des champs électromagnétiques qui leur sont associés, en négligeant le mouvement cyclotronique rapide des particules autour des lignes de champ.

Au cours de cette thèse, des modifications importantes au code gyrocinétique Eulerien, GENE, ont été apportées en collaboration avec un groupe du Max-Planck-Institute für Plasmaphysik à Garching en Allemagne. Alors que le code était initialement limité à une approche locale, où seul un volume restreint du plasma est considéré, une version globale a été développée dans laquelle les profils de densité et température, ainsi que les variations radiales de l'équilibre magnétique, sont pris en compte. Les équations gyrocinétiques ont été reformulées dans ce but, pour une géométrie magnétique générale, en considérant les variations radiales des quantités d'équilibres, et en utilisant un système de coordonnées alignées avec les lignes de champ. Le traitement de la direction radiale a par conséquent dû être modifié d'une représentation dans l'espace de Fourier dans le cas local, à une représentation dans l'espace réel dans le code global. Cette modification a nécessité d'adapter, entre autres, les dérivées radiales et le calcul des champs, ainsi que d'introduire une nouvelle méthode d'anti-aliasing dans l'espace réel pour le traitement de la non-linéarité. Une source de chaleur a également été ajoutée afin de pouvoir effectuer des simulations non-linéaires dans un état quasi-stationaire.

Une partie importante de ce travail a été également dédiée à la description de l'équilibre magnétique. Un modèle considérant des surfaces de flux concentriques circulaires a été introduit ainsi qu'un interface avec un code d'équilibre MHD. Une étude approfondie d'un autre modèle, le modèle $s - \alpha$, utilisé dans plusieurs codes locaux par le passé, a également été conduite. Cette étude a permis de mettre en évidence des incohérences dans

ce modèle, qui avaient entrainé des conclusions erronnées concernant un accord entre des codes locaux et globaux pour une valeur élevée de $\rho^* = \rho_s/a$, a étant le rayon mineur du Tokamak et ρ_s le rayon de Larmor. La convergence attendue entre simulations locales et globales a finalement été obtenue en utilisant un traitement correct de la géométrie dans les deux cas, et en considérant la limite $\rho^* \to 0$ pour les simulations globales.
Le nouveau code global a été testé et comparé avec succès à plusieurs autres codes dans la limite des électrons adiabatiques, en régimes linéaire et non-linéaire. Une convergence non-linéaire en ρ^* a en outre été conduite, vérifiant la limite locale pour $\rho^* \to 0$ et permettant d'apporter un éclairage nouveau sur un précédent désaccord entre deux autres codes globaux concernant une telle convergence en ρ^*. Des simulations linéaires avec électrons cinétiques ont finalement montré un bon accord qualitatif avec les résultats locaux.
En utilisant l'interface avec le code MHD, une étude des effets de la forme du plasma sur les instabilités ITG a été effectuée avec le code local. Un effet favorable de l'élongation et de la triangularité négative a été mis en évidence. Il a été également montré que l'effet principal de la géométrie peut être interprété en terme d'un gradient effectif, moyenné sur la surface de flux. Une observation remarquable de cette étude est l'existence d'un gradient effectif critique unique pour les différentes formes dans les simulations non-linéaires.
Le code local a finalement été utilisé pour modéliser le transport de particules et de chaleur dans une décharge TCV présentant une barrière de transport électronique (eITB). Il a été montré qu'au niveau de la transition entre les régimes dominés par les ITG et TEM, le flux de particules s'annule. Il est intéressant de remarquer qu'un tel comportement peut être reproduit au moyen d'une approche quasi-linéaire dans laquelle tous les différents modes instables sont pris en compte. Les résultats non-linéaires ont également révélé l'existence d'un minimum du flux de chaleur électronique à la transition entre les régimes TEM et ITG. Une grande variabilité de la diffusion de chaleur électronique a également été observée en fonction du gradient de densité. Des comparaisons avec des résultats expérimentaux ont montré qu'un accord entre théorie et expérience est seulement possible dans les régions de faible gradient de densité alors que les simulations flux-tube semblent surestimer le transport de chaleur si l'on considère les gradients au centre de la barrière. Une étude préliminaire au moyen de simulations globales nonlinéaires semble indiquer que les effets de ρ^* fini pourraient jouer un rôle important et par conséquent permettre d'obtenir des valeurs de diffusivité plus réalistes.

Mots clefs: plasma, Tokamak, fusion, turbulence, gyrocinétique, global, forme, barrière de transport

Contents

1 Introduction **1**

1.1 Modeling of microinstabilities 4

1.2 Contribution of this thesis 6

1.3 Outline 7

2 Physical model **9**

2.1 Gyrokinetic theory 9

2.2 The phase space Lagrangian in gyrocenter coordinates 11

2.3 The gyrokinetic equations 18

2.4 The collision operator 20

2.5 The gyrokinetic equations in field-aligned coordinates 22

2.5.1 The field aligned coordinates (x, y, z) 22

2.5.2 The gyrokinetic equation in (x, y, z) coordinates 23

2.6 Choice for the background distribution 26

2.7 Velocity moments of the distribution function 27

2.8 The field equations 29

2.9 Macroscopic quantities 32

2.9.1 Velocity moments of the gyrokinetic equation 32

2.9.2 Radial conservation equations 34

2.9.3 Flux definitions 35

2.10 The normalized equations 38

2.10.1 Normalizations 38

2.10.2 The normalized gyrokinetic equation 40

2.10.3 The normalized field equations 41

2.11 Local and global approach . . . 41
2.11.1 The flux-tube approach . . . 41
2.11.2 The global approach . . . 42
2.12 Summary . . . 44

3 Numerical implementation **45**
3.1 General description . . . 45
3.1.1 Treatment of the phase space directions . . . 46
3.1.2 The eigensolver . . . 50
3.1.3 The time evolution scheme . . . 50
3.1.4 Code performance and parallelization . . . 51
3.2 Periodicity and parallel boundary conditions . . . 53
3.2.1 The parallel boundary conditions . . . 53
3.2.2 Contour plot in the poloidal plane . . . 55
3.2.3 The local limit . . . 56
3.3 Gyro-averaging . . . 58
3.3.1 The mixed finite element and Fourier representation . . . 59
3.3.2 Double gyro-averaging . . . 60
3.3.3 Gyro-averaging by linearizing the metric in field-aligned coordinates 61
3.3.4 Gyro-averaging in quasi-Cartesian coordinates . . . 63
3.3.5 The field equations . . . 66
3.3.6 The local limit . . . 68
3.4 Real space dealiasing . . . 70
3.4.1 Aliasing issue . . . 70
3.4.2 Standard dealiasing technique . . . 72
3.4.3 Treatment in real space . . . 73
3.4.4 Lagrange interpolation . . . 75
3.4.5 Validation with nonlinear simulations . . . 77
3.5 Sources and sinks . . . 79
3.6 Summary . . . 80

4 Equilibrium models **83**

4.1 The toroidal MHD equilibrium . . . 83
4.2 The CHEASE interface . . . 86
4.2.1 Equilibrium quantities in (x, y, z) . . . 87
4.3 Circular ad-hoc model . . . 88
4.4 The $s - \alpha$ model . . . 90
4.5 Influence of the equilibrium model and code comparisons . . . 91
4.5.1 Linear flux-tube results . . . 92
4.5.2 Nonlinear flux-tube results . . . 94
4.5.3 Linear comparison between local and global simulations . . . 97
4.6 Summary . . . 99

5 Code validation and global effects **101**
5.1 The cylindrical limit . . . 101
5.2 Linear Cyclone benchmark . . . 105
5.3 Kinetic electrons and electromagnetic effects . . . 108
5.4 Field solver analysis and Rosenbluth-Hinton test . . . 114
5.5 Nonlinear benchmarks . . . 117
5.5.1 Nonlinear run without sources . . . 117
5.5.2 Nonlinear run with sources . . . 117
5.6 Nonlinear ρ^* scan . . . 123
5.7 Summary . . . 125

6 Shaping effects on ITG turbulence **129**
6.1 Methodology and parameter choice . . . 130
6.2 Influence of elongation and triangularity in terms of the effective gradient . 132
6.3 Comparison with a local dispersion relation . . . 135
6.3.1 A local dispersion relation for toroidal-ITG modes . . . 136
6.3.2 Introducing geometrical coefficients in the local dispersion relation . 137
6.4 Nonlinear results . . . 143
6.5 Summary . . . 145

7 Modeling of electron internal transport barriers in the TCV Tokamak **147**
7.1 Physical parameters . . . 148

7.2 Linear results . . . 151
7.3 Nonlinear simulations . . . 154
7.3.1 Choice of numerical parameters . . . 154
7.3.2 Nonlinear results . . . 157
7.4 Comparison with quasi-linear estimates . . . 161
7.5 Sensitivity of the computed heat diffusivity . . . 164
7.6 Global effects . . . 168
7.7 Summary and discussion . . . 172

8 Conclusions **175**
8.1 Summary . . . 175
8.2 Outlook . . . 177

A CHEASE output for gyrokinetic codes **181**

B A local dispersion relation for toroidal-ITG modes **185**

Bibliography **191**

Acknowledgments **196**

CV and list of publications **198**

1 Introduction

Since the industrial revolution, which has seen a transition from traditional economies, essentially based on muscle power, towards more complex systems based on external energy sources, such as coal and steam power, the world energy consumption has been continuously increasing: it has for instance doubled from 1970 to 2009 [1]. Nowadays most of human activities heavily rely on fossil fuels, such as oil, gas or coal, which represent 82% of the world energy consumption, while the remaining is divided between renewables (12%) and nuclear energy (6%). Fossil fuels are not renewable, at least not on a human time scale, and estimates, based on the actual energy demand trend, show that the known resources of fossil fuels will be depleted in a time scale ranging from 40 years for oil to two hundred years for coal [2]. In addition to availability issues, these resources, especially oil, are not equally distributed geographically, often leading to strong geopolitical tensions, which will inevitably increase as the resources diminish. Finally, the burning of fossil fuels is also believed to have a strong impact on our environment through the resulting CO_2 emissions, which, in the scientific community, are widely considered to play a significant role in the present global warming. These different economic, geopolitical, and environmental aspects show how important it is for our societies to undertake strong political commitments to reduce our dependence on oil, gas and coal. This will in particular require to increase the usage of existing alternative energy sources and envisage a different way of using energy. In parallel to these efforts, research is being carried out to investigate the feasibility of a potentially new energy source on earth, in fact the same energy that fuels the sun, namely the nuclear fusion of light elements.

Among the different possible reactions, the fusion of two hydrogen isotopes, deuterium (^2_1H) and tritium (^3_1H), has the highest nuclear cross section and is thus considered for

a future fusion reactor. The products of this reaction are an alpha particle ($^4_2H_e$) and a neutron:

$$^2_1H + ^3_1H \longrightarrow n + ^4_2H_e + 17.6MeV\ . \tag{1.1}$$

Most of the excess energy (14.1 MeV) is carried as kinetic energy by the neutron and the remaining (3.5 MeV) by the alpha particle. In a power plant, the fast neutrons will loose their energy by interaction with a dedicated blanket surrounding the device, and the resulting heat will then be transfered via a working fluid to a steam turbine to ultimately produce electricity. The fusion reaction is extremely energetic compared to a chemical reaction, and one kg of deuterium-tritium fuel could potentially cover the need of one GW power plant for one day [3]. Deuterium is a stable isotope of hydrogen, with a natural abundance in earths oceans of 0.015% and can be extracted by enrichment and distillation processes. Tritium, on the other hand, is radioactive, with a half-life of about 12 years, and is thus not present naturally on earth. It can be produced by neutron induced fission of lithium, which is a relatively abundant element of the lithosphere. In a reactor, tritium could be therefore produced *in situ*, using the neutrons from the fusion reactions, interacting with lithium integrated to the blanket surrounding the device. Based on the world's present total yearly energy consumption, the available deuterium would allow for several billion years of electricity production, while the limiting factor would be the availability of lithium in land resources, which could nonetheless still cover the needs for a few thousand years [3]. Lithium could also be extracted from the oceans, at a higher cost though, and the reserve would then be enough for several million years. A major positive aspect of fusion energy is therefore the potential availability of its fuel with respect to other non-renewable energy sources. Another advantage, compared to nuclear fission power plants, is that a fusion reaction does not generate long-lived nuclear by-products. A fusion reactor would not be completely free of nuclear waste, as the high energy neutrons will activate the first wall of the device. However, an appropriate choice of low activation materials could result in much more manageable waste on a human time scale than those produced by existing nuclear fission reactors.

In order to obtain fusion reactions, the positively charged deuterium and tritium nuclei need to be brought to sufficiently high energies to overcome their electrostatic repulsion, typically of the order of 100 keV. At these high energies, electrons and their nuclei are

not bound anymore and constitute a gas of charged particles which is called a plasma. In such a plasma, the fusion reaction rate is highly dependent on the temperature T, density n, as well as the energy confinement time τ_E. In order to achieve a self-sustained fusion reaction, referred to as ignition, where the heat resulting from the alpha particles is sufficient to maintain the reaction, the triple product of these quantities needs to be above a certain value, which reads for a deuterium-tritium plasma:

$$n\,T\,\tau_E > 5 \times 10^{21}\,m^{-3}\,keV\,s\;. \tag{1.2}$$

While in the sun the confinement results from the gravitational forces, two different approaches are envisioned to reproduce these conditions on earth: inertial and magnetic confinement. In an inertial fusion device, the plasma is heated and compressed using high energy beams, generally in the form of lasers. The magnetic confinement approach, on the other hand, takes advantage of the fact that the charged particles which constitute the plasma follow trajectories essentially constrained to magnetic field lines. The charged particles are indeed free to move parallel to the magnetic field, but gyrate in a so-called Larmor orbit in the direction perpendicular to the field as a result of the Lorentz force. Among different considered devices for achieving magnetically confined fusion, the Toka-

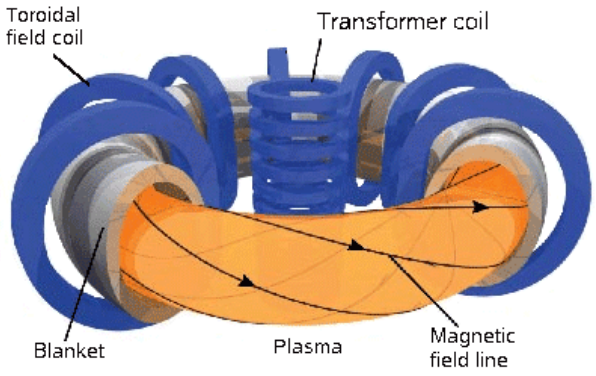

Figure 1.1: Schematic of a Tokamak fusion reactor. Source: Fusion for energy.

mak, on which we shall focus, is the most advanced and studied concept. In this toroidal device, an axisymmetric magnetic field with both toroidal and poloidal components is used to confine the charged particles. The toroidal magnetic field is obtained with external coils, while the poloidal component is generated by a toroidal current inside the plasma, which is itself created by induction with a transformer as illustrated in Fig. 1.1.

In order to heat the plasma to the required temperature for ignition, about 100 million degrees Kelvin, several mechanisms may be used, such as ohmic heating from the toroidal current, Neutral Beam Injection (NBI), and cyclotron resonance heating.

Since its invention in the late 1950s, rapid progress had been achieved in the temperature and density that could be reached in a Tokamak. It however soon became apparent that the energy confinement time, essential to reach ignition conditions, was much shorter than predicted by purely collisional processes, even when so-called neoclassical theory, which accounts for the toroidal curvature of the magnetic field lines, was considered. This anomalous energy transport is believed to result primarily from small scale and low frequency plasma instabilities, referred to as *microinstabilities*, which are driven by temperature and density gradients. Among the technical and scientific progress that is required in the way towards achieving controlled nuclear fusion, the understanding of microinstabilities and the associated turbulence is a major element, as it directly impacts the energy confinement time. The study of this so-called microturbulence is the subject of the present thesis work.

1.1 Modeling of microinstabilities

The term microinstability refers to a large variety of destabilizing mechanisms which arise from the different dynamics of electrons and ions in an inhomogeneous magnetized plasma. For typical Tokamak plasma parameters, among the dominant unstable modes are the toroidal-Ion Temperature Gradient (ITG) and Trapped Electron Modes (TEM). The toroidal-ITG mode, first identified by Horton and Tang in 1981 [4], is an interchange-type instability which results from the combined effect of an ion temperature gradient and the unfavorable curvature of the magnetic field on the low field side (outer edge) of the plasma. In a Tokamak, the helical structure of the magnetic field allows for the existence of magnetic mirrors, where particles with a low parallel velocity compared to the transverse one become trapped. The TEM instability [5] is driven unstable by the combined effect of the toroidal precessional drift of the trapped electrons and the electron pressure gradient. A detailed review of ITG modes and TEMs can be found in Ref. [6].

In addition to these main instabilities, one should also mention the Electron Temperature Gradient (ETG) modes, driven by an electron temperature gradient, which are the counterpart of ITG instabilities at electron scales [7]. Finally, in the high β limit (β measures the ratio between plasma and magnetic pressure), electromagnetic modes, the so-called kinetic ballooning modes (KBM) can be driven unstable [8].

Although some basic understanding of microinstabilities can be obtained with a fluid approach, an accurate treatment of these modes requires a full kinetic model describing the evolution of each electron and ion particle species in phase space. In the last two decades, these instabilities and associated turbulence have been actively studied by means of numerical simulations in the frame of the so-called gyrokinetic theory, in which the trajectories of particles are averaged over the fast cyclotron rotation around the magnetic field, thus dropping the information on the gyro-phase and reducing the phase space from six to five dimensions. A wide variety of codes have been developed to tackle this problem and among the different physical limits that have been considered, we shall distinguish the local and global approaches. In the local treatment, the so-called flux-tube approach [9], only a reduced simulation domain corresponding to a narrow plasma volume aligned with the magnetic field lines is considered and the radial variations of macroscopic quantities such as the density and temperature as well as magnetic field are neglected. The main advantage of this approach is that it can considerably reduce the computational power required to carry out a simulation in comparison to a global code, which models the full torus, and significant contributions to the understanding of microinstabilities have been possible thanks to this approximation. In some cases however, when the characteristic size of the turbulence is not negligible with respect to the machine size, such as in a small device, or with respect to a characteristic profile gradient length, such as found in so-called transport barriers, a global approach may be necessary.
Considering the numerical methods, three main different approaches have been used to carry out gyrokinetic simulations. In the Eulerian scheme [10, 11, 12, 13, 14], which shall be considered in this work, the gyrokinetic equation is first discretized on a fixed grid in phase space and the so-obtained system of ordinary differential equations (ODEs) for the time evolution of the discretized particle distribution function is then numerically inte-

grated. The Particle In Cell (PIC) method [15, 16, 17, 18, 19, 20, 21], on the other hand, is based on a Lagrangian description. In this case, the plasma is described by a statistical sampling of "markers" in phase space and the method then consists in following their trajectories. A third method, the so-called semi-Lagrangian scheme [22, 23, 24, 25, 26], can be seen as a hybrid method between the Eulerian and PIC approaches. At each time step, the particle distribution function is represented on a fixed grid in phase space, *i.e.* an Eulerian description. The distribution is however updated to the next time step by integrating the trajectories backward in time, starting from each phase space grid point, and invoking the invariance of the distribution along these characteristics. All these different schemes have their particular advantages and drawbacks. The Eulerian approach, for instance, is usually computationally more demanding than the PIC method, while it does not suffer from statistical sampling noise problems faced by the Lagrangian-PIC method. Since direct comparison with experiment is often not possible, the existence of such a variety of codes and methods represents a great opportunity, as cross comparisons and benchmarks enable to increase confidence in simulation results, and provide useful information to further understand the importance of the different considered approximations.

1.2 Contribution of this thesis

One of the main goals of this thesis was the extension of the local Eulerian code GENE [12, 27] to a global version, in collaboration with the group of Prof. F. Jenko at the Max-Plank-Institut für Plasmaphysik (IPP) in Garching, Germany [28]. This has in particular required to replace the original Fourier representation used in the radial direction with a real space treatment, and therefore to modify substantial parts of the code. With respect to the development of the GENE code, the present work has mostly focused on the implementation of the nonlinear $\vec{E} \times \vec{B}$ term in the gyrokinetic equation, the extension of the magnetic equilibrium models, and an alternative scheme for the treatment of the gyro-averaging operator. A Krook-type heat source was also introduced in the global code to allow for quasi-steady state nonlinear simulations. In addition to this implementation effort, numerous benchmarks and tests were carried out to validate the newly developed

code, representing a significant part of this thesis work.

The TCV Tokamak, which is located at the Centre de Recherches en Physique des Plasmas (CRPP), is a device with minor and major radius 0.24 m and 0.88 m respectively, toroidal magnetic field on axis 1.4 T and plasma current 1.2 MA, which has the particularity of being very flexible in obtaining various shapes for the plasma. Some experimental results from this machine [29, 30, 31, 32, 33] and other devices [34, 35] have shown the beneficial effect of elongation and triangularity on confinement. In order to investigate the effects of shaping on microturbulence, an interface with the equilibrium code CHEASE [36] was developed. By comparing gyrokinetic results obtained both with this interface and the so-called $s - \alpha$ analytical equilibrium model [37], inconsistencies in the standard implementation of the latter were at first pointed out. The implementation of a corrected analytical model, referred to as the "ad-hoc" model, has shown that these inconsistencies can be removed. The MHD interface was then finally used to address the effect of elongation and triangularity on ITG modes using the local code.

Another specificity of the TCV Tokamak are its powerful and flexible Electron Cyclotron Heating (ECH) sources, which make it particularly suited for the investigation of experimental electron Internal Transport Barriers (eITBs) scenarios [38, 39]. The local version of the GENE code was used to address the issue of particle and heat transport for both electrons and different ion species in the case of realistic eITBs parameters, and comparison with experimental measurement were discussed. One other main goal was also to compare these local results with global simulations. As a consequence of constraints in computational power and of some remaining issues with nonlinear global simulations when considering both kinetic electrons and ions, quantitative comparisons using the experimental parameters were however not possible during this work. A qualitative comparison was nevertheless carried out for reduced parameters, still relevant for the TCV Tokamak.

1.3 Outline

The present work is structured as follows. In Chapter 2, the key elements of the derivation of the gyrokinetic equation and associated field equations are given. These equations are then expressed in a field aligned coordinate system considering a general magnetic geometry. In accordance with the global approach, all radial variations of equilibrium

quantities are at first retained, the local limit being taken and discussed subsequently.
The numerical implementation of the GENE code is then presented in Chapter 3, and the various modifications required when extending the code from a local to a global version are addressed. In particular, the new gyro-averaging operator, as well as a real space dealiasing scheme which is used when dealing with the $\vec{E} \times \vec{B}$ nonlinearity are discussed. Finally, a Krook-type heat source is presented.
Chapter 4 is dedicated to the description of different magnetic equilibrium models which have been implemented in the code. These include an interface with the MHD equilibrium code CHEASE and the "ad-hoc" circular concentric flux surface model. These two models are valid for both the local and global versions of the code, and a comparison is finally provided with results obtained using the local $s - \alpha$ equilibrium model.
In Chapter 5, various validations and benchmarks of the newly developed global version of GENE are presented. A nonlinear ρ^* scan is in addition carried out showing the importance of global effects on ITG turbulence in small to middle size devices.
Using the interface with the MHD equilibrium code, the influence of plasma elongation and triangularity on ITG instabilities is investigated in Chapter 6 by means of local linear and nonlinear simulations. In particular, these shaping effects are interpreted in terms of effective flux-surface averaged ion temperature gradient.
In Chapter 7, linear and nonlinear local simulations are carried out with the aim of analyzing a TCV discharge presenting an electron internal transport barrier. Inspired by a previous quasi-linear study [40], ion temperature gradient values for which the electron particle flux goes to zero are identified. For such particular gradient values, the electron heat diffusivity is then compared with experimental results. Some quantitative comparisons with quasi-linear estimates of the particle flux are also provided. After investigating the sensitivity of the nonlinear heat diffusivity with respect to some key parameters, an estimate of global effects for a relevant ρ^* value is finally given using reduced physical parameters.
Conclusions are finally drawn in Chapter 8.
Two appendices are also present at the end of the thesis. In Appendix A, we provide some informations concerning the CHEASE interface, while a description of a local dispersion equation, used in Chap. 6, is given in Appendix B.

2 Physical model

2.1 Gyrokinetic theory

Particle and heat transport observed in magnetically confined fusion devices are usually orders of magnitude larger than those predicted by *neoclassical* transport theory, which considers purely collisional processes. This so-called *anomalous* transport is believed to result primarily from small-scale fluctuations, referred to as *microturbulence*, which is driven by temperature and density gradients. For typical fusion relevant plasmas, the frequency of the microinstabilities underlying microturbulence is much larger than the collision frequency and kinetic effects thus need to be retained. Although so-called gyro-fluid models have been developed [41] in order to account for kinetic corrections in fluid-like descriptions, providing useful results, the most straightforward and accurate approach consists in a fully kinetic representation, which describes the evolution of the particle distribution function in phase space. For each particle species, j, the time evolution of the associated distribution function $\mathtt{f}_j(t, \vec{x}, \vec{v})$ is described by the Vlasov equation:

$$\frac{d\mathtt{f}_j}{dt} = \frac{\partial \mathtt{f}_j}{\partial t} + \vec{v} \cdot \frac{\partial \mathtt{f}_j}{\partial \vec{x}} + \frac{\vec{F}_j}{m_j} \frac{\partial \mathtt{f}_j}{\partial \vec{v}} = 0 \,, \tag{2.1}$$

where $\vec{F}_j(t, \vec{x}, \vec{v}) = q_j[\vec{E}(t, x) + \vec{v} \times \vec{B}(t, \vec{x})]$ is the Lorentz force. The operator d/dt stands for the total time derivative along particle trajectories. Equation (2.1) thus states that the distributions f_j remain invariant along particle orbits in phase space. The Vlasov equation is coupled with Maxwell's equations for computing the self-consistent electric and magnetic fields $\vec{E}$ and $\vec{B}$. This would in principle require to solve a nonlinear problem in the 6-dimensional phase space $(\vec{x}, \vec{v})$, with different spatial and time scales varying by several orders of magnitude: from the Debye length to the machine size ($\sim$ 5 orders of magnitude) and from the cyclotron frequencies to transport time scales ($\sim$ 11 orders

of magnitude). Such problem resolution would be out of the scope for today's computers, and it is therefore necessary to introduce a set of approximations to retain only spatial and time scales relevant for the physical phenomena considered here, namely microturbulence.

In Tokamak plasmas, microinstabilities are drift-type waves, characterized by a highly anisotropic wave vector spectrum. The wavelength parallel to the magnetic field is indeed much larger than the perpendicular wavelength ($k_\perp \gg k_\parallel$), leading to a quasi-two-dimensional turbulence in configuration space. From experimental measurements, the perpendicular component of the wave vector in core plasmas is of order $k_\perp \rho_i \sim 0.4$ [42], where $\rho_i = v_{Ti}/\Omega_i \simeq 4 \times 10^{-3}\ m$ is the ion Larmor radius, $v_{Ti} = \sqrt{2\,T_i/m_i} \simeq 9.8 \times 10^5\ m\,s^{-1}$ the thermal velocity, $\Omega_i = q_i\,B/m_i \simeq 2.4 \times 10^8 s^{-1}$ the cyclotron frequency, and having considered deuterium ions, a typical magnetic field $B = 5$ Tesla, and an ion temperature $T_i = 10\ keV$. The characteristic frequency of these fluctuations is of the order of the diamagnetic frequency $w^* = k_\perp\, v_{Di} \sim 2 \times 10^5\ s^{-1}$, where the ion diamagnetic velocity is $v_{Di} = (T_i/q_i\,B)\,|\nabla_\perp \ln P_i|$, with $v_{Di} \sim 2 \times 10^3\ m\,s^{-1}$ for a characteristic inverse gradient length $L_g^{-1} = |\nabla \ln P_i| = 1\ m^{-1}$. The microinstability frequencies are therefore much smaller than the cyclotron frequency $w^*/\Omega_i \sim 10^{-3} \ll 1$, and a time scale separation between the fast gyromotion of the particles around a magnetic field line and the slower characteristic time of microinstabilities can therefore be considered. Finally, the relative fluctuation levels of the microturbulence in the core of the plasma are small compared to the background equilibrium, typically $\delta n/n \sim 10^{-2}$, where δn stands for the amplitude of the density perturbation.

The key idea of gyrokinetic theory is to "average out" the particle gyro-motion from the Vlasov equation, thus leading to a reduced 5-dimensional problem and eliminating the high frequency cyclotron time-scale. In this picture, only the information on the guiding center motion of each particle is retained, together with its finite size Larmor radius, whereas the phase of the particle on its gyro-orbit is not resolved. From the different physical quantities described above, the following gyrokinetic ordering is considered:

$$\frac{\omega}{\Omega_i} \sim \frac{\delta \mathtt{f}}{\mathtt{f}} \sim \frac{e\,\delta\Phi}{T_e} \sim \frac{|\delta\vec{B}|}{B} \sim \frac{\rho_i}{L_g} \sim \frac{\rho_i}{L_B} \sim \epsilon\ , \tag{2.2}$$

and

$$k_\perp \rho_i \sim 1 \ , \quad k_\parallel \rho_i \sim \epsilon \ , \tag{2.3}$$

where ϵ is a small dimensionless parameter, $\delta \mathtt{f}$, $\delta\Phi$, $|\delta\vec{B}|$ are respectively the fluctuating component of the distribution function, electrostatic potential, and magnetic field, while L_g is the characteristic gradient length of equilibrium density and temperature profiles, and L_B the characteristic gradient length of the magnetic field. The typical order of the gradient lengths are $L_g \sim a$ and $L_B \sim R$, where a and R are respectively the minor and major radii of the tokamak, with the inverse aspect ratio of order $a/R \sim 0.2 - 0.4$ in most experiments. In the gyrokinetic ordering, the electromagnetic fluctuations $(\delta\Phi, |\delta\vec{B}|)$ thus represent small perturbations to the particle trajectories in the background magnetic field $\vec{B}$.

The nonlinear gyrokinetic equations were first derived in the 1980's by Frieman and Chen [43] using an ordering expansion in the small parameter ϵ. A more systematic approach to derive such equations based on the Lie transform method consists in introducing a series of appropriate phase-space coordinate transforms such that the equations of motion for the particle's guiding center become independent of the gyro-angle at the desired order in the small parameter ϵ. The Lie perturbation method was first applied to guiding center theory by Littlejohn [44] and applied to the derivation of the nonlinear gyrokinetic equation considering electrostatic perturbations in Ref. [45] as well as electromagnetic perturbations in Ref. [46]. A recent review of gyrokinetic theory can be found in the paper by Brizard and Hahm [47].

2.2 The phase space Lagrangian in gyrocenter coordinates

In this section, a brief description of the guiding center equation derivation based on the Lie transform method is given.

We shall first review, following Refs. [44, 48], how one can obtain the equations of motion

for a Hamiltonian system in an arbitrary coordinate system using the variational principle:

$$\delta \int \mathcal{L}\, dt = 0 \,, \tag{2.4}$$

where $\mathcal{L}(t, z, \dot{z})$ is the so-called phase space Lagrangian. Note that the phase space Lagrangian is obtained from the Lagrangian $L(\vec{q}, \vec{p}, t) = \vec{p} \cdot \dot{\vec{q}} - H(\vec{q}, \vec{p}, t)$ expressed in canonical variables $(\vec{q}, \vec{p})$, $H(\vec{q}, \vec{p}, t)$ being the system's Hamiltonian, after an arbitrary change of variables $z = z(\vec{q}, \vec{p})$. The advantage of the variational principle approach is its validity for any given choice of phase space variables, in particular for non-canonical variables. By introducing the so-called Poincaré-Cartan one-form γ (sum over indices are implicit):

$$\gamma = \gamma_\mu \, dz^\mu = \mathcal{L}\, dt \,, \tag{2.5}$$

where $z^\mu = (z, t)$, the variational principle (2.4) reads

$$\delta \int \gamma_\mu \, dz^\mu = 0 \,, \tag{2.6}$$

which leads to the generalized Euler-Lagrange equations of motion:

$$\omega_{\mu\nu} \frac{dz^\nu}{dt} = 0 \,, \quad \text{with} \quad \omega_{\mu\nu} = \frac{\partial \gamma_\nu}{\partial z^\mu} - \frac{\partial \gamma_\mu}{\partial z^\nu} \,. \tag{2.7}$$

The integrand can then be written in any new coordinate system Z^μ using the relation:

$$\gamma_\mu \, dz^\mu = \gamma_\nu \frac{\partial z^\nu}{dZ^\mu} dZ^\mu = \Gamma_\mu \, dZ^\mu \,. \tag{2.8}$$

The equations of motion in the new coordinates are then again obtained by using the generalized Euler-Lagrange equations (derived this time from $\delta \int \Gamma_\mu \, dZ^\mu = 0$):

$$\omega_{\mu\nu} \frac{dZ^\nu}{dt} = 0 \,, \quad \text{where now} \quad \omega_{\mu\nu} = \frac{\partial \Gamma_\nu}{dZ^\mu} - \frac{\partial \Gamma_\mu}{dZ^\nu} \,. \tag{2.9}$$

In the following, we will also make use of the property that the variational principle and thus the equations of motions remain invariant under a phase space gauge transformation of the one-form γ:

$$\gamma \quad \longrightarrow \quad \gamma + dS \,, \tag{2.10}$$

where dS is the exact differential of a scalar function $S = S(z^\mu)$, called phase space gauge function.

The goal of gyrokinetic theory is thus to correctly define the guiding center of the particle through an appropriate coordinate transformation of the original particle variables $(\vec{x}, \vec{v})$ in the phase space Lagrangian frame work, such that the corresponding equations of motion are independent of the fast varying generalized gyro-angle (the gyro-angle may itself get modified by the transformation). In other words, the generalized gyro-angle becomes a cyclic variable. Through this process, the fast varying gyro-rotation thus gets separated from the so-defined slow varying guiding center motion. This is achieved systematically to increasing orders in the small parameter ϵ, introduced in section 2.1, thanks to successive combination of phase space coordinate changes based on Lie transforms and phase space gauge transformations.

We shall now start the description of the actual derivation by writing the one-form γ of a charged particle in an electromagnetic field:

$$\begin{aligned} \gamma &= \mathcal{L}\, dt = \left\{ \vec{p} \cdot \vec{v} - \left[\frac{1}{2}\, m\, v^2 + q\, \Phi(\vec{x}, t) \right] \right\} dt \\ &= \Big[\, m\, \vec{v} + q\, \vec{A}(\vec{x}, t) \,\Big] \cdot d\vec{x} - \left[\frac{1}{2} m v^2 + q \Phi(\vec{x}, t) \right] \, dt \,, \end{aligned} \tag{2.11}$$

having used the relation $\vec{p} = m\, \vec{v} + q\, \vec{A}(\vec{x}, t)$ for the canonical momentum. Assuming no equilibrium background electrostatic field, the electromagnetic potential fields $(\Phi, \vec{A})$ can be written:

$$\vec{A}(\vec{x}, t) = \vec{A}_0(\vec{x}, t) + \vec{A}_1(\vec{x}, t) \qquad \text{and} \qquad \Phi(\vec{x}, t) = \Phi_1(\vec{x}, t) \;,$$

with the background magnetic field being given by $\vec{B}_0 = \vec{\nabla} \times \vec{A}_0$ and $(\Phi_1, \vec{A}_1)$ representing the electromagnetic fluctuations. The one-form can be similarly separated into an equilibrium and a perturbation part, $\gamma = \gamma_0 + \gamma_1$, with:

$$\gamma_0 = \Big[\, m\, \vec{v} + q\, \vec{A}_0(\vec{x}) \,\Big] \cdot d\vec{x} - \frac{1}{2} m\, v^2 \; dt \;, \tag{2.12}$$

$$\gamma_1 = q\, \vec{A}_1(\vec{x}, t) \cdot d\vec{x} - q\, \Phi_1(\vec{x}, t) \; dt \;. \tag{2.13}$$

In order to remove from the unperturbed one-form γ_0 the fast gyromotion time scale associated with the background magnetic field, a first transformation to *guiding-center* coordinates $Z_g = (\vec{X}_g, v_{\parallel,g}, \mu_g, \alpha_g)$ is introduced, where $\vec{X}_g$ is the guiding center position, $v_{\parallel,g} = \vec{v} \cdot \vec{b}_0$ the velocity along the magnetic field, $\mu_g = (m v_{\perp,g}^2)/(2\, B_0)$ the magnetic

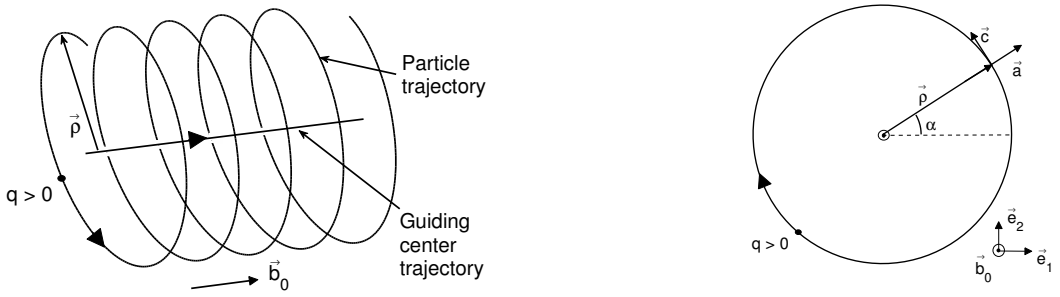

Figure 2.1: Guiding center trajectory in a magnetized plasma (left), and projection of the particle motion in the plane perpendicular to the magnetic field (right).

moment with $\vec{v}_{\perp,g} = \vec{v} - v_{\parallel,g} \cdot \vec{b}_0$, and $\vec{b}_0 = \vec{B}_0/B_0$ the local unitary vector parallel to the unperturbed magnetic field. Assuming that the background magnetic field varies slowly over the Larmor radius ($\epsilon \sim \rho_i/L_B \ll 1$), the motion of the particle in the plane perpendicular to the magnetic field line is circular to lowest order in ϵ. The coordinate transformation from particle variables $(\vec{x}, \vec{v})$ to guiding center variables Z_g is defined by:

$$\vec{x} = \vec{X}_g + \vec{\rho}, \qquad \text{with} \qquad \vec{\rho} = \frac{v_{\perp,g}}{\Omega(\vec{X}_g)} \vec{a}(\alpha_g)\,, \qquad \text{and} \qquad \vec{v} = v_{\parallel,g}\,\vec{b}_0 + v_{\perp,g}\,\vec{c}\,(\alpha_g)\,, \quad (2.14)$$

where $\vec{a}(\alpha_g) = \cos\alpha_g\,\vec{e}_1 + \sin\alpha_g\,\vec{e}_2$ and $\vec{c}\,(\alpha_g) = -\sin\alpha_g\,\vec{e}_1 + \cos\alpha_g\,\vec{e}_2$ are unit vectors in respectively the radial and tangential directions to the gyro-circle, expressed in the right-handed local Cartesian coordinate system $(\vec{e}_1, \vec{e}_2, \vec{b}_0)$, as illustrated in Fig. 2.1, and α_g is the gyro-angle. Up to first order in ϵ, the unperturbed one-form in guiding center coordinates Z_g reads:

$$\Gamma_{0,g} = \left[m\,v_\parallel\,\vec{b}_0(\vec{X}_g) + q\,\vec{A}_0(\vec{X}_g)\right] \cdot d\vec{X}_g + \frac{m}{q}\,\mu_g\,d\alpha_g - \left[\frac{1}{2}\,m\,v_{\parallel,g}^2 + \mu_g\,B_0(\vec{X}_g)\right] dt\,. \quad (2.15)$$

after an appropriate gauge transformation $\Gamma_{0,g} \to \Gamma_{0,g} + dS$. One notices that after this process, all gyro-angle dependance has been removed from $\Gamma_{0,g}$, so that α_g is indeed a cyclic variable. The associated canonical momentum appears as the magnetic moment μ_g, and is thus an invariant of motion of the unperturbed trajectories. We furthermore express here the phase space jacobian J_g of the transformation from particle variables

$(\vec{x}, \vec{v})$ to guiding center variables Z_g:

$$J_g = \left| \frac{\partial(\vec{x}, \vec{v})}{\partial Z_g} \right| = \left| \frac{\partial(\vec{x}, \vec{v})}{\partial(\vec{x}, \vec{p})} \right| \left| \frac{\partial(\vec{x}, \vec{p})}{\partial Z_g} \right| = \frac{1}{m^3} \left[\det(\omega_{0,ij}) \right]^{1/2} = \frac{B^*_{0\|}}{m_j} \,, \tag{2.16}$$

where the matrix elements $\omega_{0,ij}$ are defined in Eq. (2.9), for (i, j) such that $Z^i, Z^j \in (\vec{X}_g, v_{\|,g}, \mu_g, \alpha_g)$. In addition, one defines $B^*_{0\|} = \vec{B}^*_0 \cdot \vec{b}_0$, with $\vec{B}^*_0 = \vec{\nabla} \times \vec{A}^*_0 = \vec{B}_0 + (m/q)\, v_{\|,g}\, \vec{\nabla} \times \vec{b}_0$, *i.e.* $\vec{A}^*_0 = \vec{A}_0 + (m/q)\, v_{\|,g}\, \vec{b}_0$.

Let us now carry on by considering the perturbed system. The perturbation contribution $\Gamma_{1,g}$ to the one-form in guiding center coordinates Z_g reads to order ϵ:

$$\begin{aligned} \Gamma_{1,g} \;\; = \;\; & q\, \vec{A}_1(\vec{X}_g + \vec{\rho}, t) \cdot \left[d\vec{X}_g + \frac{1}{q\, v_\perp(\vec{X}_g)}\, \vec{a}(\alpha_g)\, d\mu_g + \frac{m\, v_\perp(\vec{X}_g)}{q\, B_0(\vec{X})}\, \vec{c}(\alpha_g)\, d\alpha_g \right] \\ & - q\, \Phi_1(\vec{X}_g + \vec{\rho}, t)\, dt \,. \end{aligned} \tag{2.17}$$

In these coordinates, $\Gamma_{1,g}$ is clearly a function of the fast varying gyro-angle α_g. Its gyro-angle dependence cannot be removed by means of a gauge transformation alone and a further change of coordinates, using Lie transformations, to the so-called *gyrocenter* coordinates $Z = (\vec{X}, v_\|, \mu, \alpha)$ is thus introduced. The Lie transforms are continuous, near identity, coordinate transformations in phase space:

$$Z_g \to Z(Z_g, \epsilon) = T^{-1}\, Z_g \,, \tag{2.18}$$

where ϵ is a small ordering parameter and with $Z(Z_g, 0) = Z_g$. In the following derivation, the small parameter ϵ measures the relative fluctuation level, see Eq. (2.2). The Lie transform can formally be expressed as

$$T = \exp(-\epsilon L) \,, \tag{2.19}$$

where L is the Lie derivative operator, which acts respectively on a scalar $\mathcal{F}_g$ as:

$$L\, \mathcal{F}_g = g^\nu\, \frac{\partial \mathcal{F}_g}{\partial Z^\nu_g} \,, \tag{2.20}$$

and on a one-form $\Gamma_g = \Gamma_{g,\mu}\, dZ^\mu_g$ as:

$$(L\, \Gamma_g)_\mu = g^\nu \left(\frac{\partial \Gamma_{g,\mu}}{\partial Z^\nu_g} - \frac{\partial \Gamma_{g,\nu}}{\partial Z^\mu_g} \right) \,. \tag{2.21}$$

where μ and ν run over all indices of the extended phase space (Z_g, t) and sums over ν are

implicit. The Lie transformation is characterized by the so-called generators g_n^ν defined by:

$$g^\nu = \frac{\partial Z_g^\nu}{\partial \epsilon}(Z, \epsilon)\,. \tag{2.22}$$

A general expression for the transformation of the one-form Γ_g resulting from (2.17) including a gauge transformation, is given by:

$$\Gamma = T\,\Gamma_g + dS\;, \tag{2.23}$$

where S denotes a gauge scalar field and the operator T stands for an overall transform, composed of individual Lie Transforms

$$T = \cdots T_3 \cdot T_2 \cdot T_1\;, \tag{2.24}$$

where the transform T_n enables to carry out the n^{th} order accurate derivation of the gyrocenter coordinate transform in the small parameter ϵ, and can be expressed as $T_n = \exp -\epsilon^n L_n$. Expanding Γ_g, Γ, S and T in terms of the small parameter ϵ, the one-form can be finally written $\Gamma = \Gamma_0 + \Gamma_1 + ...$, with:

$$\begin{aligned}
\Gamma_0 &= \Gamma_{g\,0} + dS_0\;, && (2.25)\\
\Gamma_1 &= \Gamma_{g\,1} - L_1\Gamma_{g\,0} + dS_1\;. && (2.26)\\
&\vdots
\end{aligned}$$

The key idea of this perturbative approach consists, at each order in ϵ, to specify the generators and phase-space gauge term so as to remove all gyro-angle dependences from Γ. A detailed derivation of the one-form in gyrocenter coordinates to first order in ϵ can be found in Ref. [49]. One obtains for the generators:

$$\begin{aligned}
g_1^t &= 0\;, && (2.27)\\
\vec{g}_1^{\vec{X}} &= \tilde{\vec{A}}_1 \times \frac{\vec{b}_0}{B_{0\|}^*} - \frac{\vec{B}_0^*}{B_{0\|}^*}\frac{1}{m}\frac{\partial S_1}{\partial v_\|} + \frac{1}{q}\vec{\nabla} S_1 \times \frac{\vec{b}_0}{B_{0\|}^*}\;, && (2.28)\\
g_1^{v_\|} &= \frac{1}{m}\frac{\vec{B}_0^*}{B_{0\|}^*} \cdot \left(q\,\tilde{\vec{A}}_1 + \vec{\nabla} S_1\right)\;, && (2.29)\\
g_1^\mu &= q\frac{v_\perp}{B_0}\vec{A}_1 \cdot \vec{c} + \frac{q}{m}\frac{\partial S_1}{\partial \theta}\;, && (2.30)
\end{aligned}$$

$$g_1^\theta = -\frac{q}{m}\left(\frac{1}{v_\perp}\vec{A}_1\cdot\vec{a}+\frac{\partial S_1}{\partial\mu}\right), \tag{2.31}$$

with S_1 the gauge scalar chosen as:

$$S_1 = \frac{1}{\Omega}\int^\alpha\left(q\tilde{\Phi}_1+\frac{1}{B^*_{0\|}}(\vec{b}_0\times\tilde{\vec{A}}_1)\,\mu\,\vec{\nabla}B_0 - qv_\parallel\frac{\vec{B}^*_0}{B^*_{0\|}}\cdot\tilde{\vec{A}}_1 - qv_\perp\,\widetilde{\vec{A}_1\cdot\vec{c}}\right)d\alpha' . \tag{2.32}$$

In the above relations, the notation $\tilde{\mathcal{F}}(\vec{X},\mu,\alpha)=\mathcal{F}(\vec{X}+\vec{\rho})-\bar{\mathcal{F}}(\vec{X},\mu)$ is used, where $\bar{\mathcal{F}}$ denotes the gyro-averaging of a given quantity $\mathcal{F}$, defined as:

$$\bar{\mathcal{F}}(\vec{X},\mu) = \frac{1}{2\pi}\oint\mathcal{F}(\vec{X}+\vec{\rho}(\vec{X},\mu,\alpha))d\alpha . \tag{2.33}$$

With this choice for the generators and scalar gauge, the perturbed one-form in gyro-center coordinates $Z=T^{-1}\,Z_g=(\vec{X},v_\parallel,\mu,\alpha)$ finally reads to order ϵ:

$$\begin{aligned}\mathcal{L}\,dt=\Gamma &= \Gamma_0+\Gamma_1\\ &= (m\,v_\parallel\,\vec{b}_0+q\,\vec{A}_0+q\,\bar{A}_{1\|}\,\vec{b}_0)\cdot d\vec{X}+\frac{m}{q}\,\mu\,d\alpha\\ &\quad-\left[\frac{1}{2}m\,v_\parallel^2+q\,\bar{\Phi}_1+\mu\,(B_0+\bar{B}_{1\|})\right]dt ,\end{aligned} \tag{2.34}$$

which is indeed such that the transformed gyro-angle α is cyclic, despite the presence of fluctuating fields. Note that in the following, only transverse magnetic fluctuations related to $A_{1\|}$ shall be considered, while the parallel magnetic fluctuations $B_{1\|}$ will be neglected. The operator T^{-1}, called the pull-back operator, also enables to transform the particle distribution expressed in gyrocenter variables $f(Z)$ to the particle distribution in guiding center variables $f_g(Z_g)$[1]:

$$f_g(Z_g)=(T^{-1}\,f)(Z_g). \tag{2.35}$$

Using Eqs (2.20), (2.24) and (2.27)-(2.31), one obtains to first order in ϵ for the fluctuating contribution to the distribution function:

$$f_{g,1j}=f_{1j}+\frac{1}{B_0}\left[\left(\Omega_j\frac{\partial f_{0j}}{\partial v_\parallel}-q_jv_\parallel\frac{\partial f_{0j}}{\partial\mu}\right)\tilde{A}_{1\|}+q_j\tilde{\Phi}_1\,\frac{\partial f_{0j}}{\partial\mu}\right], \tag{2.36}$$

where a splitting of the distribution function into a background and perturbation contri-

[1]Concerning the notation, the character `f` stands for the distribution function in the original particle variables $(\vec{x},\vec{v})$, f_g for the distribution function in guiding-center variables Z_g, and f for the distribution in gyrocenter variables Z. It should be emphasized that `f`, f_g and f all represent the same physical quantity: the particle distribution.

bution, $f_j = f_{0j} + f_{1j}$, have been considered. Relation (2.36) shall be used later on, when evaluating quantities such as the density or current density at the particle position, as described in section 2.7.

2.3 The gyrokinetic equations

Invoking the invariance of the distribution function along the phase space trajectories, Eq. (2.1), it is straightforward to write the Vlasov equation in gyrocenter coordinates:

$$\frac{df_j}{dt} = \frac{\partial f_j}{\partial t} + \dot{\vec{X}} \cdot \frac{\partial f_j}{\partial \vec{X}} + \dot{v}_\parallel \frac{\partial f_j}{\partial v_\parallel} + \dot{\mu} \frac{\partial f_j}{\partial \mu} + \dot{\alpha} \frac{\partial f_j}{\partial \alpha} = 0 \, . \tag{2.37}$$

The required equations of motion for the gyrocenter variables can be evaluated from the one-form (2.34) using the generalized Euler-Lagrange equations (2.9). Noticing that $\vec{\nabla} \times (A_{1\parallel} \vec{b}_0) \simeq \vec{\nabla} A_{1\parallel} \times \vec{b}_0 + \mathcal{O}(\epsilon)$ one obtains to first order in ϵ:

$$\dot{\vec{X}} = \vec{v}_G = v_\parallel \, \vec{b}_0 + \frac{B_0}{B^*_{0\parallel}} (\vec{v}_E + \vec{v}_{\nabla B} + \vec{v}_c) \, , \tag{2.38}$$

$$\dot{v}_\parallel = -\frac{1}{m_j \, v_\parallel} \, \vec{v}_G \cdot (q_j \, \vec{\nabla} \bar{\phi}_1 + q_j \, \vec{b}_0 \, \dot{\bar{A}}_{1\parallel} + \mu \vec{\nabla} B_0) \, , \tag{2.39}$$

$$\dot{\mu} = 0 \quad , \tag{2.40}$$

$$\dot{\alpha} = \Omega_j + \frac{q_j^2}{m_j} \left(\frac{\partial \bar{\Phi}_1}{\partial \mu} - v_\parallel \frac{\partial \bar{A}_{1\parallel}}{\partial \mu} \right) \, , \tag{2.41}$$

with $\vec{v}_E$ the generalized $\vec{E} \times \vec{B}$ drift velocity

$$\vec{v}_E = -\frac{\vec{\nabla} \bar{\chi}_1 \times \vec{B}_0}{B_0^2} \, , \tag{2.42}$$

where $\bar{\chi}_1$ is the gyroaveraged modified potential:

$$\bar{\chi}_1 = \bar{\Phi}_1 - v_\parallel \bar{A}_{1\parallel} \, . \tag{2.43}$$

The grad-B drift velocity is given by

$$\vec{v}_{\nabla B} = \frac{\mu}{m_j \Omega_j B_0} \, \vec{B}_0 \times \vec{\nabla} B_0 \, , \tag{2.44}$$

and the curvature drift velocity by

$$\vec{v}_c = \frac{v_\parallel^2}{\Omega_j}\left(\vec{\nabla}\times\vec{b}_0\right)_\perp = \frac{\mu_0 v_\parallel^2}{\Omega_j B_0^2}\,\vec{b}_0\times\vec{\nabla}\left(p_0+\frac{B_0^2}{2\mu_0}\right)\,, \tag{2.45}$$

having made use of the MHD equilibrium force balance relation $\vec{\nabla}p_0 = \vec{j}_0\times\vec{B}_0$ and Ampère's law $\vec{\nabla}\times\vec{B}_0 = \mu_0\,\vec{j}_0$.

To obtain the desired gyrokinetic equation, one still needs to apply the gyro-averaging operator (2.33) to Eq. (2.37). As α is a cyclic variable, all operators acting on the distribution f_j in Eq. (2.37) commute with the gyro-averaging operator (2.33), except for the term $\dot{\alpha}\,\partial f/\partial\alpha$ which average out to zero (as f_j is $2\,\pi$-periodic with respect to α). One thus obtains the so-called gyrokinetic equation:

$$\frac{\partial f_j}{\partial t} + \dot{\vec{X}}\cdot\frac{\partial f_j}{\partial\vec{X}} + \dot{v}_\parallel\,\frac{\partial f_j}{\partial v_\parallel} = 0\,, \tag{2.46}$$

having made used of Eq. (2.40). Finally, inserting Eqs. (2.38) and (2.39), the gyrokinetic equation becomes:

$$\begin{aligned}\frac{\partial f_j}{\partial t} \;+\; &\left[v_\parallel\vec{b}_0 + \frac{B_0}{B_{0\parallel}^*}(\vec{v}_E+\vec{v}_{\nabla B}+\vec{v}_c)\right]\\ &\cdot\left[\vec{\nabla}f_j - \frac{1}{m_j v_\parallel}\left(q_j\,\vec{\nabla}\bar{\phi}_1 + q_j\,\vec{b}_0\,\dot{\bar{A}}_{1\parallel} + \mu\vec{\nabla}B_0\right)\frac{\partial f_j}{\partial v_\parallel}\right] = 0\,,\end{aligned} \tag{2.47}$$

having identified, notation-wise, the gyro-averaged distribution $\bar{f}_j$ to f_j.

As already stated, the full distribution function f_j is separated into a static background distribution f_{0j}, representing the equilibrium state, and a fluctuating part f_{1j}:

$$f_j = f_{0j} + f_{1j}\,, \tag{2.48}$$

where the perturbed part is assumed to remain much smaller than the static part, $f_{1j}/f_{0j}\sim\varepsilon$. The background distribution $f_{0j}\neq f_{0j}(t)$ is assumed to be a stationary solution to the unperturbed gyrokinetic equation:

$$\left.\frac{df_{0j}}{dt}\right|_{\text{u. t.}} = \left[v_\parallel\vec{b}_0 + \frac{B_0}{B_{0\parallel}^*}(\vec{v}_{\nabla B}+\vec{v}_c)\right]\cdot\left(\vec{\nabla}f_{0j} - \frac{1}{m_j v_\parallel}\mu\vec{\nabla}B_0\frac{\partial f_{0j}}{\partial v_\parallel}\right) = 0\,. \tag{2.49}$$

where $d/dt|_{u.t.}$ stands for the total time derivative along the unperturbed trajectories. The quantities:

$$g_{1j} = f_{1j} - \frac{q_j}{m_j}\bar{A}_{1\parallel}\frac{\partial f_{0j}}{\partial v_\parallel} \qquad \text{and} \qquad \vec{\Gamma}_j = \vec{\nabla} f_{1j} - \frac{q_j}{m_j v_\parallel}\vec{\nabla}\bar{\Phi}_1\frac{\partial f_{0j}}{\partial v_\parallel}\ , \tag{2.50}$$

are now introduced and should not be confused with the Lie generators and one-form considered in the previous section. Keeping only the $\vec{v}_E$ nonlinearity ($\propto \vec{v}_E\cdot\vec{\nabla} f_{1j}$), and dropping the so-called parallel non-linearity ($\propto \vec{v}_G\cdot\vec{\nabla}\Phi_1\,\partial f_{1j}/\partial v_\parallel$, which can be neglected according to Ref. [50]), the gyrokinetic equation finally reads:

$$\begin{aligned}\frac{\partial g_{1j}}{\partial t} \quad &+ \quad \frac{B_0}{B^*_{0\parallel}}\vec{v}_E\cdot\left(\vec{\nabla} f_{0j} - \frac{\mu}{m_j v_\parallel}\vec{\nabla}B_0\frac{\partial f_{0j}}{\partial v_\parallel}\right) + \frac{B_0}{B^*_{0\parallel}}(\vec{v}_E + \vec{v}_{\nabla B} + \vec{v}_c)\cdot\vec{\Gamma}_j \\ &+ \quad v_\parallel\vec{b}_0\cdot\vec{\Gamma}_j - \frac{\mu}{m_j}\left(\vec{b}_0 + \frac{B_0}{v_\parallel B^*_{0\parallel}}\vec{v}_c\right)\cdot\vec{\nabla}B_0\,\frac{\partial f_{1j}}{\partial v_\parallel} = 0\ .\end{aligned} \tag{2.51}$$

2.4 The collision operator

As mentioned previously, the typical particle collision frequency in a hot, low density plasma, as found in a magnetic fusion reactor, is much smaller than the characteristic frequencies of microinstabilities. The gyrokinetic equation (2.51) was thus derived assuming a collisionless plasma. In this description, the interaction between particles only occurs through the macroscopic electromagnetic fields which result from collective processes. In some cases however, direct binary interactions between particles may play a sub-dominant but nonetheless significant role, and are introduced in the model through the so-called Landau collision operator C_j written in particle variables $(\vec{x},\vec{v})$ as:

$$C_j\left(\mathtt{f}_j\right) \quad = \quad \sum_{j'} C_{j\,j'}(\mathtt{f}_j,\mathtt{f}_{j'}) = \sum_{j'}\frac{\partial}{\partial\vec{v}}\cdot\left(\mathbf{D}_{j\,j'}\cdot\frac{\partial}{\partial\vec{v}} - \vec{R}_{j\,j'}\right)\mathtt{f}_j\ , \tag{2.52}$$

where $C_{j\,j'}$ represents collisions of species j with distribution $\mathtt{f}_j$ on species j' with distribution $\mathtt{f}_{j'}$. The collision operator (2.52) appears as a correction term on the right hand side of the Vlasov equation (2.1), leading to the so-called Fokker-Planck equation. Note that in the variables $(\vec{x},\vec{v})$ the Landau operator is an advection-diffusion operator local to velocity space. The quantities $\mathbf{D}_{j\,j'}$ and $\vec{R}_{j\,j'}$ in Eq. (2.52) respectively denote the diffusion

tensor and friction force:

$$\mathbf{D}_{j\,j'} = \frac{\gamma_{j\,j'}}{m_j^2}\,\frac{\partial^2 G_{j'}}{\partial\vec{v}\,\partial\vec{v}}\,, \quad \text{and} \quad \vec{R}_{j\,j'} = \frac{2\,\gamma_{j\,j'}}{m_j\,m_{j'}}\,\frac{\partial H_{j'}}{\partial\vec{v}}\,, \tag{2.53}$$

with $\gamma_{j\,j'} = q_j^2\,q_{j'}^2/(8\,\pi\epsilon_0^2)\,\ln\Lambda$, $\ln\Lambda$ being the Coulomb logarithm, and ϵ_0 the vacuum permittivity. The terms $G_{j'}$ and $H_{j'}$ are the so-called Rosenbluth potentials, function of $\mathtt{f}_{j'}$:

$$G_{j'} = \int d\vec{v}'\;\mathtt{f}_{j'}\;u\,, \quad \text{and} \quad H_{j'} = \int d\vec{v}'\;\mathtt{f}_{j'}\;\frac{1}{u}\,, \tag{2.54}$$

with $u = |\vec{v} - \vec{v}'|$. Considering the decomposition $f_j = f_{0j} + f_{1j}$, and noticing that $C_{j\,j'}$ is bilinear in its arguments f_j and $f_{j'}$, the collision operator can be linearized as follows:

$$\begin{aligned} C_{j\,j'}(f_j, f_{j'}) &= C_{j\,j'}(f_{0j}, f_{0j'}) + C_{j\,j'}(f_{1j}, f_{0j'}) + C_{j\,j'}(f_{0j}, f_{1j'}) + C_{j\,j'}(f_{1j}, f_{1j'}) \\ &\simeq C_{j\,j'}(f_{1j}, f_{0j'}) + C_{j\,j'}(f_{0j}, f_{1j'})\,. \end{aligned} \tag{2.55}$$

In the first line of relation (2.55), the term $C_{j\,j'}(f_{0j}, f_{0j'})$ describes the relaxation of the background distribution functions which occurs at much larger (transport) time scales than the characteristic time of microturbulence and is thus not considered. The neglected nonlinear contribution $C_{j\,j'}(f_{1j}, f_{1j'})$ represents the scattering between the two perturbation components of the distribution functions and is therefore a term of order ϵ^2 in the gyrokinetic ordering. In the final considered model, the term $C_{j\,j'}(f_{1j}, f_{0j'})$, which represents collisions of f_{1j} on $f_{0j'}$ and is a second order differential operator on f_{1j} [see Eq. (2.52], is treated exactly, while the back-reaction term $C_{j\,j'}(f_{0j}, f_{1j'})$, which is an integral operator on $f_{1j'}$, is replaced by a reduced model for practical reasons of implementation. The approximate form for $C_{j\,j'}(f_{0j}, f_{1j'})$ nonetheless preserves the conservation properties of the linearized collision operator, i.e. conservation of mass, momentum and energy.
In order to introduce consistently this linearized collision operator in the gyrokinetic equation (2.51), the gyro-angle dependence is finally removed by applying the gyroaveraging operator (2.33). The resulting gyroaveraged operator

$$\bar{C}_l(f_j) = \sum_{j'} \bar{C}_{j\,j'}(f_{1j}, f_{0j'}) + \sum_{j'} \bar{C}_{j\,j'}(f_{1j}, f_{0j'}) \tag{2.56}$$

is then added to the right hand side of the gyrokinetic equation (2.51). Note that the collision operator, which is a purely velocity space advection-diffusion operator in the

particle variables $(\vec{x}, \vec{v})$ becomes a mixed operator in configuration and velocity space in gyrocenter variables.

The intent of this section was to give a brief overview of the collision operator that may be considered in the model, and the reader is invited to consult Ref. [51] for a more detailed description. In the following, the different equations will however be further derived in the collisionless limit.

2.5 The gyrokinetic equations in field-aligned coordinates

2.5.1 The field aligned coordinates (x, y, z)

As already discussed, microturbulence tends to have much longer wavelengths parallel than perpendicular to the equilibrium magnetic field ($k_\perp \gg k_\parallel$). One can therefore significantly decrease the computational cost by using a field-aligned coordinate system which reflects this property. Although such a coordinate system can be defined for any type of magnetic equilibrium, as described for example in [52], only axisymmetric equilibria, as found in Tokamak devices (see Chap. 4), are considered in the present work.

In an axisymmetric system, one can define a straight field line coordinate system (Ψ, χ, ϕ), see Fig. 2.2, where Ψ is the poloidal flux function, ϕ is the toroidal angle and χ is a poloidal like angle, defined as

$$\left.\frac{d\phi}{d\chi}\right|_{\vec{B}_0} = \frac{\vec{B}_0 \cdot \vec{\nabla}\phi}{\vec{B}_0 \cdot \vec{\nabla}\chi} = q(\Psi) \,, \tag{2.57}$$

so that the field lines are straight in the (χ, ϕ) plane at constant Ψ. The safety factor $q = q(\Psi)$ represents the number of toroidal revolutions of a given field line to complete one poloidal revolution. In this coordinate system, the magnetic field can be expressed as [53]:

$$\vec{B}_0 = \vec{\nabla}\Psi \times \vec{\nabla}(q\,\chi - \phi) \,. \tag{2.58}$$

The field-aligned coordinate system (x, y, z) is then defined by the following transformation:

$$x = C_x(\Psi) - x_0 \,, \quad y = C_y\,(q\chi - \phi) - y_0 \quad \text{and} \quad z = \chi \,, \tag{2.59}$$

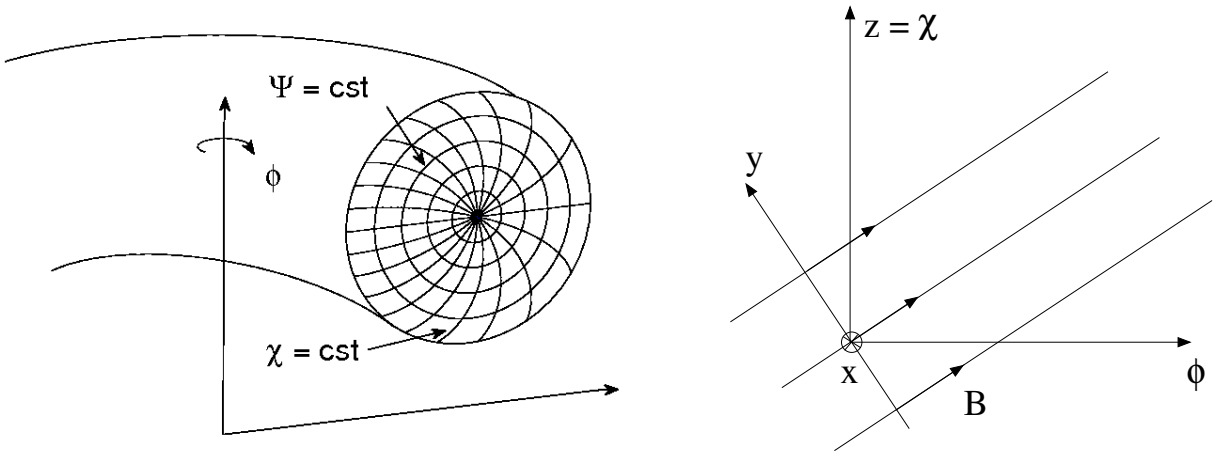

Figure 2.2: Left: Constant Ψ and χ in the poloidal plane for a circular equilibrium, ϕ is the toroidal angle; Right: Illustration of the field aligned coordinate system (x, y, z).

so that the background magnetic field (2.58) can be written:

$$\vec{B}_0 = \mathcal{C}(x)\,\vec{\nabla}x \times \vec{\nabla}y\ , \tag{2.60}$$

having defined the radially dependant quantity $\mathcal{C}(x) = (\frac{dC_x(x)}{d\Psi}\,C_y)^{-1}$. We note in addition that the factor $C_x(\Psi)$ and normalization constant C_y are chosen so that x and y take units of length. The directions $\vec{\nabla}x$ and $\vec{\nabla}y$ are perpendicular to the magnetic field, with x a radial like coordinate and y the binormal coordinate labeling the magnetic lines on a given magnetic surface (see Fig. 2.2). The center of the simulation domain is defined by (x_0,y_0), where in general x_0 is taken as $x_0 = C_x(\Psi_0)$ with Ψ_0 the poloidal flux at the center of the domain, y_0 can be chosen arbitrarily due to the axisymmetry of the magnetic equilibrium. One finally defines $z = \chi$, which, for given x and y coordinates determines the position along the corresponding magnetic line. The coordinate z will thus be referred to as the parallel coordinate.

A more detailed discussion on different Tokamak equilibrium models is provided in Chapter 4.

2.5.2 The gyrokinetic equation in (x, y, z) coordinates

In order to evaluate Eq. (2.51) in the (x, y, z) coordinates, the quantities

$$\vec{B}_0 \times \vec{\nabla}\mathcal{F} \cdot \vec{\nabla} \quad \text{and} \quad \vec{B}_0 \cdot \vec{\nabla}\ , \tag{2.61}$$

where $\mathcal{F}$ is any scalar field, need to be derived.

Using relation (2.60), one has (sums over indices are implicit):

$$\begin{aligned}
\vec{B}_0 \times \vec{\nabla}\mathcal{F} \cdot \vec{\nabla} &= \mathcal{C}(\vec{\nabla}x \times \vec{\nabla}y) \times \vec{\nabla}\mathcal{F} \cdot \vec{\nabla} \\
&= \mathcal{C}\left[(\vec{\nabla}\mathcal{F} \cdot \vec{\nabla}x)\vec{\nabla}y - (\vec{\nabla}\mathcal{F} \cdot \vec{\nabla}y)\vec{\nabla}x\right] \cdot \vec{\nabla} \\
&= \mathcal{C}\left[(\partial_i\mathcal{F}\,\vec{\nabla}u^i \cdot \vec{\nabla}x)\vec{\nabla}y - (\partial_i\mathcal{F}\,\vec{\nabla}u^i \cdot \vec{\nabla}y)\vec{\nabla}x\right] \cdot \vec{\nabla} \\
&= \mathcal{C}\left[g^{1i}\vec{\nabla}y - g^{2i}\vec{\nabla}x\right]\partial_i\mathcal{F} \cdot \vec{\nabla}u^j\partial_j \\
&= \mathcal{C}(g^{1i}g^{2j} - g^{2i}g^{1j})\partial_i\mathcal{F}\,\partial_j\ ,
\end{aligned}$$

with $g^{ij} = \nabla u^i \cdot \nabla u^j$ the metric tensor elements and $u^i = (x, y, z)$.

$$\begin{aligned}
\vec{B}_0 \cdot \vec{\nabla} &= \mathcal{C}(\vec{\nabla}x \times \vec{\nabla}y) \cdot \vec{\nabla}u^j\,\partial_i \\
&= \mathcal{C}(\vec{\nabla}x \times \vec{\nabla}y) \cdot \vec{\nabla}z\,\partial_z \\
&= \frac{\mathcal{C}}{J^{xyz}}\,\partial_z\ ,
\end{aligned}$$

where $J^{xyz} = \left[(\vec{\nabla}x \times \vec{\nabla}y) \cdot \vec{\nabla}z\right]^{-1}$ is the Jacobian of the (x, y, z) coordinate system.

Before writing in detail the different terms of the gyrokinetic equation in the (x, y, z) coordinates, some further simplifications are introduced. Using the fact that microinstabilities tend to align with the magnetic field, $|k_\parallel| \ll |k_\perp|$, $\partial/\partial z$ derivatives of perturbed quantities are neglected with respect to $\partial/\partial x$ and $\partial/\partial y$ derivatives[2]. In addition, one notes that as a result of the axisymmetry of the equilibrium, all background quantities are independent of y, so that all y-derivatives of such quantities vanish.

With the above-mentioned approximations, the different terms of the gyrokinetic equation read:

$$\begin{aligned}
\vec{v}_E \cdot \vec{\nabla} f_{0j} &\simeq \frac{\mathcal{C}}{B_0^2}\left(\gamma_2\,\partial_z f_{0j}\,\partial_x\bar{\chi}_1 - \gamma_1\,\partial_x f_{0j}\,\partial_y\bar{\chi}_1 + \gamma_3\,\partial_z f_{0j}\,\partial_y\bar{\chi}_1\right), \\
\vec{v}_E \cdot \vec{\nabla} B_0 &\simeq \frac{\mathcal{C}}{B_0^2}\left(\gamma_2\,\partial_z B_0\,\partial_x\bar{\chi}_1 - \gamma_1\,\partial_x B_0\,\partial_y\bar{\chi}_1 + \gamma_3\,\partial_z B_0\,\partial_y\bar{\chi}_1\right), \\
\vec{v}_E \cdot \vec{\Gamma}_j &\simeq \frac{\mathcal{C}\gamma_1}{B_0^2}(\partial_x\bar{\chi}_1\,\Gamma_{y,j} - \partial_y\bar{\chi}_1\,\Gamma_{x,j}),
\end{aligned}$$

[2]Some further discussion concering this approximation is provided in section 2.11.

$$
\begin{aligned}
\vec{v}_{\nabla B}\cdot\vec{\Gamma}_j &\simeq \frac{\mathcal{C}\mu}{m_j\Omega_j B_0}\left(\gamma_1\partial_x B_0\,\Gamma_{y,j}-\gamma_2\partial_z B_0\,\Gamma_{x,j}-\gamma_3\partial_z B_0\,\Gamma_{y,j}\right),\\
\vec{v}_c\cdot\vec{\Gamma}_j &\simeq \frac{\mathcal{C}v_\parallel^2}{\Omega_j B_0^2}\left(\gamma_1\partial_x B_0\,\Gamma_{y,j}-\gamma_2\partial_z B_0\,\Gamma_{x,j}-\gamma_3\partial_z B_0\,\Gamma_{y,j}\right)+\frac{\mu_0 v_\parallel^2\mathcal{C}}{\Omega_j B_0^3}\gamma_1\,\partial_x p_0\,\Gamma_{y,j},\\
\vec{b}_0\cdot\vec{\Gamma}_j &= \frac{\mathcal{C}}{B_0\,J^{xyz}}\,\Gamma_{z,j},\\
\vec{b}_0\cdot\vec{\nabla}B_0 &= \frac{\mathcal{C}}{B_0\,J^{xyz}}\,\partial_z B_0\ ,\\
\vec{v}_c\cdot\vec{\nabla}B_0 &= 0+\mathcal{O}(\beta_{\rm ref}\,\rho_{\rm ref}/L_{\rm ref})\ ,
\end{aligned}
$$

where $\beta_{\rm ref}$, $\rho_{\rm ref}$, $L_{\rm ref}$ are defined in section 2.10.1, and

$$
\Gamma_{\alpha,j}=\partial_\alpha f_{1j}-\frac{q_j}{m_j v_\parallel}\,\partial_\alpha\bar{\Phi}_1\,\frac{\partial f_{0j}}{\partial v_\parallel}\ ,\qquad \text{for }\ \alpha=(x,y,z)\ .
$$

In addition, the following notation was introduced for these particular combinations of the metric coefficients:

$$
\begin{aligned}
\gamma_1 &= g^{11}g^{22}-(g^{12})^2,\\
\gamma_2 &= g^{11}g^{23}-g^{12}g^{13},\\
\gamma_3 &= g^{12}g^{23}-g^{22}g^{13}.
\end{aligned}
$$

The gyrokinetic equation (2.51) can thus finally be written :

$$
\begin{aligned}
-\partial_t\,g_{1j} &= \frac{1}{\mathcal{C}\gamma_1}\frac{B_0}{B_{0\parallel}^*}\Big[\underbrace{\gamma_2\,\partial_z f_{0j}\,\partial_x\bar{\chi}_1}-\gamma_1\,\partial_x f_{0j}\,\partial_y\bar{\chi}_1+\underbrace{\gamma_3\,\partial_z f_{0j}\,\partial_y\bar{\chi}_1}\\
&- \frac{\mu}{m_j v_\parallel}\underbrace{\left(\gamma_2\,\partial_z B_0\,\partial_x\bar{\chi}_1-\gamma_1\,\partial_x B_0\,\partial_y\bar{\chi}_1+\gamma_3\,\partial_z B_0\,\partial_y\bar{\chi}_1\right)\partial_{v_\parallel}f_{0j}}\Big]\\
&+ \frac{1}{\mathcal{C}}\frac{B_0}{B_{0\parallel}^*}(\partial_x\bar{\chi}_1\,\Gamma_{y,j}-\partial_y\bar{\chi}_1\,\Gamma_{x,j})\\
&+ \frac{B_0}{B_{0\parallel}^*}\frac{\mu\,B_0+m_j\,v_\parallel^2}{m_j\Omega_j}\left(\mathcal{K}_x\,\Gamma_{x,j}+\mathcal{K}_y\,\Gamma_{y,j}\right)+\frac{1}{\mathcal{C}}\frac{B_0}{B_{0\parallel}^*}\frac{\mu_0\,v_\parallel^2}{\Omega_j\,B_0}\,\partial_x p_0\,\Gamma_{y,j}\\
&+ \frac{\mathcal{C}\,v_\parallel}{B_0\,J^{xyz}}\,\Gamma_{z,j}-\frac{\mathcal{C}\,\mu}{m_j\,B_0\,J^{xyz}}\partial_z B_0\,\partial_{v_\parallel}f_{1j}\ ,
\end{aligned}
\tag{2.62}
$$

where

$$
\mathcal{K}_x = -\frac{1}{\mathcal{C}}\frac{\gamma_2}{\gamma_1}\partial_z B_0,
\tag{2.63}
$$

$$\mathcal{K}_y \;=\; \frac{1}{\mathcal{C}}\left(\partial_x B_0 - \frac{\gamma_3}{\gamma_1}\partial_z B_0\right)\,, \tag{2.64}$$

and having used the relation $B_0^2 = \mathcal{C}^2\gamma_1$.

2.6 Choice for the background distribution

One considers the background distribution f_{0j} as being a local Maxwellian of the form :

$$f_{0j}(x,z,v_\parallel,\mu) = \left(\frac{m_j}{2\pi T_{0j}(x)}\right)^{\frac{3}{2}} n_{0j}(x)\ \exp\left(-\frac{m_j v_\parallel^2/2 + \mu B_0(x,z)}{T_{0j}(x)}\right)\,, \tag{2.65}$$

where the temperature and density profiles T_{0j} and n_{0j} are function of x, so that:

$$\partial_x f_{0j} \;=\; \left[\frac{d\ln n_{0j}}{dx} + \left(\frac{m_j v_\parallel^2}{2T_{0j}} + \frac{\mu B_0}{T_{0j}} - \frac{3}{2}\right)\frac{d\ln T_{0j}}{dx} - \underbrace{\frac{\mu}{T_{0j}}\partial_x B_0}\right]\ f_{0j}\,, \tag{2.66}$$

$$\partial_z f_{0j} \;=\; -\frac{\mu}{T_{0j}}\partial_z B_0 f_{0j}\,, \tag{2.67}$$

$$\partial_{v_\parallel} f_{0j} \;=\; -\frac{m_j v_\parallel}{T_{0j}} f_{0j}\,, \tag{2.68}$$

$$\partial_\mu f_{0j} \;=\; -\frac{B_0}{T_{0j}} f_{0j}\,. \tag{2.69}$$

One notes that (2.65) is only solution of Eq. (2.49) if one neglects the $\vec{v}_{\nabla B}$ and $\vec{v}_c$ drifts. In the following, it will nevertheless be assumed that Eq. (2.49) is satisfied. This choice for f_{0j} leads to a more compact form of Eq. (2.62) since the underbraced terms in Eqs. (2.62) and (2.66) cancel out.

A true solution to Eq. (2.49), *i.e.* including the finite orbit width effects resulting from the drifts $\vec{v}_{\nabla B}$ and $\vec{v}_c$, would be given by a so-called canonical Maxwellian F_{CM} [21]. The distribution F_{CM} is function of the three constants of motion of the unperturbed axisymmetric system: the kinetic energy K, the magnetic moment μ, and the canonical angular momentum P_ϕ. The local Maxwellian (2.65) can thus be seen as a canonical Maxwellian in the limit of zero finite orbit width.

2.7 Velocity moments of the distribution function

As will be seen in section 2.8, it is necessary to evaluate different velocity moments of the distribution function in order to solve the field equations. In this section, we discuss how these moments, which need to be evaluated at fixed particle positions, are computed given the particle distribution function f, solution of the gyrokinetic equation, in gyrocenter variables.

The m^{th} $v_\parallel$ and n^{th} $v_\perp$ moments of the fluctuating part of the particle distribution $\mathtt{f}_j(\vec{x},\vec{v})$ are defined as:

$$M_{j,mn}(\vec{x}) = \int \mathtt{f}_{1j}(\vec{x},\vec{v})\, v_\parallel^m v_\perp^n \, d\vec{v} \,. \tag{2.70}$$

Using a Dirac function $\delta(\vec{x\prime} - \vec{x})$, the velocity integral is converted to a full phase-space integral:

$$M_{j,mn}(\vec{x}) = \int \mathtt{f}_{1j}(\vec{x\prime},\vec{v})\ \delta(\vec{x\prime} - \vec{x})\, v_\parallel^m\, v_\perp^n\ d\vec{x\prime}\, d\vec{v} \,, \tag{2.71}$$

which facilitates a first change of variables to guiding center variables $\mathtt{f}_{1j}(\vec{x},\vec{v}) \ \rightarrow\ f_{g,1j}(\vec{Z}_g)$, where $\vec{Z}_g = (\vec{X}_g, v_{\parallel,g}, \mu_g, \alpha_g)$ are defined in Eq. (2.14). One obtains:

$$M_{j,mn}(\vec{x}) = \int f_{g,1j}(\vec{X}_g, v_{\parallel,g}, \mu_g, \alpha_g)\, \delta(\vec{X}_g + \vec{\rho} - \vec{x})\ v_{\parallel,g}^m\, v_{\perp,g}^n\, J_g\ d\vec{X}_g\, dv_{\parallel,g}\, d\mu_g\, d\alpha_g \,, \tag{2.72}$$

where the phase-space Jacobian J_g is given by relation (2.16).

One then makes use of Eq. (2.36), which enables to derive the distribution f_{1g} in guiding center variables in terms of the distribution function $f(\vec{X}, v_\parallel, \mu)$ in gyrocenter variables:

$$\begin{aligned} f_{g,1j}(\vec{Z}_g) &= T^{-1} f_{1j}(\vec{Z}_g) \\ &= f_{1j}(\vec{X}_g, \mu_g, v_{\parallel,g}) + \frac{1}{B_0(\vec{X}_g)} \Bigg\{ \Bigg[\Omega_j(\vec{X}_g)\, \frac{\partial f_{0j}}{\partial v_{\parallel,g}}(\vec{X}_g, \mu_g, v_{\parallel,g}) \\ &\quad - q_j\, v_{\parallel,g}\, \frac{\partial f_{0j}}{\partial \mu_g}(\vec{X}_g, \mu_g, v_{\parallel,g}) \Bigg]\ \tilde{A}_{1\parallel}(\vec{X}_g, \mu_g) \\ &\quad + q_j\, \tilde{\Phi}_1(\vec{X}_g, \mu_g)\ \frac{\partial f_{0j}}{\partial \mu_g}(\vec{X}_g, \mu_g, v_{\parallel,g}) \Bigg\} \,. \end{aligned} \tag{2.73}$$

Note that in the following, the subscript g shall be dropped. By replacing this last expression for $f_{g,1j}$ in the moment equation (2.72), one obtains:

$$\begin{aligned} M_{j,mn}(\vec{x}) &= \frac{1}{m_j}\int \delta(\vec{X}+\vec{\rho}-\vec{x})\, B^*_{0\|}(\vec{X},v_\|)\; v_\|^m\, v_\perp^n \left\{ f_{1j}(\vec{X},\mu,v_\|) \right. \\ &+ \frac{1}{B_0(\vec{X})}\left[\left(\Omega_j(\vec{X})\,\frac{\partial f_{0j}}{\partial v_\|}(\vec{X},\mu,v_\|)\right.\right. \\ &\quad \left.\left. -q_j\, v_\|\,\frac{\partial f_{0j}}{\partial \mu}(\vec{X},\mu,v_\|)\right)\,\left(A_{1\|}(\vec{X}+\vec{\rho})-\bar{A}_{1\|}(\vec{X},\mu)\right)\right. \\ &+ \left. q_j\,\left[\Phi_1(\vec{X}+\vec{\rho})-\bar{\Phi}_1(\vec{X},\mu)\right]\frac{\partial f_{0j}}{\partial \mu}(\vec{X},\mu,v_\|)\right]\Bigg\}\; d\vec{X}\, dv_\|\, d\mu\, d\alpha\ . \end{aligned} \tag{2.74}$$

Integrating now over the $\vec{X}$ variable leads to:

$$\begin{aligned} M_{j,mn}(\vec{x}) &= \frac{1}{m_j}\int B^*_{0\|}(\vec{x},v_\|)\; v_\|^m\, v_\perp^n \left\{ f_{1j}(\vec{x}-\vec{\rho},\mu,v_\|) \right. \\ &+ \frac{1}{B_0(\vec{x})}\left[\left(\Omega_j(\vec{x})\,\frac{\partial f_{0j}}{\partial v_\|}(\vec{x},\mu,v_\|)\right.\right. \\ &\quad \left.\left. -q_j\, v_\|\,\frac{\partial f_{0j}}{\partial \mu}(\vec{x},\mu,v_\|)\right)\,\left(A_{1\|}(\vec{x})-\bar{A}_{1\|}(\vec{x}-\vec{\rho},\mu)\right)\right. \\ &+ \left. q_j\,\left[\Phi_1(\vec{x})-\bar{\Phi}_1(\vec{x}-\vec{\rho},\mu)\right]\frac{\partial f_{0j}}{\partial \mu}(\vec{x},\mu,v_\|)\right]\Bigg\}\; dv_\|\, d\mu\, d\alpha\ , \end{aligned} \tag{2.75}$$

where the variations over the Larmor radius have been neglected for all equilibrium quantities, e.g. $B_0(\vec{x}-\vec{\rho}) \sim B_0(\vec{x})$, as one only works to lowest order in ϵ. By introducing the gyro-average $\bar{f}_{1j}$ of the fluctuating component of the distribution function, as well as the double gyro-average electrostatic potential $\bar{\bar{\Phi}}_1$ and parallel component of the vector potential $\bar{\bar{A}}_{1\|}$, Eq. (2.75) can be written:

$$\begin{aligned} M_{j,mn}(\vec{x}) &= \frac{2\pi}{m_j}\int B^*_{0\|}(\vec{x},v_\|)\; v_\|^m v_\perp^n \left\{ \bar{f}_{1j}(\vec{x},\mu,v_\|) \right. \\ &+ \frac{1}{B_0(\vec{x})}\left[\left(\Omega_j(\vec{x})\,\frac{\partial f_{0j}}{\partial v_\|}(\vec{x},\mu,v_\|)\right.\right. \\ &\quad \left.\left. -q_j\, v_\|\,\frac{\partial f_{0j}}{\partial \mu}(\vec{x},\mu,v_\|)\right)\,\left(A_{1\|}(\vec{x})-\bar{\bar{A}}_{1\|}(\vec{x},\mu)\right)\right. \\ &+ \left. q_j\,\left[\Phi_1(\vec{x})-\bar{\bar{\Phi}}_1(\vec{x},\mu)\right]\frac{\partial f_{0j}}{\partial \mu}(\vec{x},\mu,v_\|)\right]\Bigg\}\; dv_\|\, d\mu\ , \end{aligned} \tag{2.76}$$

where the double gyro-averaging of any scalar quantity $\mathcal{F}$ is given, according to (2.33), by:

$$\bar{\bar{\mathcal{F}}} = \frac{1}{2\pi} \oint d\alpha \, \bar{\mathcal{F}} \left(\hat{\vec{X}} - \hat{\vec{\rho}} \right) = \frac{1}{(2\pi)^2} \oint d\alpha \, d\alpha' \, \bar{\mathcal{F}} \left(\vec{X} - \rho - \rho' \right) . \tag{2.77}$$

Note that for a Maxwellian equilibrium distribution function f_0, the $A_{1\parallel}$ contributions vanish as a result of Eqs. (2.68) and (2.69). In addition, since the perturbed electrostatic potential does not depend on $v_\parallel$, these integrals can be evaluated analytically, see [28], leading to

$$\begin{aligned} M_{j,mn}(\vec{x}) &= \pi \left(\frac{2\,B_0}{m_j} \right)^{n/2+1} \int \frac{B^*_{0\parallel}}{B_0} \, \bar{f}_{1j} \, v_\parallel^m \, \mu^{n/2} \, dv_\parallel \, d\mu \\ &- \frac{v_{Tj}^m \, n_{0j} \, q_j \, B_0}{T_{0j}^2} \left(\frac{2\,B_0}{m_j} \right)^{n/2} \left[\mathcal{I}(m) + \frac{2\,\mu_0 \, T_{0j}}{B_0^2} \frac{j_{0\parallel}}{q_j \, v_{Tj}} \mathcal{I}(m+1) \right] \\ &\left[\left(\frac{T_{0j}}{B_0} \right)^{n/2+1} (n/2)! \, \Phi_1 - \int \bar{\bar{\Phi}}_1 \, \exp\left(-\frac{\mu B_0}{T_{0j}} \right) \mu^{n/2} d\mu \right] , \end{aligned} \tag{2.78}$$

where $j_{0\parallel} = \vec{j}_0 \cdot \vec{b}_0 = (\vec{\nabla} \times \vec{B}_0/\mu_0) \cdot \vec{b}_0$ and the function $\mathcal{I}(m)$ is

$$\begin{aligned} &\mathcal{I}(m) = 0 \,, \quad \text{for m odd} \;\; , \\ &\text{and} \;\; \mathcal{I}(m) = \frac{\Gamma(\frac{m+1}{2})}{\sqrt{\pi}} = \frac{(m-1)(m-3)...3 \cdot 1}{2^{m/2}} \,, \qquad \text{for m even} \,, \end{aligned}$$

with $\Gamma(m)$ the usual gamma function. One in particular has $I(0) = 1$.

2.8 The field equations

In order to close the system, the perturbed electrostatic potential Φ_1 and parallel component $A_{1\parallel}$ of the vector potential appearing in the gyrokinetic equations are self-consistently obtained by solving respectively the quasi-neutrality equation and the parallel component of Ampère's law.

The quasi-neutrality equation

For typical Tokamak parameters, the Debye length is much smaller than the wavelengths of the microinstabilities (typically of the order of the particle gyroradius) and one can thus

assume quasi-neutrality[3]:

$$\sum_j q_j \; n_{1j}(\vec{x}) = 0 \; . \tag{2.79}$$

The perturbed density n_{1j} is given the zeroth order moment $M_{j,00}$ of the distribution function and is obtained using Eq. (2.78). The quasi-neutrality equation (Q.N.) thus reads:

$$\sum_j \frac{2\,\pi\,q_j}{m_j} \int B^*_{0\|}\, \bar{f}_{1j}\; dv_\| \, d\mu - \frac{q_j^2\, n_{0j}}{T_{0j}} \left[\Phi_1 - \frac{B_0}{T_{0j}} \int \bar{\bar{\Phi}}_1 \; \exp(-\frac{\mu B_0}{T_{0j}}) \, d\mu \right] = 0 \; . \tag{2.80}$$

We note here that the moment equation (2.78) was obtained using the first order in ϵ pull-back operator T^{-1}, so that Eq. (2.80) is a linear integral equation for Φ_1. The first term in Eq. (2.80) is the so-called gyro-density, while the last two terms are referred to as the polarization density, which results from the difference between guiding center and gyrocenter coordinates, *i.e.* an effect related to finite amplitude field fluctuations.

Adiabatic electron case

The general equation (2.80) is used when considering the full kinetic dynamics of a given species. One can in some cases simplify computations by assuming an adiabatic electron response, that is considering the limit $\omega/(k_\| v_{the}) \to 0$. This limit is in particular invoked when studying turbulence in the ITG regime. In this case, the electron density is assumed to follow a Boltzmann distribution:

$$n_e(\vec{x}) = N(x) \exp\left(\frac{e\Phi_1(\vec{x})}{T_e(x)}\right) = N(x)\left(1 + \frac{e\Phi_1(\vec{x})}{T_e(x)}\right) + \mathcal{O}(\epsilon^2) \; , \tag{2.81}$$

where a linearization, justified by the gyrokinetic ordering $e\,\Phi_1/T_e \sim \epsilon$, has been carried out for obtaining the last equality. The coefficient $N(x)$ is set by assuming that the perturbed electron density cancels on average over a given flux surface:

$$\langle\, n_e(\vec{x}) \,\rangle = \langle\, n_{0e}(x) + n_{1e}(\vec{x}) \,\rangle = \langle\, n_{0e}(x) \,\rangle + \langle\, n_{1e}(\vec{x}) \,\rangle = n_{0e}(x) \; , \tag{2.82}$$

where the flux-surface average $\langle\, . \,\rangle$ is defined for any quantity $\mathcal{F}$ as:

$$\langle\, \mathcal{F}(\vec{x}) \,\rangle = \frac{1}{\Delta V} \int_{\Delta V} \mathcal{F} d^3x = \frac{\int \mathcal{F}(\vec{x})\; J^{xyz}(x,z)\; dz\; dy}{\int J^{xyz}(x,z)\; dz\; dy} \; , \tag{2.83}$$

[3]Finite Debye length effects can be, in fact, accounted for in GENE, thus replacing the quasi-neutrality equation with the Poisson equation. They are however never considered in the present work and $L_{\mathrm{Debye}} \to 0$ is assumed.

where ΔV is an infinitesimally small volume between two neighboring flux surfaces Ψ and $\Psi + \Delta\Psi$, $|\Delta\Psi/\Psi| \ll 1$. From Eqs. (2.81) and (2.82), one obtains for $N(x)$:

$$n_{0e}(x) = N(x) \left\langle 1 + \frac{e\Phi_1(\vec{x})}{T_e(x)} \right\rangle + \mathcal{O}(\epsilon^2) \tag{2.84}$$

$$\Rightarrow \; N(x) \simeq n_{0e}(x) \left(1 - \frac{e\langle\, \Phi_1(\vec{x})\,\rangle}{T_e(x)}\right) + \mathcal{O}(\epsilon^2)\,. \tag{2.85}$$

By inserting Eq. (2.85) in (2.81), the perturbed electron density finally reads:

$$n_{1e}(\vec{x}) = \frac{n_{0e}(\vec{x})\, e}{T_{0e}(\vec{x})}(\Phi_1 - \langle\Phi_1\rangle)\,. \tag{2.86}$$

Introducing this last relation for the electron density fluctuation into the quasi-neutrality equation, leads to:

$$\begin{aligned} -\frac{e^2\, n_{0e}}{T_{0e}}(\Phi_1 \;&-\; \langle\Phi_1\rangle) + \sum_{j\neq e} \left\{ \frac{2\,\pi\, q_j}{m_j} \int B^*_{0\|}\, \bar{f}_{1j}\, dv_\|\, d\mu \right. \\ &- \left. \frac{q_j^2\, n_{0j}}{T_{0j}} \left[\Phi_1 - \frac{B_0}{T_{0j}} \int \bar{\bar{\Phi}}_1\, \exp(-\frac{\mu B_0}{T_{0j}})\, d\mu\right] \right\} = 0\,. \end{aligned} \tag{2.87}$$

Additional approximations are made to numerically solve Eq. (2.87). These will be discussed in section 3.3.5.

Ampère's law

The potential $A_{1\|}$ is obtained by solving the parallel component of Ampère's law for the fluctuation fields:

$$-\nabla^2_\perp A_{1\|} = \mu_0 \sum_j j_{1\|,j}\,, \tag{2.88}$$

having neglected the displacement current, as well as made use of the gyrokinetic ordering (2.2) and (2.3), which enable to write:

$$(\nabla^2 \vec{A}_1)\cdot\vec{b}_0 \simeq \nabla^2_\perp(\vec{A}_1\cdot\vec{b}_0) = \nabla^2_\perp(\vec{A}_{1\|})\,. \tag{2.89}$$

The perturbed parallel current $j_{1\|,j}$ is given by the first order $v_\|$ moment of the perturbed distribution function and is obtained using Eq. (2.78) for $M_{j,10}$. One thus obtains:

$$\begin{aligned} -\nabla^2_\perp A_{1\|} \;&=\; \mu_0 \sum_j \left\{ \frac{2\pi q_j}{m_j} \int B^*_{0\|}\, v_\|\, \bar{f}_{1j}(\vec{x}, v_\|, \mu)\, dv_\|\, d\mu \right. \\ &\left. - \frac{q_j\, n_{0j}\, \mu_0\, j_{0\|}}{B_0^2} \left(\Phi_1 - \frac{B_0}{T_{0j}} \int \bar{\bar{\Phi}}_1(\vec{x})\, \exp\left(-\frac{\mu\, B_0}{T_{0j}}\right)\, d\mu\right) \right\}. \end{aligned} \tag{2.90}$$

One notes that given the electrostatic potential Φ_1 solution of Eq. (2.80), Eq. (2.90) is a linear differential equation for $A_{1\parallel}$.

2.9 Macroscopic quantities

In order to compare simulation results with experimental measurements and in particular to address the issue of anomalous particle and heat transport, relevant macroscopic quantities, namely particle and heat fluxes need to be evaluated. An appropriate form for these different fluxes can be derived by considering velocity moments of the gyrokinetic equation, thus obtaining conservation laws for the density and energy of each species.
We note that as the gyrokinetic equation describes the evolution of the particle distribution in gyrocenter variables, one obtains in this way conservation equations for the gyrocenter density $\tilde{n}_j$ and energy density $\tilde{p}_j$:

$$\tilde{n}_j = \int f_j \, J \, dv_\parallel \, d\mu; \quad \text{and} \quad \tilde{p}_j = \frac{1}{3} \int m_j \, v^2 \, f_j \, J \, dv_\parallel \, d\mu \, , \tag{2.91}$$

where J is the phase-space Jacobian of the transformation from particle to gyrocenter variables:

$$J = |B^*_{0\parallel} + \vec{\nabla} \times (A_{1\parallel} \, \vec{b}_0) \cdot \vec{b}_0|/m = B^*_{0\parallel}/m + \mathcal{O}(\epsilon^2) \, , \tag{2.92}$$

2.9.1 Velocity moments of the gyrokinetic equation

As a starting point, one first seeks to write the gyrokinetic equation in a conservative form, which can be obtained by considering Liouville's theorem:

$$\frac{\partial J}{\partial t} + \sum_i \frac{\partial}{\partial Z_i} (J \, \dot{Z}_i) = 0 \, , \tag{2.93}$$

where J is the phase space Jacobian (2.92). The gyrokinetic equation (2.46) can thus be written as:

$$\frac{\partial}{\partial t} (\, J \, f_j) + \frac{\partial}{\partial \vec{X}} \cdot (\, J \dot{\vec{X}} \, f_j) + \frac{\partial}{\partial v_\parallel} (\, J \dot{v}_\parallel \, f_j) = 0 \, , \tag{2.94}$$

where $\dot{\vec{X}}$ and $\dot{v}_\parallel$ are given by Eqs. (2.38) and (2.39). Let us now consider the general velocity moment $s = s(\vec{X}, v_\parallel, \mu)$ of Eq. (2.94):

$$\int s \frac{\partial}{\partial t}(J\, f_j)\, dv_\parallel\, d\mu + \int s \frac{\partial}{\partial \vec{X}} \cdot (\, J\dot{\vec{X}}\, f_j)\, dv_\parallel\, d\mu + \int s \frac{\partial}{\partial v_\parallel}(\, J\dot{v}_\parallel\, f_j)\, dv_\parallel\, d\mu = 0\ . \quad (2.95)$$

Considering that s may be a function of $v_\parallel$ and $\vec{X}$, and that the distribution function vanishes for $v_\parallel \to \pm\infty$, Eq. (2.95) can be express after integration by pasts as:

$$\frac{\partial}{\partial t}\int s\, f_j\, J\, dv_\parallel\, d\mu - \frac{\partial}{\partial \vec{X}}\cdot\int s\, \dot{\vec{X}}\, f_j\, J\, dv_\parallel\, d\mu - \int \dot{\vec{X}}\cdot\frac{\partial s}{\partial \vec{X}}\, f_j\, J\, dv_\parallel\, d\mu + \int \dot{v}_\parallel \frac{\partial s}{\partial v_\parallel}\, f_j\, J\, dv_\parallel\, d\mu = 0\ . \quad (2.96)$$

Noticing that the total time derivative of s reads:

$$\frac{ds}{dt} = \dot{\vec{X}} \cdot \frac{\partial s}{\partial \vec{X}} + \dot{v}_\parallel \frac{\partial s}{\partial v_\parallel}\ , \quad (2.97)$$

and using the notation, $\vec{v}_G = \dot{\vec{X}}$, the moment equation can finally be written in the more compact form:

$$\frac{\partial}{\partial t}\int s\, f_j\, J\, dv_\parallel\, d\mu + \frac{\partial}{\partial \vec{X}} \cdot \int s\, \vec{v}_G\, f_j\, J\, dv_\parallel\, d\mu - \int \frac{ds}{dt}\, f_j\, J\, dv_\parallel\, d\mu\ . \quad (2.98)$$

By considering first the $s = 1$ moment, one obtains the continuity equation:

$$\frac{\partial\, \tilde{n}_j}{\partial t} + \frac{\partial}{\partial \vec{X}} \cdot \vec{\tilde{\Gamma}}_j = 0\ , \quad (2.99)$$

where the gyrocenter density $\tilde{n}_j(\vec{X})$ is defined in Eq. (2.91) and the notation

$$\vec{\tilde{\Gamma}}_j = \int \vec{v}_G\, f_j\, J\, dv_\parallel\, d\mu \quad (2.100)$$

is used to denote the gyrocenter flux.

An equation describing the conservation of energy is obtained with $s = m_j\, v^2/2 = m_j\, v_\parallel^2 + B_0\, \mu$:

$$\frac{3}{2}\frac{\partial\, \tilde{p}_j}{\partial t} + \frac{\partial}{\partial \vec{X}} \cdot \vec{\tilde{Q}}_j = \tilde{P}_j\ , \quad (2.101)$$

where the gyrocenter energy density has already been introduced in Eq. (2.91) and with energy flux defined as:

$$\vec{\tilde{Q}}_j = \int m_j\, \frac{v^2}{2}\, \vec{v}_G\, f_j\, J\, dv_\parallel\, d\mu\ . \quad (2.102)$$

To obtain the power density, one starts by computing the total derivative of v^2:

$$\begin{aligned}\frac{m_j}{2}\frac{d\,v^2}{dt} &= \frac{m_j}{2}\left(\dot{\vec{X}}\cdot\frac{\partial}{\partial\vec{X}}+\dot{v}_\parallel\frac{\partial}{\partial v_\parallel}\right)\left(v_\parallel^2+\frac{2\,B_0\,\mu}{m_j}\right)\\ &= \mu\,\dot{\vec{X}}\cdot\vec{\nabla}B_0+m_j\,v_\parallel\dot{v}_\parallel\\ &= q_j\,\vec{v}_G\cdot\vec{E}\end{aligned} \tag{2.103}$$

where relation (2.39) has been used for $\dot{v}_\parallel$ and with the electric field $\vec{E}=-\vec{\nabla}\bar{\Phi}_1-\vec{b}_0\;\dot{\bar{A}}_{1\parallel}$, considering only $A_{1\parallel}$ magnetic fluctuations. The power density finally reads:

$$\tilde{P}_j=\int q_j\,\vec{v}_G\cdot\vec{E}\,f_j\,J\,dv_\parallel\,d\mu\;. \tag{2.104}$$

2.9.2 Radial conservation equations

The conservation equations (2.99) and (2.101) describe the evolution of density and energy in the three spatial dimensions. However, as transport processes relevant to confinement take place in the radial direction, one is mostly interested in the radial evolution of the flux-surface averaged density and energy.

By integrating Eq. (2.99) over the volume V enclosed by the flux surface $x=$ const. and using the divergence theorem, one obtains:

$$\int_V\frac{\partial\,\tilde{n}_j}{\partial t}\,dV+\int_{\partial V}\vec{\tilde{\Gamma}}_j\cdot\frac{\vec{\nabla}x}{|\vec{\nabla}x|}\,dS=0 \tag{2.105}$$

where the elementary surface element is $dS=|\vec{\nabla}x|\,J^{xyz}\,dy\,dz$, with J^{xyz} the Jacobian to the (x,y,z) field-aligned coordinates.

The volume integral over the density can be express as:

$$\int_V\tilde{n}_j\,dV=\int_0^x dx\int\tilde{n}_j\,J^{xyz}\,dy\,dz=\int_0^x dx\,\langle\tilde{n}_j\rangle\,V'\;, \tag{2.106}$$

having introduced

$$V'=\frac{\partial V}{\partial x}=\int J^{xyz}\,dy\,dz\;. \tag{2.107}$$

and where $\langle.\rangle$ is the flux-surface average operator, defined in Eq. (2.83). Finally, differentiating Eq. (2.106) with respect to x, one obtains:

$$\frac{\partial}{\partial t}[\langle\tilde{n}_j\rangle\,V']+\frac{\partial}{\partial x}[\,\langle\vec{\tilde{\Gamma}}_j\cdot\vec{\nabla}x\rangle\,V']=0\;. \tag{2.108}$$

Similarly a radial energy conservation equation is derived from (2.101):

$$\frac{3}{2}\frac{\partial}{\partial t}[\langle \tilde{p}_j \rangle V'] + \frac{\partial}{\partial x}[\langle \vec{\tilde{Q}}_j \cdot \vec{\nabla} x \rangle V'] + \langle \tilde{P}_j \rangle V' = 0 \,. \tag{2.109}$$

We note that if one would solve the gyrokinetic equation (2.47) without further approximations, Eqs. (2.108)-(2.109) would represent exact conservation equations and could thus be used for instance to monitor the accuracy of the numerical simulations. In the following, we will however explicit only approximate conservation equations, which are consistent with the various approximations considered to derive (2.62).

2.9.3 Flux definitions

One now considers the decomposition of the distribution function $f_j = f_{0j} + f_{1j}$ and again assumes that f_{0j} represents a stationary state, so that in particular

$$\vec{\tilde{\Gamma}}_0 \cdot \vec{\nabla} x = \int \left[v_\parallel \vec{b}_0 + \frac{B_0}{B^*_{0\parallel}} (\vec{v}_{\nabla B} + \vec{v}_c) \right] \cdot \vec{\nabla} x \, f_{0j} \, J \, dv_\parallel \, d\mu \; = 0 \,. \tag{2.110}$$

Equation (2.108) thus becomes a continuity equation for the perturbed terms:

$$\frac{\partial}{\partial t}[\langle \tilde{n}_1 \rangle V'] + \frac{\partial}{\partial x}[\langle \vec{\tilde{\Gamma}}_1 \cdot \vec{\nabla} x \rangle V'] = 0 \,, \tag{2.111}$$

where

$$\tilde{n}_{1j} = \int f_{1j} \, J \, dv_\parallel \, d\mu \,, \tag{2.112}$$

and

$$\vec{\tilde{\Gamma}}_1 \cdot \vec{\nabla} x = \int \left[\frac{B_0}{B^*_{0\parallel}} \vec{v}_E \, f_{0j} + [v_\parallel \vec{b}_0 + \frac{B_0}{B^*_{0\parallel}} (\vec{v}_E + \vec{v}_{\nabla B} + \vec{v}_c)] \, f_{1j} \right] \cdot \vec{\nabla} x \, J \, dv_\parallel \, d\mu \,. \tag{2.113}$$

The projection of the $\vec{v}_E$ velocity (2.42) onto the radial direction reads:

$$\vec{v}_E \cdot \vec{\nabla} x = -\frac{\vec{\nabla}\chi_1 \times \vec{B}_0}{B_0^2} \cdot \vec{\nabla} x \simeq -\frac{1}{\mathcal{C}} \frac{\partial \chi_1}{\partial y} \,, \tag{2.114}$$

where $\mathcal{C}$ is defined in Eq. (2.60) and having again neglected the $\partial/\partial z$ terms with respect to the $\partial/\partial x$ contributions. From the definition of the generalized potential, Eq. (2.42), one furthermore separates the electrostatic and electromagnetic contributions, leading to:

$$\vec{v}_E \cdot \vec{\nabla} x \simeq -\frac{1}{\mathcal{C}} \frac{\partial \bar{\Phi}_1}{\partial y} + \frac{v_\parallel}{\mathcal{C}} \frac{\partial \bar{A}_{1\parallel}}{\partial y} \,. \tag{2.115}$$

The two contribution from $\vec{v}_{\nabla B}$ and $\vec{v}_c$ are regrouped together as:

$$(\vec{v}_{\nabla B} + \vec{v}_c) \cdot \vec{\nabla} x = -\mathcal{C}\, \frac{\mu\, B_0 + m_j\, v_\parallel^2}{m_j\, \Omega_j\, B_0^2} \gamma_2 \frac{\partial B_0}{\partial z}\ . \tag{2.116}$$

Considering the definition of the field-aligned coordinates, one has $\vec{b}_0 \cdot \vec{\nabla} x \propto (\vec{\nabla} x \times \vec{\nabla} y) \cdot \vec{\nabla} x = 0$ such that the $v_\parallel\, \vec{b}_0$ term vanishes in Eq. (2.113). Noticing furthermore that all equilibrium terms $(B_0, B_{0\parallel}^*, f_{0j})$ are independent of y, the flux-surface average of the $f_{0j}\, \vec{v}_E$ term in Eq. (2.113) will cancel out, and this contribution is thus not retained. One finally defines the turbulent radial gyrocenter flux as:

$$\tilde{\Gamma}_j(x) = \langle \vec{\tilde{\Gamma}}_1 \cdot \vec{\nabla} x \rangle = \tilde{\Gamma}_{j,es}(x) + \tilde{\Gamma}_{j,em}(x) + \tilde{\Gamma}_{j,B}(x) \tag{2.117}$$

with the electrostatic and electromagnetic contributions respectively defined as:

$$\tilde{\Gamma}_{j,es}(x) \;=\; -\frac{1}{\mathcal{C}} \left\langle \int \frac{B_0}{B_{0\parallel}^*} \frac{\partial \bar{\Phi}_1}{\partial y}\, f_{1j}\, J\, dv_\parallel\, d\mu \right\rangle\ , \tag{2.118}$$

$$\tilde{\Gamma}_{j,em}(x) \;=\; \frac{1}{\mathcal{C}} \left\langle \int \frac{B_0}{B_{0\parallel}^*}\, v_\parallel \frac{\partial \bar{A}_{1\parallel}}{\partial y}\, f_{1j}\, J\, dv_\parallel\, d\mu \right\rangle\ . \tag{2.119}$$

The contribution related to the gradient and curvature of the equilibrium magnetic field $\vec{B}_0$ is given by

$$\tilde{\Gamma}_{j,B}(x) = -\frac{\mathcal{C}}{m_j} \left\langle \int \frac{\mu\, B_0 + m_j\, v_\parallel^2}{\Omega_j\, B_0\, B_{0\parallel}^*}\, \gamma_2\, \frac{\partial B_0}{\partial z}\, f_{1j}\, J\, dv_\parallel\, d\mu \right\rangle\ , \tag{2.120}$$

which averages out to zero, at least for non-axisymmetric fluctuation modes, and will thus be neglected.

Considering now the energy conservation and assuming again that the unperturbed distribution f_0 is a stationary state, one obtains from Eq. (2.109) a conservation equation for the perturbed energy density:

$$\frac{3}{2} \frac{\partial}{\partial t} [\langle \tilde{p}_1 \rangle\, V'] + \frac{\partial}{\partial x} [\, \langle \vec{\tilde{Q}}_1 \cdot \vec{\nabla} x \rangle\, V'] = \langle \tilde{P}_1 \rangle\, V'\ . \tag{2.121}$$

As for the gyrocenter flux, one distinguishes the different contributions to the radial heat flux:

$$\tilde{Q}_j(x) = \langle \vec{\tilde{Q}}_1 \cdot \vec{\nabla} x \rangle = \tilde{Q}_{j,es}(x) + \tilde{Q}_{j,em}(x) + \tilde{Q}_{j,B}(x)\ . \tag{2.122}$$

The electrostatic and electromagnetic heat fluxes respectively read:

$$\tilde{Q}_{j,es}(x) = -\frac{1}{2\,\mathcal{C}} \left\langle \int \frac{B_0}{B_{0\|}^*} \left(m_j\, v_\|^2 + 2\, B_0\, \mu\right) \frac{\partial \bar{\Phi}_1}{\partial y}\, f_{1j}\; J\; dv_\|\, d\mu \right\rangle , \tag{2.123}$$

$$\tilde{Q}_{j,em}(x) = \frac{1}{2\,\mathcal{C}} \left\langle \int \frac{B_0}{B_{0\|}^*} \left(m_j\, v_\|^2 + 2\, B_0\, \mu\right) v_\| \frac{\partial \bar{A}_{1\|}}{\partial y}\, f_{1j}\; J\; dv_\|\, d\mu \right\rangle . \tag{2.124}$$

and the curvature term is:

$$\tilde{Q}_{j,C}(x) = -\frac{\mathcal{C}}{m_j} \left\langle \int \left(\frac{1}{2}\, m_j\, v_\|^2 + B_0\, \mu\right) \frac{\mu\, B_0 + m_j\, v_\|^2}{\Omega_j\, B_0\, B_{0\|}^*}\, \gamma_2\, \frac{\partial B_0}{\partial z}\, f_{1j}\; J\; dv_\|\, d\mu \right\rangle , \tag{2.125}$$

Note that as for the gyrocenter flux, this last contribution is essentially zero for an up-down symmetric plasma.

Finally, the perturbed power density reads:

$$\begin{aligned} \tilde{P}_1 &= q_j \int [v_\|\, \vec{b}_0 + \frac{B_0}{B_{0\|}^*}(\vec{v}_E + \vec{v}_{\nabla B} + \vec{v}_c)] \cdot \vec{E}\, f_{1j}\, J\, d\mu\, dv_\| \\ &= q_j \int [v_\|\, E_\| + \frac{B_0}{B_{0\|}^*}(\vec{v}_{\nabla B} + \vec{v}_c)] \cdot \vec{\nabla}\bar{\Phi}\, f_{1j}\, J\, d\mu\, dv_\| , \end{aligned} \tag{2.126}$$

having made use of the relations $\vec{E} = -\vec{\nabla}\bar{\Phi}_1 - \dot{\vec{b}}_0\, \bar{A}_{1\|}$, $\vec{v}_E \cdot \vec{E} = 0$ and $(\vec{v}_{\nabla B} + \vec{v}_c) \cdot \vec{b}_0 = 0$. Equations (2.111) and (2.121) can in particular be used to monitor the conservation properties, up to order ϵ, in a numerical simulation. We note however that the final relations for the fluxes (2.100) and (2.102) which have been obtained here by taking velocity moments of the gyrokinetic equation, *i.e.* at fixed gyrocenter position $\vec{X}$, differ from the relations that one would have obtained by taking velocity moments of the original Vlasov equation, *i.e.* at fixed particle position $\vec{x}$:

$$\vec{\Gamma}_j = \int \vec{v}\, \mathtt{f}_j(t, \vec{x}, \vec{v}) , \tag{2.127}$$

and

$$\vec{Q}_j = \int \frac{m_j\, v^2}{2}\, \vec{v}\, \mathtt{f}_j(t, \vec{x}, \vec{v})\, d\vec{v} , \tag{2.128}$$

which are strictly speaking the physical quantities of interest. The previous definitions (2.100) and (2.102) will thus differ from (2.127) and (2.128) by diamagnetic and the polarization drift terms. The diamagnetic drift corrections are however normal to the radial direction and since we are mainly interested in radial fluxes, this contribution is not relevant. Polarization drift terms can on the other hand have a radial component, nut

their contribution is expected to be small for these macroscopic quantities. As a result, many gyrokinetic codes, including *e.g.* the ORB5 [54] or GT5D [14], make use of the gyrocenter fluxes Eqs. (2.118)-(2.119) and (2.123)-(2.124) as approximate diagnostics of the exact physical fluxes (2.127) and (2.128). More details on the differences between fluxes definitions can be found in [48].

In Ref. [55], approximate relations for the fluxes (2.127) and (2.128) are derived, which which are consistent with the gyrokinetic ordering and read:

$$\vec{\Gamma}_j = \int \vec{v}_\chi \, \mathtt{f}_j(t,\vec{x},\vec{v}) \, d\vec{v} \qquad \text{and} \qquad \vec{Q}_j = \int \frac{m_j \, v^2}{2} \, \vec{v}_\chi \, \mathtt{f}_j(t,\vec{x},\vec{v}) \, d\vec{v} \, , \tag{2.129}$$

where

$$\vec{v}_\chi = -\frac{\vec{\nabla}\chi_1 \times \vec{B}_0}{B_0^2} \, , \qquad \text{with} \qquad \chi_1 = \Phi_1 - v_\parallel A_{1\parallel} \, . \tag{2.130}$$

We remark that the drift velocity $\vec{v}_\chi$ in relation (2.129) is essentially equal to $\vec{v}_E$, apart from the perturbed fields Φ_1 and $A_{1\parallel}$, which are not gyroaveraged in (2.130). These latter fluxes definitions are currently used in the GENE code and one again separates the electrostatic and electromagnetic radial contributions, which can be expressed in terms of the velocity moments $M_{j,mn}$ of the particle distribution, given in Eq. (2.78), as follows:

$$\Gamma_{j,es}(x) = -\frac{1}{\mathcal{C}} \left\langle M_{j,00}(\vec{x}) \, \frac{\partial \Phi_1}{\partial y} \right\rangle \, , \tag{2.131}$$

$$\Gamma_{j,em}(x) = \frac{1}{\mathcal{C}} \left\langle M_{j,10}(\vec{x}) \, \frac{\partial A_{1\parallel}(\vec{x})}{\partial y} \right\rangle \, , \tag{2.132}$$

and

$$Q_{j,es}(x) = -\frac{m_j}{2\mathcal{C}} \left\langle [M_{j,20}(\vec{x}) + M_{j,02}(\vec{x})] \, \frac{\partial \Phi_1(\vec{x})}{\partial y} \right\rangle \, , \tag{2.133}$$

$$Q_{j,em}(x) = \frac{m_j}{2\mathcal{C}} \left\langle [M_{j,30}(\vec{x}) + M_{j,12}(\vec{x})] \, \frac{\partial A_{1\parallel}(\vec{x})}{\partial y} \right\rangle \, . \tag{2.134}$$

2.10 The normalized equations

2.10.1 Normalizations

In view of the numerical implementation, the different quantities appearing in the gyrokinetic and field equations are normalized appropriately so that the resulting di-

mensionless quantities are all of order ~ 1. The dimensional reference quantities are $n_{\rm ref}, T_{\rm ref}, B_{\rm ref}, m_{\rm ref}$ and $L_{\rm ref}$ for the density, temperature, magnetic field, mass, and length respectively. The choice for these normalization quantities may depend on the physical problem, in most cases however they are taken as $n_{\rm ref} = n_i, T_{\rm ref} = T_e, B_{\rm ref} = B_0, m_{\rm ref} = m_i$ and $L_{\rm ref} = R$. From these quantities, one can further derive reference velocity $c_{\rm ref}$, cyclotron frequency $\Omega_{\rm ref}$ and Larmor radius $\rho_{\rm ref}$:

$$c_{\rm ref}^2 = \frac{T_{\rm ref}}{m_{\rm ref}} , \qquad \Omega_{\rm ref} = \frac{eB_{\rm ref}}{m_{\rm ref}} , \qquad \rho_{\rm ref} = \frac{c_{\rm ref}}{\Omega_{\rm ref}} .$$

The hat notation ' $\hat{}$ ' is used for normalized quantities. The normalization of time and the coordinates (x, y, z) are:

$$t = \frac{L_{\rm ref}}{c_{\rm ref}} \hat{t} , \qquad x = \rho_{\rm ref}\, \hat{x} , \qquad y = \rho_{\rm ref}\, \hat{y} , \qquad z = \hat{z} .$$

Note that when considering equilibrium quantities, derivatives with respect to x shall be normalized to the macroscopic length $L_{\rm ref}$ rather than $\rho_{\rm ref}$. One therefore introduces a second normalized radial variable $\hat{x}_{eq}$:

$$x = L_{\rm ref}\, \hat{x}_{eq} .$$

The velocity variables are normalized to:

$$v_\parallel = \hat{v}_{Tj}(x_0)\, c_{\rm ref}\, \hat{v}_{\parallel j} , \qquad \mu = \hat{T}_{0,j}(x_0)\, \frac{T_{\rm ref}}{B_{\rm ref}}\, \hat{\mu}_j ,$$

where $v_{Tj}(x) = \sqrt{2\, T_{0j}(x)/m_j} = c_{\rm ref}\, \hat{v}_{Tj}(x)$ is the thermal velocity of each species and x_0 is the center of the simulation domain. A subscript j has been added to the velocity variables $(\hat{v}_{\parallel j}, \hat{\mu}_j)$ since they are now species dependent. In addition, the notation $T_{0j}(x) = T_{\rm ref}\, \hat{T}_{0j}(x)$ and $n_{0j}(x) = n_{\rm ref}\, \hat{n}_{0j}(x)$ is used for the normalized temperature and density of each species.

The other equilibrium quantities are normalized as follows:

$$\gamma_1 = \hat{\gamma}_1 , \qquad \gamma_2 = \frac{1}{L_{\rm ref}} \hat{\gamma}_2 , \qquad \gamma_3 = \frac{1}{L_{\rm ref}} \hat{\gamma}_3 , \qquad J^{xyz} = L_{\rm ref}\, \hat{J}^{xyz} .$$

According to Eq. (2.60), the coefficient $\mathcal{C}$ has the same units as the magnetic field $\vec{B}_0$, and is therefore normalized to $B_{\rm ref}$: $\hat{\mathcal{C}} = \mathcal{C}/B_{\rm ref}$.

The distribution functions are normalized by:

$$f_{0j} = \frac{n_{\rm ref}}{c_{\rm ref}^3} \frac{\hat{n}_{0j}(x_0)}{\hat{v}_{Tj}^3(x_0)} \hat{f}_{0j} , \qquad f_{1j} = \frac{\rho_{\rm ref}}{L_{\rm ref}} \frac{n_{\rm ref}}{c_{\rm ref}^3} \frac{\hat{n}_{0j}(x_0)}{\hat{v}_{Tj}^3(x_0)} \hat{f}_{1j} ,$$

and the electromagnetic fields by :

$$\Phi_1 = \frac{\rho_{\rm ref}}{L_{\rm ref}} \frac{T_{\rm ref}}{e} \hat{\Phi}_1 \ , \qquad A_{1\|} = \frac{\rho_{\rm ref}}{L_{\rm ref}} B_{\rm ref} \rho_{\rm ref} \hat{A}_{1\|} \ .$$

We also define

$$\hat{\omega}_{Tj,x} = -L_{\rm ref} \frac{d \ln T_{j0}}{dx} \ , \qquad \hat{\omega}_{nj,x} = -L_{\rm ref} \frac{d \ln n_{j0}}{dx} \ , \qquad \hat{\omega}_p = -L_{\rm ref} \frac{d \ln p_0}{dx} \ .$$

The plasma pressure is normalized to $p_0(x) = p_{\rm ref}\, \hat{p}_0(x) = T_{\rm ref}\, n_{\rm ref}\, \hat{p}_0(x)$, and one defines $\beta_{\rm ref} = 2\, \mu_0\, p_{\rm ref} / B_{\rm ref}^2$.

2.10.2 The normalized gyrokinetic equation

Using the normalizations introduced above, the gyrokinetic equation (2.62) reads

$$\begin{aligned}
\frac{\partial \hat{g}_{1j}}{\partial \hat{t}} \ = \ & -\frac{1}{\hat{\mathcal{C}}} \frac{\hat{B}_0}{\hat{B}^*_{0\|}} \left[\hat{\omega}_{nj} + \hat{\omega}_{Tj} \left(\frac{\hat{v}_{\|j}^2 + \hat{\mu}_j \hat{B}_0}{\tau_{0j}} - \frac{3}{2} \right) \right] \hat{f}_{0j} \partial_{\hat{y}} \hat{\bar{\chi}}_1 \\
& - \frac{\hat{B}_0}{\hat{B}^*_{0\|}} \frac{\hat{T}_{0j}(x_0)}{Z_j} \frac{2\, \hat{v}_{\|j}^2 + \hat{\mu}_j \hat{B}_0}{\hat{B}_0} \hat{K}_x \hat{\Gamma}_{j,x} \\
& - \frac{\hat{B}_0}{\hat{B}^*_{0\|}} \frac{\hat{T}_{0j}(x_0)}{Z_j} \left[\frac{2\, \hat{v}_{\|j}^2 + \hat{\mu}_j \hat{B}_0}{\hat{B}_0} \hat{K}_y - \frac{\hat{v}_{\|j}^2}{\hat{\mathcal{C}}} \beta_{\rm ref} \frac{\hat{p}_0}{\hat{B}_0^2} \hat{\omega}_p \right] \hat{\Gamma}_{j,y} \\
& - \frac{\hat{B}_0}{\hat{B}^*_{0\|}} \frac{1}{\hat{\mathcal{C}}} \left(\partial_{\hat{x}} \hat{\bar{\chi}}_1 \, \hat{\Gamma}_{j,y} - \partial_{\hat{y}} \hat{\bar{\chi}}_1 \, \hat{\Gamma}_{j,x} \right) \\
& - \hat{v}_{Tj}(x_0) \frac{\hat{\mathcal{C}}}{\hat{J}^{xyz}\, \hat{B}_0} \hat{v}_{\|j} \, \hat{\Gamma}_{j,z} + \frac{\hat{v}_{Tj}(x_0)}{2} \frac{\hat{\mathcal{C}}}{\hat{J}^{xyz}\, \hat{B}_0} \hat{\mu}_j \, \partial_{\hat{z}} \hat{B}_0 \, \frac{\partial \hat{f}_{1j}}{\partial \hat{v}_{\|j}} \ , \qquad (2.135)
\end{aligned}$$

having defined $\tau_{0j}(x) = T_{0j}(x)/T_{0j}(x_0)$, $\mathcal{N}_{0j}(x) = n_{0j}(x)/n_{0j}(x_0)$, $Z_j = q_j/e$. The other normalized quantities read:

$$\begin{aligned}
\hat{g}_{1j} \ &= \ \hat{f}_{1j} + \frac{Z_j\, \hat{v}_{Tj}(x_0)}{\hat{T}_{0j}(x)} \, \hat{v}_{\|j} \, \hat{\bar{A}}_{1\|} \, \hat{f}_{0j} \ , \\
\hat{\Gamma}_{\alpha,j} \ &= \ \partial_{\hat{\alpha}} \hat{f}_{1j} + \frac{Z_j}{\hat{T}_{0j}(x)} \, \partial_{\hat{\alpha}} \hat{\bar{\Phi}}_1 \, \hat{f}_{0j} \qquad \text{for} \qquad \hat{\alpha} = (\hat{x}, \hat{y}, \hat{z}) \ , \\
\hat{f}_{0j} \ &= \ \frac{\mathcal{N}_{0j}(x)}{[\pi \tau_{0j}(x)]^{3/2}} \, \exp\left(- \frac{\hat{v}_{\|j}^2 + \hat{\mu}_j \, \hat{B}_0(x,z)}{\tau_{0j}(x)} \right) \ , \\
\hat{\bar{\chi}}_1 \ &= \ \hat{\bar{\Phi}}_1 - \hat{v}_{Tj}(x_0) \, \hat{v}_{\|j} \, \hat{\bar{A}}_{1\|} \ ,
\end{aligned}$$

$$
\begin{aligned}
\hat{B}^*_{0\|} &= \hat{B}_0 \left(1 + \beta_{\mathrm{ref}} \sqrt{\frac{\hat{m}_j \hat{T}_{0j}(x_0)}{2}} \frac{\hat{j}_{0\|}}{Z_j \hat{B}_0^2} \hat{v}_{\|j} \right) , \\
\hat{j}_{0\|} &= \frac{j_{0\|}}{e\, n_{\mathrm{ref}}\, c_{\mathrm{ref}}} , \\
\hat{\mathcal{K}}_x &= -\frac{1}{\hat{\mathcal{C}}} \frac{\hat{\gamma}_2}{\hat{\gamma}_1} \partial_{\hat{z}} \hat{B}_0, \\
\hat{\mathcal{K}}_y &= \frac{1}{\hat{\mathcal{C}}} \left(\partial_{\hat{x}_{eq}} \hat{B}_0 - \frac{\hat{\gamma}_3}{\hat{\gamma}_1} \partial_{\hat{z}} \hat{B}_0 \right) .
\end{aligned}
$$

2.10.3 The normalized field equations

The field equations derived in section 2.8 can now as well be written in normalized units.

The normalized quasi-neutrality equation reads:

$$
\sum_j \left\{ \pi \hat{n}_{0j}(x_0) Z_j \int \hat{B}^*_{0\|}\, \hat{\bar{f}}_{1j}\, d\hat{v}_\| d\hat{\mu}_j - \frac{Z_j^2 \hat{n}_{0j}}{\hat{T}_{0j}} \left[\hat{\Phi}_1 - \frac{\hat{B}_0}{\tau_{0j}} \int \hat{\bar{\Phi}}_1 \, \exp(-\frac{\hat{\mu}_j \hat{B}_0}{\tau_{0j}})\, d\hat{\mu}_j \right] \right\} = 0 , \tag{2.136}
$$

and for the adiabatic electrons case:

$$
\begin{aligned}
-\frac{\hat{n}_{0e}}{\hat{T}_{0e}} (\hat{\Phi}_1 &- \langle \hat{\Phi}_1 \rangle) + \sum_{j \neq e} \left\{ \pi\, Z_j\, \hat{n}_{0j}(x_0) \int \hat{B}^*_{0\|}\, \hat{\bar{f}}_{1j}\, d\hat{v}_\|\, d\hat{\mu}_j \right. \\
&- \left. \frac{Z_j^2\, \hat{n}_{0j}}{\hat{T}_{0j}} \left[\hat{\Phi}_1 - \frac{\hat{B}_0}{\tau_{0j}} \int \hat{\bar{\Phi}}_1 \, \exp(-\frac{\hat{\mu}_j \hat{B}_0}{\tau_{0j}})\, d\hat{\mu}_j \right] \right\} = 0 .
\end{aligned} \tag{2.137}
$$

Finally, the normalized Ampère's law is given by:

$$
\begin{aligned}
-\hat{\nabla}_\perp^2 \hat{A}_{1\|} &= \sum_j \left\{ \frac{\beta_{\mathrm{ref}}}{2}\, Z_j\, \hat{n}_{0j}(x_0)\, \hat{v}_{Tj}(x_0)\, \pi \int \hat{B}^*_{0\|} \hat{\bar{f}}_{1j}\, d\hat{v}_\|\, d\hat{\mu}_j \right. \\
&\left. - \frac{\beta_{\mathrm{ref}}^2}{4} \frac{\hat{n}_{0j} \hat{j}_{0\|}}{\hat{B}_0^2} Z_j \left[\hat{\Phi}_1 - \frac{\hat{B}_0}{\tau_{0j}} \int \hat{\bar{\Phi}}_1(\vec{x}) \, \exp(-\frac{\hat{\mu}_j \hat{B}_0}{\tau_{0j}})\, d\hat{\mu}_j \right] \right\} .
\end{aligned} \tag{2.138}
$$

2.11 Local and global approach

2.11.1 The flux-tube approach

With the hypothesis that turbulent transport is essentially a local process and in view of reducing the computational effort, several gyrokinetic codes have been developed in

the so-called flux tube or local approximation [9, 18, 11, 12]. In this approach, the limit $\rho^* = \rho_i/a \to 0$, where ρ_i is the ion Larmor radius and a the minor radius, is considered, and the variation of equilibrium quantities over the typical spatial turbulence correlation length, which is of order $a\,\rho^*$ (Gyro-Bohm) or $a\,\sqrt{\rho^*}$ (Bohm), are neglected. Considering this approximation, the simulation domain can be reduced to a narrow tube, elongated along a given field line, and spanning only a small fraction of the minor radius in the radial direction. The flux tube width typically represents a few correlation lengths. Although temperature and density profiles are assumed constant over this width, their derivatives are kept in the equation so as to retain the essential driving terms. The local equations are simply recovered by removing radial dependencies of equilibrium quantities in Eqs. (2.135)-(2.138):

$$\begin{aligned} \hat{\mathcal{C}}(x),\, \hat{B}_0(x,z),\, \hat{B}^*_{0\|}(x,z,v_\|),\, \hat{K}_{x,y}(x,z),\, \hat{J}^{xyz}(x,z) \quad &\longrightarrow \quad \hat{\mathcal{C}},\, \hat{B}_0(z),\, \hat{B}^*_{0\|}(z,v_\|),\, \hat{K}_{x,y}(z),\, \hat{J}^{xyz}(z), \\ \hat{\omega}_{nj}(x)\,,\, \hat{\omega}_{Tj}(x)\,,\, \hat{T}_{0j}(x)\,,\, \hat{n}_{0j}(x)\,,\, \hat{p}_0(x) \quad &\longrightarrow \quad \hat{\omega}_{nj}\,,\, \hat{\omega}_{Tj}\,,\, \hat{T}_{0j}\,,\, \hat{n}_{0j}\,,\, \hat{p}_0\,. \end{aligned}$$

2.11.2 The global approach

In the frame of this thesis, the gyrokinetic code GENE [12, 27, 12] has been extended from a local to a nonlocal or global version where the ρ^* effects associated with radial variations of equilibrium quantities are retained. In particular the essential global effect related with gradient profiles variations [56] are accounted for. Remaining ρ^* effects are however still neglected and these different terms shall be compared and classified among each other by introducing some further sub-ordering. Assuming the typical size of turbulent eddies to be $\Delta \sim \sqrt{\rho_i L_g}$ (gyro-Bohm scaling), we can estimate, as reference, the corrections introduced in the present global equations by retaining variations of gradient profiles to be of order

$$(\Delta\omega'_{T,n})/\omega_{T,n} \sim \sqrt{\rho_i L_g}/L_g \sim \sqrt{\rho^*}\,. \tag{2.139}$$

The remaining neglected terms are given in the following list, with corresponding scaling:

- The $v_\|$ nonlinearity: Nonlinear term $\propto \vec{v}_G \cdot \vec{\nabla}\Phi_1\, \partial f_{1j}/\partial v_\|$, dropped when deriving Eq. (2.51); of order ρ^*.

- Derivatives $\partial/\partial z$ of fluctuating quantities have been neglected with respect to $\partial/\partial x$ and $\partial/\partial y$ terms. These terms are of order $\rho^* a/r$, where r is the local radius. A scaling may be derived by considering the gradient of any fluctuating field, such as Φ:

$$\vec{\nabla}\Phi = \vec{\nabla}x \frac{\partial \Phi}{\partial x} + \vec{\nabla}y \frac{\partial \Phi}{\partial y} + \vec{\nabla}y \frac{\partial \Phi}{\partial y} \ . \tag{2.140}$$

  So that *e.g* $|(\vec{\nabla}z\,\partial\Phi/\partial z)/(\vec{\nabla}x\,\partial\Phi/\partial x)| \sim |\vec{\nabla}\chi/k_\perp| \sim \rho_i/r \sim \rho^* a/r$. Note that similar terms scaling has $1/r$ are also neglected in the gyroaveraging and are further discussed in section 3.3.

- The equilibrium distribution f_0 is assumed to be a local Maxwellian, instead of a canonical Maxwellian. The differences between these two distribution is of order ρ^*.

- Neglected equilibrium gradient terms in the computations of moments (2.78), e.g. $B_0(\vec{x}+\vec{\rho}) \sim B_0(\vec{x})$, which enter the field equations and are terms order ρ^*.

This sub-ordering thus justifies the approximations made in the derivation of the gyrokinetic equation, as the currently retained terms related to radial variations of equilibrium have a dominant scaling over the neglected ones in most of the plasma volume. We note, however, that the terms related to derivatives in the z direction, which are of order $\rho^* a/r$, might become important if one considers regions close to the magnetic axis, and they may have to be corrected in the future. Since these approximations have been introduced at different steps in the derivation, it might be somewhat tedious at this point to identify all the terms dropped in the final gyrokinetic equation (2.135). An illustrative way to identify and summarize the missing terms in the currently considered gyrokinetic equation is to derive the underlying gyrocenter equations of motion in field-aligned coordinate (x, y, z). This has been done in Ref. [57] keeping all terms of order $\epsilon = \rho_{\rm ref}/L_{\rm ref} \sim \rho^*$ and we reproduce here the resulting equations. In normalized units, see section 2.10.1, and considering only a perturbed electrostatic potential, one has:

$$\frac{\mathrm{d}x}{\mathrm{d}t} = -\frac{1}{\mathcal{C}}\left[\frac{\partial \bar{\phi}_1}{\partial y} + \frac{T_0(x_0)}{Z_j}\frac{2v_\parallel^2 + \mu B_0}{B_0}\frac{\gamma_2}{\gamma_1}\frac{\partial B_0}{\partial z} + \epsilon\,\frac{\gamma_2}{\gamma_1}\frac{\partial \bar{\phi}_1}{\partial z}\right] \tag{2.141}$$

$$\frac{\mathrm{d}y}{\mathrm{d}t} = \frac{1}{\mathcal{C}}\left[\frac{\partial \bar{\phi}}{\partial x} + \frac{T_0}{Z_j}\left(\frac{2v_\parallel^2 + \mu B_0}{B_0}\left(\frac{\partial B_0}{\partial x} - \frac{\gamma_3}{\gamma_1}\frac{\partial B_0}{\partial z}\right) - \beta_{\rm ref}\, v_\parallel^2\, \frac{p_0}{B_0^2}\omega_p\right) - \epsilon\,\frac{\gamma_3}{\gamma_1}\frac{\partial \bar{\phi}_1}{\partial z}\right] \tag{2.142}$$

$$\frac{\mathrm{d}z}{\mathrm{d}t} = v_T(x_0)\,\frac{\mathcal{C}\,v_\parallel}{B_0\,J} + \frac{\epsilon}{\mathcal{C}}\left[\frac{\gamma_2}{\gamma_1}\frac{\partial\bar{\phi}_1}{\partial x} + \frac{\gamma_3}{\gamma_1}\frac{\partial\bar{\phi}_1}{\partial y} + \frac{T_0(x_0)}{Z_j}\left(\frac{2v_\parallel^2+\mu B_0}{B_0}\frac{\gamma_2}{\gamma_1}\frac{\partial B_0}{\partial x} - \beta_{\mathrm{ref}}\,v_\parallel^2\frac{p_0}{B_0^2}\frac{\gamma_2}{\gamma_1}\omega_p\right)\right] \tag{2.143}$$

$$\frac{\mathrm{d}v_\parallel}{\mathrm{d}t} = -\frac{v_T(x_0)}{2}\,\frac{\mathcal{C}}{B_0\,J}\,\mu\,\frac{\partial B_0}{\partial z} - \epsilon\frac{1}{\alpha\,B_0\,J}\,\frac{\partial\hat{\phi}_1}{\partial z}, \tag{2.144}$$

where the hat symbol over the normalized variables, and the species index have been dropped so has to lighten notations, and $B^*_{0\parallel} \simeq B_0$ was considered. This normalized form of the gyrocenter equations of motion clearly reveals the terms which are not retained in our model, corresponding to all the contributions $\sim \epsilon$ in Eqs (2.141)-(2.144). We in particular identify in Eqs. (2.141)-(2.143) the ϵ order terms related to ∂/∂_z derivatives. Keeping the ϵ order term in (2.144) would lead, on the other hand, to the so-called parallel nonlinearity.

2.12 Summary

In this Chapter, the gyrokinetic and associated field equations have been expressed in field aligned coordinates in an appropriate form for their numerical implementation. These equations in particular retains radial variations of equilibrium quantities suitable with a global approach. A discussion of the local limit was then provided, as well as a summary of the different remaining approximations. In the next chapter, a detailed description of the numerical aspects of the GENE code is given.

3 Numerical implementation

3.1 General description

The GENE (Gyrokinetic Electromagnetic Numerical Experiment) code is an Eulerian gyrokinetic code which solves the time evolution of the particle distribution functions on a fixed grid in phase space. Its development was initiated by F. Jenko [12] and continued by T. Dannert [27] at the IPP Garching, Germany. The original version of the code considered the flux tube approximation, see section 2.11, and the time evolution of both purely electrostatic and electromagnetic fluctuations. The code was then further improved by F. Merz [51], who introduced in particular a collision operator and the possibility to use the code as an eigensolver.

The present code has now been extended to a global version where most of the flux tube assumptions have been relaxed, see discussion in section 2.11. This code development was carried out in a close collaboration between the IPP Garching, and the CRPP Lausanne, and was in particular part of T. Görler's PhD [28] and the present thesis work.

The GENE code follows the method of line approach, where the right-hand side of Eq. (2.135) is discretized on the $(x, y, z, v_\parallel, \mu)$ grid, thus leading to large set of coupled ordinary differential equations in t, which can then be solved as an initial value problem or as an eigenvalue problem. A general overview of the different numerical aspects of the code for both local and global versions is given in this section. It is then followed in later sections by more detailed explanations concerning various parts of the global code which are more specific to the present thesis work. This concerns the implementation of the parallel boundary conditions, the gyro-averaging operator and fields solver, as well as the real space dealiasing which is used when dealing with the nonlinear term. Finally, an additional chapter, see Chap. 4, is dedicated to the description and discussion of different magnetic equilibria which are considered to obtain the magnetic field and associated

metric coefficients appearing in Eq. (2.47).

3.1.1 Treatment of the phase space directions

The radial direction x

The treatment of the radial direction x represents one of the main differences between the local and global versions of the code. In the flux-tube version of the code one neglects the radial variation of all equilibrium profiles and their gradients, and periodic boundary conditions are considered. The radial direction can thus be treated in Fourier space and radial derivatives in Eq. (2.135), are thus simply transformed as follows:

$$\frac{\partial}{\partial x} \quad \rightarrow \quad i\,k_x\ , \quad \text{where} \quad k_x = \frac{2\,\pi\,j}{l_x} \quad \text{and} \quad j \quad \text{is an integer .}$$

One notes that in order to justify the radial periodic boundary conditions, the radial box length l_x needs to be larger than the radial correlation length of the turbulence.
On the other hand, in the global version of the code, radial variations of equilibrium quantities are retained which makes it inconsistent to consider the periodic boundaries in this direction. Dirichlet boundary conditions are used instead, and the radial direction is treated in real space. The radial derivatives are discretized with centered fourth order finite differences, see [28]:

$$\left.\frac{\partial f}{\partial x}\right|_{x=x_i} \simeq \frac{f_{i-2} - 8\,f_{i-1} + 8\,f_{i+1} - f_{i+2}}{12\,\Delta x} + \mathcal{O}(\Delta x^4)\ , \tag{3.1}$$

with notation $f_i = f(x_i)$. We also explicit here the second order x-derivative which are required in the field solver:

$$\left.\frac{\partial^2 f}{\partial x^2}\right|_{x=x_i} \simeq \frac{-f_{i-2} + 16\,f_{i-1} - 30\,f_i + 16\,f_{i+1} - f_{i+2}}{12\,\Delta x^2} + \mathcal{O}(\Delta x^4)\ . \tag{3.2}$$

The length l_x is in this case defined as a fraction of the minor radius, so that the simulation volume represents a toroidal annulus excluding a finite volume around the magnetic axis. We note that it is in fact required for practical reasons to exclude the magnetic axis as the considered field aligned coordinate system, which is polar-like, becomes singular on the axis.
As a result of the fourth order centered finite difference scheme, see Eq. (3.1), the grid

points are strongly coupled to their second next neighbors while only weakly to their direct neighbors, which can lead to a divergence of the odd and even subsets of grid points. In order to couple these two subsets a hyperdiffusion term is added to the right-hand side of Eq. (2.135):

$$\mathrm{hyp}_x = -\nu_x \frac{\partial^4 f}{\partial x^4} \simeq h_x \frac{-f_{i-2} + 4\, f_{i-1} - 6\, f_i + 4\, f_{i+1} - f_{i+2}}{16} + (O)(\Delta x^2)\ . \tag{3.3}$$

where $h_x = \nu_x/\Delta x^4$ is a damping coefficient, normalized to c_s/R, which is typically of the order of the linear growth rate. In most cases however, this term is not required for linear simulations, and h_x is set to zero.

The binormal direction y

The binormal direction y is treated in both versions of the code in Fourier space with periodic boundary conditions, and the y derivatives are transformed as follows:

$$\frac{\partial}{\partial y} \quad \rightarrow \quad i\, k_y\ , \quad \text{where} \quad k_y = \frac{2\,\pi\, j}{l_y} \quad \text{and} \quad j \quad \text{is an integer}\ .$$

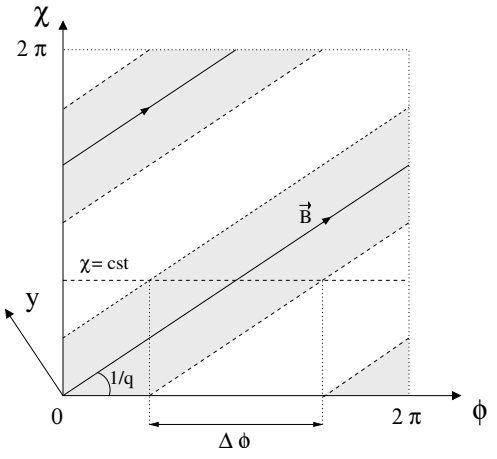

Figure 3.1: Part of a given flux surface covered by the simulation domain (in gray) in the (ϕ, χ) plane.

On a given flux surface, the simulation domain does not necessarily cover the whole surface, as illustrated in Fig. 3.1. Using the definition of $y = C_y\,(q\chi - \phi) - y_0$, the l_y length can be related to the fraction of toroidal angle $\Delta\phi = 2\,\pi/n_0$ occupied by the

simulation domain on a constant χ surface by

$$l_y = C_y \frac{2\,\pi}{n_0}\,. \tag{3.4}$$

For $n_0 = 1$ the full annulus is covered, and the periodicity condition in y reflects the natural periodicity in the toroidal direction. When $n_0 > 1$ only part of the flux surface is covered and the periodic boundary conditions are only justified if the correlation length of the turbulence in the y direction is smaller than the l_y length. In order to allow for the reconstruction of physical quantities on the whole flux surface using the y periodicity and without overlapping, n_0 is imposed to be an integer, which in turn quantizes the allowed l_y values.

Another point to notice relative to the y direction is that the k_y wave number is uniquely related to the toroidal mode number n. Indeed for a given quantity $A(\Psi, \chi, \phi)$, with toroidal mode number n, one has:

$$\begin{aligned} A(\Psi,\chi,\phi) &= \hat{A}(\psi,\chi)\,\exp(i\,n\,\phi) \\ &= \hat{A}(\psi,\chi)\,\exp(-i\,n\,[(y+y_0)/C_y + q\chi]) \\ &= \tilde{\mathcal{A}}(x,z)\,\exp(-i\,n\,y/C_y) \\ &= \tilde{\mathcal{A}}(x,z)\,\exp(i\,k_y\,y)\;, \end{aligned}$$

so that $k_y = -n/C_y$. The allowed wavenumbers in the y-direction are however given by $k_y = j\,2\,\pi/l_y = j\,n_0/C_y$ according to (3.4), with j integer. In case the flux tube only covers a fraction of the magnetic surface, i.e. $n_0 > 1$, only the toroidal mode numbers $n = j\,n_0$ can be thus represented.

The $E \times B$ nonlinearity

As a result of the Fourier representation in x and y in the local code, and in y in the global code, the nonlinear multiplication in the $E \times B$ term would require to evaluate a convolution. Such an evaluation is computationally very costly and it is much more efficient to first transform the perturbed quantities to real space using the fast Fourier transform algorithm, then to evaluate the multiplication in real space and finally transform back to Fourier space. In order to avoid pollution of the spectrum by unresolved modes, resulting from the nonlinear multiplication, an anti-aliasing technique is applied.

In the local code, the so-called 3/2 rule is employed in both x and y directions, which consist in extending the numerical grid in these directions by adding small scale modes with zero amplitude before the transformation to real space. The two extended quantities are then multiplied in real space, and finally the product function is back-transformed to Fourier space and the extended mode spectrum is removed.
In the global version of the code, the same procedure is applied to the y direction, whereas aliasing effects are partially removed in the x direction by using a real space anti-aliasing scheme, which consits in an interpolation before the nonlinear multiplication followed by a smoothing operation acting on the product function. This procedure is described in detail in section (3.4). The real space anti-aliasing scheme alone is not enough to ensure numerical stability of global nonlinear simulations, and the hyper-diffusion coefficient h_x, see Eq.(3.3), needs also to be adapted.

The parallel direction z

The spatial parallel direction z is treated in real space with centered fourth order finite differences for both versions of the code, see 3.1. The boundary conditions are defined so as to be consistent with the physical periodicity of each magnetic surface in variables (χ, ϕ).

$$\mathcal{F}(x, y, z + 2\,\pi) = \mathcal{F}(x, y - C_y\, q\, 2\,\pi, z)\,. \tag{3.5}$$

These boundary conditions are further discussed in section 3.2.1.
As for the x direction an hyper-diffusion term is is added to the right-hand side of Eq. (2.135) in order to couple odd and even points:

$$\mathrm{hyp}_z = -\nu_z \frac{\partial^4 f}{\partial z^4}\,. \tag{3.6}$$

the 4th order derivative is discretize as in Eq. (3.3), and one introduces the hyperdiffusion coefficient $h_z = \nu_z/\Delta z^4$.

The velocity space

The advection in the parallel velocity direction is also computed with fourth order finite differences in both the local and global code, and Dirichlet boundary conditions are

considered at the edges. As for the x and z directions an hyper-diffusion term is used:

$$\mathrm{hyp}_{v_\parallel} = -\nu_{v_\parallel} \frac{\partial^4 f}{\partial v_\parallel^4} \,, \tag{3.7}$$

and one again introduces $h_{v_\parallel} = \nu_{v_\parallel}/\Delta v_\parallel^4$. Derivatives in the μ direction are only needed when considering collisions. In this case, the collision operator is treated separately using a finite volume scheme for the velocity derivatives, see [51].

3.1.2 The eigensolver

When considering linear calculations, the code can be run as an eigensolver thanks to an interface with the SLEPc/PETSc library [58]. The computation is carried out with a matrix-free iterative solver which solves for the (eigenvalue,eigenvector) pairs $(\lambda, \{g_{1j}\})$ of the discretized right hand side operator of Eq. (2.135):

$$\frac{\partial g_{1j}}{\partial t} = \mathcal{L}(\,\{g_{1j}\}\,) \,, \quad \text{i.e.} \quad \mathcal{L}(\{g_{1j}\}) = \lambda\,\{g_{1j}\} \,. \tag{3.8}$$

The real and imaginary parts of the eigenvalues λ are then identified respectively to the growth rates and frequencies of the eigenvectors $\{g_{1j}\}$. An iterative solver is particularly efficient compared to a direct solver when only a small subset of the eigenvalues are needed. In particular, one can search for the eigenvalue with the largest imaginary part, that is corresponding to the largest frequency, so as to determine the maximal time step (CFL condition) for ensuring numerically stable initial value calculations, see section 3.1.3. For the physical study of micro-instabilities, one can also solve for a given number of eigenvalues with the largest real part, corresponding to the most unstable modes. A detailed description of the eigensolver capability of GENE is presented in [51].

3.1.3 The time evolution scheme

Explicit time scheme

Although any part of the spectrum is accessible with the eigensolver, for cases where only the most unstable mode is of interest or for nonlinear computations, the code can be run as an initial value solver. In such case, the time derivative of Eq. (2.135) is discretized, and an explicit time scheme is used for solving the time evolution of the distribution function. Explicit time schemes are relatively straightforward to implement

compared to implicit schemes, which in general require a matrix inversion, but are however only conditionally stable, i.e. the time step needs to be below a certain limit, the so-called Courant-Friedrich-Levy (CFL) limit. Several Runge-Kutta schemes of different orders are implemented in the code, and an optimum needs to be found between the maximal stable time step achievable , the computational cost, which both increase with the order of the scheme, and accuracy. A complete discussion on the different implemented schemes is provided in [51], and in most simulations, a so-called modified fourth order Runge-Kutta scheme proposed in [59] is used.

Time step adaption

When considering only the linear part of the gyrokinetic equation, the maximal time step Δt_{lin} can be obtained using the eigensolver capability of GENE, solving for the mode with the highest real frequency $\omega_{\mathrm{r,max}}$ and applying $\omega_{\mathrm{r,max}}\,\Delta t < 1$. When considering nonlinear simulations, an additional constraint on the time step arises from the $E \times B$ advection term. The $E \times B$ advection velocity field evolves in time and the corresponding time step constraint needs therefore to be adapted at each time step:

$$\Delta t = s_c \, \min(\Delta t_{\mathrm{lin}}, \Delta t_{\mathrm{nl}}) \, , \tag{3.9}$$

where Δt_{lin} is the maximal time step of the linear gyrokinetic equation, and Δt_{nl} is the maximal time step associated with the $E \times B$ velocity.

3.1.4 Code performance and parallelization

For typical TEM nonlinear turbulence studies, the grid resolution requirement in the $(x, k_y, z, v_\parallel, \mu)$ directions and considering two active species, is about $128 \times 32 \times 24 \times 48 \times 8 \times 2$ for local runs and up to $300 \times 32 \times 24 \times 64 \times 16 \times 2$ for global runs. Considering the different stages of the 4th order Runge-Kutta scheme, and the different pre-factors entering the equations, one can evaluated that the equivalent of 5 high dimensional double complex arrays for the distributions need to be stored at each time step, the memory requirement is respectively 6 GB and 35 GB for local and global simulations. In addition to the high memory requirement, the computational power, measured in CPU hours, needed for these simulations is very high. Indeed, considering a single core (2.93 GHz), the typical time per

time step to advance one grid point in a nonlinear simulation is around $1.2 \times 10^{-6}\ s$ for the local code and $2.3 \times 10^{-6}\ s$ for the global code. Considering a realistic mass ratio between

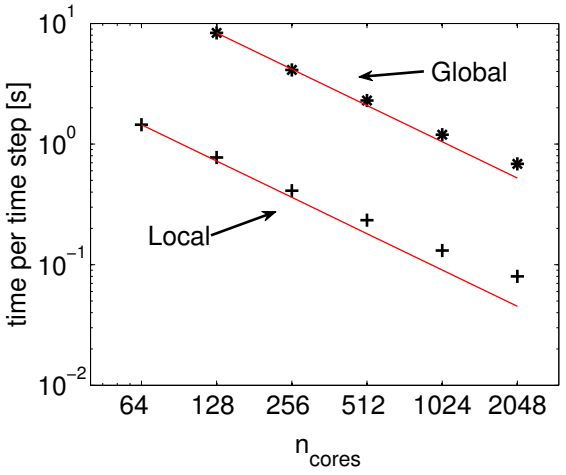

Figure 3.2: CPU time per time step as a function of the number of processors for a local and global computations with respective resolution $n_x \times n_{ky} \times n_z \times n_{v_\parallel} \times n_\mu \times n_{spec} = 128 \times 32 \times 24 \times 48 \times 8 \times 2$ and $300 \times 32 \times 24 \times 64 \times 16 \times 2$. This strong scaling test was carried out on the Jülich HPCFF linux cluster.

electrons and ions, the typical number of time steps required to reach a saturated turbulent state with enough statistics is about 1 000 000. The overall computational power required is thus of the order of 25 000 CPU hours for a local nonlinear simulation and 300 000 CPU hours for a global computation. Gyrokinetic simulations would thus be out of reach without massive parallelization. The code is parallelized with mixed OpenMP and MPI parallelization along all the $(x, y, z, v_\parallel, \mu)$ directions and over species, and shows a very good scaling with increasing number of processors [60]. Note that the x-parallelization is only used for the global version of the code. A strong scaling, i.e. increasing the number of cores while keeping the system size constant, computed on the Jülich HPC-FF linux cluster machine for the local and global parameters described above is shown in Fig. (3.2). In addition, a scaling performed by T. Dannert on the Jülich BlueGene/P supercomputer for a much larger local case, where both electron and ion scales are considered, is shown in Fig. (3.3), for a resolution $1024 \times 512 \times 24 \times 48 \times 8 \times 2$.

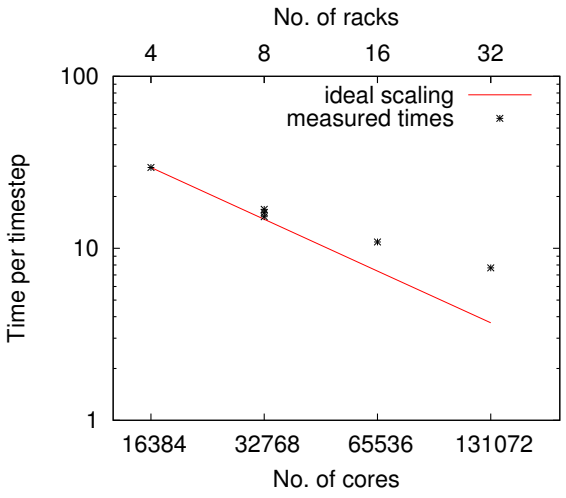

Figure 3.3: Strong scaling of the GENE code on the Jülich BlueGene/P supercomputer for a local multi-scale simulation with resolution $n_x \times n_{ky} \times n_z \times n_{v_\parallel} \times n_\mu \times n_{spec} = 1024 \times 512 \times 24 \times 48 \times 8 \times 2$.

3.2 Periodicity and parallel boundary conditions

3.2.1 The parallel boundary conditions

When dealing with field-aligned coordinates in a toroidal system, the boundary conditions in the parallel direction are of great importance and need to be consistent with the natural periodicity of each magnetic surface. This periodicity can easily be expressed in variables (Ψ, χ, ϕ), indeed for any quantity $\mathcal{F}(\Psi, \chi, \phi)$ one has:

$$\mathcal{F}(\Psi, \chi + 2\,\pi, \phi) = \mathcal{F}(\Psi, \chi, \phi) \tag{3.10}$$

$$\mathcal{F}(\Psi, \chi, \phi + 2\,\pi) = \mathcal{F}(\Psi, \chi, \phi)\ , \tag{3.11}$$

In the field aligned coordinate system $(x = C_x(\Psi) - x_0\ ,\ y = C_y(\Psi)\,(q\chi - \phi) - y_0, z = \chi)$, see Eq. 2.59, these conditions respectively read:

$$\mathcal{F}(x, y, z + 2\,\pi) = \mathcal{F}(x, y - C_y\,q\,2\,\pi, z)\,, \tag{3.12}$$

$$\mathcal{F}(x, y + C_y\,2\,\pi, z) = \mathcal{F}(x, y, z)\,. \tag{3.13}$$

As stated earlier, see section 3.1.1, the simulation domain may not always cover the whole flux surface, and in this case a statistical periodicity is assumed in the ϕ direction:

$$\mathcal{F}(\Psi, \chi, \phi + \Delta\phi) = \mathcal{F}(\Psi, \chi, \phi)\ , \quad \text{with}\ \ \Delta\phi = 2\pi/n_0. \tag{3.14}$$

We note that Eq. (3.14) naturally reduces to (3.11) for $n_0 = 1$. These boundary conditions are illustrated in Fig. 3.4. Note that when $n_0 > 0$, as in Fig. 3.4, $\mathcal{F}(x, y - C_y\, q\, 2\,\pi, z)$ may be outside of the simulation domain and the periodicity in y is then invoked. In general, conditions (3.12) and (3.13) in (x, y, z) variables becomes:

$$\mathcal{F}(x, y + l_y, z) = \mathcal{F}(x, y, z)\ , \tag{3.15}$$

$$\mathcal{F}(x, y, z + 2\,\pi) = \mathcal{F}(x, \mathrm{mod}_{l_y}(y - C_y\, q\, 2\,\pi y), z)\ , \tag{3.16}$$

having made used of the definition (3.4) for l_y.

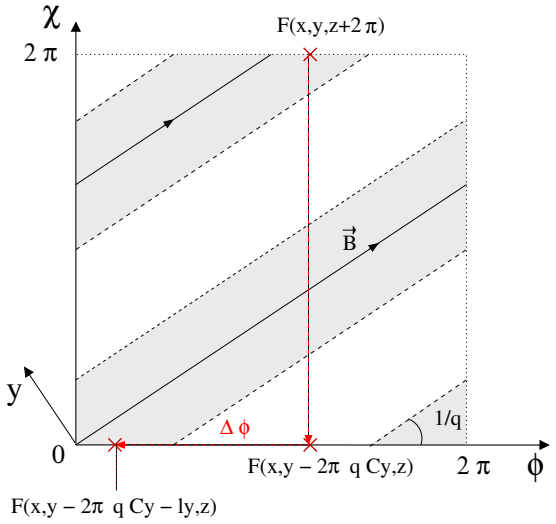

Figure 3.4: Illustration of the parallel boundary conditions for $n_0 = 2$.

In GENE's representation, the y coordinate is treated in Fourier space:

$$\mathcal{F}(x, y, z) = \sum_k \hat{\mathcal{F}}_k(x, z)\ \exp(2\,\pi\, i\, k\, (y - y_0)/l_y)\ . \tag{3.17}$$

and the periodic boundary condition in y, Eq. (3.15), is naturally contained in this representation. Boundary condition Eq. (3.16) however reads:

$$\sum_k \hat{\mathcal{F}}_k(x, z + 2\,\pi)\ \exp(2\,\pi\, i\, k\, (y - y_0)/l_y) = \sum_k \hat{\mathcal{F}}_k(x, z)\ \exp[2\,\pi\, i\, k\, (y - C_y\, q\, 2\,\pi - y_0)/l_y]\ . \tag{3.18}$$

One thus identifies for each y-mode k:

$$\hat{\mathcal{F}}_k(x, z + 2\,\pi) = \hat{\mathcal{F}}_k(x, z)\ \exp(-i\, k\, 2\,\pi\, C_y\, q\, 2\,\pi/l_y)\ . \tag{3.19}$$

Making use of the relation $l_y = C_y\, 2\,\pi/n_0$ the parallel boundary condition in z finally reads:

$$\hat{\mathcal{F}}_k(x, z + 2\,\pi) = \hat{\mathcal{F}}_k(x, z)\, \exp(-\,i\,k\,n_0\,q\,2\,\pi)\ . \tag{3.20}$$

To summarize, when $n_0 = 1$, the full magnetic surface is covered by the flux tube and in this case, the physical periodicities in the χ and ϕ angles are exactly recovered. For $n_0 > 1$ only a fraction $1/n_0$ of the annulus is covered, χ periodicity is ensured and a statistical periodicity in the ϕ direction is assumed.

3.2.2 Contour plot in the poloidal plane

To illustrate that the choice of parallel boundary conditions in z satisfy the natural periodicity condition in χ, we shall now describe how one can reconstruct contours of any field quantity in the poloidal plane, knowing its values in GENE coordinates (x, k_y, z). Considering a field quantity $\mathcal{F}$ in the coordinates $x = x(\Psi)$, $y - y_0 = C_y(q\chi - \phi)$, $z = \chi$:

$$\mathcal{F}(x, y, z) = \sum_k \hat{\mathcal{F}}_k(x, z) \exp(2\,\pi\,i\,k(y - y_0)/l_y)\ , \tag{3.21}$$

one can write

$$\begin{aligned} \mathcal{F}(\Psi, \chi, \phi) &= \mathcal{F}(x = x(\Psi), y = C_y(q\chi - \phi), z = \chi) \\ &= \sum_k \hat{\mathcal{F}}_k(x, \chi) \exp[i\,k\,n_0\,(q\,\chi - \phi)]\ . \end{aligned} \tag{3.22}$$

The periodicity condition in χ is well satisfied:

$$\begin{aligned} \mathcal{F}(\Psi, \chi + 2\pi, \phi) &= \sum_k \hat{\mathcal{F}}_k(x, \chi + 2\pi) \exp(i\,k\,n_0\,(q\,(\chi + 2\,\pi) - \phi)) \\ &= \sum_k \hat{\mathcal{F}}_k(x, \chi) \exp(-n_0\,i\,k\,q\,2\,\pi) \exp[i\,k\,n_0(q(\chi + 2\,\pi) - \phi)] \\ &= \mathcal{F}(\Psi, \chi, \phi)\,, \end{aligned} \tag{3.23}$$

having made use of Eq. (3.19). The periodicity in ϕ is clearly also verified:

$$\begin{aligned} \mathcal{F}(\Psi, \chi, \phi + 2\pi) &= \sum_k \hat{\mathcal{F}}_k(x, \chi) \exp[i\,k\,n_0\,(q\,\chi - \phi - 2\,\pi)] \\ &= \mathcal{F}(\Psi, \chi, \phi)\,. \end{aligned} \tag{3.24}$$

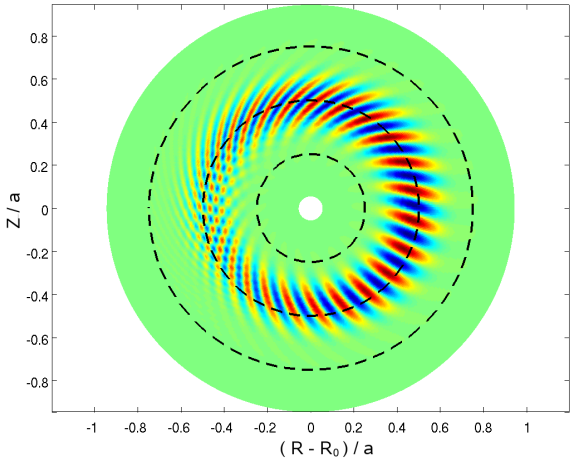

Figure 3.5: Contour plot of the electric potential reconstructed in the poloidal plane. Note the absence of any discontinuity.

Using this transformation, the electric potential computed with the global version of GENE for a linear Ion Temperature Gradient instability with toroidal mode number $n = 19$ is shown in Fig. 3.5. The periodicity condition in χ is clearly satisfied. For this example, we consider a plasma with circular concentric flux surfaces of the form:

$$R = R_0 + r\cos\theta \tag{3.25}$$

$$Z = r\sin\theta \tag{3.26}$$

where θ is the geometrical poloidal angle. The relations $\theta = \theta(r, \chi)$ and $r = f(\Psi)$ are given in Chap. 4.

Note that for representing $\mathcal{F}(\Psi, \chi, \phi)$ a more dense mesh in χ is required than the z mesh for representing $\mathcal{F}_(x, y, z)$. Indeed, in the latter case the fast phase dependence of the mode is entirely contained in the y dependence, while in the former the fast phase variation is in both χ and ϕ.

3.2.3 The local limit

In the local code, the safety factor profile, $q(x)$ is linearized

$$\begin{aligned} q(x) &\approx q_0\left(1 + \frac{r_0}{q_0}\frac{\mathrm{d}q}{\mathrm{d}x}\frac{x}{r_0}\right) \\ &= q_0\left(1 + \hat{s}\frac{x}{r_0}\right), \end{aligned} \tag{3.27}$$

where $\hat{s} = (r_0/q_0)dq/dx$ is defined as the magnetic shear. The parallel boundary condition (3.20) thus becomes

$$\begin{aligned}\hat{\mathcal{F}}_k(x, z + 2\,\pi) &= \hat{\mathcal{F}}_k(x, z) \exp\left[-\,\mathrm{i}\,k\,n_0\,q_0\,2\,\pi\right] \exp\left[-2\,\pi\mathrm{i}\,\frac{k\,C_y\,2\,\pi}{l_y}\,\frac{q_0}{r_0}\,\hat{s}\,x\right] \\ &= \mathcal{F}_k(x, z) \exp\left[-\,\mathrm{i}\,k\,n_0\,q_0\,2\,\pi\right] \exp\left[-2\pi\mathrm{i}\frac{k\;2\,\pi}{l_y}\hat{s}x\right], \end{aligned} \tag{3.28}$$

having used the particular definition $C_y = r_0/q_0$ used in the flux tube code.
Considering now the local code representation where x is treated in Fourier space, (3.28) becomes:

$$\begin{aligned}&\sum_l \hat{\hat{\mathcal{F}}}_{lk}(z + 2\,\pi) \exp(2\,\pi i\,l\,x/l_x) = \\ &\quad \sum_l \hat{\hat{\mathcal{F}}}_{lk}(z) \exp\left[-2\,\pi\,\mathrm{i}\,n_0\,q_0\,k\right] \exp\left[-2\,\pi\,\mathrm{i}\frac{k\,2\,\pi}{l_y}\hat{s}x\right] \exp\left[2\,\pi\mathrm{i}lx/l_x\right]. \end{aligned} \tag{3.29}$$

By imposing the following condition on the length l_x:

$$l_x = n_c\,\frac{l_y}{2\,\pi\hat{s}}\;, \tag{3.30}$$

where n_c is an integer, one can write:

$$\begin{aligned}&\sum_l \hat{\hat{\mathcal{F}}}_{lk}(z + 2\,\pi) \exp(2\,\pi i\,l\,x/l_x) = \\ &\quad \sum_l \hat{\hat{\mathcal{F}}}_{lk}(z) \exp\left[-2\,\pi\,\mathrm{i}\,n_0\,q_0\,k\right] \exp\left[2\,\pi\mathrm{i}(l - n_c\,k)/l_x\right]. \end{aligned} \tag{3.31}$$

One can therefore identify for a given $(k_x = 2\,\pi\,l/l_x, k_y = 2\,\pi\,k/l_y)$ mode:

$$\hat{\mathcal{F}}_{lk}(z + 2\,\pi) \;=\; \hat{\mathcal{F}}_{l+n_c\,k,k}(z) \exp(-2\,\pi\,i\,n_0\,q_0\,k)\,. \tag{3.32}$$

A given (k_y, k_x) mode is thus coupled to different $(k_y, k'_x = k_x + p\,\delta k_x)$ modes as a result of the parallel boundary conditions, where $\delta k_x = 2\,\pi\,n_c\,k/l_x$.
For convenience, it is assumed in addition that $n_0\,q_0$ is an integer, so that the corresponding phase factor in (3.32) is unity. We note that depending on the choice for q_0, n_0 is thus not necessarily an integer when using the local version of the code.

3.3 Gyro-averaging

The gyro-averaging scheme for the global code was first implemented by T. Dannert [61], using a linearization of the metric to evaluate the particle position around the gyro-orbit. In this section, this procedure is described in detail and some of its limitations are discussed. Finally, an alternative scheme is proposed where the particle position is evaluated through a transformation to a quasi-Cartesian coordinate system.
The gyro-average of several quantities is required in the fields and Vlasov equations, and is defined for a given field $\mathcal{F}$ as:

$$\begin{aligned} \bar{\mathcal{F}}(\vec{X},\mu) &= \frac{1}{2\pi}\oint \mathcal{F}(\vec{X}+\vec{\rho}(\mu,\alpha))\,d\alpha \\ &= \frac{1}{2\pi}\oint \mathcal{F}(x(\vec{X}+\vec{\rho}),y(\vec{X}+\vec{\rho}),z(\vec{X}+\vec{\rho}))\,d\alpha\,, \end{aligned} \tag{3.33}$$

where the Larmor vector $\vec{\rho}$ lies in the plane perpendicular to the magnetic field at position $\vec{X}$. Defining $(\vec{e}_1,\vec{e}_2)$ such that $(\vec{e}_1,\vec{e}_2,\vec{b})$ provides a local, unitary, orthogonal system with $\vec{b}=\vec{B}(x)/B(x)$, one can write:

$$\vec{\rho}=\rho\,(\cos\alpha\,\vec{e}_1+\sin\alpha\,\vec{e}_2)\;,\quad \text{with}\quad \rho=\frac{v_\perp}{\Omega_j}=\frac{1}{q_j}\left(\frac{2\,m_j\,\mu}{B_0}\right)^{1/2}\;. \tag{3.34}$$

As discussed in section 2.11, the $z-$variations of fluctuating quantities (terms $\sim\partial/\partial z$) are neglected with respect to (x,y) variations:

$$\mathcal{F}(x(\vec{X}+\vec{\rho}),y(\vec{X}+\vec{\rho}),z(\vec{X}+\vec{\rho}))\simeq\mathcal{F}(x(\vec{X}+\vec{\rho}),y(\vec{X}+\vec{\rho}),z(\vec{X}))\;. \tag{3.35}$$

Thus, in order to compute the gyro-average of a quantity $\mathcal{F}$, which is known on the fixed grid (x,y), one needs to evaluate it around the gyro-circle at positions $[x(\vec{X}+\vec{\rho}),y(\vec{X}+\vec{\rho})]$. These positions do not coincide in general with the (x,y) grid, and interpolations are thus required. In the global version of the code, as described below, the evaluation of $\mathcal{F}$ in the x direction is carried out with finite elements, whereas the Fourier representation used in the y direction already provides a continuous description and no further treatment is required for interpolation. In the local version of the code, the x direction is also treated in Fourier space, in this case gyro-averaging can simply be described as an analytical, algebraic operator, as will be presented at the end of this section.

3.3.1 The mixed finite element and Fourier representation

In the global code, the quantity $\mathcal{F}$ which needs to be gyro-averaged is represented in terms of its k_y Fourier components and finite elements in the x direction:

$$\mathcal{F}(x,y,z) = \sum_{k_y} \hat{\mathcal{F}}_{k_y}(x,z)\; e^{ik_y y} = \sum_{n,k_y} \hat{\mathcal{F}}_{n,k_y}(z)\; \Lambda_n(x)\; e^{ik_y y}\;, \tag{3.36}$$

where $\Lambda_n(x)$ are the radial basis functions, and $\hat{\mathcal{F}}_{n,k_y}$ are the corresponding finite element coefficients for each k_y mode. In the present version of the code, a 5th order Hermite representation is used [28]:

$$\hat{\mathcal{F}}_{k_y}(x,z) = \sum_{n} \hat{\mathcal{F}}_{n,k_y}(z)\; H_{0,n}(x) + \hat{\mathcal{F}}'_{n,k_y}(z)\; H_{1,n}(x) + \hat{\mathcal{F}}''_{n,k_y}(z)\; H_{2,n}(x) \tag{3.37}$$

where $\hat{\mathcal{F}}_{n,k_y} = \hat{\mathcal{F}}_{k_y}(x_n)$, and the 5th order piecewise polynomials $H_{m,n}(x)$ are the Hermite elements defined on $[x_{n-1}\; x_{n+1}]$ through the relations:

$$\left.\frac{d^u}{dx^u} H_{m,n}\right|_{x=x_j} = \delta_{jn}\,\delta_{um} \tag{3.38}$$

with $u = 0, 1, 2$ and zero outside $[x_{n-1}\; x_{n+1}]$. The x-derivatives $\hat{\mathcal{F}}'_{n,k_y}(z)$ and $\hat{\mathcal{F}}''_{n,k_y}(z)$ are evaluated with 4th order centered finite differences, see Eq. (2.83), such that one can write:

$$\hat{\mathcal{F}}_{k_y}(x,z) = \sum_{n} \hat{\mathcal{F}}_{n,k_y}(z)\; \Lambda_n(x)\;, \tag{3.39}$$

with

$$\begin{aligned}\Lambda_n(x) = H_{0,n}(x) + \frac{H_{1,n-2}(x) - 8\,H_{1,n-1}(x) + 8\,H_{1,n+1}(x) - H_{1,n+2}(x)}{12\,\Delta x} \\ - \frac{H_{2,n-2}(x) - 16\,H_{2,n-1}(x) + 30\,H_{2,n} - 16\,H_{2,n+1}(x) + H_{2,n+2}(x)}{12\,\Delta x^2}\end{aligned} \tag{3.40}$$

The gyro-average of $\mathcal{F}$ can now be expressed as:

$$\begin{aligned}\bar{\mathcal{F}}(\vec{X},\mu) &= \sum_{n,k_y} \hat{\mathcal{F}}_{n,k_y}(z)\; e^{ik_y y(\vec{X})} \frac{1}{2\pi} \oint \Lambda_n(x(\vec{X}+\vec{\rho}))\; e^{ik_y (y(\vec{X}+\vec{\rho}) - y(\vec{X}))} d\alpha \\ &= \sum_{n,k_y} \hat{\mathcal{F}}_{n,k_y}(z)\; e^{ik_y y}\; \mathcal{J}(x,n,k_y,z,\mu)\;,\end{aligned} \tag{3.41}$$

having defined

$$\mathcal{J}(x,n,k_y,z,\mu) = \frac{1}{2\pi}\oint \Lambda_n(x(\vec{X}+\vec{\rho}))\, e^{ik_y(y(\vec{X}+\vec{\rho})-y(\vec{X}))}d\alpha \ , \tag{3.42}$$

where $x = x(\vec{X})$, $y = y(\vec{X})$, $z = z(\vec{X})$ are the field aligned coordinates of the guiding center position $\vec{X}$. We note that $\mathcal{J}$ is independent of y as a result of the assumed axisymmetry of the magnetic geometry.

For a given k_y component one can thus write:

$$\hat{\bar{\mathcal{F}}}_{k_y}(x_i,z,\mu) = \sum_n \mathcal{J}_{i,n}(k_y,z,\mu)\, \hat{\mathcal{F}}_{n,k_y}(z) \ , \quad \forall x_i \tag{3.43}$$

with the notation $\mathcal{J}_{i,n}(k_y,z,\mu) = \mathcal{J}(x_i,n,k_y,z,\mu)$. Relation (3.43) can be expressed in matrix-vector notation:

$$\vec{\hat{\bar{\mathcal{F}}}}_{k_y}(z,\mu) = \mathcal{J}(k_y,z,\mu)\, \vec{\hat{\mathcal{F}}}_{k_y}(z) \ , \tag{3.44}$$

where $\mathcal{J}$ is a two dimensional matrix composed of the elements $\mathcal{J}_{i,n}$, and $\vec{\hat{\mathcal{F}}} = \{\mathcal{F}(x_i)\}$.

3.3.2 Double gyro-averaging

In addition to the simple gyro-averaging, the double gyro-averaging $\bar{\bar{\mathcal{F}}}$ is needed when computing the quasi-neutrality equation (2.136). This operation on $\mathcal{F}$ is defined as:

$$\begin{aligned}
\bar{\bar{\mathcal{F}}}(\vec{X},\mu) &= \frac{1}{(2\pi)^2}\oint\oint \mathcal{F}(\vec{X}+\vec{\rho}-\vec{\rho}')\, d\alpha d\alpha' \\
&= \frac{1}{2\pi}\oint \sum_{n,k_y} \hat{\mathcal{F}}_{n,k_y}(z(\vec{X}+\vec{\rho}))\mathcal{J}(x(\vec{X}+\vec{\rho}),n,k_y,z(\vec{X}+\vec{\rho}),\mu)\, e^{ik_y y(\vec{X}+\vec{\rho})}\, d\alpha \\
&\simeq \sum_{n,k_y} \hat{\mathcal{F}}_{n,k_y}(z)\, e^{ik_y y}\frac{1}{2\pi}\oint \mathcal{J}(x(\vec{X}+\vec{\rho}),n,k_y,z,\mu)\, e^{ik_y(y(\vec{X}+\vec{\rho})-y)}\, d\alpha
\end{aligned} \tag{3.45}$$

where again $z(\vec{X}+\vec{\rho}) \simeq z(\vec{X}) = z$ and $y(\vec{X}) = y$.

Using the finite element representation

$$\mathcal{J}(x(\vec{X}+\vec{\rho}),n,k_y,z,\mu) = \sum_l \mathcal{J}_{l,n}(k_y,z,\mu)\Lambda_l(x(\vec{X}+\vec{\rho})) \ , \tag{3.46}$$

one can write

$$\begin{aligned}\bar{\bar{\mathcal{F}}}(\vec{X},\mu) &= \sum_{k_y,n,l} \hat{\mathcal{F}}_{n,k_y}(z)\, e^{ik_y y(\vec{X})} \mathcal{J}_{l,n}(k_y,z,\mu)\, \frac{1}{2\pi} \int \Lambda_l(x(\vec{X}+\vec{\rho}))\, e^{ik_y(y(\vec{X}+\vec{\rho})-y)}\, d\alpha \\ &= \sum_{k_y,n,l} \hat{\mathcal{F}}_{n,k_y}(z) e^{ik_y y(\vec{X})} \mathcal{J}_{l,n}(k_y,z,\mu) \mathcal{J}(x,l,k_y,z,\mu)\ . \end{aligned} \tag{3.47}$$

For a given k_y mode one thus has:

$$\hat{\bar{\bar{\mathcal{F}}}}_{k_y}(x_i,z,\mu) = \sum_n \sum_l \mathcal{J}_{il}(k_y,z,\mu)\ \mathcal{J}_{ln}(k_y,z,\mu)\ \hat{\mathcal{F}}_{n,k_y}(z)\ ,\ \forall x_i \tag{3.48}$$

which in matrix vector notation can be written as:

$$\vec{\hat{\bar{\bar{\mathcal{F}}}}}_{k_y}(z,\mu) = \mathcal{J}^2(k_y,z,\mu)\ \vec{\hat{\mathcal{F}}}_{k_y}(z) \tag{3.49}$$

having defined $\mathcal{J}^2$ as the matrix with elements $\mathcal{J}_{in} = \sum_l \mathcal{J}_{il}\mathcal{J}_{ln}$.

3.3.3 Gyro-averaging by linearizing the metric in field-aligned coordinates

In the previous sections we have described how one can compute gyro-averaged and double gyro-averaged quantities using a finite element approach. In order to complete the procedure and to calculate the α integrals, one still needs to evaluate the field-aligned coordinates $x' = x(\vec{X}+\vec{\rho})$, $y' = y(\vec{X}+\vec{\rho})$ of the particle along the gyroring. As a first approach, the field-aligned coordinates x' and y' are estimated approximately by linearizing the metric around the guiding center position:

$$x' = x(\vec{X}+\vec{\rho}) = x(\vec{X}) + \vec{\nabla}x\cdot\vec{\rho} + \mathcal{O}(\rho^2)\ , \tag{3.50}$$

$$y' = y(\vec{X}+\vec{\rho}) = y(\vec{X}) + \vec{\nabla}y\cdot\vec{\rho} + \mathcal{O}(\rho^2)\ . \tag{3.51}$$

By choosing $(\vec{e}_1,\vec{e}_2)$ as follows:

$$\vec{e}_1 = \frac{\vec{\nabla}x}{|\vec{\nabla}x|} = \frac{\vec{\nabla}x}{\sqrt{g^{xx}}}\ , \tag{3.52}$$

$$\vec{e}_2 = \vec{b}\times\vec{e}_1 = \frac{(\vec{\nabla}x\times\vec{\nabla}y)\times\vec{\nabla}x}{|(\vec{\nabla}x\times\vec{\nabla}y)\times\vec{\nabla}x|} = \frac{g^{xx}\vec{\nabla}y - g^{xy}\vec{\nabla}x}{g\sqrt{g^{xx}}}\ , \tag{3.53}$$

with $g^2 = g^{xx}g^{yy} - (g^{xy})^2$, one obtains:

$$\rho^x = \vec{\nabla}x \cdot \vec{\rho} = \sqrt{g^{xx}}\rho\cos\alpha \ , \tag{3.54}$$

$$\rho^y = \vec{\nabla}y \cdot \vec{\rho} = \frac{g^{xy}}{\sqrt{g^{xx}}}\rho\cos\alpha + \frac{g}{\sqrt{g^{xx}}}\rho\sin\alpha \ , \tag{3.55}$$

which leads to:

$$\mathcal{J}(x, n, k_y, z, \mu) = \oint \Lambda_n(x + \rho^x)\ e^{ik_y\rho^y} d\alpha \ . \tag{3.56}$$

The approximation used in Eqs. (3.50)-(3.51) are problematic near a singularity of the coordinate system, as is the case close to the center of a polar-like coordinate system. Indeed, near such a singularity, the metric can vary significantly over the Larmor radius and lead to unwanted approximations in metric effects.

Illustration in a cylindrical system

In order to illustrate which effects are neglected when the particle position is estimated by expanding the field-aligned coordinates metric around the guiding center position, we

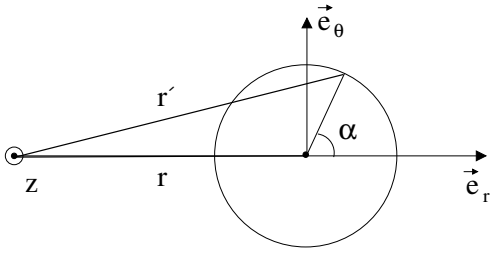

Figure 3.6: Larmor radius in a cylindrical system.

consider the simpler problem of computing the gyro-average $\bar{\mathcal{F}}$ of a cylindrical symmetric field $\mathcal{F}$. Considering cylindrical coordinates (r, θ, z), one thus has $\mathcal{F} = \mathcal{F}(r)$ and $\bar{\mathcal{F}}$ is evaluated as follows:

$$\bar{\mathcal{F}} = \frac{1}{2\pi}\int \mathcal{F}(r(\vec{X} + \vec{\rho}))d\alpha \ . \tag{3.57}$$

The particle position $r' = r(\vec{X} + \vec{\rho})$, see Fig. 3.6, is given by:

$$\begin{aligned} r' &= \sqrt{(r + \rho\,\cos\alpha)^2 + \rho^2\,\sin^2\alpha} \\ &= \sqrt{r^2 + 2\,r\,\rho\,\cos\alpha + \rho^2} \\ &\simeq r\left[1 + \frac{1}{2}\left(\frac{2\,\rho\,\cos\alpha}{r} + \frac{\rho^2}{r^2}\right) - \frac{1}{8}\left(\frac{2\,\rho\cos\alpha}{r}\right)^2\right] + \mathcal{O}(\rho^3) \\ &= r + \rho\,\cos\alpha + \underbrace{\frac{1}{2r}\rho^2\sin^2\alpha}\, + \mathcal{O}(\rho^3)\;, \end{aligned} \tag{3.58}$$

having defined $r = r(\vec{X})$, and chosen $(\vec{e}_1, \vec{e}_2)$ as $(\vec{e}_r, \vec{e}_\theta)$. In Eq. (3.58) the underbrace term is a higher order term, not accounted for in Eqs.(3.50)-(3.51), and kept here to highlight the differences.

Using a long wavelength approximation, one expands $\mathcal{F}$, further tracking the additional term in Eq. (3.58):

$$\begin{aligned} \bar{\mathcal{F}} &= \frac{1}{2\pi}\oint\left[\mathcal{F}(r) + (\,\rho\cos\alpha + \underbrace{\frac{1}{2r}\rho^2\sin^2\alpha}\,)\,\frac{\partial\mathcal{F}}{\partial r}\right. \\ &\quad \left. + \frac{\rho^2\,\cos^2\alpha}{2}\,\frac{\partial^2\mathcal{F}}{\partial r^2}\right]\,d\alpha + \mathcal{O}(\rho^3) \\ &= \mathcal{F}(r) + \frac{\rho^2}{4}(\underbrace{\frac{1}{r}\frac{\partial\mathcal{F}}{\partial r}} + \frac{\partial^2\mathcal{F}}{\partial r^2}) \qquad (3.59) \\ &= \mathcal{F}(r) + \frac{\rho^2}{4}\frac{1}{r}\frac{\partial}{\partial r}\left(r\frac{\partial\mathcal{F}}{\partial r}\right)\,. \qquad (3.60) \end{aligned}$$

From Eq. (3.59) one observes that when evaluating the particle position by simply linearizing the metric as in Eqs.(3.50)-(3.51), the $\frac{1}{r}\frac{\partial\mathcal{F}}{\partial r}$ term would be missing. This term clearly becomes significant when approaching the axis $r = 0$.

3.3.4 Gyro-averaging in quasi-Cartesian coordinates

In order to avoid the issues described above with linearizing the metric, one could compute the field-aligned coordinates (x', y', z') of the particles exactly. To this end, one could map the guiding center position $\vec{X}$ from the field-aligned coordinates (x, y, z) to the cylindrical coordinate system (R, Z, ϕ) in which the position $\vec{x} = \vec{X} + \vec{\rho}$ of the particle can be conveniently computed. The cylindrical coordinates of the particle than need to be mapped back to the field aligned coordinates (x', y', z'). Although exact, the implementation of this procedure presents itself as quite cumbersome due to the required

mapping steps, and a more practical alternative is thus suggested here instead.
As discussed in section 3.3.3 the main issue results from the fact that one is linearizing the (x, y, z) metric which is singular on axis. A pragmatic approach to overcome this problem is thus to evaluate the particle position $\vec{x} = \vec{X} + \vec{\rho}$ in the quasi-Cartesian coordinates (ξ, η):

$$\begin{cases} \xi &= x \cos z \quad , \\ \eta &= x \sin z \quad , \end{cases} \tag{3.61}$$

which is not singular at the axis, as illustrated in Fig 3.7. Note that here x is assumed to go like r at the axis, which is the case when using the circular model since $x = r$, as well as with the interface with the MHD equilibrium code by choosing $x \sim \sqrt{\Psi}$, see Chapter 4. In the limit $x \to 0$ the (ξ, η) coordinate system clearly tends towards a local Cartesian coordinate system instead of the singular (x, z) polar-like system.

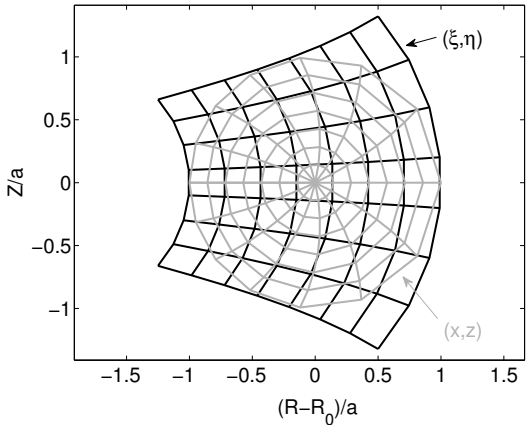

Figure 3.7: (x, z) and (ξ, η) grids in the poloidal plane for a circular equilibrium plasma.

The particle position can now be evaluated by first linearizing the metric in the (ξ, η) coordinate system and then analytically mapped back to the field-aligned coordinate system (x, y, z) using the transformation:

$$\begin{cases} x^2 &= \xi^2 + \eta^2 \quad , \\ \tan z &= \eta / \xi \qquad . \end{cases} \tag{3.62}$$

One thus obtains:

$$\begin{aligned} x'^2 = x^2(\vec{X}+\vec{\rho}) &= \xi^2(\vec{X}+\vec{\rho}) + \eta^2(\vec{X}+\vec{\rho}) \\ &\simeq \left[\xi(\vec{X}) + \vec{\rho}\cdot\vec{\nabla}\xi\right]^2 + \left[\eta(\vec{X}) + \vec{\rho}\cdot\vec{\nabla}\eta\right]^2 \\ &= x^2 + 2\,\xi\,\vec{\rho}\cdot\vec{\nabla}\xi + 2\,\eta\,\vec{\rho}\cdot\vec{\nabla}\eta + (\vec{\rho}\cdot\vec{\nabla}\xi)^2 + (\vec{\rho}\cdot\vec{\nabla}\eta)^2 \\ &= x^2 + 2\,x\,\vec{\rho}\cdot\vec{\nabla}x + (\vec{\rho}\cdot\vec{\nabla}x)^2 + x^2(\vec{\rho}\cdot\vec{\nabla}z)^2\ , \end{aligned} \tag{3.63}$$

having used the relations $\vec{\nabla}\xi = \cos z\,\vec{\nabla}x - x\,\sin z\,\vec{\nabla}z$ and $\vec{\nabla}\eta = \sin z\,\vec{\nabla}x + x\,\cos z\,\vec{\nabla}z$. From the definition of $\vec{\rho}$ in Eq. (3.34), and of the local basis vectors $\vec{e}_1$ and $\vec{e}_2$ in Eqs. (3.52)-(3.53), one obtains:

$$\vec{\rho}\cdot\vec{\nabla}x = \sqrt{g^{xx}}\,\rho\,\cos\alpha\,, \tag{3.64}$$

$$\vec{\rho}\cdot\vec{\nabla}z = \frac{g^{xz}}{\sqrt{g^{xx}}}\rho\cos\alpha + \frac{g^{xx}g^{yz} - g^{xy}g^{xz}}{g\sqrt{g^{xx}}}\rho\sin\alpha\ . \tag{3.65}$$

In the same way, the z coordinate is estimated as follows:

$$\begin{aligned} z' = z(\vec{X}+\vec{\rho}) &= \arctan\left(\frac{\eta(\vec{X}+\vec{\rho})}{\xi(\vec{X}+\vec{\rho})}\right) \\ &\simeq \arctan\left(\frac{\eta + \sin z\,\vec{\rho}\cdot\vec{\nabla}x + x\,\cos z\,\vec{\rho}\cdot\vec{\nabla}z}{\xi + \cos z\,\vec{\rho}\cdot\vec{\nabla}x - x\,\sin z\,\vec{\rho}\cdot\vec{\nabla}z}\right) \\ &= \arctan\left(\frac{(x + \vec{\rho}\cdot\vec{\nabla}x)\,\sin z + x\,\cos z\,\vec{\rho}\cdot\vec{\nabla}z}{(x+\vec{\rho}\cdot\vec{\nabla}x)\cos z\ - x\,\sin z\,\vec{\rho}\cdot\vec{\nabla}z}\right) \\ &= z + \arctan\left(\frac{x\,\vec{\rho}\cdot\vec{\nabla}z}{x + \vec{\rho}\cdot\nabla x}\right)\ , \end{aligned} \tag{3.66}$$

where the trigonometric relation $\tan(z_1+z_2) = (\tan z_1 + \tan z_2)/(1 - \tan z_1\,\tan z_2)$ has been used. One finally still needs to evaluate $y' - y$, appearing in Eq. (3.42) , with:

$$\begin{aligned} y' - y = y(\vec{X}+\vec{\rho}) - y &= C_y\left[q(\vec{X}+\vec{\rho})\,\chi(\vec{X}+\vec{\rho}) - \phi(\vec{X}+\vec{\rho})\right] - C_y\left[q(\vec{X})\,\chi(\vec{X}) - \phi(\vec{X})\right] \\ &\simeq C_y\left[q(x')\,z' - q(x)\,z(x) - \vec{\rho}\cdot\vec{\nabla}\phi)\right]\,, \end{aligned} \tag{3.67}$$

where $\phi(\vec{X}+\vec{\rho})$ was linearized, and:

$$\vec{\rho}\cdot\vec{\nabla}\phi = -\frac{\sqrt{g^{xx}}}{g}\frac{C_y}{R^2}\rho\,\sin\alpha\,. \tag{3.68}$$

The safety factor is linearized around x: $q(x') = q(x) + (x\prime - x)dq/dx$.

In Cylinder

Considering again the previous example in a cylinder, we verify that the missing $\frac{1}{r}\frac{\partial}{\partial r}$ term is recovered. Starting from Rel.(3.63), the position x' is expanded to second order in ρ:

$$\begin{aligned} x' &\simeq \sqrt{x^2 + 2\,x\,\vec{\rho}\cdot\vec{\nabla}x + (\vec{\rho}\cdot\vec{\nabla}x)^2 + x^2(\vec{\rho}\cdot\vec{\nabla}z)^2} \\ &\simeq x + \vec{\rho}\cdot\vec{\nabla}x + \frac{x}{2}(\vec{\rho}\cdot\vec{\nabla}z)^2 + \mathcal{O}(\rho^3)\ . \end{aligned} \tag{3.69}$$

In the cylindrical limit, the metric coefficients read (see Sec. 4.3):

$$g^{xx} = 1\,,\ \ g^{xy} = \hat{s}z\ \ , g^{yy} = 1 + (\hat{s}z)^2 \tag{3.70}$$

$$g^{xz} = 0\ \ ,\ g^{yz} = \frac{1}{r}\ \ ,\ g^{zz} = \frac{1}{r^2}\ , \tag{3.71}$$

which, using (3.64) and (3.65), leads to:

$$\vec{\rho}\cdot\vec{\nabla}x = \rho\,\cos\alpha\ \ ,\ \vec{\rho}\cdot\vec{\nabla}z = \frac{1}{r}\rho\,\sin\alpha\ . \tag{3.72}$$

One thus finally obtains for x':

$$x' = x + \rho\,\cos\alpha + \frac{\rho^2}{2r}\sin^2\alpha + \mathcal{O}(\rho^3)\ , \tag{3.73}$$

where we indeed recover the higher order correction term of Eq. (3.58).

3.3.5 The field equations

With the finite element representation in x described above for the gyro-averaging and double gyro-averaging, the different field equations can be written as matrix equations for the discrete fields.

The quasi-neutrality equation

Using Eqs. (3.43) and (3.48), the quasi-neutrality equation (2.136) reads for all spatial positions:

$$\begin{aligned} &\sum_j \Bigg\{ \pi\,\hat{n}_{0j}(x_0)\,Z_j \int \hat{B}^*_{0\|,i}(\hat{z},\hat{v_\|}) \sum_n \mathcal{J}_{i,n}(k_y,z,\mu)\ \vec{\hat{f}}_{1j,n}\ \ d\hat{v_\|}\,d\hat{\mu} \\ -\ &\frac{Z_j^2\,\hat{n}_{0j,i}}{\hat{T}_{0j,i}}\left[\hat{\Phi}_i(k_y,z) - \frac{\hat{B}_{0,i}}{\tau_{0j,i}}\sum_n\sum_l \int \mathcal{J}_{il}(k_y,z,\mu)\ \mathcal{J}_{ln}(k_y,z,\mu)\ \exp(-\frac{\mu\hat{B}_{0,i}}{\tau_{0j,i}})\,d\hat{\mu}\ \hat{\Phi}_n(k_y,z)\ \right]\Bigg\} \\ =\ &0\quad \forall x_i \end{aligned} \tag{3.74}$$

which can be expressed for each k_y and $z = z_k$ in matrix vector notation as a linear system for $\vec{\Phi} = \{\hat{\Phi}_i(k_y, z_k)\}$, $i = [1, n_x]$, (the hat is dropped here):

$$M\vec{\Phi} = \vec{S}_1 \ , \tag{3.75}$$

with

$$M_{in} = \sum_j \frac{Z_j^2 \, \hat{n}_{0j,i}}{\hat{T}_{0j,i}} \left[\delta_{in} - \frac{\hat{B}_{0,i}}{\tau_{0j,i}} \sum_l \int \mathcal{J}_{il} \, \mathcal{J}_{ln} \, \exp(-\frac{\mu \hat{B}_{0,i}}{\tau_{0j,i}}) \, d\hat{\mu} \right] , \tag{3.76}$$

and

$$S_{1i} = \sum_j \pi \, \hat{n}_{0j}(x_0) \, Z_j \int \hat{B}^*_{0\|,i} \sum_n \mathcal{J}_{i,n} \, \hat{f}_{1j,n} \ d\hat{v}_\| \, d\hat{\mu} \ . \tag{3.77}$$

The equation for $\vec{\Phi}$ defined by (3.76) can then be solved using standard numerical methods for linear algebraic systems of equations. In GENE, Eq. (3.76) is solved with a direct method for each (k_y, z_k) using an LU decomposition. Note that as M depends only on the magnetic equilibrium and background distribution f_0, this LU decomposition needs only to be done once for each (k_y, z_k) during the initialization phase of the simulation.

The adiabatic electron case

Similarly, when considering adiabatic electrons, Eq. (2.137) can be written:

$$\left(M' + \frac{\hat{n}_{0e}}{\hat{T}_{0e}} \right) \ \vec{\Phi} = \vec{S}'_1 + \frac{\hat{n}_{0e}}{\hat{T}_{0e}} \langle \vec{\Phi} \rangle \ , \tag{3.78}$$

where M' and $\vec{S}'_1$ are the same matrix and vector as in Eqs. (3.76) and (3.77) except that the sums $\sum_j$ are running over $j \neq e$. In order to solve Eq. (3.78) one first needs to evaluate the unknown flux-surface average $\langle \vec{\Phi} \rangle$ of the electric potential. Taking the flux-surface average of Eq. (3.78), one obtains:

$$\left\langle \left(M' + \frac{\hat{n}_{0e}}{\hat{T}_{0e}} \right) \ \vec{\Phi} \right\rangle = \langle \vec{S}'_1 \rangle + \frac{\hat{n}_{0e}}{\hat{T}_{0e}} \langle \vec{\Phi} \rangle \ , \tag{3.79}$$

Using Eqs (3.78) and (3.79) would in principle require to solve an integral equation for Φ. However, a further simplification is introduced here in order to evaluate $\langle \vec{\Phi} \rangle$, which

consists in neglecting the poloidal variation of equilibrium quantities such that:

$$\left\langle \left(M' + \frac{\hat{n}_{0e}}{\hat{T}_{0e}} \right) - \left\langle M' + \frac{\hat{n}_{0e}}{\hat{T}_{0e}} \right\rangle \right\rangle \simeq 0 \,, \tag{3.80}$$

leading to:

$$\left\langle \left(M' + \frac{\hat{n}_{0e}}{\hat{T}_{0e}} \right) \vec{\Phi} \right\rangle \simeq \left\langle M' + \frac{\hat{n}_{0e}}{\hat{T}_{0e}} \right\rangle \langle \vec{\Phi} \rangle = \left[\langle M' \rangle + \frac{\hat{n}_{0e}}{\hat{T}_{0e}} \right] \langle \vec{\Phi} \rangle \,. \tag{3.81}$$

With this approximation Eq. (3.79) becomes:

$$\langle M' \rangle \langle \vec{\Phi} \rangle = \langle \vec{S}_1' \rangle \,, \tag{3.82}$$

which can now be solved as a linear system for the flux-surface averaged electric potential $\langle \vec{\Phi} \rangle$.

Ampère's law

From Eq. (2.138), the discrete equation for $A_{1\parallel,i}(k_y, z_k) = A_{1\parallel}(x_i, k_y, z_k)$ can be written in matrix-vector form:

$$D\vec{A} = \vec{S}_A \tag{3.83}$$

where D is the matrix associated with the discretized $\nabla_\perp^2 = g^{xx}\frac{\partial^2}{\partial x^2} + i\,2\,g^{xy}k_y\frac{\partial}{\partial x} - g^{yy}k_y^2$ operator, where the derivatives are evaluated with centered 4th order finite differences, see Eqs. (3.1) and (3.2), and $\vec{S}_A = S_{Ai=1,..n_x}$ with:

$$S_{A,i} = \sum_j \left\{ \frac{\beta_{\text{ref}}}{2} Z_j \, \hat{n}_{0j}(x_0) \, \hat{v}_{Tj}(x_0) \, \pi \int \hat{B}^*_{0\parallel,i} \sum_n \mathcal{J}_{i,n} \, \vec{\hat{f}}_{1j,n} \, d\hat{v}_\parallel \, d\hat{\mu} \right. \tag{3.84}$$

$$\left. - \frac{\beta_{\text{ref}}^2}{4} \, \frac{\hat{n}_{0j,i} \, \hat{j}_{0\parallel,i}}{\hat{B}^2_{0,i}} \left(Z_j \, \hat{\Phi}_{1,i} - \frac{\hat{B}_{0,i}}{\tau_{0j,i}} \sum_n \sum_l \int \mathcal{J}_{il} \, \mathcal{J}_{ln} \, e^{-\hat{\mu}\hat{B}_0/\tau_{0j}} \, d\hat{\mu} \, \Phi_{1,n} \right) \right\} \tag{3.85}$$

note that the sum over l is pre-computed in the initialization phase.

3.3.6 The local limit

In the local limit, thanks to the considered Fourier representation in both the x and y directions, the gyro-averaging operator (3.33) with the approximation (3.35) can be

simply expressed as:

$$\begin{aligned}\bar{\mathcal{F}}(x,y) &= \frac{1}{2\,\pi}\oint \mathcal{F}(x(\vec{X}+\vec{\rho}),y(\vec{X}+\vec{\rho}))\;d\alpha \\ &= \sum_{k_x,k_y}\hat{\mathcal{F}}_{k_x,k_y}\;\frac{1}{2\,\pi}\oint e^{i\,[k_x\,x(\vec{X}+\vec{\rho})+k_y\,y(\vec{X}+\vec{\rho})]}\;d\alpha \\ &= \sum_{k_x,k_y}\hat{\mathcal{F}}_{k_x,k_y}\;e^{i(\,k_x\,x+k_y\,y)}\;\frac{1}{2\,\pi}\oint e^{i(k_x\,\vec{\nabla}x\cdot\vec{\rho}+k_y\,\vec{\nabla}y\cdot\vec{\rho})}\;d\alpha \end{aligned} \tag{3.86}$$

where the particle position has been evaluated by linearizing the metric, see Eqs. (3.50) and (3.51). Using now relations (3.54) and (3.55), one has:

$$\begin{aligned} k_x\,\vec{\nabla}x\cdot\vec{\rho}+k_y\,\vec{\nabla}y\cdot\vec{\rho} &= \rho\left[\left(k_x\,\sqrt{g^{xx}}+k_y\,\frac{g^{xy}}{\sqrt{g^{xx}}}\right)\cos\alpha+k_y\,\frac{g}{\sqrt{g^{xx}}}\,\sin\alpha\right] &(3.87)\\ &= \rho\,k_\perp\,\cos(\alpha+\phi)\;, &(3.88)\end{aligned}$$

with

$$\begin{aligned} k_\perp^2 &= \left(k_x\,\sqrt{g^{xx}}+k_y\,\frac{g^{xy}}{\sqrt{g^{xx}}}\right)^2+k_y^2\,\frac{g^2}{g^{xx}} &(3.89)\\ &= g^{xx}\,k_x^2+g^{yy}\,k_y^2+2\,k_x\,k_y\,g^{xy}\;, &(3.90)\end{aligned}$$

and

$$\tan\phi=-\left(k_y\,\frac{g}{\sqrt{g^{xx}}}\right)\Big/\left(k_x\,\sqrt{g^{xx}}+k_y\,\frac{g^{xy}}{\sqrt{g^{xx}}}\right) \tag{3.91}$$

The gyro-averaging operator finally reads for a given (k_x,k_y) mode:

$$\bar{\mathcal{F}}(k_x,k_y)=J_0(\lambda_j)\,\mathcal{F}(k_x,k_y)\,, \tag{3.92}$$

where $J_0=\pi^{-1}\int_0^\pi e^{\mathtt{i}\,x\,\cos\alpha}\,d\alpha$ is the zeroth order Bessel function of the first kind, $\lambda_j=\sqrt{(2\,B_0\,\mu/m_j)}\,k_\perp/\Omega_j$. In this representation, the field equations become algebraic expressions and thus are trivially solved. The electrostatic potential, solution to the quasi-neutrality equation, reads:

$$\hat{\Phi}=\frac{\sum_j\,\hat{n}_{0j}\,\pi\,Z_j\,\int\,\hat{B}^*_{0\|}J_0(\lambda_j)\,\hat{f}_{1j}\,d\hat{v}_\|d\hat{\mu}}{\sum_j\,\hat{n}_{0j}\frac{Z_j^2}{\hat{T}_{0j}}\,[1-\Gamma_0(b_j)]} \tag{3.93}$$

where $\Gamma_0(b)=\exp(-b)\,I_0(b)$ is the zeroth order scaled modified Bessel function and $b_j=(v_{Tj}^2\,k_\perp^2)/(2\,\Omega_j^2)$. When considering adiabatic electrons, the solution to the quasi-neutrality

equation equation becomes:

$$\hat{\Phi} = \frac{\sum_{j\neq e} \hat{n}_{0j}\,\pi\,Z_j \int \hat{B}^*_{0\|} J_0(\lambda_j)\,\hat{f}_{1j}\,d\hat{v}_\|\,d\hat{\mu} + \frac{\hat{n}_{0e}}{\hat{T}_{0e}}\langle\hat{\Phi}\rangle}{\frac{\hat{n}_{0e}}{\hat{T}_{0e}} + \sum_{j\neq e}\hat{n}_{0j}\frac{Z_j^2}{\hat{T}_{0j}}\left[1-\Gamma_0(b_j)\right]}\,, \tag{3.94}$$

where the flux-surface average of Φ is computed using the same approximation as in the global case:

$$\langle\hat{\Phi}\rangle = \frac{\left\langle\sum_{j\neq e}\hat{n}_{0j}\,\pi\,Z_j\int\hat{B}^*_{0\|}J_0(\lambda_j)\,\hat{f}_{1j}\,d\hat{v}_\|\,d\hat{\mu}\right\rangle}{\left\langle\sum_j \hat{n}_{0j}\frac{Z_j^2}{\hat{T}_{0j}}\left[1-\Gamma_0(b_j)\right]\right\rangle}\,. \tag{3.95}$$

Finally Ampère's law reads:

$$\hat{A}_{1\|} = -\frac{1}{k_\perp^2}\sum_j\left\{\frac{\beta_{\mathrm{ref}}}{2}\,Z_j\,\hat{n}_{0j}\,\hat{v}_{Tj}(x_0)\,\pi\int\hat{B}^*_{0\|}\,J_0(\lambda_j)\,\hat{f}_{1j}\,d\hat{v}_\|\,d\hat{\mu}\right. \tag{3.96}$$

$$\left. -\frac{\beta_{\mathrm{ref}}^2}{4}\,\frac{\hat{n}_{0j}\hat{j}_{0\|}Z_j}{\hat{B}_0^2}\left[1-\Gamma_0(b_j)\right]\hat{\Phi}\right\}. \tag{3.97}$$

More details to the derivation of the local gyro-averaging and field equations can be found in [51].

3.4 Real space dealiasing

3.4.1 Aliasing issue

The numerical discretization of the physically continuous space defines a smallest resolved scale (i.e. highest Fourier mode) which results from the finite number of grid points in the simulation domain. In a nonlinear simulation, even when the linear drive region is well contained inside the resolved region of the spectrum, the quadratic nonlinear $\vec{E}\times\vec{B}$ term will generate smaller and smaller structures. In the absence of physical damping, these small scales will eventually reach the grid size and will therefore result in unresolved scales leading to so-called aliasing effects. In order to get a better insight concerning this issue we shall first consider a discrete Fourier representation of the discretized fields and discuss how aliasing effects can be suppressed in a graceful way in this representation, which shall then lead us to an equivalent real space procedure.

To understand the basic aliasing effect, let us first consider two real periodic one-dimensional functions f_1 and f_2 discretized on N grid points, each containing a single Fourier mode

with non zero amplitude. Their respective mode numbers k_1 and k_2 are assumed to be such that the sum $k_1 + k_2$ is greater than the Nyquist limit, $k_1 + k_2 > N/2$. When multiplying the two functions together, $f_{12} = f_1 \times f_2$, the spectrum will contain both a Fourier mode at $k_1 - k_2$ and an unresolved mode with mode number $k_{12} = k_1 + k_2$. This unresolved mode will effectively reappear at position $k_{12} - N$ in the spectrum of the product function f_{12} as a result of the N periodicity of the Fourier components. The generation of this unphysical mode at $k_{12} - N$ is what is called aliasing.

In order to further clarify this effect, let us now consider a one dimensional example with the two real functions discretized over $N = 32$ points:

$$f_1(x) = 2\sin(2\pi k_1/L_x) \tag{3.98}$$

$$f_2(x) = 2\sin(2\pi k_2/L_x) \tag{3.99}$$

and assuming $k_1 = 10$, and $k_2 = 8$. In this case, the product $f_{12} = f_1 \times f_2$ should contain a mode $k_1 - k_2 = 2$ and a mode $k_1 + k_2 = 18$. The mode number 18 is above the Nyquist limit of $N/2 = 16$ and thus reappears in the spectrum at position $18 - N = -14$ due to the N periodicity of the Fourier components which is illustrated in Fig. 3.8. Note that as all considered fields are real, their complex Fourier spectra always contains pairs of coefficients (f_k, f_{-k}) verifying the reality condition $f_{-k} = f_k^*$.

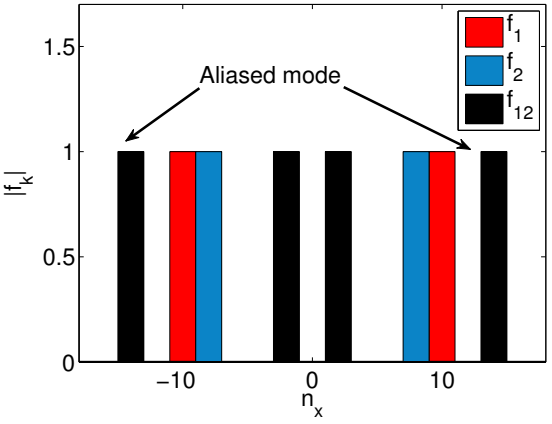

Figure 3.8: Fourier spectra of f_1, f_2 and $f_{12} = f_1 \times f_2$

3.4.2 Standard dealiasing technique

When working in Fourier space, the standard method to avoid aliased modes generated by non-linear terms to pollute the spectrum consists of two steps. Each spectrum of the two functions to be multiplied is (1) first extended and padded with zeros before the nonlinear multiplication. In practice both theses extended spectra are temporarily transformed to real space where the product is straightforward to carry out. Back to Fourier space the resulting product function is thus still given on the extended spectrum, and (2) the eventual modes now appearing in the extended spectrum region are then removed to obtain a function defined on the original spectrum. Note that this so-called anti-aliasing procedure clearly does not treat exactly the non-linear spectrum evolution but simply enables to gracefully remove from the numerical simulation any unresolved Fourier modes that may be generated.

Going back to our previous example functions Eqs. (3.98)-(3.99), the real space and Fourier representations of the product function f_{12} with and without anti-aliasing procedure is shown on Fig. 3.9.

This Fourier space anti-aliasing technique is used in the local version of GENE for both x and y directions and for the y direction in the global code. In practice a so-called 3/2 rule is considered, that is the extended spectrum contains $3\,N/2$ modes.

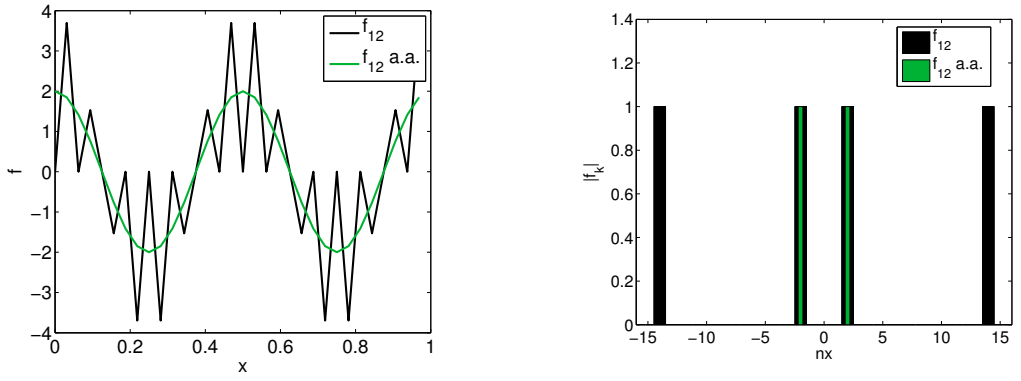

Figure 3.9: Real space (left) and Fourier (right) representation of the product function f_{12}, with and without anti-aliasing procedure

3.4.3 Treatment in real space

In the global version of the code, the x direction is no longer treated in Fourier space, which requires an alternative approach. The two steps described above correspond in real space to (1) an interpolation, since the same functions are now defined on a finer grid, followed by (2) a smoothing operation, or filtering on the product function. When carrying out these two steps in real space, one can only approximately reproduce the Fourier space treatment and will introduce damping and/or apparition of spurious modes in the resolved spectrum which should be controlled.

In view of quantifying the effects of this real space treatment and to compare different interpolation and smoothing schemes, the procedure is applied to periodic functions such that a Fourier analysis can be easily carried out.

Let f be a periodic function represented on the initial equidistant N-point grid and $\bar{f}$ the corresponding interpolated function on the refined $2\,N$-point grid, obtained from the original grid by adding mid-point mesh nodes. One notes that although for the Fourier space dealiasing the refined mesh contains only $3\,N/2$ points, we use for the real space scheme a $2\,N$ mesh, such that the grid point values of f can be used for $\bar{f}$. In order to analyse how the interpolation affects the spectrum, one can write the corresponding linear operator in Fourier space in the form $\hat{\bar{f}}_{\bar{k}} = H(\bar{k})\hat{f}_{\bar{k}}$, $\bar{k} = [-N, N]$, where $H(\bar{k})$ will be referred to as the spectral extension function, and relates the Fourier components of the interpolated function $\hat{\bar{f}}_{\bar{k}}$ to the Fourier components of the initial function $\hat{f}_{\bar{k}}$. A practical example of the derivation of $H(k)$ for the Lagrange interpolation is provided in Eq. (3.108). Noticing that $\hat{f}_k$ is periodic with period N, $\hat{f}_k = \hat{f}_{k+N}$, a given mode $\hat{f}_k$ will therefore in general give rise to two modes in the $\hat{\bar{f}}$ spectrum:

$$\hat{f}_k \rightarrow \begin{cases} 1)\ \hat{\bar{f}}_k & = H(k)\,\hat{f}_k \\ 2)\ \hat{\bar{f}}_{k+N} & = H(k+N)\,\hat{f}_k \end{cases} . \tag{3.100}$$

The spectral extension function H verifies $H(k) + H(k+N) = 1$, see for example Eq. (3.108), reflecting the fact that the information on the initial grid is kept, and that one recovers the original function f when removing mid-point values from the interpolated function $\bar{f}$. The splitting of mode $\hat{f}_k$ into two modes $\hat{\bar{f}}_k$ and $\hat{\bar{f}}_{k+N}$ also show how the spectrum may get deformed by the interpolation step. Different interpolation schemes

have been tested, and their corresponding spectral extension functions are plotted on Fig. 3.10. Only the box-shaped extension function of the Fourier anti-aliasing scheme avoids deformation of the spectrum according to (3.100). All real space interpolation schemes considered have corresponding extension functions which are only approximations of this box-shape. Since $x-$parallelization is considered in the implementation of

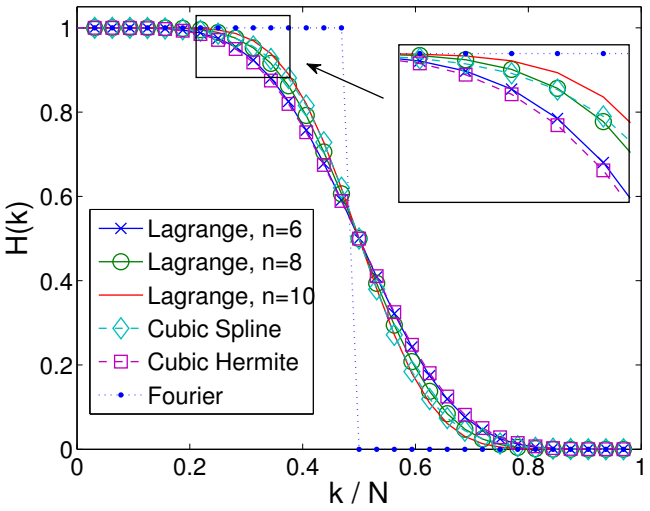

Figure 3.10: Spectral extension function for different interpolation schemes: Lagrange interpolation of various orders $p = n - 1$, Cubic Spline, Cubic Hermite. For comparison, the box-shaped extension function of the standard Fourier anti-aliasing scheme is also shown.

the global GENE code, a local interpolation scheme is more favorable, and because of its simplicity, high order Lagrange interpolation was finally implemented. The default value is the $n = 10$ points stencil (9th order polynomial) interpolation.

There exist various ways to construct a smoothing operator. In the present work, considering that the $H(k)$ functions for the different interpolation schemes approach well the ideal box-shaped function, it was decided to design the smoothing operator so that its transfer function $S(k)$ in Fourier space would be identical to $H(k)$. The smoothed function on the extended grid reads in Fourier space:

$$\langle \hat{\bar{f}} \rangle_{\bar{k}} = S(\bar{k}) \hat{\bar{f}}_{\bar{k}} \tag{3.101}$$

Restricting to the coarse N-point grid by dropping every 2^{nd} point reads in Fourier space:

$$\langle \hat{f} \rangle_k = \langle \hat{\bar{f}} \rangle_k + \langle \hat{\bar{f}} \rangle_{k+N} = S(k) \hat{\bar{f}}_k + S(k+N) \hat{\bar{f}}_{k+N} \ , \tag{3.102}$$

where we note the contribution of the $\langle \hat{\bar{f}}_{k+N} \rangle$ to the spectrum of $\langle f \rangle$ as a result of aliasing. In particular this contribution vanishes, $\langle \hat{\bar{f}}_{k+N} \rangle = 0$, in the case of the box-shaped filtering used in the standard Fourier anti-aliasing scheme.
Relation (3.102) is then used to derive the corresponding real space operator which can be implemented in the code.

3.4.4 Lagrange interpolation

In order to better illustrate the real space anti-aliasing procedure, the derivation of the spectral extension function $H(k)$ for the Lagrange interpolation is now described together with the corresponding smoothing operator.
First of all, the discrete periodic function $f_i = f(x_i)$, defined on the equidistant grid x_i, is represented using an n point Lagrange interpolation by

$$f(x) = \sum_{j=j_{min}}^{j_{max}} L_j(x - x_i)\, f_{i+j} \ , \quad \forall\, x \,\epsilon\, [x_i, x_{i+1}] \, , \tag{3.103}$$

where $j_{min} = -[(n-1)/2]$ and $j_max = [n/2]$, with $[z]$ the nearest integer to z towards minus infinity. The $L_j(x)$ are the $p = (n-1)$th order polynomials defined by $L_j(j'\,\Delta x) = \delta_{j\,j'}$ $\forall j,\, j' = j_{min} \dots j_{max}$. In the following we restrain ourselves to midpoint interpolation, and to even stencils, i.e. odd order polynomials, so that the interpolated value at $x_{i+1/2}$ is computed using the same number of f_i values on the left and on the right.
The interpolated function $\bar{f}_l$ is represented on the dense mesh $\bar{x}_l$ for $l \,\epsilon\, [0, 2N-1]$ with,

$$\bar{x}_{2i} = x_i \quad \text{and} \quad \bar{x}_{2i+1} = x_{i+1/2} \quad , \tag{3.104}$$

$$\bar{f}_{2i} = f_i \quad \text{and} \quad \bar{f}_{2i+1} = \sum_{j=-s+1}^{s} L_j(\Delta x/2)\, f_{i+j} \ , \tag{3.105}$$

where $s = n/2$. The stencil for such a Lagrange interpolation is shown in Fig. 3.11.
Using these definitions, the Fourier coefficients of $\bar{f}$ can then be expressed in terms of the

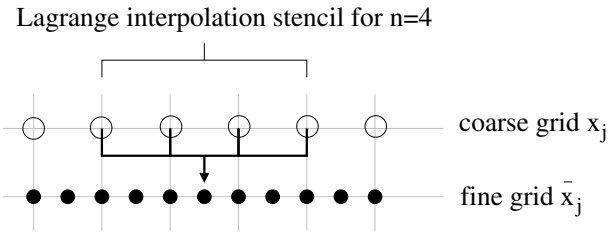

Figure 3.11: Schematic of the Lagrange interpolation stencil for $n = 4$.

Fourier coefficients of f:

$$\begin{aligned}
\hat{\bar{f}}_k &= \frac{1}{2N}\sum_{l=0}^{2N-1} \bar{f}_l e^{-\mathrm{i}\,\pi\,l\,k/N} \\
&= \frac{1}{2N}\left[\sum_{l=0}^{N-1} \bar{f}_{2l}\; e^{-\mathrm{i}\,2\,\pi\,l\,k/N} + \sum_{l=0}^{N-1} \bar{f}_{2l+1}\; e^{-\mathrm{i}\,2\,\pi\,(l+1/2)\,k/N}\right] \\
&= \frac{1}{2}\hat{f}_k + \frac{e^{-\mathrm{i}\,\pi\,k/N}}{2}\frac{1}{N}\sum_{l=0}^{N-1}\sum_{j=-s+1}^{s} L_j(\Delta x/2)\; f_{l+j}\; e^{-\mathrm{i}\,2\,\pi\,l\,k/N} \\
&= \frac{1}{2}\hat{f}_k + \frac{e^{-\mathrm{i}\,\pi\,k/N}}{2}\sum_{j=-s+1}^{s}\frac{1}{N} L_j(\Delta x/2)\sum_{l=j}^{N-1+j} f_l\; e^{-\mathrm{i}\,2\,\pi\,(l-j)\,k/N}
\end{aligned} \tag{3.106}$$

using the periodicity of f, the last sum reads:

$$\begin{aligned}
\frac{1}{N}\sum_{l=j}^{N-1+j} f_l\; e^{-\mathrm{i}\,2\,\pi\,(l-j)\,k/N} &= \frac{1}{N}\sum_{l=0}^{N-1} f_l\; e^{-\mathrm{i}\,2\,\pi\,(l-j)\,k/N} \\
&= \hat{f}_k\; e^{\mathrm{i}\,2\,\pi\,j\,k/N}\;.
\end{aligned} \tag{3.107}$$

The spectral extension function $H(k)$ is thus finally given by:

$$\hat{\bar{f}}_k = H(k)\; f_k = \frac{1}{2}\left[1 + \sum_{j=-s+1}^{s} L_j(\Delta_x/2)\, e^{-\mathrm{i}\,\pi\,(1-2j)\,k/N}\right] f_k\;. \tag{3.108}$$

The $H(k)$ function is shown in Fig. 3.10 for various stencil sizes n. The fact that $L_j(\Delta x/2)$ are real, naturally leads to the reality condition $H^*(k) = H(-k)$. But for n even, the additional symmetry $L_j(\Delta x/2) = L_{-j+1}(\Delta x/2)$ results in $H(k)$ being real valued, as can be easily shown from Eq. (3.108).

As discussed in the previous section, the smoothing operator $S(k)$ is chosen to be identical to $H(k)$ so that:

$$\langle\hat{f}\rangle_k = H(k)\,\hat{\bar{f}}_k + H(k+N)\,\hat{\bar{f}}_{k+N}\;. \tag{3.109}$$

From this relation, the point values of the smoothed function $\langle f \rangle$ can be expressed in terms of the values of $\bar{f}$:

$$\begin{aligned}
\langle f \rangle_l &= \sum_{k=0}^{N-1} \langle \hat{f} \rangle_k \, e^{\mathtt{i}\, 2\pi\, k\, l/N} \\
&= \sum_{k=0}^{N-1} \left(H(k)\, \hat{\bar{f}}_k + H(k+N)\, \hat{\bar{f}}_{k+N} \right) e^{\mathtt{i}\, 2\pi\, k\, l/N} \\
&= \sum_{k=0}^{N-1} H(k) e^{\mathtt{i}\, 2\pi\, k\, l/N}\, \hat{\bar{f}}_k + \sum_{k=0}^{N-1} H(k+N)\, \hat{\bar{f}}_{k+N}) \, e^{\mathtt{i}\, 2\pi\, k\, l/N}\, e^{\mathtt{i}\, 2\pi\, k\, N/N} \\
&= \sum_{k=0}^{N-1} H(k) e^{\mathtt{i}\, 2\pi\, k\, l/N}\, \hat{\bar{f}}_k + \sum_{k'=N}^{2N-1} H(k)\, \hat{\bar{f}}_{k'}\, e^{\mathtt{i}\, 2\pi\, k'\, l/N} \\
&= \sum_{k=0}^{2N-1} H(k) e^{\mathtt{i}\, 2\pi\, k\, 2l/2\, N}\, \hat{\bar{f}}_k
\end{aligned} \tag{3.110}$$

Using Eq. (3.108) one finally obtains the relation

$$\begin{aligned}
\langle f \rangle_l &= \frac{1}{2} \left[\sum_{k=0}^{2N-1} \hat{\bar{f}}_k \, e^{\mathtt{i}\, \pi\, k\, 2\, l/N} + \sum_{j=-s+1}^{s} L_j(\Delta_x/2) \sum_{k=0}^{2N-1} \hat{\bar{f}}_k \, e^{-\mathtt{i}\, 2\pi\, (1-2j-2l)\, k/2\, N} \right] \\
&= \frac{1}{2} \left(\bar{f}_{2l} + \sum_{j=-s+1}^{s} L_j(\Delta_x/2) \bar{f}_{2(l+j)-1} \right)
\end{aligned} \tag{3.111}$$

which is used to compute the smoothed function f on the the N points grid. The stencil for such a "Lagrange smoothing" is shown in Fig. 3.12.

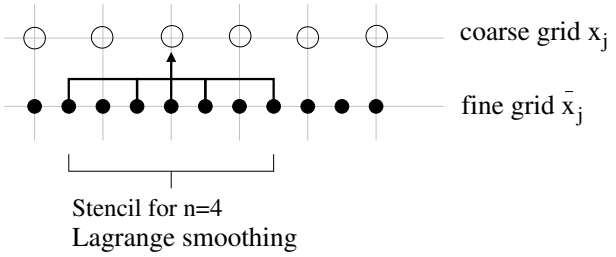

Figure 3.12: Schematic of the Lagrange smoothing stencil for $n = 4$.

3.4.5 Validation with nonlinear simulations

The anti-aliasing procedure was first tested in a version of the GENE code which still uses Fourier treatment of the x derivatives and field solver, but with a real space anti-aliasing scheme. Results in Fig. 3.13 are obtained with 9th order Lagrange interpolation

(i.e. $n = 10$) and the corresponding smoothing operator, and are compared with nonlinear simulations using the standard Fourier space dealiasing or no dealiasing. For the simulations with real space dealiasing or without dealiasing a hyperdiffusion term, see Section 3.1.1, is required and the results are shown in each case for the minimal hyperdiffusion coefficient, h_x, ensuring a stable simulation.

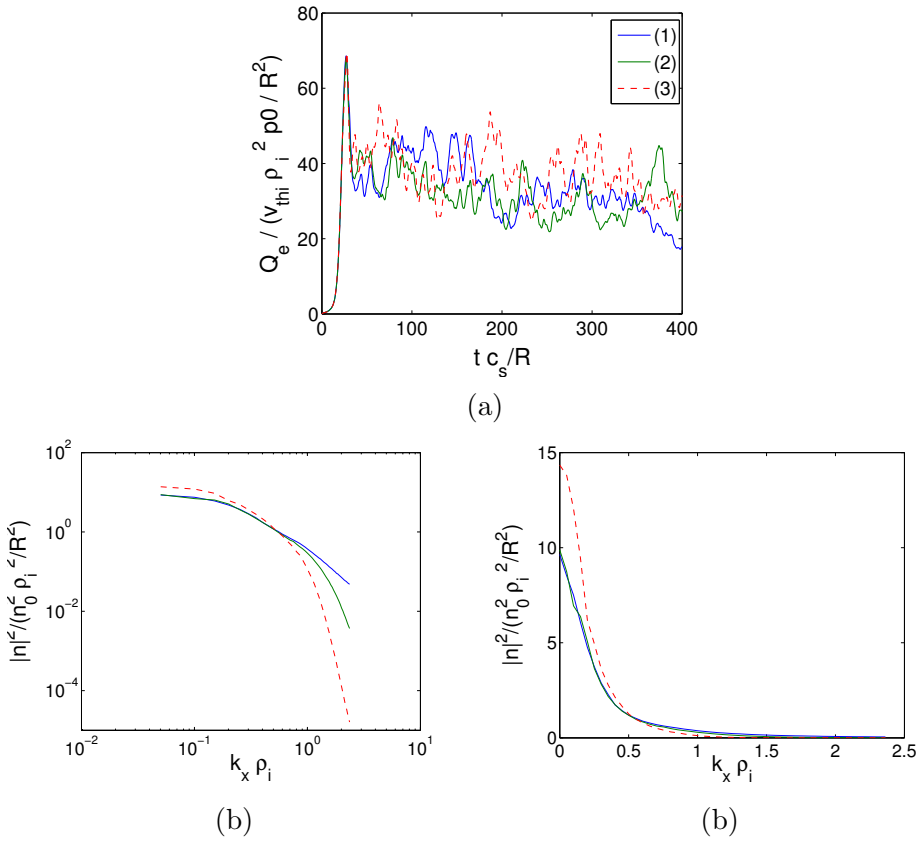

Figure 3.13: (a) Electrostatic heat flux time trace, (b) k_x density spectrum in logarithmic and (c) linear scale. The different curves are obtained using (1) the standard Fourier anti-aliasing and $h_x = 0$, (2) the real space anti-aliasing with Lagrange interpolation of order 9 and $h_x = 0.6$, and (3) no anti-aliasing and $h_x = 4$.

The real space anti-aliasing enables one to use a lower value of the hyperdiffusion coefficient h_x required to obtain a stable simulation compared to the case where no anti-aliasing was used. In addition, the resulting k_x density spectrum is much closer to the simulations with Fourier space anti-aliasing. The efficiency of the real space anti-aliasing technique was thus clearly validated.

3.5 Sources and sinks

In the absence of any additional source, the profiles in a global nonlinear simulation tend to relax towards sub-critical gradients. They eventually becomes close to the critical gradient values, the turbulence drive is strongly decreased and a state close to marginality is reached.

In the version of the global code used in this work, Dirichlet boundary conditions are considered in the radial direction. The temperature and density at both ends of the

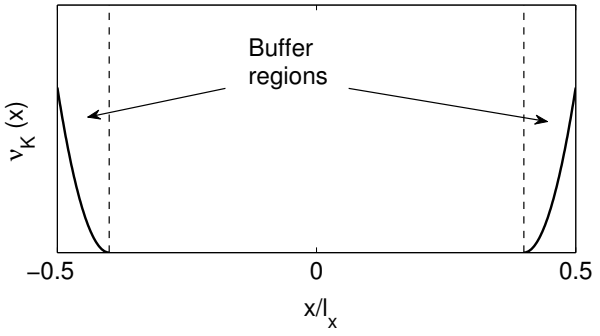

Figure 3.14: Coefficient profile $\hat{\nu}_k(x)$ of the damping Krook operator applied within edge buffer regions in nonlinear simulations.

simulation domain are thus constraints to their initial values, while a profile relaxation may occur in the center of the domain. This was observed to potentially lead to strong, unphysical profiles variations close to the boundaries, which in turn generated strong turbulence in the edge regions. In order to avoid such behavior an artificial Krook damping operator is applied in buffer regions. This operator is added to the right hand side of the gyrokinetic equation (2.135):

$$\hat{h}_K = -\hat{\nu}_K(x)\, \hat{g}_{1j} \; . \tag{3.112}$$

Where the function $\hat{\nu}_K(x)$ is zero outside of the buffer regions, and is determined by fourth order polynomial ramp inside, as illustrated in Fig. 3.14. The maximal amplitude of ν_k is set to be comparable to the linear growth rates, while the width of the buffer regions typically represent $5 - 10\%$ of the simulation domain on each sides.

In order to facilitate achieving quasi-steady state nonlinear simulations, an artificial Krook-type heat source was in addition implemented. This source, similar to the one in Ref. [62], is applied over the whole system and is designed to control the temperature

profile, while conserving the flux-surface averaged density and parallel momentum. The following term is thus added to the right hand side of the gyrokinetic equation (2.135):

$$\hat{S}_K(x,|v_\parallel|,\mu) = -\hat{\gamma}_h \left[\langle \hat{f}_{1j}(\vec{X},|v_\parallel|,\mu)\rangle - \langle \hat{f}_{0j}(\vec{X},|v_\parallel|,\mu)\rangle \frac{\left\langle \int d\vec{v}\, \langle \hat{f}_{1j}(\vec{X},|v_\parallel|,\mu)\rangle \right\rangle}{\left\langle \int d\vec{v}\, \langle \hat{f}_{0j}(\vec{X},v_\parallel,\mu)\rangle \right\rangle} \right] , \tag{3.113}$$

where $\langle . \rangle$ refers to the flux-surface average and

$$\hat{f}_{1j}(\vec{X},|v_\parallel|,\mu) = \frac{\hat{f}_{1j}(\vec{X},v_\parallel,\mu) + \hat{f}_{1j}(\vec{X},-v_\parallel,\mu)}{2} . \tag{3.114}$$

The conservation of density is ensured through the correction term $\langle \int \cdots \rangle / \langle \int \cdots \rangle$, while the conservation of parallel momentum is verified since S_K is even in $v_\parallel$ as result of the symmetrization of the distribution with respect to this variable. The zeroth and first $v_\parallel$ moments of S_K indeed cancel. In Ref. [62], the heating operator in fact only depends on the radial position r and kinetic energy ϵ. The approximate version (3.113), which is a function of $(x,|v_\parallel|,\mu)$, was considered here for practical reasons, as a reconstruction of $f_{1j}(x,\epsilon)$ would have required costly numerical interpolations.

This artificial heat source is particularly appropriate for code comparisons, see section 5.5.2, as it enables to rapidly reach a steady state, or to investigate transport features for a prescribed gradient profile. However, an alternative and more physically relevant approach for a global code is to perform flux driven simulations. In this case, a local heat source is applied to model realistic plasma heating, and the temperature profiles are free to evolve. Such a realistic heat source has recently been implemented in global-GENE by T. Görler, together with alternative von Neumann boundary conditions at the inner radial boundary to allow for free temperature and potential field evolution at this point.

3.6 Summary

In this chapter, the different numerical algorithms used in the GENE code were presented. While the initial version of the code could only be run in the local approximation, it has now been extended to a global version which fully includes radial variation of equilibrium quantities. In this global version, the radial boundary conditions have been changed from periodic to Dirichlet and the original Fourier representation for the radial direction

has been replaced by a real space treatment, where the radial derivatives are now computed using 4th order centered finite differences. In addition, the Fourier space gyro-averaging operator has been replaced in the x-direction by a real space gyro-averaging integral, for which a Hermite interpolation is applied. With this formulation, the field equations can be expressed as linear systems of equations for the discretized fields which are then solved using with a direct method based on LU decomposition.A real space dealiasing operator, inspired from the equivalent Fourier space treatment and using Lagrange interpolation was, in addition, introduced when dealing with the nonlinear term. Finally a Krook-type heat source was implemented to allow for quasi-steady state nonlinear simulations.
Various tests and benchmarks have been carried out in order to validate the global version of the code and will be discussed in Chapter 5.

4 Equilibrium models

4.1 The toroidal MHD equilibrium

In Chap. 2 the field-aligned coordinate system (x, y, z) was defined through the relation $\vec{B}_0 = \mathcal{C}\vec{\nabla}x \times \vec{\nabla}y$, having assumed a prescribed axisymmetric magnetic field. In this Chapter, various equilibrium models are presented to describe the equilibrium magnetic field configuration and corresponding metric coefficients used in GENE.

Following [63], we shall first give an overview of the different properties of an axisymmetric stationary magnetically confined system. The equilibrium state in a magnetized plasma can be described by the time independent ideal magnetohydrodynamic (MHD) equations:

$$\vec{J}_0 \times \vec{B}_0 = \vec{\nabla} p_0 \tag{4.1}$$

$$\vec{\nabla} \times \vec{B}_0 = \mu_0 \vec{J}_0 \tag{4.2}$$

$$\vec{\nabla} \cdot \vec{B}_0 = 0 \,, \tag{4.3}$$

where $\vec{B}_0$ denotes the equilibrium magnetic field, $\vec{J}_0$ is the current density, p_0 the total plasma pressure, and having assumed no equilibrium flows.

A Tokamak plasma can, to a good approximation, be assumed axisymmetric. In this case, considering the cylindrical coordinate system (R, Z, ϕ) all equilibrium quantities are independent of the toroidal angle ϕ and the general solution of Eq. (4.3) for the magnetic field is of the form:

$$\vec{B}_0 = \vec{\nabla}\phi \times \vec{\nabla}\Psi + I\,\vec{\nabla}\phi \quad \text{with} \quad \Psi = -r\,A_\phi \,, \tag{4.4}$$

where A_0 is the potential vector, $\vec{B}_0 = \vec{\nabla} \times \vec{A}_0$. The magnetic field is thus decomposed in its toroidal $\vec{B}_{0\phi} = I\,\vec{\nabla}\phi$ and poloidal $\vec{B}_{0p} = \vec{\nabla}\phi \times \vec{\nabla}\Psi$ components, with Ψ the poloidal magnetic flux function, defined as the magnetic flux through a toroidal ribbon between

the magnetic axis and a toroidal line, see Fig. 4.1:

$$\Psi(R,Z) = \frac{1}{2\pi}\int_{\Sigma} \vec{B}_0 \cdot d\vec{\sigma} \tag{4.5}$$

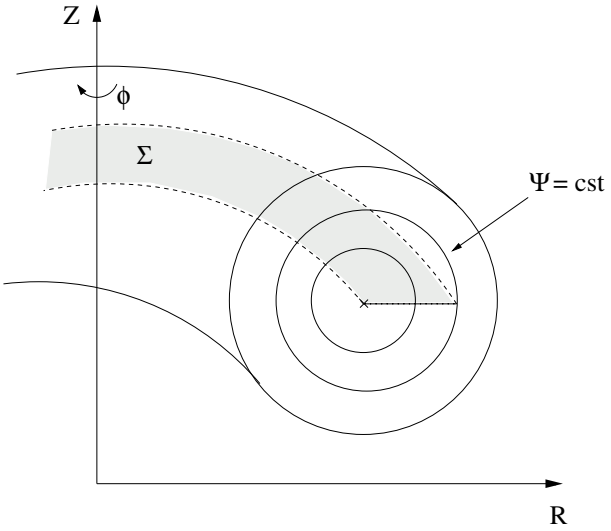

Figure 4.1: Cylindrical coordinates (R, Z, ϕ) in toroidal geometry.

Similarly the general solution of Eq. (4.2) for the current density in an axisymmetric system is:

$$\vec{J_0} = \vec{\nabla}\phi \times \nabla f + R\, J_\phi\, \vec{\nabla}\phi \quad \text{with} \quad f = -\frac{R\, B_\phi}{\mu_0}\ . \tag{4.6}$$

In such axisymmetric configuration, Eq. (4.4) implies that $\vec{B}_0 \cdot \vec{\nabla}\Psi = 0$, and $\Psi = \text{cst}$ is thus a magnetic surface. From Eq. (4.6) one also has $\vec{J_0} \cdot \vec{\nabla} f$, and $f = \text{cst}$ is therefore a current surface. The relation (4.1) shows, finally, that magnetic and current surfaces are both identical and given by $p = p(\Psi) = \text{cst}$. We also note that $f = f(\Psi)$ implies that $RB_\phi = I = I(\Psi)$. Substituting now Eq. (4.1) in (4.4) leads to:

$$-\mu_0\, R\, J_\phi = -\triangle^*\Psi = -R^2\, \vec{\nabla}\cdot\frac{1}{R^2}\vec{\nabla}\Psi = \mu_0\, R^2\, p'(\Psi) + I\, I'(\Psi)\ , \tag{4.7}$$

where the prime notation stands for the derivative with respect to Ψ. This elliptic non-linear equation for Ψ is referred to as the Grad-Shafranov equation [63] and relates the equilibrium Ψ to the pair of independent profiles $p = p(\Psi)$ and $I = I(\Psi)$.
The relative strength between the poloidal and the toroidal magnetic field is a key element of the Tokamak configuration and results in a twisting of the magnetic field lines around

the magnetic surfaces. The number of toroidal revolutions of such a line to complete one poloidal revolution is given by the safety factor :

$$q(\Psi) = \frac{1}{2\pi} \int_0^{2\pi} \left.\frac{d\phi}{d\theta}\right|_{along\ \vec{B}_0} d\theta = \frac{1}{2\pi} \int_0^{2\pi} \frac{\vec{B}_0 \cdot \nabla\phi}{\vec{B}_0 \cdot \nabla\theta}\, d\theta \tag{4.8}$$

where θ is the geometrical poloidal angle.

In this chapter three different equilibrium models are described: 1) an interface with the MHD equilibrium code CHEASE, which actually solves numerically Eq. (4.7), 2) a circular ad-hoc concentric flux surface model, and finally 3) the so-called $s-\alpha$ model. This last model, which provides a simple, comprehensive, analytic magnetic equilibrium, consists of circular shifted flux surfaces, with s the shear and α the Shafranov shift between centers of consecutive magnetic surfaces resulting from the pressure gradient. It has been widely used in past local gyrokinetic simulations.

In the standard application of the $s-\alpha$ model some terms of order $\epsilon = a/R$ are neglected, such that the resulting metric coefficients are essentially those of a cylindrical system. This can lead to significant differences with respect to the other equilibrium models. Differences between simulations with $s-\alpha$ and true MHD equilibrium were first pointed out in [64]. They were however assigned to the remaining Shafranov shift present in the low pressure MHD equilibrium plasma, which had been neglected in the $s-\alpha$ model. It was also noted in Ref. [65] that results with an $s-\alpha$ model significantly differ from those obtained with a Miller [66] geometry in the limit of circular parameters and no Shafranov shift, but no actual explanation was provided.

Following results published in [67], it will be shown in the following that the above mentioned differences in fact mainly result from the approximation made in the standard flux-tube implementation of the $s-\alpha$ model, in which the straight field line poloidal angle (essential for the definition of field-aligned coordinates) is identified to the geometrical poloidal angle, which leads to inconsistencies of order ϵ. Discrepancies in simulations between the $s-\alpha$ and the other equilibrium models will be illustrated in the following for the Cyclone base case [68] since it is considered as a reference Benchmark in the gyrokinetic community.

Finally, some local and global simulations are compared, and it is shown that the ge-

ometry issues can lead to a coincidental agreement between the flux tube results with $s - \alpha$ equilibrium and global results with a correct treatment of the equilibrium at finite $\rho^* = \rho_s/a = 1/180$. A true agreement is in fact achieved when the flux tube and global simulations both correctly treat the equilibrium, and when the global computation is carried out for conditions approaching the $\rho^* \to 0$ limit, intrinsic to the flux tube implementation.

4.2 The CHEASE interface

The equilibrium code CHEASE solves the nonlinear Grad-Shafranov equation (4.7) for Ψ using an iterative method with finite element representation [36]. The code maps the computed equilibrium on a flux coordinate system (Ψ, χ, ϕ), where Ψ is the poloidal flux function, χ the generalized poloidal angle and ϕ the toroidal angle. The CHEASE code has been modified to output all quantities required for gyrokinetic computation such as the q profile, the metric coefficients, the Jacobian, the magnetic field and its derivatives, as well as several other quantities, all given on a (Ψ, χ) grid (all equilibrium quantities are independent of ϕ), where in this case χ is chosen as the straight field line poloidal angle. Note that in order to remain more general, CHEASE provides the equilibrium on a (Ψ, χ) grid and not directly on the (x, y, z) grid used in GENE, so that this output can easily be used by other gyrokinetic codes as well, such as the ORB5 code [54] also developed at the CRPP, Lausanne. Some further details on the CHEASE output are provided in Appendix A.

To compute an equilibrium, one needs to provide a pressure and a current profile (i.e. p' and $I\,I'$) as well as the shape of the last closed flux surface. These quantities can be either specified by reading experimental data from an EXPEQ file or from the more standard EQDSK equilibrium file [69], or can be set using analytical profiles. The latter option is in particular useful when investigating the influence of flux surfaces shaping on microturbulence, as presented in Chapter 6, since it allows us to compute equilibria with arbitrary triangularity and elongation.

4.2.1 Equilibrium quantities in (x, y, z)

The equilibrium quantities provided by CHEASE on the (Ψ, χ) grid are transformed to the field-aligned coordinate system (x, y, z), see Fig. 2.2, according to the relations

$$x = C_x(\Psi) - x_0 \,, \quad y = C_y\,(q\chi - \phi) - y_0 \quad \text{and} \quad z = \chi \,, \tag{4.9}$$

which were already defined in (2.59). Note that in (x, y, z) coordinates, the axisymmetry of the system results in all equilibrium quantities being independent of y. Following this coordinate transform one obtains:

$$\begin{aligned} \vec{\nabla} x &= \frac{dC_x}{d\Psi}\,\vec{\nabla}\Psi \,, \\ \vec{\nabla} y &= C_y\,\left[q'\chi\vec{\nabla}\Psi + q\vec{\nabla}\chi - \vec{\nabla}\phi\right] \,, \\ \vec{\nabla} z &= \vec{\nabla}\chi \,, \end{aligned} \tag{4.10}$$

so that the metric tensor in (x, y, z) coordinates is expressed in terms of the metric tensor in (Ψ, χ, ϕ) coordinates:

$$\begin{aligned} g^{xx} &= \left(\frac{dC_x}{d\Psi}\right)^2 g^{\Psi\Psi} \,, \quad g^{xy} = \frac{dC_x}{d\Psi}\,C_y\,\left(q'\chi\, g^{\Psi\Psi} + q\, g^{\Psi\chi}\right) , \\ g^{yy} &= C_y^2\,\left[(q')^2\chi^2 g^{\Psi\Psi} + 2\,qq'\chi\, g^{\Psi\chi} + q^2 g^{\chi\chi} + g^{\phi\phi}\right] , \\ g^{xz} &= \frac{dC_x}{d\Psi} g^{\Psi\chi} \,, \quad g^{yz} = C_y\,\left(q'\chi\, g^{\Psi\chi} + q\, g^{\chi\chi}\right) , \\ g^{zz} &= g^{\chi\chi}, \end{aligned} \tag{4.11}$$

with $g^{\alpha\beta} = \vec{\nabla}\alpha \cdot \vec{\nabla}\beta$ and $q' = dq/d\Psi$. The other required quantities are

$$\frac{\partial B}{\partial x} = \left(\frac{dC_x}{d\Psi}\right)^{-1} \frac{\partial B}{\partial \Psi} \,, \quad \frac{\partial B}{\partial z} = \frac{\partial B}{\partial \chi} \,, \quad \text{and} \quad J^{xyz} = \left(\frac{dC_x}{d\Psi}\,C_y\right)^{-1} J^{\Psi\chi\Phi} \,, \tag{4.12}$$

where $J^{abc} = [(\nabla a \times \nabla b)\cdot\nabla c]^{-1}$ is the Jacobian related to the coordinates (a, b, c). In principle $C_x(\Psi)$ and C_y can be chosen arbitrarily and in the current version of the code three possible definitions of C_x have been implemented:

$$C_x = a\sqrt{\frac{\Psi}{\Psi_{\text{edge}}}} \,, \quad C_x = a\sqrt{\frac{\Phi_t}{\Phi_{\text{t,edge}}}} \,, \quad C_x = a\sqrt{\frac{V}{V_{\text{edge}}}} \quad \text{or} \quad C_x = \frac{q_0}{r_0 B_{\text{ref}}}\Psi \,, \tag{4.13}$$

where Φ_t is the toroidal flux, V is a volume inside a Ψ = cst surface, a is the minor radius of the edge flux surface, measured at the equatorial midplane, , r_0 and q_0 are

respectively the minor radius and the safety factor of the flux surface located at $x = 0$, and B_{ref} is a reference magnetic field, usually chosen as the magnetic field on the axis. Finally, the constant C_y is set to $C_y = r_0/q_0$, so that y takes a units of length. Any C_x definition could be used with the local code. When considering the global code however, it is necessary to have an equidistant grid $\{x_i = C_x(\Psi_i) - x_0\}$, and although the CHEASE code could potentially adapt the mesh for any definitions, only the $C_x = a\sqrt{\Psi/\Psi_{\text{edge}}}$ or $C_x = a\sqrt{V/V_{\text{edge}}}$ are at the present implemented, see Appendix A.

When using the local version of the code, one neglects the x-dependence of all equilibrium quantities across the simulation domain. All geometrical coefficients therefore only need to be known on the magnetic surface of interest ($x = 0$), and are thus only functions of z in the axisymmetric system considered here. The axisymmetry of the equilibria indeed translates into the independence with respect to y of the coefficients. In the global version of the code, equilibrium quantities are however (x, z) dependent.

Note that the metric coefficients can also be obtained from MHD equilibria using the interface with the Tracer code [52], which can also compute local geometrical parameters along a given field line in 3-dimensional system, i.e. for Stellarator geometry.

4.3 Circular ad-hoc model

For many applications, it can be useful to consider a simpler analytical model for the magnetic equilibrium configuration. By considering $I = \text{cst}$ and $p \propto \Psi$ in Eq. (4.7), one obtains a so-called Solovev type solution:

$$\Psi = \frac{\Psi_{\text{edge}}}{(R_0\, a)^2}\left[(R\, Z)^2 + \frac{1}{4}\,(R^2 - R_0^2)^2\right] . \tag{4.14}$$

In the large aspect ratio limit $R_0/a >> 1$, where again a is the minor radius, this equation reduces to $\Psi = \Psi_{\text{edge}}(r/a)^2$, where r is the radius local to a given flux surface as illustrated in Fig. 4.3. In this limit, the magnetic surfaces thus have a circular cross section, and according to Eq. 4.4, the magnetic field reads in the toroidal coordinates, (r, θ, ϕ), (see Fig. 4.2):

$$\vec{B_0} = \frac{R_0\, B_{\text{ref}}}{R}\left[\vec{e}_\phi + \frac{r}{R_0\,\bar{q}}\,\vec{e}_\theta\right] , \tag{4.15}$$

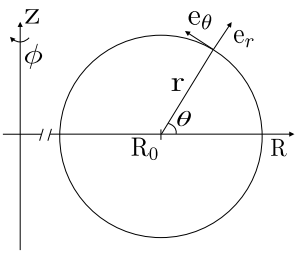

Figure 4.2: Circular flux surface in toroidal coordinates (r, θ, Φ).

where $B_{\rm ref}$ is again the magnetic field at the magnetic axis, and $\bar{q}$ is a pseudo safety factor which can be related to the real safety factor using Eq. (4.8):

$$q(r) = \frac{1}{2\pi}\int_0^{2\pi} \frac{\vec{B}_0\cdot\vec{\nabla}\phi}{\vec{B}_0\cdot\vec{\nabla}\theta}\,d\theta = \frac{\bar{q}(r)}{2\pi}\int_0^{2\pi}\frac{d\theta}{1+\varepsilon\,\cos\theta} = \frac{\bar{q}(r)}{\sqrt{1-\varepsilon^2}}\,, \tag{4.16}$$

having defined the inverse aspect ratio $\varepsilon = r/R_0$. Note that for $\Psi = \Psi_{\rm edge}(r/a)^2$, $\bar{q}$ would be constant, $\bar{q} = (B_{\rm ref}\,a^2)/(2\,\Psi_{\rm edge})$. In Eq. (4.16) one considered the possibility of a profile $\bar{q} = \bar{q}(r)$, corresponding to the ad-hoc relation $d\Psi/dr = B_{\rm ref}\,r/\bar{q}(r)$. In turn the straight field line angle χ is defined such that $(\vec{B}_0\cdot\vec{\nabla}\phi)/(\vec{B}_0\cdot\vec{\nabla}\chi) = q$, which leads to the relation $d\chi/d\theta = \vec{B}_0\cdot\vec{\nabla}\phi/(q\,\vec{B}_0\cdot\nabla\theta)$. Integrating over θ yields:

$$\chi(r,\theta) = \frac{1}{q}\int_0^{\theta}\frac{\vec{B}_0\cdot\vec{\nabla}\phi}{\vec{B}_0\cdot\nabla\theta'}\,d\theta' = \frac{\bar{q}}{q}\int_0^{\theta}\frac{d\theta'}{1+\varepsilon\,\cos\theta'} = 2\arctan\left[\sqrt{\frac{1-\varepsilon}{1+\varepsilon}}\tan\left(\frac{\theta}{2}\right)\right]. \tag{4.17}$$

From these definitions of Ψ and χ, the metric in (Ψ, χ, ϕ) coordinates can be obtained from the known metric in the (r, θ, ϕ) coordinates through the relations:

$$\vec{\nabla}\Psi = \frac{B_{\rm ref}\,r}{\bar{q}}\,\vec{\nabla}r = \frac{B_{\rm ref}\,r}{\bar{q}}\,\vec{e}_r\,, \tag{4.18}$$

$$\vec{\nabla}\chi = \frac{\partial\chi}{\partial r}\,\vec{\nabla}r + \frac{\partial\chi}{\partial\theta}\,\vec{\nabla}\theta = \frac{\partial\chi}{\partial r}\,\vec{e}_r + \frac{1}{r}\,\frac{\partial\chi}{\partial\theta}\,\vec{e}_\theta\,, \tag{4.19}$$

$$\vec{\nabla}\phi = \frac{1}{R}\,\vec{e}_\phi = \frac{1}{R_0 + r\,\cos(\theta)}\,\vec{e}_\phi\,, \tag{4.20}$$

with

$$\frac{\partial\chi}{\partial r} = \frac{-\sin\chi}{R_0(1-\varepsilon^2)}\,, \quad \frac{\partial\chi}{\partial\theta} = \frac{\bar{q}}{q}\frac{R_0}{R}\,. \tag{4.21}$$

This leads to the metric tensor:

$$g^{\Psi\Psi} = \frac{B_{\rm ref}^2\,r^2}{\bar{q}^2}\,, \quad g^{\chi\chi} = \frac{1}{r^2}\left[\frac{R_0^2\,\bar{q}^2}{R^2\,q^2} + \frac{\varepsilon^2\sin^2\chi}{(1-\varepsilon^2)^2}\right]\,,$$

$$g^{\Psi\chi} = -\frac{B_{\rm ref}\,\varepsilon}{\bar{q}}\frac{\sin\chi}{(1-\varepsilon^2)}\,, \quad g^{\phi\phi} = \frac{1}{R^2}\,,$$

$$g^{\Psi\phi} = g^{\chi\phi} = 0\,. \tag{4.22}$$

In addition, the Jacobian reads:

$$J^{\Psi\chi\phi} = \frac{qR}{B_\phi} = \frac{qR^2}{B_{\rm ref}R_0}\,. \tag{4.23}$$

When using the circular model, the x variable is chosen as $x = r - x_0$, i.e $dC_x/d\Psi = \bar{q}/(r\,B_{\rm ref})$, and $C_y = r_0/q_0$. The metric tensor in the (x, y, z) coordinate system is then obtained using relations (4.11) and (4.22), and is valid for both the local and the global versions of the code.

In order to compare with the $s-\alpha$ model described later on, we explicit here the corresponding metric coefficients to first order in ε and consider only the local case, i.e. at $x = 0$:

$$\begin{aligned}
g^{xx} &= 1\,, \quad g^{xy} = \hat{s}\chi - \varepsilon\sin\chi\,,\\
g^{yy} &= 1 + (\hat{s}\chi)^2 - 2\,\varepsilon\cos\chi - 2\,\hat{s}\chi\,\varepsilon\sin\chi\,,\\
g^{xz} &= -\frac{\varepsilon\sin\chi}{r_0}\,, \quad g^{yz} = \frac{1 - 2\,\varepsilon\cos\chi - \hat{s}\chi\varepsilon\sin\,\chi}{r_0}\,,\\
g^{zz} &= \frac{1 - 2\,\varepsilon\cos\chi}{r_0^2}\,.
\end{aligned} \tag{4.24}$$

where the magnetic shear is $\hat{s} = (r/q)dq/dr$. Finally, note that to the same order in ε one has from Eq. (4.17): $\chi = \theta - \varepsilon\sin\theta + \mathcal{O}(\varepsilon^2)$.

4.4 The $s-\alpha$ model

The last model that has been considered is the so-called $s-\alpha$ model for $\alpha = 0$, which is described here considering only the local approximation, i.e. the x dependencies are not retained. One again assumes circular, concentric, magnetic surfaces as in the previous model. The (x, y, z) coordinates are defined as in Eq. (4.9), with $x = r$, except for the straight field line angle χ which is approximated to the geometrical angle θ so that $y = (r_0/q_0)(q\theta - \phi) - y_0$ and $z = \theta$. Despite this approximation, (x, y, z) is still considered here as a field-aligned coordinate system. The metric coefficients to first order in ε are:

$$g^{xx} = 1\,,\;\; g^{xy} = \hat{s}\theta\,,\;\; g^{yy} = 1 + (\hat{s}\theta)^2\,,\;\; g^{xz} = 0\,,$$

$$g^{yz} = 1/r_0 \,, \quad g^{zz} = 1/r_0^2 \,. \tag{4.25}$$

A comparison with Eq. (4.24) exhibits differences of order ε between the two models, which points out that the approximation concerning the straight field line angle is only valid in the limit of an infinite aspect ratio Tokamak ($\varepsilon \to 0$). According to Eq. (4.17), one indeed has $\chi = \theta$ for $\varepsilon = 0$. In order to retain trapping effects, the magnetic field amplitude is, nevertheless, defined for this model as

$$\frac{B_0}{B_{\rm ref}} \simeq \frac{B_\phi}{B_{\rm ref}} = \frac{R_0}{R} = \frac{1}{1+\varepsilon\cos\theta} \,, \tag{4.26}$$

thus keeping finite aspect ratio terms. On the other hand, from the definition of the field-aligned coordinate system, one has $B_0 = B_{\rm ref}\nabla x \times \nabla y$, which, from the metric coefficients (4.25) implies

$$(B_0/B_{\rm ref})^2 = (\nabla x \times \nabla y)^2 = (\nabla x)^2(\nabla y)^2 - (\nabla x \cdot \nabla y)^2 = g^{xx}g^{yy} - (g^{xy})^2 = 1 \,. \tag{4.27}$$

Comparing Eq. (4.26) with Eq. (4.27) underlines an inconsistency of order ε in the $s-\alpha$ model, namely the metric is computed as if $\varepsilon = 0$ but the magnetic field amplitude still retains an ε dependence. As will be shown in the next section, this inconsistency leads, for finite ε cases, to significant differences between microturbulence simulations considering the $s-\alpha$ model and simulations using either an MHD equilibrium or the previous concentric, circular model.

4.5 Influence of the equilibrium model and code comparisons

In this section the different equilibrium models are compared using Cyclone-like parameters [68], namely $n_i \equiv n_e$, $T_e/T_i \equiv 1$, $q = 1.4$, $\hat{s} = (\rho/q)dq/d\rho = 0.8$, and $\varepsilon_0 = r_0/R_0 = 0.18$. Here, the normalized radial variable is defined for the MHD equilibrium as $\rho = \sqrt{\Phi_{\rm t}/\Phi_{\rm t,edge}}$, Φ_t is the toroidal flux, and $\Phi_{\rm t,edge}$ is the value of the toroidal flux at the edge. For the ad-hoc circular and $s-\alpha$ models, one identifies $\rho = r/a$. The gradient values are defined at $\rho = \rho_0 = 0.5$ as $R_0/L_{Ti} = R_0\langle|\nabla \ln T_i|\rangle = 6.96$, $R_0/L_n = R_0\langle|\nabla \ln n|\rangle = 2.23$, where $\langle\,.\,\rangle$ stands for the flux-surface average, defined in

Eq. (2.83).

Discrepancies observed with the different equilibrium model are first discussed considering local simulations. In a second step we analyse how previous comparisons between local and global gyrokinetic codes may have been mis-interpreted due to such equilibrium model issues.

4.5.1 Linear flux-tube results

Let us start by considering linear flux tube simulations, and in order to gain confidence in the results, outputs from different codes are compared. In Fig. 4.3 the linear growth rates and real frequencies of toroidal-Ion Temperature Gradient (toroidal-ITG) modes are shown as a function of the poloidal wave number k_y in units of ρ_s, where ρ_s has been evaluated with $T_e(\rho_0)$ and the magnetic field $B_{\rm ref}$ on axis. The results have been obtained

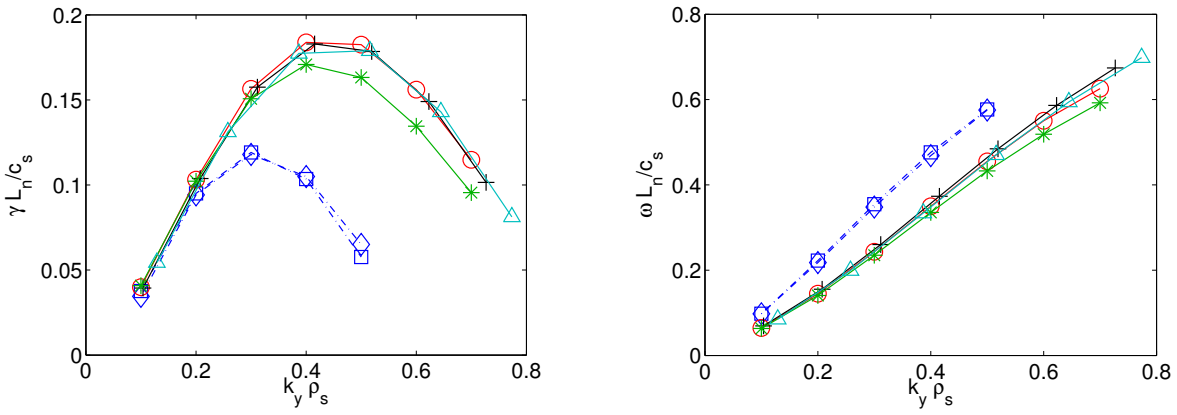

Figure 4.3: Growth rate (left) and real frequency (right) as a function of the poloidal wave number k_y of linear ITG modes for the Cyclone test case. Three equilibrium models are considered: MHD (circles: GENE; crosses: GS2; triangles: GKW), $s-\alpha$ (diamonds: GENE; squares: GS2), and ad-hoc circular concentric (stars: GENE).

from the flux-tube codes GENE, GS2 [11] and GKW (formerly known as LINART [70]) using an MHD equilibrium or the usual $s-\alpha$ model, as well as from a GENE simulation using the ad-hoc circular model. The MHD equilibrium used here is computed with the CHEASE code such that the last closed flux surface is circular and the Cyclone local parameters are matched at $\rho_0 = 0.5$. The pressure profile is chosen such that the value of $\beta = \langle p \rangle 2\mu_0/B^2$ is small ($\sim 10^{-5}$), where $\langle p \rangle$ is the volume-averaged pressure, and the

current density profile is set in order to obtain the required values of the safety factor q and of the shear $\hat{s}$ at ρ_0. The growth rates and frequencies are of the order of the ion diamagnetic frequency which itself is of order c_s/L_{ref}, where L_{ref} is a characteristic gradient length of the system. Choosing $L_{ref} = L_n$, frequencies and growth rates are thus normalized to c_s/L_n. This is the same normalization as considered in Ref. [68], which facilitates comparisons.

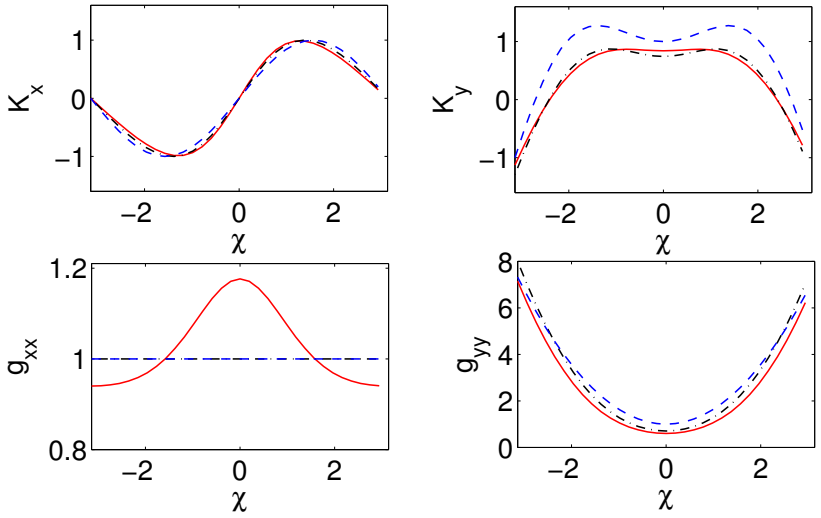

Figure 4.4: Geometrical coefficients for different equilibrium models : MHD (solid line), $s-\alpha$ (dashed line), and ad-hoc circular concentric (dash-dotted line).

As clearly appears in Fig. 4.3, significant differences are observed, in agreement with [64], when comparing results using the reduced $s-\alpha$ model or the MHD equilibrium. In particular the maximum linear growth rates differ by almost a factor of two for the here considered Cyclone parameters. However, when using the analytical circular model, agreement with the MHD equilibrium case is reached within 10%. This latter point clearly shows that the differences observed in this finite aspect ratio circular cross section geometry between simulations considering either the $s-\alpha$ or a realistic MHD equilibrium mainly result from the inconsistencies of order ε in the $s-\alpha$ model pointed out in section 4.4. By exchanging one geometrical term at a time in GENE's equations between the $s-\alpha$ model and the circular analytic model, it can be shown that the differences result primarily from the discrepancies in the g^{yy} and K_y terms. In Fig. 4.4, the most relevant geometrical coefficients are plotted as a function of χ for the different equilibrium models.

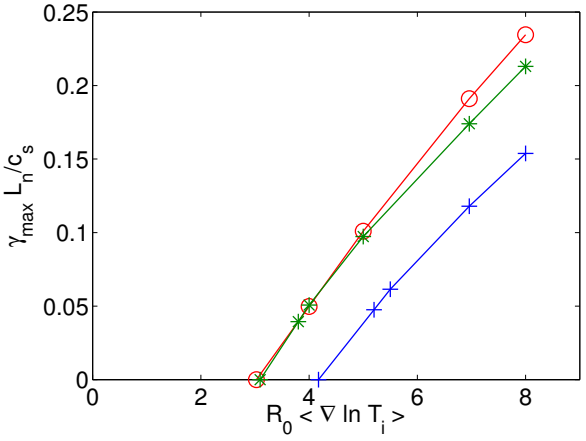

Figure 4.5: Growth rate of the most unstable ITG mode as a function of the ion temperature gradient for MHD (circles), ad-hoc circular concentric (stars), and $s-\alpha$ (crosses) equilibrium models. All other parameters as in the Cyclone test case.

The g^{yy} and K_y terms present the largest relative differences in the vicinity of $\chi = 0$ where ITG modes balloon. We note also that differences in the g^{xx} coefficient do not in fact influence these linear results since the growth rate is essentially determined by the dominant $k_x = 0$ mode, corresponding to the perpendicular wave number $k_\perp^2 = g^{yy}k_y^2$. After this first linear comparison with the nominal Cyclone parameters, GENE simulations using the three different equilibria have also been carried out for various values of the temperature gradient while keeping all other parameters. In Fig. 4.5, the maximum linear growth rate over all k_y for ITG modes is given with respect to the normalized, flux-surface averaged temperature gradient R_0/L_{Ti}. The linear critical temperature gradient obtained when using the $s-\alpha$ model is found around $R_0/L_{Ti} = 4$, which is in agreement with Ref. [68], and is decreased to $R_0/L_{Ti} = 3$ for realistic MHD equilibrium models as observed in [64]. The MHD results are well recovered using the circular ad-hoc equilibrium. This observation is of particular importance when using critical gradient values in semi-empirical transport models [71].

4.5.2 Nonlinear flux-tube results

As in the linear case, nonlinear simulations considering Cyclone test case parameters show strong discrepancies between results using $s-\alpha$ and MHD equilibria, while com-

putations using the corrected circular model recover well those obtained with the MHD equilibrium.

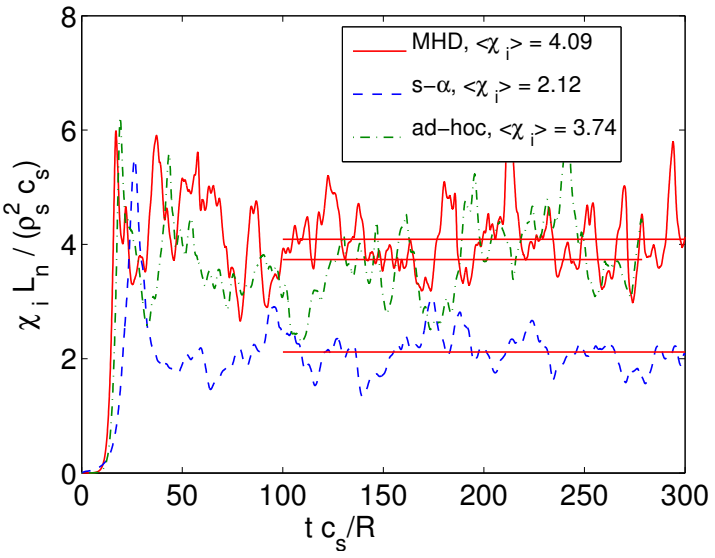

Figure 4.6: Ion heat diffusivity χ_i obtained by nonlinear GENE simulations for the Cyclone test case using MHD (solid line), $s-\alpha$ (dashed line) and ad-hoc circular (dash-dotted) equilibrium models.

Nonlinear simulations with the three different equilibria have been compared for Cyclone base parameters, with a numerical resolution $n_x \times n_y \times n_z \times n_{v_\parallel} \times n_\mu = 128 \times 48 \times 16 \times 32 \times 8$ and a perpendicular flux-tube box of dimensions $L_x \times L_y = 118\,\rho_s \times 96\,\rho_s$. Figure 4.6 shows the ion heat diffusivity time trace. When using the MHD equilibrium, the time-integrated ion heat diffusivity χ_i is estimated at $\chi_i\, L_n/(\rho_s^2 c_s) = 4.1$ (corresponding to $\chi_i/\chi_{GB} = 3.3$, using the standard Gyro-Bohm normalization $\chi_{GB} = \rho_s^2 c_s/a$), which differs by almost a factor of two from the value obtained using the $s-\alpha$ model, for which $\chi_i L_n/(\rho_s^2 c_s) = 2.1$ ($\chi_i/\chi_{GB} = 1.7$). We note that the value χ_i for the $s-\alpha$ case agrees with the LLNL GK fit

$$\chi_i L_n/(\rho_s^2 c_s) = 15.4\,[\,1.0 - 6.0\,(L_T/R)]\,, \tag{4.28}$$

presented in Ref. [68], which also provides $\chi_i L_n/(\rho_s^2 c_s) = 2.1$ for $R/L_T = 6.96$. The simulation using the ad-hoc circular model gives $\chi_i\, L_n/(\rho_s^2 c_s) = 3.7$ ($\chi_i/\chi_{GB} = 3.0$) and thus agrees within 10% with the result using the MHD equilibrium. Strong discrepancies,

for slightly different physical parameters, between nonlinear simulations using either the $s-\alpha$ model or a corrected circular equilibrium obtained from the Miller model [66] were also stated in Ref. [65], but no detailed explanation of the actual cause was provided.

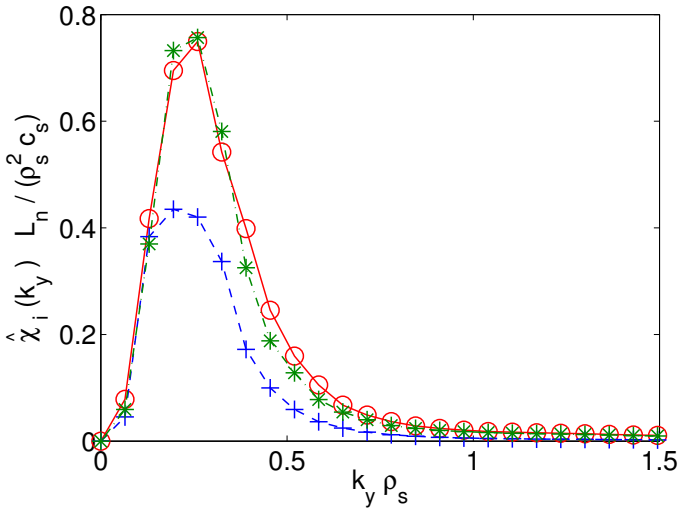

Figure 4.7: k_y spectra of time-averaged ion heat diffusivity $\hat{\chi}_i(k_y)$ obtained via nonlinear GENE simulations for the Cyclone test case using MHD (circles), $s-\alpha$ (crosses), and ad-hoc circular (stars) equilibrium models.

In Fig. 4.7, the time-averaged ion heat diffusivity spectrum $\hat{\chi}_i(k_y)$, defined such that $\chi_i = \sum_{k_y} \hat{\chi}_i(k_y)$ (where the sum is over all $k_y = n\,2\pi/l_y$, $n = 0 \cdots, n_y/2$ modes considered in the simulation), is presented as a function of the normalized poloidal wave number $k_y\rho_s$. The spectrum obtained using the $s-\alpha$ model strongly differs from the one using either the ad-hoc circular model or the MHD model, especially for $k_y\rho_s$ above 0.2 which corresponds to its maximum amplitude.

Figure 4.8 shows the time-averaged ion heat diffusivity using both the $s-\alpha$ and MHD models for different values of the temperature gradient. The nonlinear critical gradients $R/L_{T,\mathrm{crit}}$ are shifted upward with respect to the corresponding linear critical gradients according to the well known Dimits-shift [68] effect. For the $s-\alpha$ model, the resulting $R/L_{T,\mathrm{crit}}$ is around 6, identical to results in Ref. [68], and contained in the fit given by Eq. (4.28), while its value is around 5 using the MHD equilibrium.

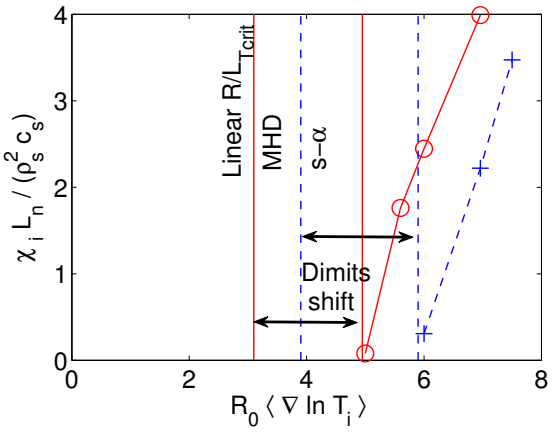

Figure 4.8: Ion heat diffusivity χ_i for the Cyclone test case as a function of the ion temperature gradient. Results are given for simulations using either the MHD (circles) or the $s-\alpha$ (crosses) equilibrium model.

4.5.3 Linear comparison between local and global simulations

In view of the significant effects on the linear growth rates and nonlinear diffusivities resulting from the approximations in the $s-\alpha$ model local simulations, the agreements between these same flux-tube results and global simulations reported in Ref.[68] appear surprising. Indeed, no similar approximations in implementing the equilibrium in the global simulations had been made. In order to address this apparent paradox, such local-

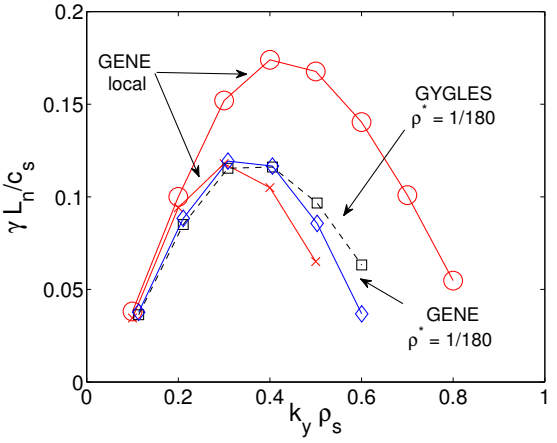

Figure 4.9: Growth rate spectra of linear ITG modes for the Cyclone test case. Local GENE simulations with either the $s-\alpha$ (crosses) or the ad-hoc circular analytical model (circles) are compared with results from the global version of GENE (diamonds) and from the global code GYGLES (squares) both for $\rho^* = 1/180$ and using the circular ad-hoc model.

global comparisons are repeated for linear simulations, using both the local flux-tube and global versions of the GENE code, as well as the global, linear PIC code GYGLES [72]. The global GENE and GYGLES codes are run using the analytical equilibrium with concentric, circular flux surfaces, described in Section 4.3, with no further approximations on the geometry. For the corresponding simulations, the safety factor profile is chosen to be $q = 0.85 + 2.2\,(r/a)^2$, corresponding to $q(r_0) = 1.4$ and $\hat{s}(r_0) = (r_0/q)dq(r_0)/dr = 0.8$ at $r_0/a = 0.5$. The temperature and density gradient profiles are defined as

$$\frac{R_0}{T}\frac{dT}{dr} = -\kappa_T \cosh^{-2}\left(\frac{r-r_0}{\Delta r}\right), \qquad \frac{R_0}{n}\frac{dn}{dr} = -\kappa_n \cosh^{-2}\left(\frac{r-r_0}{\Delta r}\right), \tag{4.29}$$

with peak gradients $\kappa_T = 6.96$, $\kappa_n = 2.23$ matching those considered in the local GENE simulations and the radial width of the global profiles is chosen as $\Delta r = 0.3\,a$.

In Fig. 4.9, growth rates of ITG modes from local GENE simulations using the ad-hoc

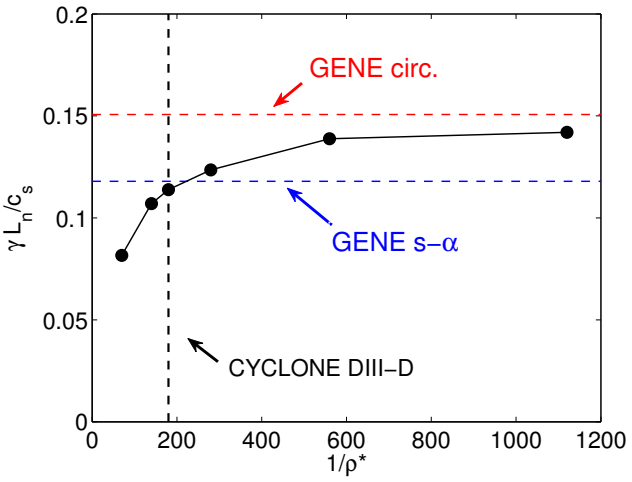

Figure 4.10: ρ^* scaling of ITG growth rate at $k_y\rho_s = 0.3$ for the global code GYGLES. GENE results are obtained with the $s-\alpha$ or the circular analytical equilibrium model.

circular and the $s-\alpha$ models are compared with global GENE and GYGLES simulations using the ad-hoc circular model. The global simulations were carried out for $\rho^* = \rho_s/a = 1/180$ which corresponds to the experimental value from which the Cyclone base case was derived. The growth rate spectrum of the global simulations for $\rho^* = \rho_s/a = 1/180$ basically matches with the local $s-\alpha$ results. This agreement is however purely coincidental. This is indeed illustrated by the ρ^* scan in Fig. 4.10, where

global GYGLES results truly converge toward the local GENE results with ad-hoc circular equilibrium (correct treatment of the geometry), in the limit $\rho^* \to 0$.
In Fig. 4.10 a small offset seems nonetheless to remain in the limit $\rho^* \to 0$. This difference may arise from the fact that the mode $k_x = 0$ is considered in the flux tube simulation whereas the radial mode number remains finite in the global simulations. Such deviations are investigated in [28] where it is shown that an even better agreement between local and global results can be reached when choosing a finite k_x value in the local simulations.

4.6 Summary

In this Chapter we have presented three different magnetic equilibrium models which can be used in the GENE code. First, an interface with the equilibrium code CHEASE was described, for which the CHEASE code was adapted to provide the required quantities on the straight field line (Ψ, χ) grid. This approach through a representation on this (Ψ, χ) grid is kept general, i.e. it does not depend on the coordinate choice in GENE, and the equilibrium output can also be used for the gyrokinetic code ORB5. In GENE, a further transformation to the field aligned coordinates (x, y, z) is carried out via the interface which is valid for both the global and local version of the code. For comparison purpose, and when an exact magnetic equilibrium is not necessary, an ad-hoc circular concentric flux surface model was also implemented, and is applicable to both local and global simulations. Finally, the so-called $s - \alpha$ model, which has been widely used in past flux tube simulations, was discussed.
Comparisons between these equilibrium models have been carried out for Cyclone base case parameters, and significant differences were observed in linear and nonlinear simulations obtained with the $s - \alpha$ model or a circular MHD equilibrium. It was shown that these discrepancies result from approximating the poloidal angle to the straight field line angle in the standard implementation of the $s - \alpha$ model, which leads to inconsistencies of the order of the inverse aspect ratio ε. These differences reach a factor of almost two in the predicted turbulence induced heat-flux for the standard Cyclone parameters. It is also found that using the $s - \alpha$ model the linear and nonlinear critical gradients $R/L_{T,\mathrm{crit}}$ are overestimated by at least 20%. As a consequence, one should not only be aware of

this issue when comparing flux tube codes among each other, but also when applying flux-tube results, and in particular the so-obtained critical gradients, to semi-empirical transport models. When considering the ad-hoc circular concentric flux surfaces model which correctly treats the straight field line angle, one obtains, on the other hand, a very good agreement with the circular MHD equilibrium simulations.

The importance of using a correct geometrical model is of further interest when comparing results from flux-tube and global codes. In particular, we have shown that the previously reported apparent agreement between flux tube and global simulations [68] had resulted from the unfortunate combination of two different effects, namely the inconsistencies of order ε in the equilibrium model of the flux tube codes and the physical finite size ρ^* effects in the global simulations. True convergence between linear flux tube results with a correct treatment of the geometry and global simulations in the appropriate limit of $\rho^* \to 0$ was demonstrated.

5 Code validation and global effects

As discussed in the previous chapter, the implementation of the global version of GENE has required to modify large parts of the code and enables to investigate physical effects associated with finite $\rho^* = \rho_s/a$. In order to validate this new version, detailed tests and comparisons with other codes were carried out in various physical limits. This chapter is dedicated to the current state of this validation procedure. At first linear tests are presented. In particular the cylindrical limit is addressed, followed by linear benchmarks with the global PIC codes ORB5 [54] and GYGLES [72] for Cyclone base case parameters [68]. Simulations with kinetic electrons are also shown, as well as the so-called Rosenbluth-Hinton test [73]. Finally, some nonlinear benchmarks with the global PIC code ORB5 are presented, including a ρ^* scan. We would like to stress the fact that the extensive code comparisons which are shown in this chapter were made possible thanks to users and developers of GYGLES and ORB5 at the CRPP Lausanne, in particular B. McMillan who has dedicated great effort in providing simulation results from the ORB5 code, enabling us to get better confidence in the global version of GENE.

5.1 The cylindrical limit

In this section, we aim at investigating the cylindrical limit of the global-GENE code, and in particular whether the slab Ion Temperature Gradient (ITG) instability can be accurately described.

For this study, our reference case is a toroidal plasma with concentric circular flux surfaces, having an inverse aspect ratio and safety factor profile respectively:

$$a/R = 0.18 \qquad q(x) = 1.25 + 3\,(x/a)^2\,, \tag{5.1}$$

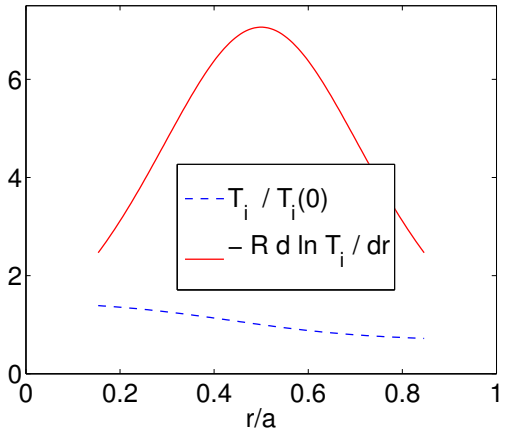

Figure 5.1: Ion temperature and logarithmic temperature gradient profiles, for $\kappa_{T_i} = 7.4$.

where a is the minor radius, R the major radius and $x = r$. The $\rho^* = \rho_s/a$ parameter is set to $1/\rho^* = 65$ and the ion temperature and density profiles are given by:

$$\hat{A}(x) = \frac{A(x)}{A(x_0)} = \exp\left[-\kappa_A \frac{a}{L_{\text{ref}}} \Delta A \tanh\left(\frac{(x - x_0)/a}{\Delta A}\right)\right] , \tag{5.2}$$

where A stands for T_i or n. Such a function form leads to a peaked gradient profiles centered at x_0 and with width ΔA (in units of A), see Fig. 5.1:

$$L_{\text{ref}} \frac{d \ln A}{dx} = -\kappa_A \cosh^{-2}\left(\frac{(x - x_0)/a}{\Delta A}\right) . \tag{5.3}$$

The temperature and density profile parameters are set here to $\kappa_{T_i} = 7.4$, $\kappa_{n_i} = 0$, $\Delta T_i = \Delta n = 0.3$, $x_0 = 0.5\,a$ and $L_{\text{ref}} = R$. Furthermore the electron response is assumed adiabatic and the temperature ratio $\tau = T_e/T_i$ is equal to $\tau = 1$. Finally, one considers the toroidal mode number $n = 4$, which corresponds to

$$k_y \rho_s = \frac{n\, q_0}{r_0} \rho_s = 0.25 , \tag{5.4}$$

with $q_0 = q(r/a = 0.5) = 2$ and $r_0 = x_0 = 0.5\,a$. For these physical parameters and wave number, ITG modes are unstable.

In the following, the toroidal limit is taken by increasing the radius R while holding $R\,q$, n/R, and a constant, so that the considered mode number $k_y \rho_s = 0.25$ remains constant. We note that the length L_{ref} entering the gradient definition, as well as in the

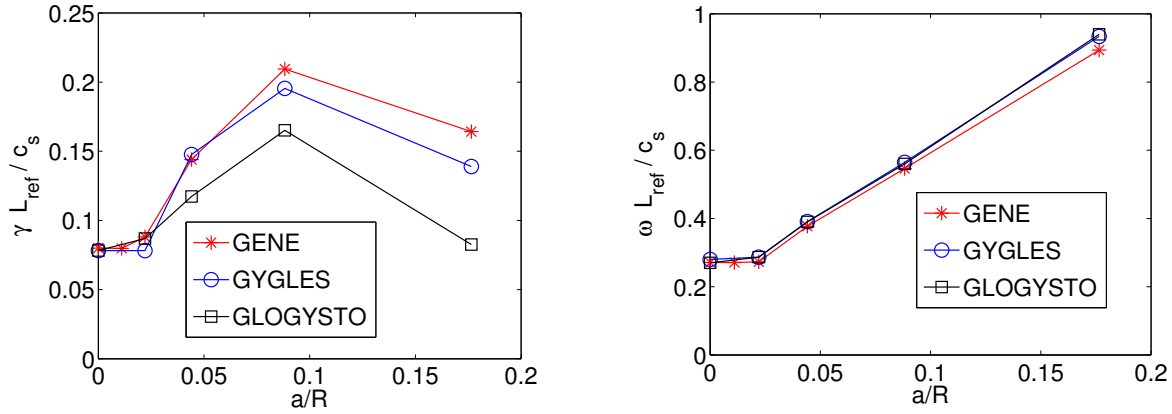

Figure 5.2: Growth rate (left) and real frequency (right) of the ITG mode as a function of the inverse aspect ratio a/R obtained with the GENE, GYGLES and GLOGYSTO codes.

normalizations of the growth rates and real frequencies in Fig. 5.2, is also kept at a constant value equal to the reference major radius. The numerical box used for these simulations is $l_x \times l_z \times l_{v_\parallel} \times l_\mu = 45\,\rho_i \times 2\,\pi \times 3.2\,v_{th,i} \times 10.2\,T_i/B_{\rm ref}$ with grid size $n_x \times n_z \times n_{v_\parallel} \times n_\mu = 120 \times 16 \times 48 \times 16$. The resulting growth rates and real frequencies are shown in Fig. 5.2 and are compared with results in Ref. [74] obtained with the spectral code GLOGYSTO, as well as with results in [72] obtained with the PIC code GYGLES. Although some differences exist in the physical model considered in the different codes, we remark a similar dependence with respect to the aspect ratio and a very good agreement on both the growth rates and real frequencies in the limit $a/R \to 0$. One can notice that the growth rate and real frequency of the mode become essentially independent of a/R for $a/R < 0.3$, illustrating the transition from the toroidal to the slab-ITG instability.

In Fig. 5.3, the contour plots obtained with GENE and GLOGYSTO are compared for different inverse aspect ratios. The transition from the toroidal to the slab ITG can be clearly observed as the radial coupling becomes weaker when going from $a/R = 0.18$ to $a/R \to 0$. In the toroidal limit $a/R \simeq 0$, a very good agreement is reached between the two codes concerning the mode structure, which clearly exhibits a slab-like character. The most unstable mode is in both cases localized around $r/a \simeq 0.4$ which corresponds to the mode rational surface with poloidal mode number $m = n\,q = 7$. For the toroidal case, $a/R = 0.18$, the overall mode structure obtained with the two codes are also in good agreement, one notes however that the radial coupling seems stronger in the GENE

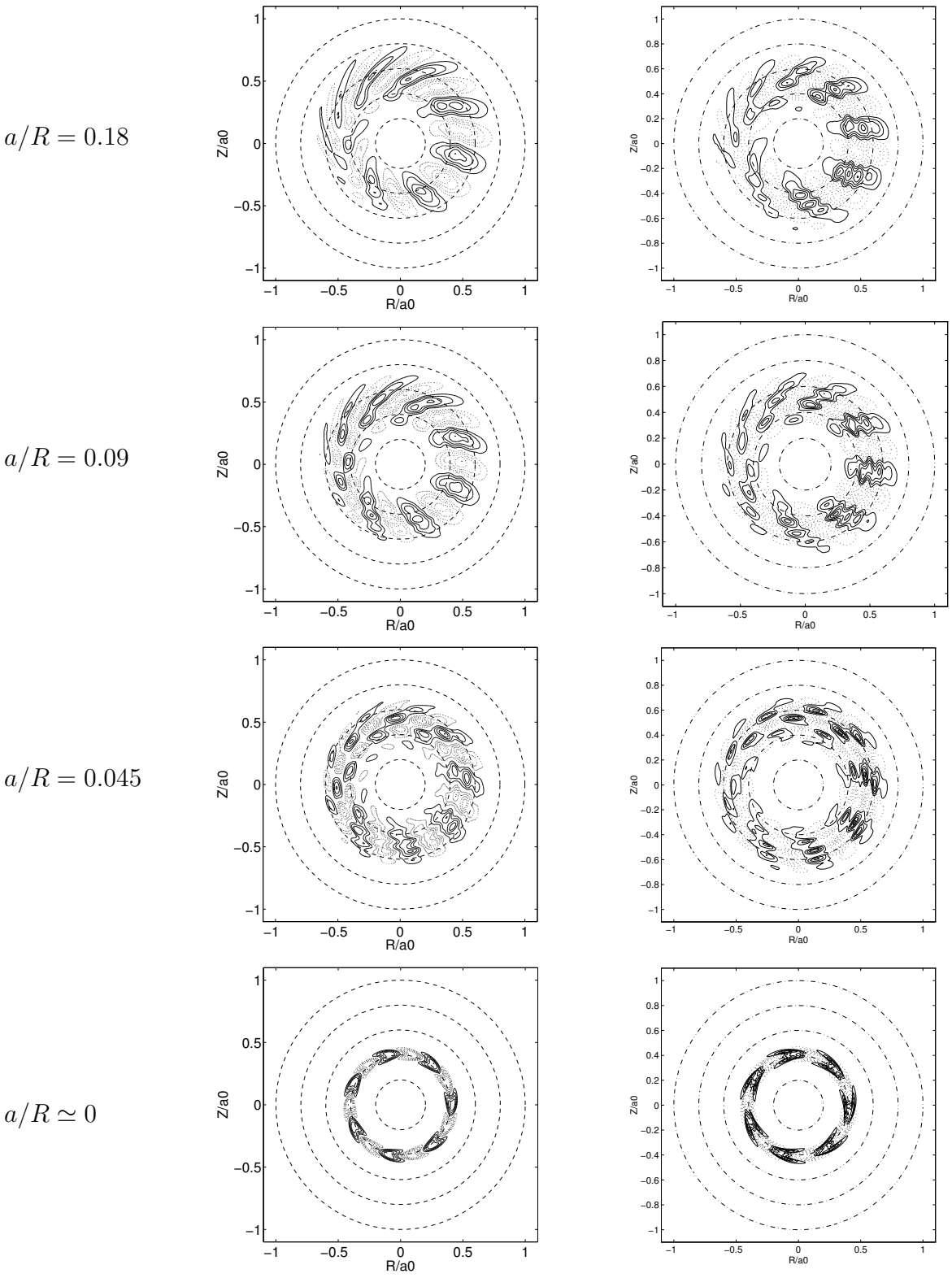

Figure 5.3: Contour plots of the electrostatic potential Φ obtained with GENE (left) and GLOGYSTO (right) for different inverse aspect ratios. Note that the plot identified as $a/R \simeq 0$ corresponds to $a/R = 1.8 \cdot 10^{-6}$ for GENE and $a/R = 0$ for GLOGYSTO.

simulation. This difference on the mode structure, together with the different growth rate obtained for $a/R = 0.18$ in Fig. 5.2 can be explained in part by approximations made in GLOGYSTO, where the drifts of passing particles, at the origin of the radial coupling, are evaluated using an iterative scheme. From these results, one may conclude that the global version of GENE correctly describes the cylindrical limit and the corresponding slab-ITG regime.

5.2 Linear Cyclone benchmark

In this section, linear comparisons of global-GENE with other codes in the case of the Cyclone Base Case (CBC) parameters [68] are presented. This study is thus similar to the one carried out with the local-GENE code in section 4.5. For all the following simulations, the ad-hoc circular equilibrium model is considered with inverse aspect ratio $a/R = 0.36$ and safety factor profile:

$$q(x) = 0.85 + 2.2\,(x/a)^2\ . \tag{5.5}$$

The parameter $\rho^* = \rho_s/a$ is taken as $\rho^* = 1/180$ and an adiabatic electron response is assumed. The ion temperature and density profiles, are again defined using Eq. (5.2),

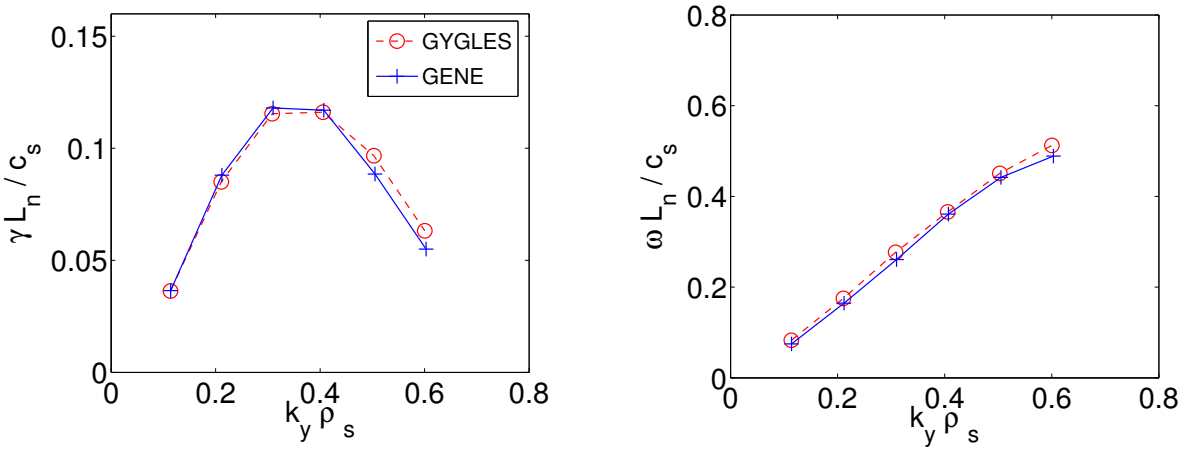

Figure 5.4: Linear growth rates (left) and real frequencies (right) of ITG modes as a function of $k_y\rho_s$ obtained with the global version of GENE and with the PIC code GYGLES, for CBC parameters.

with $\kappa_{Ti} = 6.96$, $\kappa_n = 2.23$, $\Delta T_i, n = 0.3$ and $x_0 = 0.5\,a$ corresponding to peaked

gradient profiles, and the temperature ratio $\tau = T_e/T_i$ is $\tau = 1$. For these parameters, the growth rates and real frequencies computed with GENE are compared in Fig. 5.4 with GYGLES [72] results for different toroidal mode numbers $k_y = n\,q_0/r_0$. A detailed discussion of the required resolution for the linear Cyclone base case is given in [28]. In particular, we note that for the higher $k_y\,\rho_s$ values larger $v_\parallel$ and μ resolutions are required. This higher velocity resolution is necessary for correctly resolving the gyro-averaging operations, leading to the finite $k_\perp\,\rho_s$ effects. In the following the simulation domain considered for each fixed linear run with fixed k_y is $l_x \times l_z \times l_{v_\parallel} \times l_\mu = 140\,\rho_s \times 2\,\pi \times 3.7\,v_{th,i} \times 13\,T_i/B_{\rm ref}$ with resolution $n_x \times n_z \times n_{v_\parallel} \times n_\mu = 200 \times 16 \times 32 \times 16$ for $k_y\,\rho_s < 0.5$. For the larger $k_y\,\rho_s$ an increased $n_{v_\parallel} \times n_\mu = 64 \times 32$ for the larger $k_y\rho_s$.

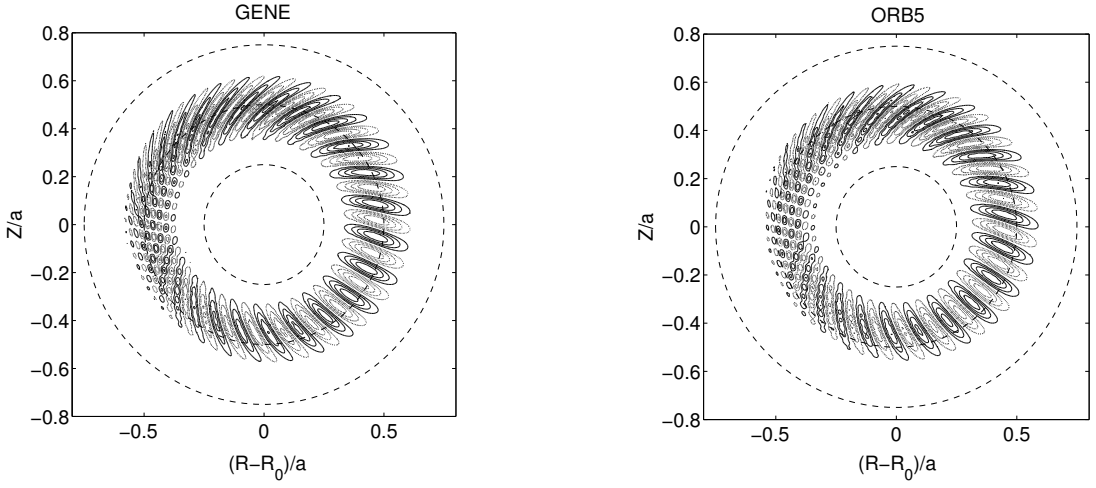

Figure 5.5: Contour plots of the electrostatic potential Φ for toroidal mode number $n = 19$ for CBC parameters, obtained with GENE and ORB5.

As observed, a very good agreement is reached between the two codes. We note however some small deviations, especially in the growth rates, for $k_y\,\rho_s \geq 0.4$. This could result from differences in the field solver as the GYGLES code considers a second order expansion in $k_\perp\,\rho_s$ of the polarization density contribution to the quasi-neutrality equation, while GENE keeps all orders in $k_\perp\,\rho_s$ of this term.

In addition to these quantitative investigations of linear growth rates and real frequencies a detailed comparison of the mode structures was carried out with the global PIC code ORB5 [54], in view of later nonlinear comparisons. In Fig. 5.5, the contour plots of the electrostatic potential are shown for the toroidal mode number $n = 19$ ($k_y\rho_s = 0.3$) and

remarkable agreement is observed. In order to further quantify differences between the mode structures obtained from the two codes comparison of the electrostatic potentials as a function of the straight field line poloidal angle χ is carried out on the fixed magnetic surface $r = r_0 = 0.5\,a$. The fields $\Phi(r, \chi)$ are obtained in GENE and ORB5 at the end of

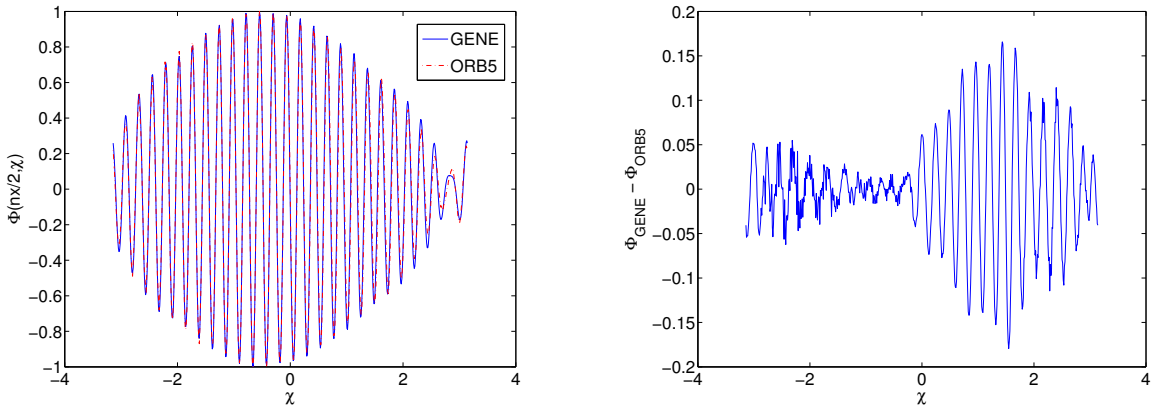

Figure 5.6: Electrostatic potential at $r = r_0 = 0.5\,a$ as a function of the straight field line poloidal angle χ (left). Difference between GENE and ORB5 results, $\tilde{\Phi}_{\mathrm{GENE}}(r_0, \chi) - \tilde{\Phi}_{\mathrm{ORB5}}(r_0, \chi)$ (right).

the simulations, i.e. when the linear growth rates are converged. As a consequence, the overall phases and amplitudes are in general different. In order to be able to compare the two potentials, amplitudes and phases of the fields $\Phi(r = r_0, \chi)$ are renormalized so as to match. This is achieved by making use of a poloidal Fourier transform of $\Phi(r_0, \chi)$:

$$\Phi(r = r_0, \chi) = \frac{1}{2} \sum_{m=-M/2}^{M/2} (\Phi_m + \Phi^*_{-m})\, e^{i\,m\,\chi}\ , \tag{5.6}$$

having invoked the reality condition. The renormalized field $\tilde{\Phi}(r_0, \chi)$ is then given by:

$$\tilde{\Phi}(r_0, \chi) = \frac{A}{2} \sum_{m=-M/2}^{M/2} (\Phi_m\, e^{i\,\Delta\theta} + \Phi^*_{-m}\, e^{-i\,\Delta\theta})\, e^{i\,m\,\chi}\ , \tag{5.7}$$

where the real amplitude A and phase $\Delta\theta$ are adapted so that the dominant poloidal Fourier mode Φ_m obtained from the two codes match. Following this procedure the two electrostatic potentials are shown in Fig. 5.5. As can be seen, the relative difference is at most of the order of 15%, which represents a very good agreement.

5.3 Kinetic electrons and electromagnetic effects

After having studied the standard Cyclone base case using adiabatic electrons, we shall now discuss simulations carried out considering a full kinetic electron response. Note that the results presented in this section have been obtained thanks to the work of J. Chowdhury, who has participated to the global-GENE validation effort during a visit at the CRPP in fall 2009. The electron and ion temperature profiles, as well as the density profile are defined using Eq. (5.2) with $\kappa_{Ti} = \kappa_{Te} = 6.96$, $\kappa_n = 2.23$, $\Delta(T_i, T_e, n) = 0.3$ and $x_0 = 0.5$. The same safety factor profile as in section 5.2 is considered and $\beta = 2\,\mu_0\,T_e\,n_e/B_0^2$ is set to $\beta = 10^{-3}$. In addition, the ion to electron mass ratio has been reduced for practical reasons to $m_i/m_e = 400$.

When considering the full kinetic dynamic of electrons, their response becomes non-adiabatic around mode rational surfaces. Fine radial structures are generated in these non-adiabatic response regions [75, 76], which could lead to badly-converged results or even to numerical instabilities when not properly resolved. Let us recall that for a mode with frequency ω and parallel wave number $k_\parallel$ the electrons respond adiabatically in the limit $|\omega/(k_\parallel v_{the})| \to 0$. Considering a Fourier component with poloidal and toroidal mode numbers (m, n) respectively, the corresponding parallel wave number $k_\parallel$ is given for a straight field line coordinate system by

$$k_\parallel = (m\,\vec{\nabla}\chi + n\,\vec{\nabla}\Phi)\cdot\vec{b} = \frac{B_\phi}{B}\frac{1}{R\,q}\,(n\,q - m) \simeq \frac{1}{R\,q}\,(n\,q - m)\,. \tag{5.8}$$

Clearly, $k_\parallel$ goes to zero at the associated mode rational surface $r = r_{m,n}$, where the safety factor $q = q(r_{m,n}) = m/n$. The condition for adiabatic electron response to such a Fourier component is thus not met in the vicinity of $r_{m,n}$. By estimating the transition from adiabatic to non-adiabatic electron response with the condition:

$$\frac{|\omega|}{k_\parallel} \simeq v_{the}\ , \tag{5.9}$$

the radial width of the non-adiabatic region around $r_{m,n}$ can be evaluated as follows. The safety factor is first linearized around $r_{m,n}$ leading to:

$$k_\parallel = \frac{1}{R\,q}\,[n\,q(r_{m,n} + \Delta r) - m] \simeq \frac{1}{R\,q}\left[n\,q + n\,\Delta r\,\frac{dq}{dr}\Big|_{r_{m,n}} - m\right] = \frac{\Delta r}{r_{m,n}\,R}\,n\ \hat{s}\,, \tag{5.10}$$

with the shear $\hat{s} = (r/q)(dq/dr)|_{m,n}$. Considering $v_{the} = \sqrt{T_e/m_i}$, the condition (5.9) is then expressed as a relation for the normalized radial width $\Delta r/\rho_s$ of the non-adiabatic region centered on the mode rational surface $r_{m,n}$:

$$\frac{\Delta r}{\rho_s} = |\omega| \frac{R}{c_s} \sqrt{\frac{m_e}{m_i}} \frac{q}{k_y \rho_s \hat{s}} , \tag{5.11}$$

having used $k_y = n\, q/r_{m,n}$. Note that for microinstabilities, $\omega R/c_s \sim 1$. For the present parameters, where $q = 1.4$ and $\hat{s} \simeq 0.8$, the typical radial width of the non-adiabatic response region can thus be estimated as $\Delta r/\rho_s \sim 0.8$ for $k_y\rho_s = 0.1$ and $\Delta r/\rho_s = 0.08$ for $k_y\rho_s = 1$. A very high radial resolution is therefore required for the high k_y modes in order to properly handle the small radial structures that develop in these regions. According to Eq. 5.11 the radial resolution should be at least small as $\Delta x/\rho_s \sim (k_y\, \rho_s)^{-1}$.

Keeping in mind this constraint on the x-resolution, we show in Fig. 5.7 the growth rates and real frequencies obtained for different k_y modes. Note that the growth rates and frequencies are normalized here to L_n/c_s for easier comparison with [68]. For these computations, we consider a simulation domain in the z, $v_\parallel$, and μ-directions of size $l_z \times l_{v_\parallel} \times l_\mu = 2\,\pi \times 4\, v_{th,i} \times 16\, T_i/B_{\rm ref}$ with grid resolutions $n_z \times n_{v_\parallel} \times n_\mu = 16 \times 48 \times 16$. In the radial direction, the resolution was adapted for each k_y by decreasing the box size l_x as the radial width of modes shrank, from $l_x = 80\rho_s$ at $k_y\rho_s = 0.1$ to 20 at $k_y\rho_s = 0.9$ while increasing the number of x points from 160 to 560. This corresponds to a radial resolution of $\Delta x/\rho_s = 0.5$ and $\Delta x/\rho_s = 0.03$ respectively. These simulations obtained with the global version of GENE are compared with the local version of GENE, as well as with the ORB5 code. Based on the sign of the real frequencies, one observes for both local and global GENE simulations, as well as for ORB5, a transition from Ion Temperature Gradient (ITG, $\omega > 0$) to Trapped Electron Mode (TEM, $\omega < 0$) around $k_y\, \rho_s = 0.7$. Quantitatively, although a good agreement is reached between ORB5 and the global version of GENE concerning the real frequency, important differences are observed in the growth rates. These discrepancies are still being investigated. It should be in particular pointed out that the ORB5 simulations were carried out here considering only trapped kinetic electrons, while passing electrons are still assumed adiabatic. In GENE however, full kinetic electrons are retained, which could be a possible explanation for the differences. In addition, we also remark a different behavior at large $k_y\rho_i$, as the growth rates

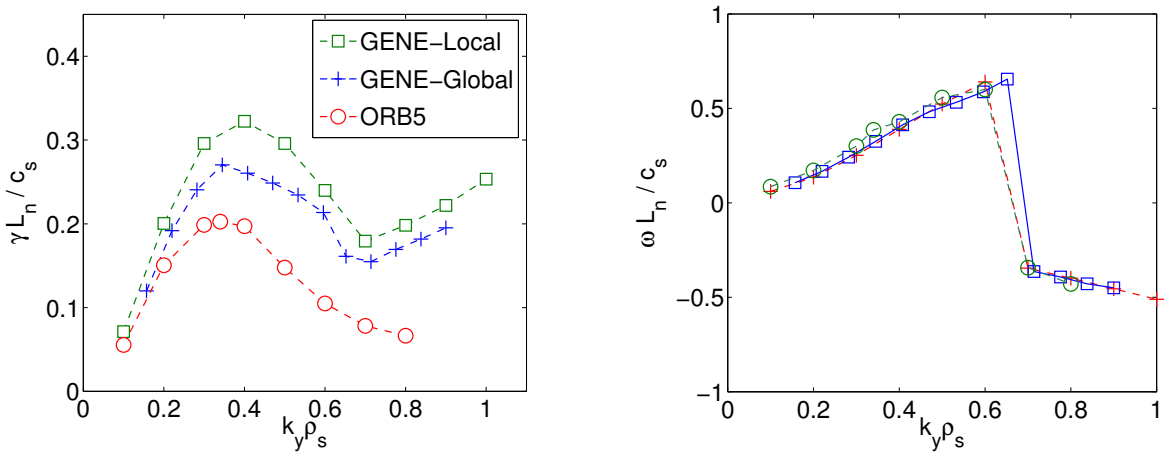

Figure 5.7: Linear growth rates (left) and real frequencies (right) as a function of $k_y\rho_s$ obtained with GENE and with the PIC code ORB5, for CBC parameters. The local and global GENE simulations both include full kinetic electrons while only trapped electrons are considered in the ORB5 results.

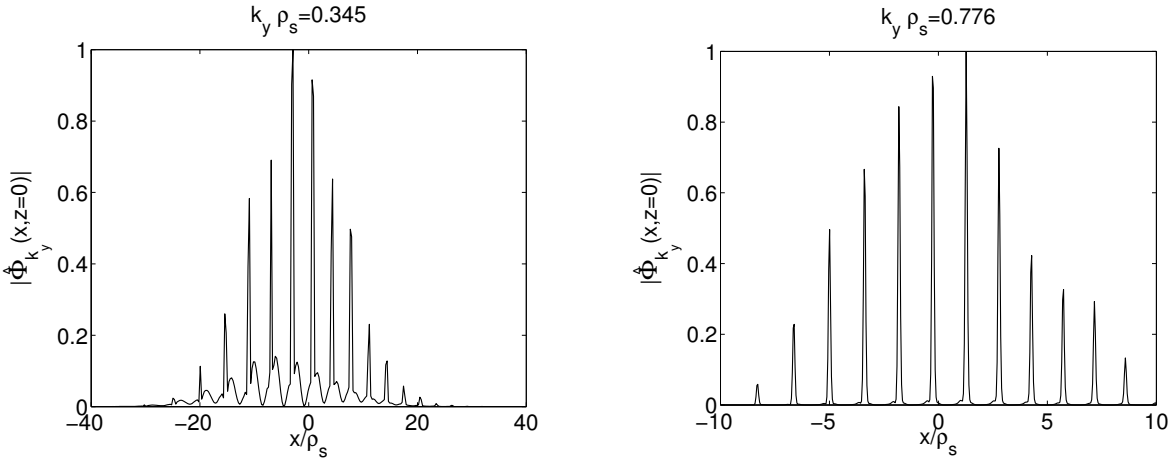

Figure 5.8: Fourier component of $\hat{\Phi}_{k_y}$ at $z = 0$ (outer mid-plane) as a function of the radial coordinate x for the two modes $k_y\rho_s = 0.345$ and $k_y\rho_s = 0.776$. Note that the amplitudes have been normalized so that the maximum value is 1.

obtained with ORB5 do not increase in the TEM region. This in turn may be related to the differences in the field solver between the two codes (already noted in section 5.2 for GYGLES) which is only second order accurate in $k_y\rho_s$ in ORB5 while all orders are kept in GENE. Finally, we observe that ρ^* effects seem less pronounced when using kinetic electrons compared to the adiabatic electron case, see for instance Fig. 4.9, since the local and global growth rate curves are here much closer to each other.

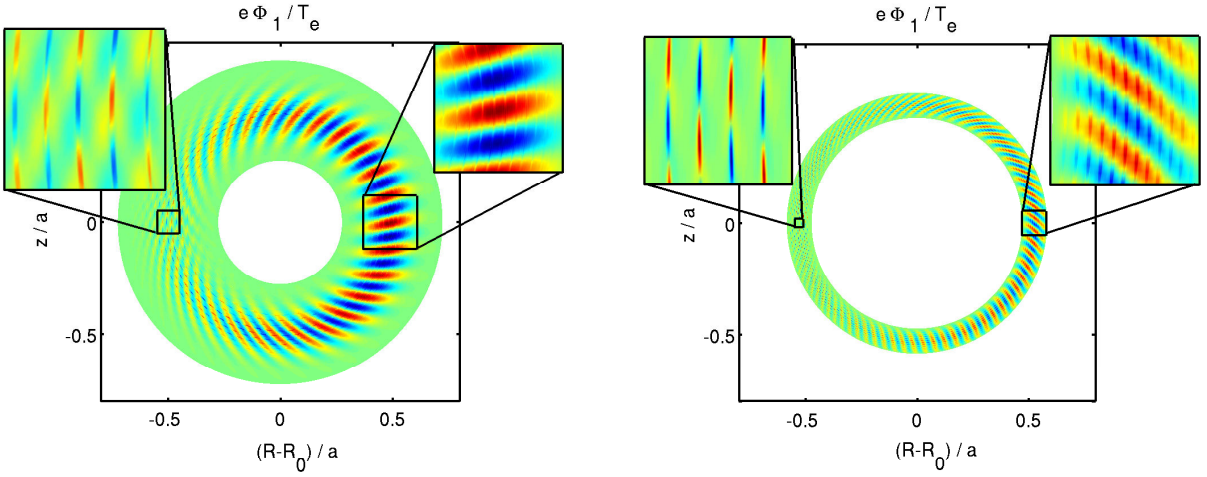

Figure 5.9: Contour plots of the electrostatic potential Φ in the poloidal plane for toroidal mode number $k_y\rho_s = 0.345$ and $k_y\rho_s = 0.776$.

In order to further investigate issues related to the non-adiabatic electron response region, the k_y Fourier components of Φ are represented in Fig. 5.8 at $z = 0$ as a function of x for the two modes $k_y\rho_s = 0.345$ ($n = 22$) and $k_y\rho_s = 0.776$ ($n = 50$). For each mode, one observes peaks localized at mode rational surfaces $r_{m,n}$, where $q(r_{mn}) = m/n$. By estimating the width of the non-adiabatic response region as the width of the largest peak (measured at mid amplitude), one obtains $\Delta x = 0.51\rho_s$ for $k_y\rho_s = 0.345$ and $\Delta x = 0.11\rho_s$ for $k_y\rho_s = 0.776$. These values are in good agreement with the estimate (5.11) from which one obtains respectively $\Delta x = 2\,\Delta r = 0.43\,\rho_s$ and $\Delta x = 2\,\Delta r = 0.20\,\rho_s$ for $k_y\rho_s = 0.345$ and $k_y\,\rho_s = 0.776$. In Fig. 5.9, the contour plots in the poloidal plane of the electrostatic potential are also shown for modes $k_y\rho_s = 0.345$ and $k_y\rho_s = 0.776$. One clearly observes the slab-like structure of the mode at mode rational surfaces and the small radial structures resulting from the non-adiabatic electron response, which are here well resolved.

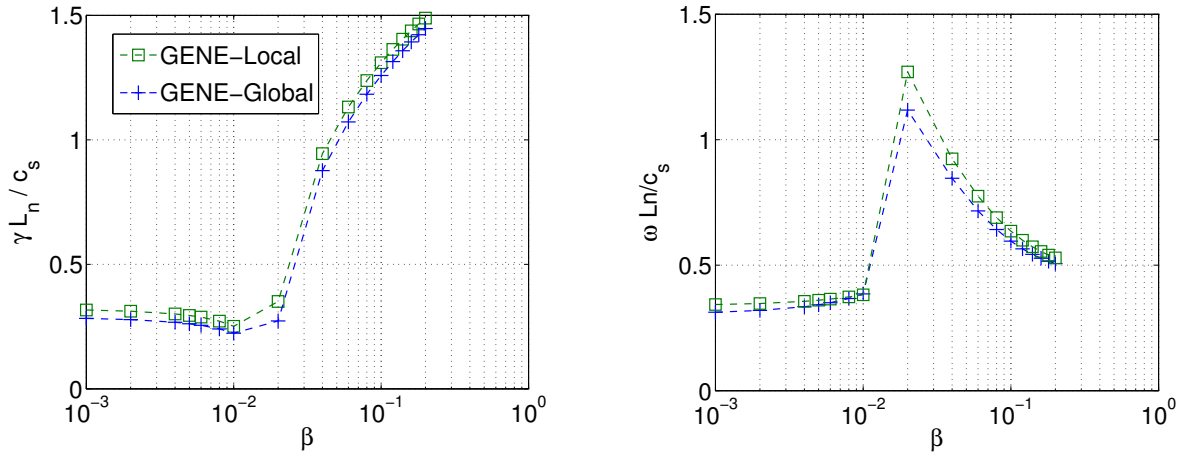

Figure 5.10: Linear growth rates (left) and real frequencies (right) for the mode $k_y\rho_s = 0.345$ as a function of β obtained with the local and global versions of GENE. A transition from ITG to KBM is observed around $\beta = 2 \cdot 10^{-2}$.

Using the same CBC parameters as before, a scan in $\beta = 2\,\mu_0\,T_e\,n_e/B_0^2$ was also carried out to test the global code when electromagnetic effects become important. The growth rates and real frequencies obtained with the local and global versions of GENE are shown in Fig. 5.10. The global code reproduces well the β dependence with respect to local results, in particular the jump in the real frequency, observed at $\beta \simeq 2 \cdot 10^{-2}$, which is attributed to a transition from ITG to the so-called Kinetic Ballooning Mode (KBM).

The contour plots of the perturbed electrostatic potential Φ_1 and parallel component $A_{1\parallel}$ of the vector potential are shown in Fig. 5.11 for $\beta = 2 \cdot 10^{-3}$ and $\beta = 2 \cdot 10^{-2}$. One observes an anti-ballooned structure of $A_{1\parallel}$, in agreement with results from local simulations. When comparing the two fields, the relative amplitude of $A_{1\parallel}$ with respect to $\Phi_{1\parallel}$ is increased by almost an order of magnitude when going from $\beta = 2 \cdot 10^{-3}$ to $\beta = 2 \cdot 10^{-2}$.

These first electromagnetic results obtained with the global version of GENE are thus very encouraging, and benchmarks with other codes are planed to further validate the code in the high β regime.

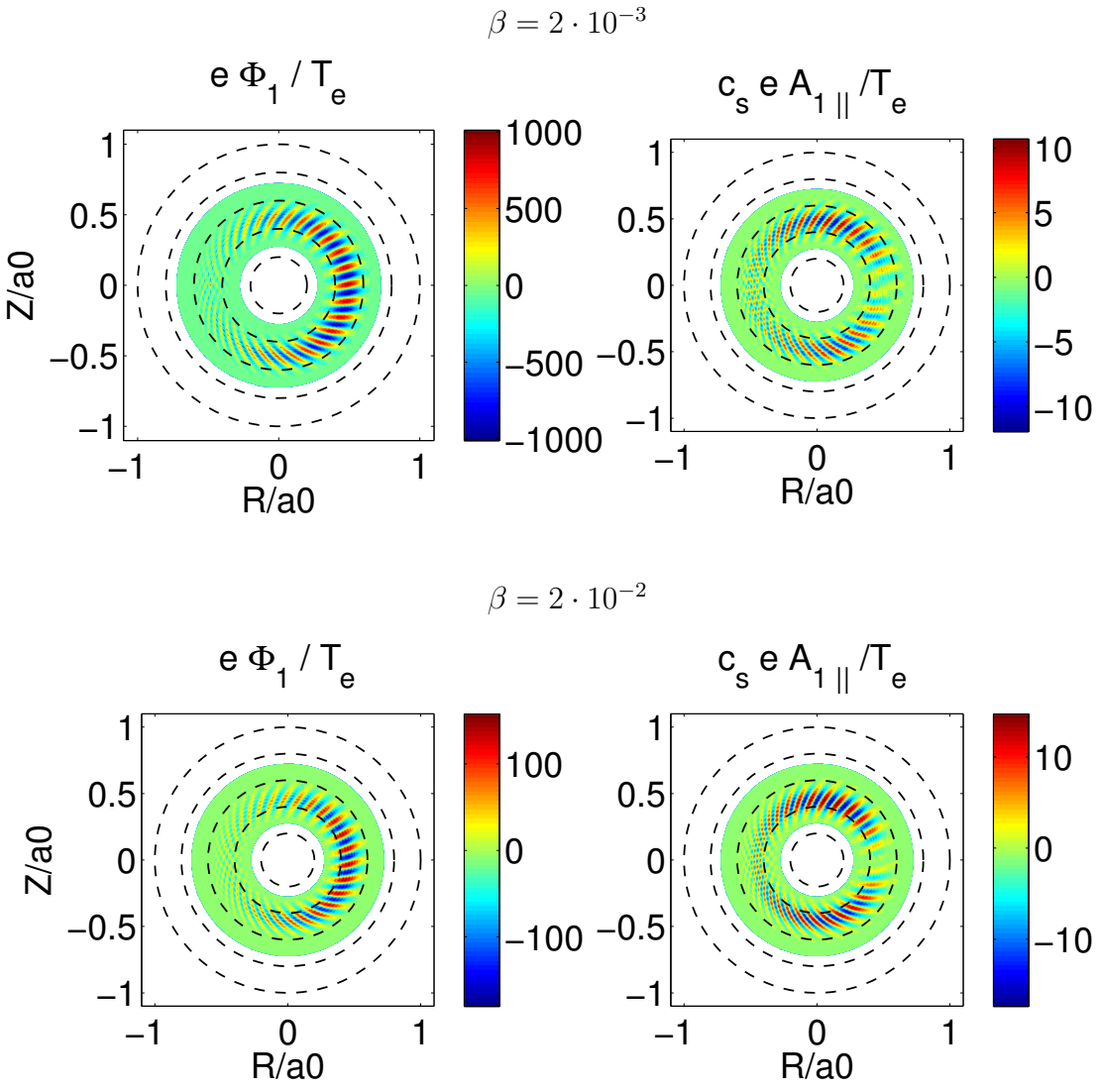

Figure 5.11: Contour plots of the perturbed electrostatic potential Φ_1 and parallel component of the vector potential $A_{1\parallel}$ for $\beta = 2 \cdot 10^{-3}$ (top) and $\beta = 2 \cdot 10^{-2}$ (bottom) obtained with the global version of GENE.

5.4 Field solver analysis and Rosenbluth-Hinton test

The Rosenbluth-Hinton test consists of computing the linear evolution of the zonal flow component ($n = 0, m = 0$) for an initial electrostatic perturbation Φ. From the analytical resolution of the gyrokinetic equation for $n = 0$ [73], and local to a given magnetic surface, one expects to observe a damped oscillation of the Geodesic Acoustic Modes (GAM) relaxing towards the so-called zonal flow residual. The time evolution of the the zonal flow component can thus be written:

$$\frac{E_x(t)}{E_x(0)} = (1 - A_R)\, e^{-\gamma_R t}\, \cos(w_g\, t) + A_R\ , \tag{5.12}$$

where $E_x = -\,\partial\langle\Phi\rangle/\partial x$ is the radial perturbed electric field, , $\langle\Phi\rangle$ being the flux-surface averaged potential. The residual is

$$A_R = \frac{1}{1 + 1.6\, q^2/\sqrt{r/R}}\ , \tag{5.13}$$

with r the local minor radius of the considered magnetic surface, R the major radius, and ω_G and γ_G respectively the GAM frequency and damping rate. A correct prediction of this residual level is an important test for gyrokinetic codes, as zonal flows are identified to be a key saturation mechanism in turbulent regimes, in particular for ITG turbulence. In Ref. [28], a detail comparison between GENE's predicted residual level and analytical values was carried out showing an excellent agreement. In order to obtain such good quantitative comparison with the analytical results it is however necessary to use a constant or linear safety factor to be consistent with the local assumptions considered to derive Eq. (5.13). In this section, we shall carry out the Rosenbluth-Hinton test assuming a more realistic quadratic safety factor profile and using the ORB5 code as a benchmark instead of the analytical relations. The physical parameters used in the following are:

$$a/R = 0.1\ , \qquad q(x) = 0.96 + 0.75\,(x/a)^2\ , \tag{5.14}$$

$\rho^* = \rho_s/a = 1/160$, flat temperature and density profiles $\kappa_{Ti} = \kappa_{ni} = 0$, and an adiabatic electron response is assumed.

Before considering the actual Rosenbluth-Hinton test, we shall first carry out a com-

parison of the field solver in ORB5 and GENE. As discussed in section 3.3, in the original implementation of the gyro-averaging, the particle position is evaluated by linearizing the metric in the field aligned coordinates (x, y, z). This approach neglects some $1/r$ terms, and an alternative scheme was thus proposed which consist in computing the particle position in a pseudo-Cartesian coordinate system (ξ, η). Note that in the ORB5 code the treatment of the field solver retains the above mentioned $1/r$ terms.

Considering an initial axisymmetric perturbation of the distribution function $f_1(x, y, z, t = 0) \sim \cos(\pi x/l_x)$, the electrostatic potential Φ computed at time $t = 0$ with GENE using both the original and the alternative [*i.e.* (ξ, η) coordinates] gyro-averaging schemes are compared to the ORB5 results in Fig. 5.12. One clearly observes a better agreement

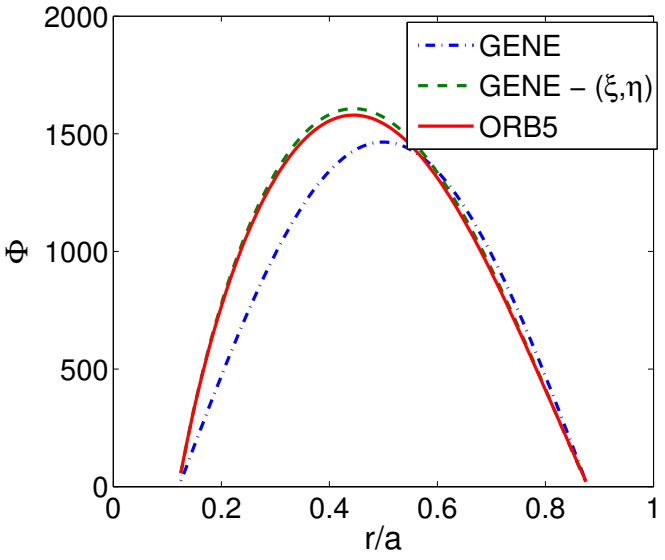

Figure 5.12: Electrostatic potential computed at $t = 0$ with GENE using the original and (η, χ) gyro-averaging, and with ORB5. The initial perturbation is $f_1(t = 0) \sim \cos(\pi x/l_x)$

between GENE and ORB5 when using the gyro-averaging operator in (ξ, η) coordinates. Although this new treatment provides a better model for the gyro-averaging and thus the field solver, it has led to an unphysical growing amplitude of the zonal flow when carrying out the Rosenbluth-Hinton time evolution problem. Quite extensive tests have already been carried out to investigate this issue, but unfortunately it has not yet been solved. The current hypothesis is that, when introducing the $1/r$ terms related to the singularity

of the coordinate system, in the gyro-averaging this leads to inconsistencies between the field solver and the gyrokinetic equation, where some similar $1/r$ terms are neglected, see section 2.11. It may well be that one needs to correct all these terms together to obtain a fully consistent improved model. In the present version of the code, the original gyro-averaging, *i.e.* with the linearization of the metric in (x, y, z) coordinates, is therefore used.

Going back to the Rosenbluth Hinton test, the time evolution of the zonal flow component of the electric field, using the gyro-averaging in (x, y, z) coordinates, is shown in Fig. 5.13. For this simulation, a domain $l_x \times l_z \times l_{v_\parallel} \times l_\mu = 120\,\rho_s \times 2\,\pi \times 3\,v_{th,i} \times 9\,T_i/B_{\rm ref}$ with grid size $n_x \times n_z \times n_{v_\parallel} \times n_\mu = 160 \times 16 \times 128 \times 64$ is considered. One observes similar GAM damping rate and frequencies obtained with GENE and ORB5, and a reasonable agreement, within 10%, on the residual level is finally reached.

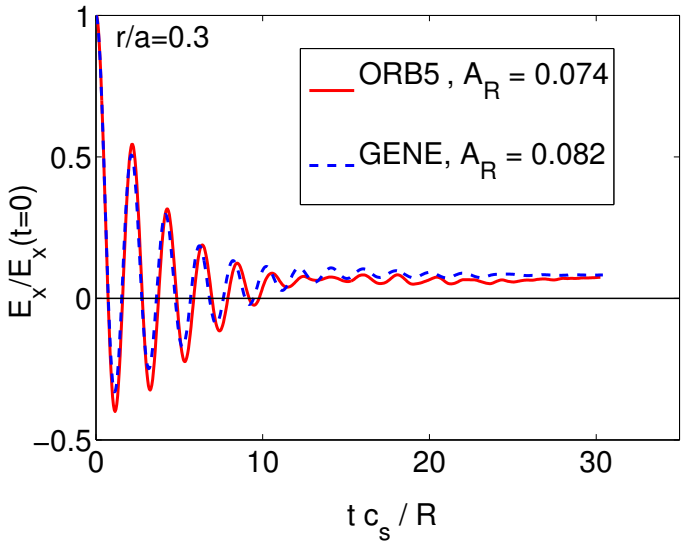

Figure 5.13: Time evolution of the normalized electric field at $r/a = 0.3$, obtained with GENE and ORB5.

Considering this benchmark and other comparisons with analytical results in [28], one concludes that, despite the inaccuracies of the currently used gyro-averaging operator near the magnetic axis, the code successfully satisfies the Rosenbluth-Hinton test.

5.5 Nonlinear benchmarks

After having validated the global GENE code in the linear limit, in particular with respect to the Rosenbluth-Hinton test, we shall now focus on nonlinear results. Note that only adiabatic electron simulations are considered in this section.

5.5.1 Nonlinear run without sources

The first simulations are carried out using essentially the same Cyclone parameters, as in section 5.2, with $a/R = 0.36$, $\rho^* = \rho_s/a = 1/180$, as well as peaked ion temperature and density logarithmic gradient profiles, defined through Eq. (5.2), with $\kappa_{Ti} = 6.96$, $\kappa_n = 2.23$. The safety factor profile considered here is however given by

$$q(x) = 0.85 - 0.01\,x/a + 2.28\,(x/a)^2 - 0.09\,(x/a)^3 + 0.22\,(x/a)^4\,, \tag{5.15}$$

which was chosen to match simulation parameters considered previously for running the ORB5 code. This q profile is thus slightly different from the one given by Eq. 5.5 in section 5.2 but still is such that $q(x = 0.5) = 1.4$ and $\hat{s}(x = 0.5) = 0.8$. The temperature ratio is $\tau = T_e/T_i = 1$ throughout the plasma. The radial size of the simulation domain is $l_x = 120\,\rho_s$ including buffer regions at the edge of the system which represent 5% of the simulation box on each side and in which a damping Krook operator is applied. The time evolutions of the nonlinear ion heat diffusivity χ_i obtained with ORB5 and GENE are shown in Fig. 5.14, and are given in gyro-Bohm units $\chi_{GB} = \rho_s^2\,c_s/a$. In order to enable a detailed comparison of the initial linear phase, as well as of the nonlinear saturation, the two codes considered exactly the same initial conditions. As result a very good agreement is observed. In particular, we note that the first bursts are identical in both simulations. As no sources are considered here, the ion temperature profile rapidly relaxes towards a flat profile, which leads to a decrease of the heat diffusivity. It is therefore difficult to evaluate precisely in Fig. 5.14 the differences between the two time traces after the first burst as no steady state is reached.

5.5.2 Nonlinear run with sources

In order to carry out quantitative comparisons, the Krook-type heat source (3.113) is now switched on for the ions, with $\gamma_h\,R/c_s = 0.035$. This value is chosen about ten

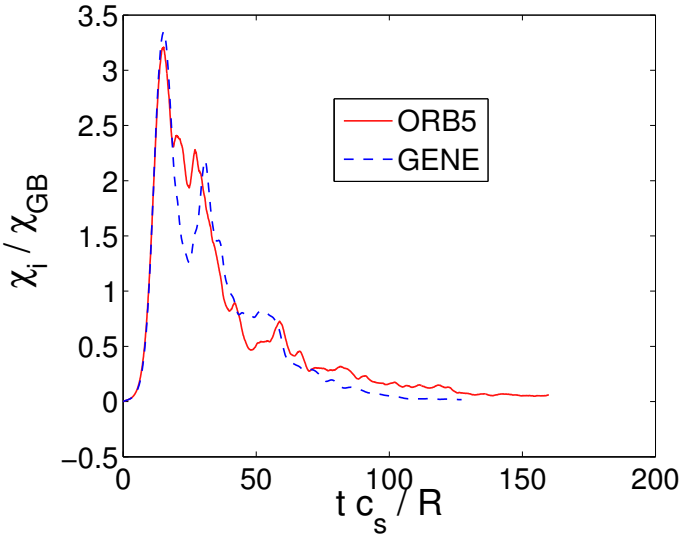

Figure 5.14: Time evolutions of the nonlinear heat diffusivity χ/χ_{GB} ($\chi_{GB} = \rho_s^2 c_s/a$) obtained with ORB5 and GENE for CBC parameters. Note the decrease of the heat diffusivity as no source are included.

times smaller than the typical linear growth rate, so that the time scale on which the heat source affects the temperature profile is smaller than the characteristic time of the turbulence. For these simulations, the same background state is considered as for the previous case without sources, except for the logarithmic gradient profiles of the density and temperature which are chosen to be flatter, according to the following relation:

$$R\,\frac{d\ln(T_i,n)}{dx} = \kappa_{(T_i,n)}\left[1-\cosh^{-2}\left(\frac{x-x_0-\Delta x/2}{a\,\Delta(T_i,n)}\right)-\cosh^{-2}\left(\frac{x-x_0+\Delta x/2}{a\,\Delta(T_i,n)}\right)\right] \quad (5.16)$$

taken for $x \in [x_0-\Delta x/2, x_0+\Delta x/2]$ and zero outside. The different constant parameters are set to $\kappa_{Ti} = 7.1$, $\kappa_n = 2.2$, $\Delta_x = 0.8\,a$ and $\Delta T_i = \Delta n = 0.04$. The corresponding temperature and density profiles are shown in Fig. 5.15.

The considered numerical box is $l_x \times l_y \times l_z \times l_{v_\parallel} \times l_\mu = 144\,\rho_s \times 132\,\rho_s \times 2\,\pi \times 4\,v_{th,i} \times 16\,T_i/B_{\rm ref}$ with grid resolution $n_x \times n_y \times n_z \times n_{v_\parallel} \times n_\mu = 150 \times 64 \times 16 \times 64 \times 16$. Note that the box size in the y-direction is chosen so that:

$$l_y = \frac{2\,\pi}{n_0}\,\frac{r_0}{q_0}\,, \quad \text{with} \quad n_0 = 3\,. \quad (5.17)$$

The simulation domain thus covers only one third of each flux surface, which in Fourier space translates to one out of every three modes kept in the k_y-spectrum, with the smallest

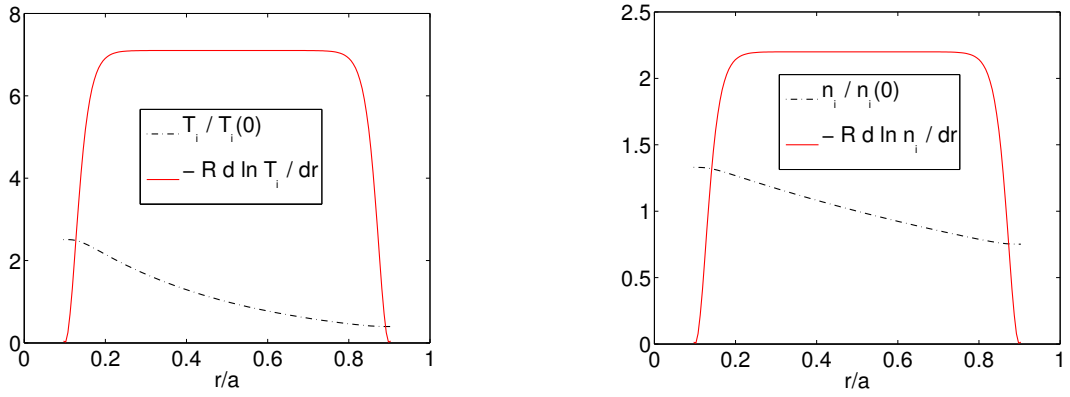

Figure 5.15: Temperature and density profiles together with their normalized logarithmic gradients, for $\kappa_{Ti} = 7.1$, $\kappa_n = 2.2$, $\Delta x = 0.8\,a$ and $\Delta T_i = \Delta n = 0.04$ [see Eq. (5.16)].

mode number in the system being:

$$k_{y,min}\,\rho_s = 2\,\pi\,\rho_s/l_y = 0.0476\,. \tag{5.18}$$

In addition, by setting the numerical parameters $h_x = 2$, $h_z = 2$, and $h_{v_\parallel} = 0.5$, one relies on hyperdiffusion in the $x-$, $z-$ and $v_\parallel-$directions, respectively, to ensure numerical stability.

Using these numerical parameters, the time evolution of the heat diffusivity and normalized logarithmic gradient of the total temperature $T_{i,\mathrm{tot}} = T_{i0} + T_{i1}$ are shown in Fig. 5.16, together with their running time-average starting at $t_0 = 150R/c_s$, defined for a quantity A as:

$$A_{\mathrm{av}}(t) = \frac{1}{t - t_0}\int_{t_0}^{t} A(t)\;dt\;. \tag{5.19}$$

Note that 200 000 time steps were computed for this simulation, which has required about 10 000 CPU hrs. As opposed to the case with no sources, a quasi-steady state is reached here, thus validating the use of the Krook-type heat source for this code comparison. These results are compared with an ORB5 simulation obtained for the same physical parameters and a similar form of the heat source (see Ref. [62]). The averaged heat diffusivity is $\chi_i/\chi_{GB} = 1.95$ for GENE and $\chi_i/\chi_{GB} = 1.76$ for ORB5, *i.e.* a relative difference of about 10%. A first element that could account for this small discrepancy are the remaining ρ^* terms that are still neglected in the gyrokinetic equation considered by GENE, see Sections 2.11 and 5.4, while they are retained in ORB5. The differences in

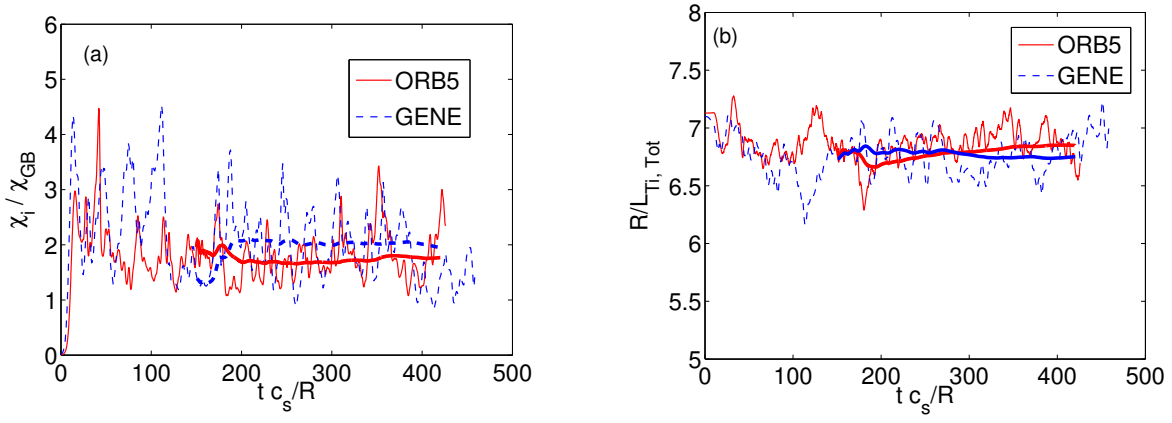

Figure 5.16: Time evolution of (a) the ion heat diffusivity χ_i in units of $\chi_{GB} = c_s\,\rho_s/a^2$ and of (b) the normalized logarithmic gradient $R_{L_{Ti,\mathrm{Tot}}}$ of the total ion temperature $T_i = T_{0i} + T_{1i}$ for CBC like parameters. These two quantities have been obtained by radial averaging in the range $x/a = [0.4, 0.6]$. The bold lines represent the running time-average starting from $t_0 = 150R/c_s$.

the field solver which is only second order accurate in $k_y\rho_s$ in ORB5 while all orders are kept in GENE may also account for the differences. Indeed the mode numbers $k_y\rho_s > 0.6$ contributes to 15% of the total heat diffusivity in GENE, while these contributions may be underestimated in ORB5 as a result of the $k_y\rho_s$ approximation in ORB5. From a numerical point of view we notice also that somewhat high hyperdiffusion coefficients $h_x = 2$, $h_z = 2$ were necessary for stability reasons, which may lead to small variations in the heat diffusivity. The ORB5 simulations is in addition using a noise control system which is known to decrease the computed heat diffusivity, also leading to an uncertainty of about 5% according to convergence tests in the number of markers. Finally, some earlier studies carried out with ORB5 have shown that the heat diffusivity computed with different initial conditions could vary within 10%. This variability is due to the chaotic nature of the turbulence, see *e.g.* Ref. [62]. This is also the reason of the differences observed in the detailed burst sequence between two simulations, such as those in Fig. 5.14 and 5.16. Considering these different numerical and physical aspects, the present results were judged satisfactory to validate the nonlinear behavior of the global version of GENE. When considering the time evolution of the total ion temperature logarithmic gradient in Fig. 5.16, one observes that its quasisteady state value is smaller than its initial value. This can be explained by value of γ_h used for the heat source, which is chosen about 10 time lower than the typical growth rate, so that the time scale on which the heat source modifies

the temperature profile remains smaller than the characteristic time of the turbulence. The quasisteady state value of the total temperature gradient reflects therefore an equilibrium between the turbulent transport which tends to flatten the temperature profile, and the Krook-type heat source which tends to restore the temperature profile towards the initial background profile.

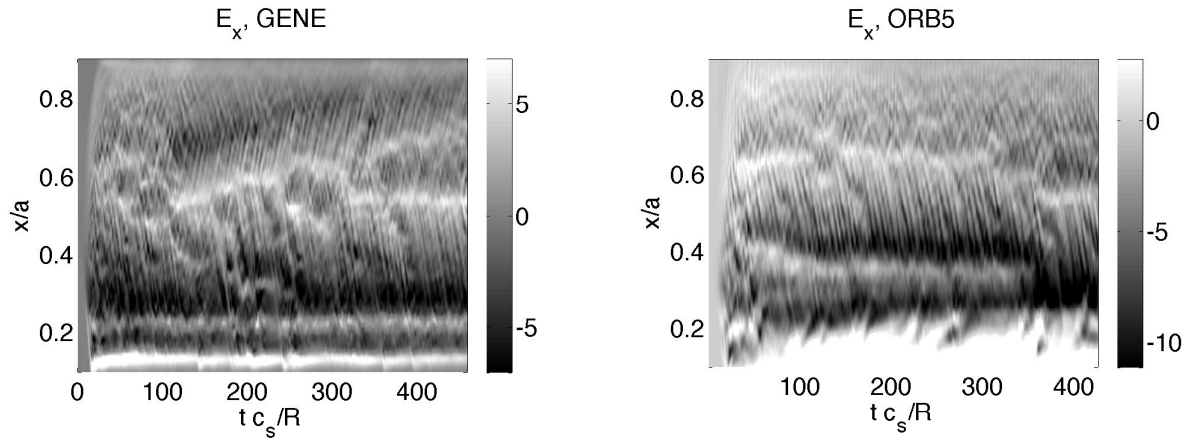

Figure 5.17: Normalized flux-surface averaged electric field E_x obtained with GENE and ORB5 as a function of the radial coordinate x and time t.

As discussed in the previous section, the zonal flow component $k_y = 0$ (or $n = 0$) is the main saturation mechanism for the ITG saturation, and an accurate description of its structure is therefore of particular importance. In Fig. 5.17, we show a two-dimensional representation of the normalized flux-surface averaged radial electric field $E_x(t, x)$, defined as:

$$E_x(t,x) = \frac{\rho_s^2\, e}{R\, T_e} \frac{\int -\partial/\partial x \left[\Phi(t,x,y,z)\right] J^{xyz}(x,z)\, dz\, dy}{\int J(x,z)\, dz\, dy}\,, \tag{5.20}$$

with $\Phi(t, x, y, z)$ the electrostatic potential and J^{xyz} the Jacobian of the field aligned coordinate system (x, y, z). Note that by taking the flux-surface average of Φ, only the $k_y = 0$ contribution remains. When comparing GENE and ORB5 results in the inner part of the simulation domain ($x/a = [0.3, 0.7]$), one observes similar small-scale avalanche-like structures in both cases [77]. The envelope shape of the radial electric fields E_x at the end of the simulation ($t \simeq 400R/c_s$) are in addition comparable, showing in both cases a local maximum around $x/a = 0.5-0.6$. One notes, however that the absolute amplitudes of the

field are different, which can in fact be explained by the different boundary conditions used in the two codes. In GENE, Dirichlet boundary conditions are considered for the electrostatic potential in the radial direction, on both ends of the simulation domain, while a free boundary condition is used in ORB5 at the inner edge, and Dirichlet only on the outer edge.

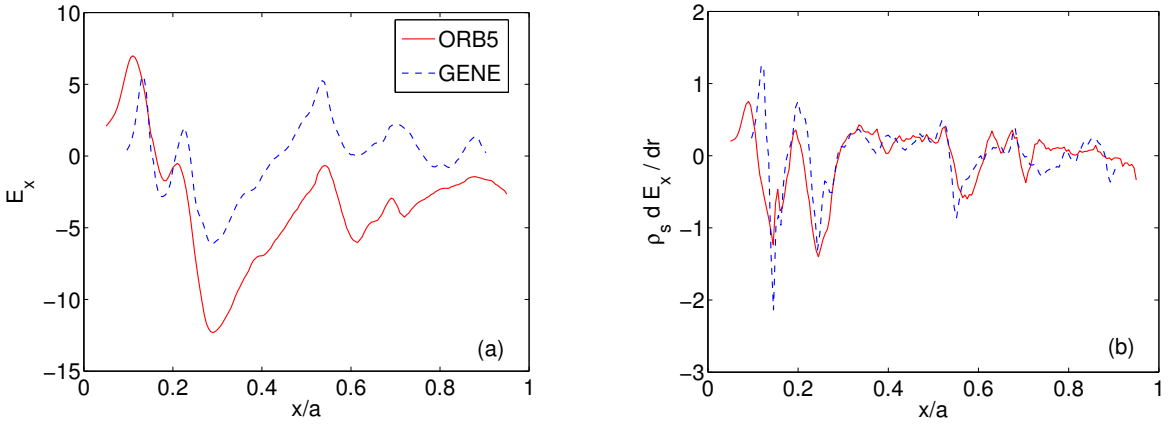

Figure 5.18: Radial profile of the normalized flux-surface averaged electric field E_x (a) and its radial derivative dE_x/dr (b), obtained with GENE and ORB5, and averaged over the time interval $t\,c_s/R = [380\,420]$.

In order to compare quantitatively the radial structure of the flux-surface averaged electric fields, the time-average of $E_x(t,x)$ over the interval $t\,c_s/R = [380, 420]$ is shown in Fig. 5.18.a. Although the amplitudes differ as a consequence of the different radial boundary conditions for ϕ, the radial structures are indeed observed to be very similar. The influence of zonal flow on microturbulence results from its capability to shear the radial coherent turbulent structures, see Ref. [78]. This effect in fact depends on the shearing rate $\omega_{E\times B}$, which is proportional to the first radial derivative of the electric field (i.e. second derivative of the electrostatic potential):

$$\omega_{E\times B} \propto \frac{dE_x}{dx} \ . \tag{5.21}$$

By comparing in Fig. 5.18.b the radial profiles of dE_x/dx, one observes very good agreement between the two codes. This further explains the similar values obtained for the heat diffusivity and shows that the choice of boundary conditions in the radial direction

for ϕ has essentially no effect on the physical simulation results.

5.6 Nonlinear ρ^* scan

In order to evaluate how global effects influence the nonlinear turbulence in the case of these Cyclone-type parameters, a $\rho^* = \rho_s/a$ scan is carried out and the results are compared to a local GENE simulation. As already discussed, when using the Krook-type heat source, the steady state temperature gradient, $R/L_{Ti,Tot}$, will nonetheless differ from the initial temperature gradient. This deviation may in fact vary when changing ρ^*. In

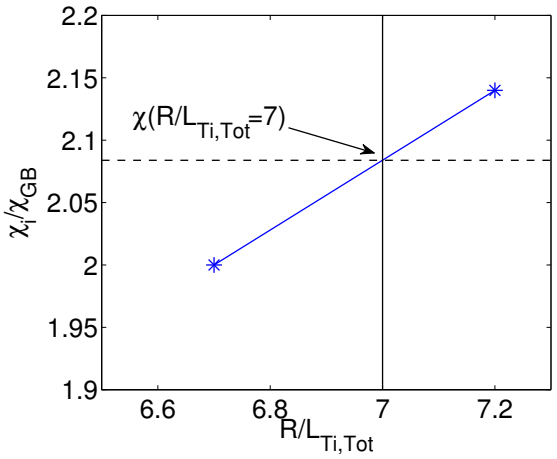

Figure 5.19: Time-averaged heat diffusivity χ_i/χ_{GB} ($\chi_{GB} = c_s\,\rho_s^2/a$) as a function of the time-averaged normalized logarithmic gradient of the total temperature obtained with GENE for $\rho^* = 1/180$. The two points corresponding to the effective gradients $\kappa_{Ti} = 6.7$ and $\kappa_{Ti} = 7.2$ have been obtained starting from equilibrium temperature gradient profiles with parameters $\kappa_{Ti} = 7.1$ and $\kappa_{Ti} = 7.5$ respectively. The value $\chi(R/L_{Ti,Tot} = 7)$ is then obtained from these two points by linear interpolation.

order to compute in a meaningful way the heat diffusivity over this ρ^* scan, *i.e.* for fixed profiles, two simulations were carried out for each ρ^* value, with respectively $\kappa_{Ti} = 7.1$ and $\kappa_{Ti} = 7.5$ for the background ion temperature profiles. The time-averaged ion heat diffusivity χ_i corresponding to the target gradient $R/L_{Ti,Tot} = 7$ is then obtained from these two points by linear interpolation. An illustration of this procedure is provided in Fig. 5.19 for $\rho^* = 1/180$. In Fig. 5.20, the resulting heat diffusivities $\chi(R/L_{Ti,Tot} = 7)$

obtained with both global-GENE and ORB5 are shown in Gyro-Bohm units ($\chi_{GB} = c_s\,\rho_s^2/a$) as a function of ρ^*, and the results are compared to a local GENE simulation. For this scan, the ratio l_x/a is kept constant and the number n_x of grid points in x is accordingly increased to keep a constant resolution $\Delta x/\rho_i = l_x/\,n_x\,\rho_i$. Thus n_x must scale as $1/\rho^*$. In addition, a hyperdiffusion $h_x = 4$ is used for stability reasons for the GENE simulation at $\rho^* = 1/560$, while $h_z = 2$ and $h_{v_\parallel} = 0.5$ are kept for all ρ^* values. We note, that the computational requirement for one simulation at $\rho^* = 1/560$ was 60 000 CPU hrs on the HPC-FF linux cluster at Jülich, Germany, and the total computational resources used for the whole ρ^* scan was of the order of 220 000 CPU hrs. Focussing first on GENE's results, one observes, as expected, that the heat diffusivity obtained with the global code converges towards the local value in the limit $\rho^* \to 0$, thus providing a further validation of the nonlinear behavior of the global code. The

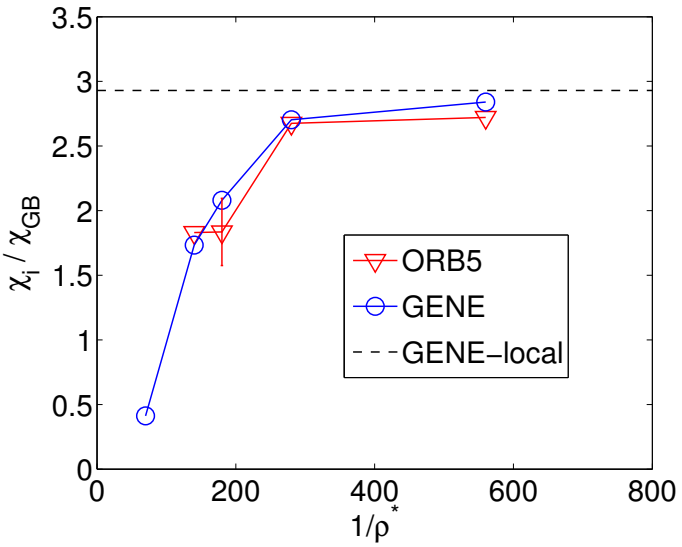

Figure 5.20: Ion heat diffusivity χ_i/χ_{GB} ($\chi_{GB} = \rho_s^2 c_s/a$) obtained with global-GENE and ORB5 as function of $1/\rho^*$. The results are compared with the corresponding local GENE simulation. The errorbar associated with the ORB5 data for $1/\rho^* = 180$ has been estimated by carrying out three simulations with different initial conditions.

relative difference between the local and global heat diffusivity is below 10% for $1/\rho^* \gtrsim 280$, such that global effects can be assumed negligible beyond this value for the present parameters. Comparing now the ORB5 and global-GENE results, we observe a similar ρ^*

dependence, as well as an excellent overall agreement, within 10%, between the two codes. An estimate of the error on χ_i has been obtained for the $1/\rho^* = 180$ case by carrying out three independent ORB5 simulations with different initial conditions, showing that the diffusivities predicted by the two codes are essentially within the error bars. The present GENE and ORB5 results can be compared with two previous ρ^* scans obtained with the global codes GTC and GYRO in Refs. [79] and [80] respectively, for similar Cyclone base case parameters. In Ref. [79], the GTC results converge towards $\chi_i/\chi_{GB} \simeq 3.4$ in the limit $1/\rho^* \to 0$, which is in relatively good agreement with the present results $\chi_i/\chi_{GB} \simeq 2.8 - 2.9$. On the other hand, global GYRO results in Ref. [80] converge towards a smaller value of $\chi_i/\chi_{GB} \simeq 1.9$ in the limit $1/\rho^* \to 0$. We note that this χ_i/χ_{GB} value obtained with GYRO is in fact very close to the flux tube results obtained when using the approximate s-α model instead of the correct circular concentric model as shown in section 4.5 and in Ref. [67]. Although not clearly stated in Refs. [79] and [80], we thus assume that the GYRO simulations had indeed been carried out with the reduced $s - \alpha$ model, while the GTC runs considered an equilibrium similar to GENE's "ad-hoc" analytical model (see Sec. 4.3).

5.7 Summary

In this chapter, extensive validation tests and benchmarks of the newly developed global-GENE version were presented. When considering linear ITG simulations with adiabatic electron response, the code has shown a correct description of the cylindrical limit, as well as excellent agreement with the GYGLES PIC code concerning the growth rate and real frequencies for the Cyclone base case parameters. The mode structures obtained with the global codes ORB5 and GENE for these parameters have also shown remarkable similarities. Using full kinetic electrons, the global code reproduces well the ITG/TEM transition with respect to local results and to the ORB5 code. Significant differences with the ORB5 results were however observed in the growth rates. This may be explained both by the electron model used in ORB5, which only treats the trapped particles kinetically, as well as by the quasi-neutrality equation in ORB5, which is only second order accurate in $k_\perp \rho_i$. Further investigations of these regimes need to be carried

out in the future. Electromagnetic effects were also addressed through a β scan, and a similar dependence of the real frequency and growth rate as compared to the local-GENE code results was observed, in particular the transition from ITG to KBM occurs at the same β value. These first electromagnetic results are very encouraging, and benchmarks with other global codes shall be carried out to further validate the code in the high β regime.

In view of the so-called Rosenbluth Hinton test, solution to the quasi-neutrality equation for the $n = 0$ component of the electrostatic potential have been compared between global-GENE and ORB5. Differences observed between the two codes have been identified to result from the approximations made in GENE on the gyro-averaging operator where the metric is linearized in the polar like (x, y, z) curvilinear coordinate system. By using the corrections proposed in section 3.3, which considers quasi-Cartesian coordinates, a very good agreement between the two codes could be reached concerning the initial, $n = 0$ component of the electrostatic potential. Unphysical growth in the time evolution of the $n = 0$ component are however observed when using this corrected gyro-averaging operator, which are not yet fully understood, and the current version of the code is therefore not using this alternative gyro-averaging scheme. The Rosenbluth-Hinton test has nonetheless shown satisfying agreement between GENE and ORB5 concerning the residual level.

Detailed comparisons of nonlinear ITG simulations with adiabatic electrons were also carried out between the two global codes. When including a Krook-type source term, a steady state is reached and agreement within 20% was obtained in the ion heat diffusivity. Analysis of the zonal flow component of the electric field has shown the presence of small avalanche like structures in both codes, as well as very similar radial profiles of the shearing rates. Finally, a ρ^* scan was carried showing again an excellent agreement between the two global code, as well as an appropriate convergence towards the flux tube results in the limit $\rho^* \to 0$. This scan also showed that global effects are essentially negligible for machines with $1/\rho^* > 280$ for Cyclone base case like parameters and considering flat gradient profiles. These results can finally shed light on previous disagreements between the global gyrokinetic codes GTC and GYRO concerning a similar ρ^* scan.

Although some further tests may be required, in particular when using kinetic electrons, these different benchmarks and validations have shown that the global version of GENE

behaves as expected in both linear and nonlinear regimes and is now ready for investigating physical effects beyond the usual parameters. In particular, the global code is appropriate to investigate microturbulence in small to moderate machines ($1/\rho^* \lesssim 280$), such as the TCV or DIII-D Tokamaks, or for transport barriers, where gradient profiles may vary over a few Larmor radii only.

6 Shaping effects on ITG turbulence

The influence of flux surface shaping on plasma stability and confinement has been investigated in many experimental Tokamaks, such as TCV, DIII-D or JET, and is recognized as a key element in fusion research. A well known and documented favorable effect is the stabilizing influence of elongation on MHD modes, allowing to operate at higher plasma current (at fixed safety factor) which in turn increases the maximum achievable β according to the Troyon scaling. Concerning the influence of triangularity, some experiments in the Tokamak à Configuration Variable (TCV), which was specially designed for investigating such shaping effects, have shown an increased electron confinement time when going from positive to negative triangularity [33].

In order to fully understand how shaping could lead to better confinement, it is of particular interest to investigate its influence on microturbulence, and several studies have so far addressed this issue by means of gyrokinetic simulations. Results in [81, 82, 65, 83, 84] suggested a stabilizing effect of elongation on ITG modes and Trapped Electron Modes and a smaller effect of triangularity. In [85], a specific study was carried out concerning the effect of triangularity on TEM in the TCV experiment.

In the present chapter, the effects of elongation and triangularity on ITG modes are interpreted in terms of their influence on the effective temperature gradient, in line with results published in [84] which were however only considering the effect of elongation. In a first section, the methodology of the geometry scan is described and, in particular, the question of which physical quantities shall remain constant while modifying the plasma shape is addressed. In a second section, linear simulation results are presented for different plasma shapes, which are then compared in a third section with results obtained using a local dispersion relation. Finally, the influence of shaping is investigated by means of nonlinear simulations.

6.1 Methodology and parameter choice

In order to investigate the influence of shaping on microturbulence, a series of equilibria are computed with the MHD equilibrium code CHEASE [36] by prescribing different analytical geometry for the last closed flux surface, defined by the functional form:

$$R = R_0 + a\,\cos(\theta + \delta\,\cos\theta) \tag{6.1}$$

$$Z = a\,\kappa\,\sin(\theta) \tag{6.2}$$

where θ is the geometrical poloidal angle, a the minor radius, R_0 the major radius, κ the elongation and δ the triangularity. As a starting point, one considers the same plasma equilibrium as in section 4.5, *i.e.* with a circular cross section ($\kappa = 1, \delta = 0$) and with pressure and current profiles such that the safety factor and shear are respectively $q_0 = 1.4$ and $\hat{s} = (\rho_t/q)dq/d\rho_t = 0.8$ at position $\rho_t = 0.5$. The flux surface label is here $\rho_t = \sqrt{\Phi_t/\Phi_{t,\mathrm{edge}}}$, where Φ_t is the toroidal flux, and the inverse aspect ratio is $a/R_0 = 0.36$. From this initial equilibrium, which essentially matches the Cyclone test case parameters [68], a set of equilibria are computed by increasing the elongation κ of the last closed flux surface up to $\kappa = 1.75$ while keeping the minor radius on the equatorial mid-plane constant. A scan in the triangularity δ, at constant $\kappa = 1.75$ is then considered covering both positive and negative values of δ, see Fig. 6.1. We note that the DIII-D shot from which the Cyclone test case was derived has an elongation $\kappa = 1.75$ and a triangularity $\delta = 0.3$. For each of these equilibria the pressure and current profiles are adjusted so as to keep the safety factor q_0 and shear $\hat{s}$ constant at the position $\rho_t = 0.5$ where the flux tube simulations are carried out. The elongations and triangularities have been specified for the last closed flux surface (LCFS), the corresponding values at $\rho_t = 0.5$ are reported in tables 6.1 and 6.2 and will be used in the following to characterize the different equilibria. In addition, when considering the triangularity scan, the Shafranov shift of the considered flux surface changes for the different equilibria, the resulting local aspect ratio $\varepsilon = (R_{max} - R_{min})/(R_{max} + R_{min})$ at $\rho_t = 0.5$ is thus not exactly constant and varies from $\varepsilon = 0.188$ for $\delta = -0.6$ to $\varepsilon = 0.202$ for $\delta = 0.6$, i.e. a relative variation of 7%.

The present study focuses on the effect of shaping on Ion Temperature Gradient (ITG)

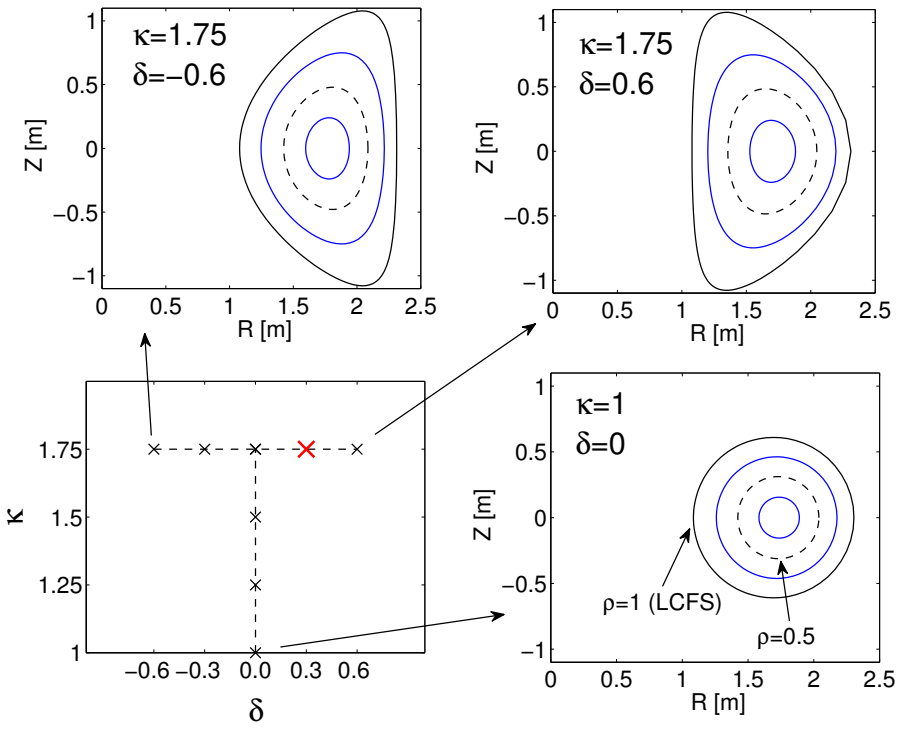

Figure 6.1: Elongations and triangularities of the last flux surface considered for the scan, as well as poloidal cross section of the MHD equilibria at limiting values of this scan. The actual parameters of the DIII-D shot from which the Cyclone test case was inspired is pointed out with a red cross.

Table 6.1: Elongation scan, at constant triangularity $\delta_{LCFS} = 0$

κ_{LCFS}	1.0	1.25	1.5	1.75
κ, δ at $\rho = 0.5$	$1.01, 0.0$	$1.19, 0.0$	$1.35, 0.0$	$1.52, 0.0$

Table 6.2: Triangularity scan, at constant elongation κ_{LCFS}=1.75

δ_{LCFS}	-0.6	-0.3	0.0	0.3	0.6
κ, δ at $\rho = 0.5$	$1.45, -0.16$	$1.51, -0.091$	$1.52, 0.00$	$1.48, 0.086$	$1.41, 0.16$

instabilities, and a flat density profile is considered together with adiabatic electrons so as to restrain the number of physical parameters which may vary. Concerning the ion temperature profile, the question may be raised as to what should be kept constant when going from a circular equilibrium to a shaped equilibrium. Indeed for an equilibrium with circular concentric flux surfaces, the temperature gradient $|\vec{\nabla}T|$ is a flux function, i.e. it only depends on the radial position, Ψ, whereas in a non-circular equilibrium it becomes a functions of both the poloidal flux Ψ and the straight field line poloidal angle χ. When changing the geometry of the flux surfaces, one could thus either keep $|\vec{\nabla}T|$ constant at a given χ position, e.g. $\chi = 0$, or some flux-surface averaged gradient $\langle\, |\vec{\nabla}T| \,\rangle$. In order to allow for different interpretations, simulations are carried out for different temperature gradient values for each considered equilibrium.

6.2 Influence of elongation and triangularity in terms of the effective gradient

The results presented in this section are obtained with the flux tube version of the GENE code considering the above mentioned physical parameters. For each equilibrium a scan in the temperature gradient parameter $\hat{\omega}_{Ti} = L_{\text{ref}}\ d\ln T_i/dx$, see Eq. (2.135), is carried out. It is then interpreted in terms of the temperature gradient on the low field side of the equatorial midplane (*i.e.* $\chi = 0$, noted $R/L_{Ti}(0)$):

$$\frac{R}{L_{Ti}}(0) \equiv R\left|\vec{\nabla}[\ln T_i](\chi=0)\right| = R\left|\vec{\nabla}x(\chi=0)\right|\ \left|\frac{d\ln T_i}{dx}\right| = \hat{\omega}_{Ti}\ \left|\vec{\nabla}x(\chi=0)\right|\ , \quad (6.3)$$

or in terms of the flux-surface averaged gradient, noted $\langle R/L_{Ti}\rangle$:

$$\left\langle\frac{R}{L_{Ti}}\right\rangle \equiv R\left\langle\left|\vec{\nabla}[\ln T_i](\chi)\right|\right\rangle = R\left\langle\left|\vec{\nabla}x(\chi)\right|\right\rangle\ \left|\frac{d\ln T_i}{dx}\right| = \hat{\omega}_{Ti}\ \left\langle\left|\vec{\nabla}x(\chi)\right|\right\rangle \quad (6.4)$$

which can be viewed as an effective spatial gradient. Note that the reference length is chosen here as $L_{\text{ref}} = R$ where $R = R_0$ is the major radius. In the above relations the flux-surface average is defined as:

$$\langle A\rangle = \frac{\int_{\Delta V} A\ d^3x}{\int_{\Delta V}\ d^3x}\ , \quad (6.5)$$

where ΔV is the volume between two magnetic surfaces.

In order to study the effect of shaping on the stability properties of ITG modes, linear spectra are computed for $k_y\,\rho_s$ values in the range $k_y\rho_s = [0.1 - 0.8]$ so as to determine the most unstable mode for each considered MHD equilibrium and ion temperature gradient. In Fig. 6.2 the maximum linear growth rates $\gamma_{\max} = \max_{k_y}[\gamma(k_y)]$ for the different

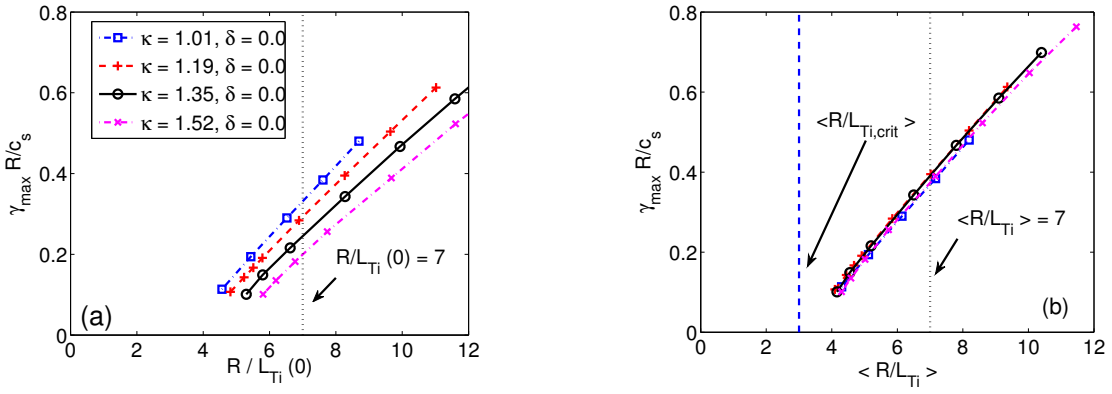

Figure 6.2: Elongation scan: Linear growth rate of the most unstable mode as a function of (a) the temperature gradient at $\chi = 0$, $R/L_{Ti}(0)$, and (b) the flux-surface averaged gradient $\langle R/L_{Ti}\rangle$, for different elongations at constant triangularity.

equilibria corresponding to the elongation scan of Table 6.1 are shown as a function of the temperature gradient at $\chi = 0$ and as a function of the flux-surface average gradient for the elongation scan. In addition, the particular gradient $R/L_{Ti}(0) = 7$ on the equatorial midplane, as well as the flux-surface averaged gradient $\langle R/L_{Ti}\rangle = 7$ have been pointed out, and the corresponding growth rates as a function of elongation are plotted in Fig. 6.3.a.

When first considering the growth rates as a function of the temperature gradient at $\chi = 0$, $R/L_{Ti}(0)$, an effect of the elongation on the ITG modes is observed, namely the growth rate decreases with increasing elongation at fixed $R/L_{Ti}(0)$, see Figs. 6.2.a and 6.3.a. We note that since the different equilibria have been computed with fixed minor radius on the equatorial midplane, changing the shape of the flux surfaces at constant $R/L_{Ti}(0)$ can thus be interpreted as keeping a constant temperature difference between the center and the edge of the plasma. Assuming that the linear growth rates may provide an estimate of nonlinear turbulent fluxes (through mixing length estimate), results in Figs. 6.2, thus

show a favorable effect of elongation for fusion plasmas, in line with [86, 83], since a similar inner and outer temperature difference would lead to a lower level of turbulent fluxes in a more elongated plasma. This last affirmation will be further discussed in a later section by carrying out nonlinear simulations.

Coming back to the comparison of linear growth rates, it is clearly shown in Fig. 6.2.b that the $\gamma_{\max}$ curves corresponding to the different elongation values essentially align on each other when represented as a function of the flux-surface average gradient $\langle R/L_{Ti} \rangle$. The same result can be seen in Fig. 6.3.a where $\gamma_{\max}$ becomes independent of κ at constant $\langle R/L_{Ti} \rangle$. For a given temperature profile $T_i(\Psi)$, the ITG mode therefore seems to "feel" an effective temperature gradient which results from the relative stretching and compression of neighboring magnetic surfaces when deforming the magnetic geometry, see Fig.6.1. This interpretation in terms of an effective gradient is supported by the observation that the ITG mode has non-zero extension in the parallel direction to the magnetic field $z = \chi$, and is in agreement with similar results in [84] obtained with the global code ORB5. From Fig. 6.2.b one notes that a unique effective linear critical gradient can be obtained with $\langle R/L_{Ti} \rangle_{l,crit} = 3.1$, valid for all elongations.

In a similar way as for the elongation scan, a comparison of the maximum linear growth

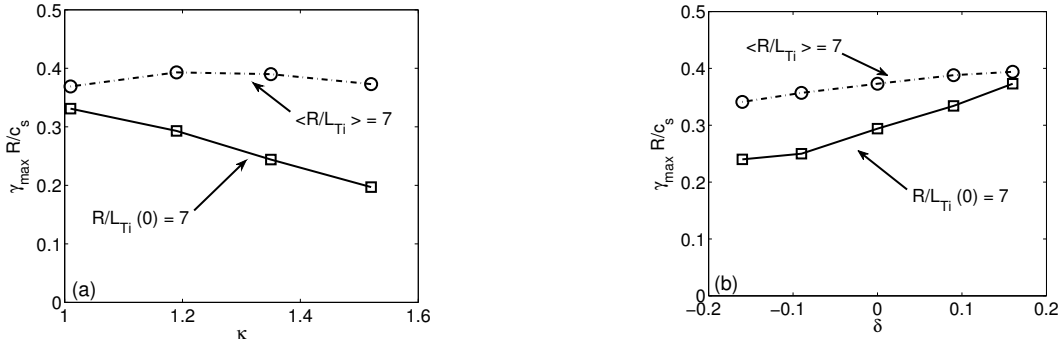

Figure 6.3: Maximum linear growth rate as a function of (a) the elongation, or (b) the triangularity, at constant temperature gradient $R/L_{Ti}(0) = 7$ on the equatorial midplane (squares) or constant flux surface averaged gradient $\langle R/L_{Ti} \rangle = 7$ (circles).

rates for the triangularity scan of Table 6.2 are shown in Fig. 6.4. One observes that the maximum growth rate is reduced when going from positive to negative triangularity at constant $R/L_{Ti}(0)$, see Figs. 6.4.a and 6.3.b. This can be interpreted as a favorable

effect of negative triangularity, as in [85]. When representing γ_{max} as a function of the flux surface average temperature gradient the different curves get closer to each other, see Fig. 6.4.b, showing that the modification of the effective gradient can partially account for the effect of triangularity. This can be further confirmed by noticing in Fig. 6.3.b that the dependence of γ_{max} with respect to triangularity is much reduced when considered at constant $\langle R/L_{Ti} \rangle$ instead of constant $R/L_{Ti}(0)$. Although the alignment of the different γ_{max} is not as good as for the elongation scan, one can still extract from Fig. 6.4.b an approximate linear critical gradient, which is approximately $\langle R/L_{Ti} \rangle_{l,crit} = 3.1 \pm 0.3$. Note that contrary to the elongation scan the local aspect ratio at $\rho_t = 0.5$ varies for the different triangularities, see discussion in section 6.1, which may partly explain why the superposition of the curves in Fig. 6.4.b is not as good as in Fig. 6.2.

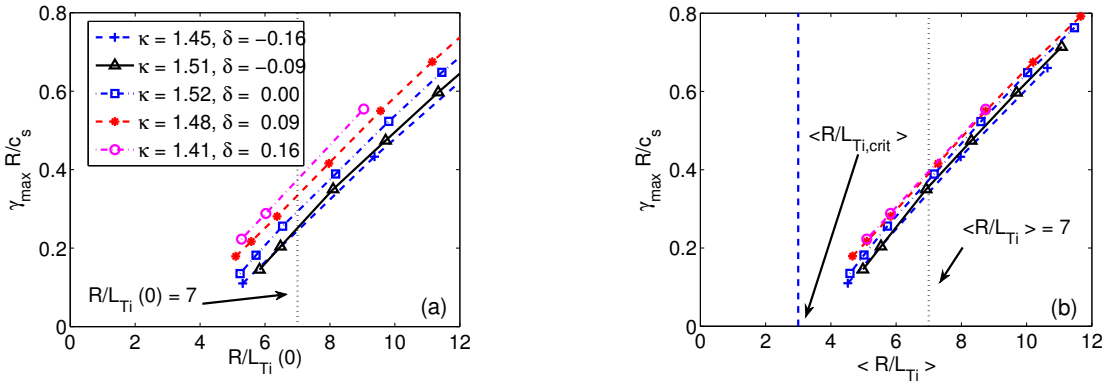

Figure 6.4: Triangularity scan: Linear growth rate of the most unstable mode as a function of (a) the temperature gradient $R/L_{Ti}(0)$ on the equatorial midplane and (b) the flux surface averaged gradient $\langle R/L_{Ti} \rangle$ for different triangularities at essentially constant elongation.

6.3 Comparison with a local dispersion relation

In the previous section it was shown that the variations of the effective flux- surface averaged gradient appears as a good parameter to account for the effects of elongation and, to a lesser extent, of triangularity on linear ITG modes. However, considering that the ITG mode in toroidal geometry is in fact an interchange-type instability, resulting from the combination of the temperature and, magnetic field curvature and gradient, the

interpretation in terms of a unique parameter is not straightforward. One would rather expect a combined effect of (1) the temperature gradient and (2) the curvature driving terms in (Eq. 2.135):

$$(1) \;\rightarrow\; \frac{1}{\hat{\mathcal{C}}}\left[\hat{\omega}_{Tj}\left(\frac{\hat{v}_{\|j}^2+\hat{\mu}_j\hat{B}_0}{\tau_{0j}}-\frac{3}{2}\right)\right]\hat{f}_{0j}\partial_{\hat{y}}\hat{\bar{\phi}}_1\,,$$

$$(2) \;\rightarrow\; \left[\frac{\hat{T}_{0j}(x_0)}{Z_j}\frac{2\,\hat{v}_{\|j}^2+\hat{\mu}_j\hat{B}_0}{\hat{B}_0}\hat{K}_y\right]\hat{\Gamma}_{j,y}\,,$$

where the terms have been expressed in the electrostatic limit and assuming $\hat{\omega}_{nj}=0$. In addition, only the $\hat{K}_y$ contribution from the curvature term is shown since the $k_x=0$ mode is the most unstable mode and is thus the only one considered here. We note that in the two terms described above the coefficients $\hat{K}_y/\hat{B}_0$ and $\hat{\omega}_{Tj}$ are modified when changing the elongation or the temperature gradient. In addition, the coefficient $\hat{\mathcal{C}}=q_0/(B_0\,r_0)\,d\Psi/dx$, with $x=a\,\rho_t$ in general varies when changing the equilibrium at the considered ρ_t position.

6.3.1 A local dispersion relation for toroidal-ITG modes

In order to obtain a better insight into how both the temperature and curvature gradient terms influence the ITG instability, we shall consider a simple local dispersion relation. This kinetic model, which is derived in Appendix B, is similar to the one described in Chap. 8 of Ref. [87] and considers a slab geometry where the the effect of curvature and gradient of the magnetic field is introduced through an external force (assuming a low pressure plasma):

$$\vec{F}=-m\left(\frac{v_\perp^2}{2}+v_\|^2\right)\vec{\nabla}\ln B\,. \tag{6.6}$$

For the local dispersion relation obtained from this model to ultimately account for geometrical effects, the terms related to the curvature and gradient will be replaced by some effective values taking into account the parameters $\hat{\mathcal{C}}$, $\hat{K}_y/\hat{B}_0$ and $\hat{\omega}_{Tj}$ which were introduced previously.

Let $(\vec{e}_x,\vec{e}_y,\vec{e}_z)$ be a orthonormal local Cartesian coordinate system with $\vec{e}_z\|\vec{B}$. A temperature gradient is assumed in the x-direction, opposite to the force $\vec{F}$, while the density n is assumed to be flat, see Fig. 6.5.

Considering only electrostatic perturbation, a solution of the linearized Vlasov equation is obtained for the amplitude of the perturbed distribution function $\delta\hat{f}$ by integrating along

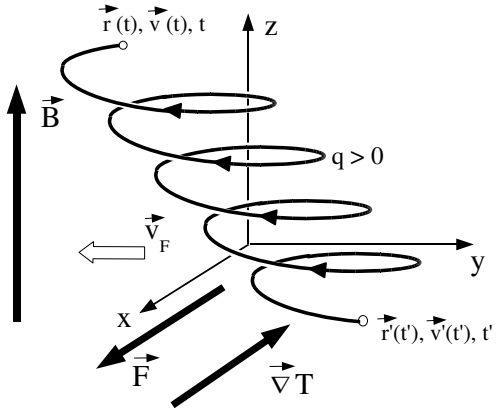

Figure 6.5: Particle trajectories in the local $(\vec{e}_x, \vec{e}_y, \vec{e}_z)$ orthogonal Cartesian coordinate system.

the particle trajectories, see Appendix B for more details. The resulting relation between $\delta\hat{f}$ and the electrostatic potential fluctuation amplitude $\delta\hat{\Phi}$ is then used together with the quasi-neutrality equation leading to the following dispersion relation:

$$\frac{1}{Z_i\,\tau} + 1 - \int d\vec{v}\,(\omega_{Ti} - \omega)\,\frac{f_{0i}}{n_{0i}}\,\frac{J_0^2(\frac{k_y v_\perp}{\Omega_i})}{\omega_{Fi} - \omega} = 0\,, \tag{6.7}$$

where ω and k_y are respectively the frequency and y-mode number of the perturbation, $\tau = T_e/T_i$ and $Z_i = q_i/e$. Note that an adiabatic electron response is assumed to derive Eq. 6.7 and the approximations $\omega << \Omega$ and $k_z \to 0$ are in addition considered. The drift frequencies related to the ion temperature gradient and magnetic field gradient are respectively given by:

$$\omega_{Ti} = \vec{v}_{\nabla p}\cdot\vec{k} = \frac{(-\vec{\nabla}T_i)\times\vec{B}}{q_i\,B^2}\,\mathcal{E}\cdot\vec{k}\,, \tag{6.8}$$

$$\omega_{Fi} = \vec{v}_{Fi}\cdot\vec{k} = -\frac{m_i}{q_i\,B^2}\left(\frac{v_\perp^2}{2} + v_\parallel^2\right)\vec{\nabla}\ln B\times\vec{B}\cdot\vec{k}\ \ , \tag{6.9}$$

having defined $\mathcal{E}(v) = K(v)/T - 3/2$.

6.3.2 Introducing geometrical coefficients in the local dispersion relation

In order to introduce the effects of shaping in the dispersion relation (6.7) the term ω_{Ti} is now replaced by the corresponding expression computed in the toroidal geometry and

considering the field aligned coordinate system (x, y, z), as defined in Chapter 2:

$$\begin{aligned}\omega_{Ti} &= \frac{T_i}{q_i}\,\vec{k}\cdot\frac{(-\vec{\nabla}\ln T_i)\times\vec{B}}{B^2}\,\mathcal{E} \\ &= \frac{T_i}{q_i}\,\frac{k_y\,\vec{\nabla}y\cdot\mathcal{C}\,(\vec{\nabla}x\times\vec{\nabla}y)\times\vec{\nabla}x}{\mathcal{C}^2\,(\vec{\nabla}x\times\vec{\nabla}y)^2}\,\frac{d\ln T_i}{dx}\,\mathcal{E} \\ &= \frac{T_i}{q\,\mathcal{C}}\frac{d\ln T_i}{dx}\,\mathcal{E}\,k_y\,, \end{aligned} \tag{6.10}$$

having used $\vec{k}\simeq k_y\,\vec{\nabla}y$ (i.e. neglecting the radial component $k_x\,\vec{\nabla}x$ of the wave vector) and $\vec{B}=\mathcal{C}\,(\vec{\nabla}x\times\vec{\nabla}y)$. Similarly the term ω_{Fi} related to the curvature and gradient of the magnetic field reads:

$$\begin{aligned}\omega_{Fi} &= -\frac{m_i}{q_i\,B^2}\left(\frac{v_\perp^2}{2}+v_\parallel^2\right)\vec{\nabla}\ln B\times\vec{B}\cdot\vec{k} \\ &= \frac{m_i}{q_i\,B^3}\left(\frac{v_\perp^2}{2}+v_\parallel^2\right)\mathcal{C}\,(\vec{\nabla}x\times\vec{\nabla}y)\times\left(\frac{\partial B}{\partial x}\vec{\nabla}x+\frac{\partial B}{\partial z}\vec{\nabla}z\right)\cdot\vec{k}_y\,\vec{\nabla}y \\ &= \frac{m_i}{q_i\,B}\left(\frac{v_\perp^2}{2}+v_\parallel^2\right)\mathcal{K}_y\,k_y\,, \end{aligned} \tag{6.11}$$

where the curvature coefficient $\mathcal{K}_y$ is defined according to equation (2.63). We first note that the x variations of the different equilibrium quantities are not retained here since we are only interested in perturbations local to the $x=0$ surface. Furthermore, in order to introduce in a consistent manner these expressions for ω_{Ti} and ω_{Fi} in the local dispersion equation (6.7) they both need to be independent of z. The temperature gradient drift frequency in Eq. (6.10) is already z independent, while the curvature drift frequency as defined in Eq. (6.11) is a function of z, through the geometrical coefficient $\mathcal{K}_y$ and the magnetic field B. The drift frequency ω_{Fi} needs therefore to be replace by some effective coefficient $<\omega_{Fi}>$ which does not depend on z. Recalling again that the toroidal ITG mode is an interchange-type mode which is unstable when the temperature and magnetic field gradients are in the same direction, we propose to use as effective coefficient $<\omega_{Fi}>$ the ponderate flux-surface averaged of ω_{Fi}:

$$<\omega_{Fi}>=\frac{\int_0^2\,\pi\omega_{Fi}(z)\,h(z)\,J(z)\,dz}{\int_0^2\,\pi\,h(z)\,J(z)\,dz} \tag{6.12}$$

where J is the Jacobian where $h(z)$ is chosen as box shaped function which is equal to one when $\omega_{Fi}<0$ (i.e. $\vec{\nabla}T_i$ and $\vec{\nabla}B$ in the same direction), and zero otherwise. The choice of

the effective coefficient is of course not unique, and one could have used for instance the local value at $z = 0$ (low field side) instead, $< \omega_{Fi} >= \omega_{Fi}(0)$. The approach retained here however tries to captured part of the effects related with the variations of the geometrical coefficients along the filed line.

Using these relations for ω_{Ti} and $< \omega_{Fi} >$, the dispersion relation reads:

$$\frac{1}{Z_i\,\tau} + 1 - \int\; d\;v\; \left(\frac{T_i}{q_i\,\mathcal{C}} \frac{d\ln T_i}{dx}\,\mathcal{E}\,k_y - \omega \right) \frac{f_{0i}}{n_{0i}} \frac{J_0^2(\frac{k_y v_\perp}{\Omega_i})}{\frac{m_i}{q_i}\left(\frac{v_\perp^2}{2} + v_\parallel^2\right)\left\langle \frac{\mathcal{K}_y}{B} \right\rangle\; k_y - \omega} = 0\;. \quad (6.13)$$

Introducing now the normalized quantities $\hat{\mathcal{K}_y} = L_{\rm ref}\,\mathcal{K}_y$, $\hat{\mathcal{C}} = \mathcal{C}/B_{\rm ref}$, $\hat{k}_y = k_y\,\rho_i$ and the two normalized driving parameters:

$$\hat{D}_T = -\frac{L_{\rm ref}}{\hat{\mathcal{C}}}\frac{d\ln T_i}{dx} \quad \text{and} \quad \hat{D}_c = \left\langle -\frac{\hat{\mathcal{K}_y}}{\hat{B}} \right\rangle\;, \quad (6.14)$$

where the minus sign are used so that $\hat{D}_T$ and $\hat{D}_c$ are positive coefficients, one can write:

$$\frac{1}{Z_i\,\tau} + 1 - \int\; d\vec{v}\; \left(\frac{c_i}{L_{\rm ref}} \hat{D}_T\,\mathcal{E}\,\hat{k}_y + \omega \right) \frac{f_{0i}}{n_{0i}} \frac{J_0^2(\frac{k_y v_\perp}{\Omega})}{\frac{1}{c_i^2}\left(\frac{v_\perp^2}{2} + v_\parallel^2\right)\frac{c_i}{L_{\rm ref}}\,\hat{D}_c\,\hat{k}_y + \omega} = 0\;. \quad (6.15)$$

By multiplying the numerator and denominator in the integral by $(c_i/L_{\rm ref}\,\hat{D}_c)^{-1}$ one finally obtains:

$$\frac{1}{Z_i\,\tau} + 1 - \int\; d\vec{\hat{v}}\; c_i^3\; \left(p\,\mathcal{E}\,\hat{k}_y + \hat{\omega} \right) \frac{f_{0i}}{n_{0i}} \frac{J_0^2(\hat{k}_y\,\hat{v}_\perp)}{\left(\frac{\hat{v}_\perp^2}{2} + \hat{v}_\parallel^2\right)\hat{k}_y + \hat{\omega}} = 0\;. \quad (6.16)$$

where $\hat{\omega} = \omega\,L_{\rm ref}/(c_i\hat{D}_c)$, $\hat{v} = v/c_i$ and having defined the effective parameter $p = \hat{D}_T/\hat{D}_c$. One note that in the circular concentric flux surfaces geometry case, and if one replaces the effective drift frequency $< \omega_{Fi} >$ by its local value $\omega_{Fi}(z = 0)$ the parameter p simply reduces to $p = -R\,d\ln T/dr = -R/L_T$, where R is the major radius.

Assuming $Z_i = 1$ and $\tau = 1$, one can solve equation (6.16) for $\hat{\omega}(\hat{k}_y)$ and for different values of the parameter p. A Matlab code is used to numerically integrate and solve Eq. (6.16) for the complex solution $\hat{\omega} = \hat{\omega}_r + i\,\hat{\gamma}$. A scan in the parameter p is carried out and for each value of p the dispersion relation is solved for different values of $\hat{k}_y$. The resulting growth rate of the most unstable $\hat{k}_y$ mode is shown as a function of p in Fig. 6.6. Using a second order polynomial fit, the normalized maximal growth rate $\hat{\gamma}$ can then be

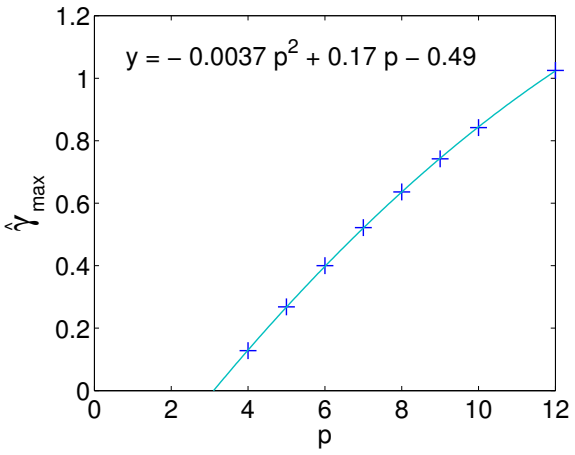

Figure 6.6: Growth rate of the most unstable ITG mode $\hat{\gamma} = \gamma\, L_{\rm ref}/(c_i \hat{D}_c)$ as function of the parameter $p = \hat{D}_T/\hat{D}_c$, computed using the local dispersion relation (6.16).

expressed as a function of the parameter p:

$$\hat{\gamma} = -0.0037\, p^2 + 0.17\, p - 0.49\ . \tag{6.17}$$

One then finally obtains a relation for $\gamma\, L_{\rm ref}/c_i$ as a function of $\hat{D}_T$ and $\hat{D}_c$, by multiplying (6.17) by $\hat{D}_c$:

$$\gamma \frac{L_{\rm ref}}{c_i} = -0.0037\, \frac{\hat{D}_T^2}{\hat{D}_c} + 0.17\, \hat{D}_T - 0.49\, \hat{D}_c\,. \tag{6.18}$$

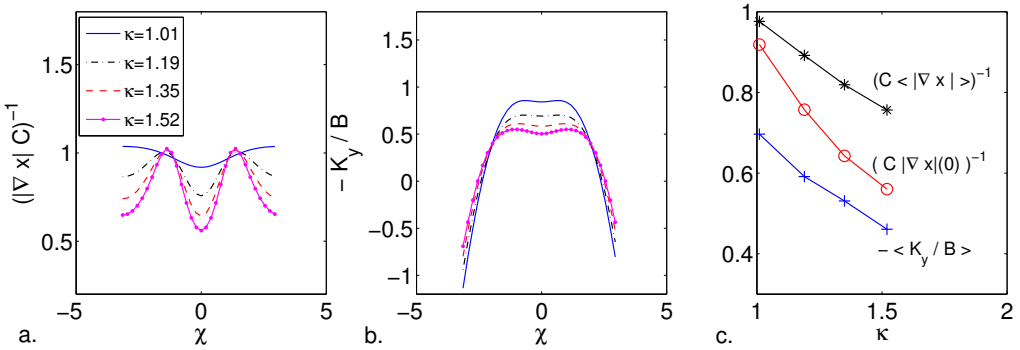

Figure 6.7: Elongation scan: Geometrical coefficients $\hat{\mathcal{C}}|\vec{\nabla}x|$ and $-\hat{\mathcal{K}}_y/\hat{B}$ as a function of the straight field line poloidal angle χ (a-b), and effective coefficients $\langle\hat{\mathcal{C}}|\vec{\nabla}x|\rangle$, $\hat{\mathcal{C}}|\vec{\nabla}x|(0)$ and $-\langle\hat{\mathcal{K}}_y/\hat{B}\rangle$ as a function of elongation κ.

In order to interpret the influence of shaping in terms of the effective driving terms,

the coefficients $\hat{D}_T$ and $\hat{D}_C$ can be replaced in equation (6.18) by their numerical values obtained for the different equilibrium scans and considering either a constant temperature gradient on the equatorial midplane, at $\chi = 0$:

$$\hat{D}_T = \frac{R}{L_{T_i}(0)} \; \frac{1}{\hat{\mathcal{C}}\,|\vec{\nabla}x(0)|} \; , \tag{6.19}$$

or a constant flux-surface averaged gradient:

$$\hat{D}_T = \left\langle \frac{R}{L_{T_i}} \right\rangle \; \frac{1}{\hat{\mathcal{C}}\,\langle|\vec{\nabla}x|\rangle} \; , \tag{6.20}$$

where one sets $L_{\rm ref} = R$, and having used relations (6.3) and (6.4) for expressing $d\ln T_i/dx$ in terms of $R/L_{Ti}(0)$ and $\langle R/L_{Ti}\rangle$ respectively.

Considering first the elongation scan, the geometrical coefficients $\hat{\mathcal{C}}|\vec{\nabla}x|$ and $\hat{\mathcal{K}}_y/\hat{B}$ are

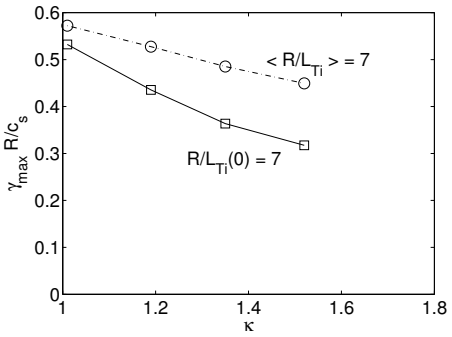

Figure 6.8: Linear growth rates obtained by replacing $\hat{D}_T$ and $\hat{D}_c$ in the local dispersion relation (6.18) as a function of κ, considering a constant $R/L_{Ti}(0) = 7$ (squares) or $\langle R/L_{Ti}\rangle = 7$ (circles).

shown as a function of the straight field line poloidal angle χ in Figs. 6.7.a and b. The effective coefficients $\langle\hat{\mathcal{C}}|\vec{\nabla}x|\rangle$, $\hat{\mathcal{C}}|\vec{\nabla}x|(0)$ and $\langle\hat{\mathcal{K}}_y/\hat{B}\rangle$ as a function of the elongation κ are shown in Fig. 6.7.c. The linear growth rates obtained by replacing $\hat{D}_T$ and $\hat{D}_c$ in relation (6.18) for the different elongations are shown in Fig. 6.8. The results obtained with this simplified model are in relatively good qualitative and semi-quantitative agreement with GENE's computations shown in Fig. 6.3.a. Indeed, when considering a constant $R/L_{Ti}(0)$, a reduction of the growth rate with increasing elongation is observed, whereas this dependence is reduced when considering a constant $\langle R/L_{Ti}\rangle$. The growth rate for $\langle R/L_{Ti}\rangle = 7$ is in addition found around $\gamma R/c_s = 0.5$ for the reduced model, while a

comparable value $\gamma R/c_s = 0.4$ is obtained with GENE.

These results can therefore provide useful information toward shedding light on the observations from the previous section, where it was shown that the dependence of the linear ITG growth rate with respect to elongation can be removed when keeping a constant flux-surface average temperature gradient. The present study indeed suggests that when changing the elongation at constant $\langle R/L_{Ti}\rangle$, the value chosen for $L_{\mathrm{ref}} d\ln T_i/dx$ is such that the contributions from the effective temperature and curvature drives, $\hat{D}_T$ and $\hat{D}_c$, tend to compensate each other.

A similar analysis is also carried out for the triangularity scan. The corresponding geo-

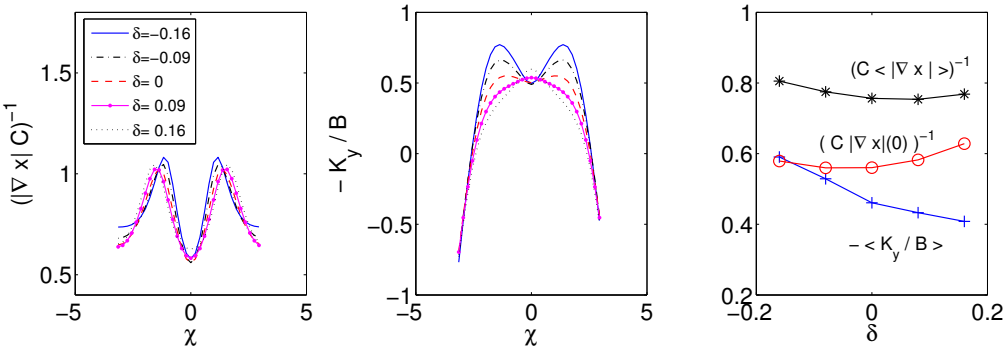

Figure 6.9: Triangularity scan: Geometrical coefficients $\hat{\mathcal{C}}|\vec{\nabla}x|$ and $\hat{\mathcal{K}}_y/\hat{B}$ as a function of the straight field line poloidal angle χ (a-b), and effective coefficients $\langle\hat{\mathcal{C}}|\vec{\nabla}x|\rangle$, $\hat{\mathcal{C}}|\vec{\nabla}x|(0)$ and $\langle\hat{\mathcal{K}}_y/\hat{B}\rangle$ as a function of the triangularity δ.

metrical coefficients and effective coefficients are shown in Fig. 6.9, and the linear growth rates obtained by replacing the effective drives $\hat{D}_T$, $\hat{D}_c$ in the local dispersion relation (6.18) are shown in Fig. 6.10. When considering a constant $R/L_{Ti}(0)$ the growth rate of the ITG mode is shown to decrease when going from positive to negative triangularity, in good agreement with GENE's linear simulations in Fig 6.3. The present results also confirm that for a constant $\langle R/L_{Ti}\rangle$ the driving coefficients, $\hat{D}_T$ and $\hat{D}_c$, tend to compensate each other, although the difference between the two curves in Fig. 6.10 is not as clear as for the elongation case.

When comparing the different driving coefficients $-\hat{\mathcal{K}}_y/B$ related to the magnetic field gradient, one notices that in the case of the elongation scan they have a similar χ dependence, see Fig. 6.7, and only vary in amplitude, whereas a different χ dependence is

observed when changing the triangularity, Fig. 6.9. Indeed, for all κ values at constant $\delta = 0$, the coefficients $-\hat{\mathcal{K}}_y/B$ present a local minimum at $\chi = 0$ and two maxima around $\pi/2$ and $-\pi/2$. On the other hand, considering the triangularity scan, a similar χ dependence with one local minimum and two maxima is observed for $\delta \leq 0$ whereas the $\delta > 0$ cases present a global maximum at $\chi = 0$. When introducing the effective coefficient $< \omega_F >$, the information on these different χ dependencies is lost, which could explain why an interpretation in terms off effective drives is less accurate for the triangularity scan, and could also account for the differences in Fig. 6.3.b where the linear growth rates do not perfectly align when considering a constant $\langle R/L_{Ti} \rangle$.

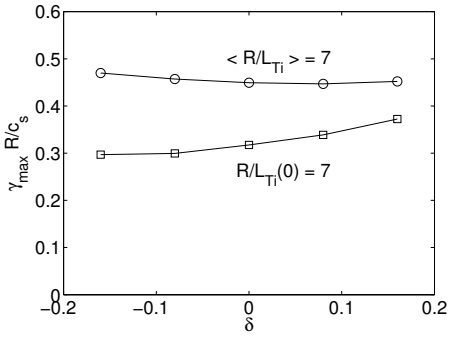

Figure 6.10: Linear growth rates obtained by replacing $\hat{D}_T$ and $\hat{D}_c$ in the local dispersion relation (6.18) as a function of the triangularity δ considering a constant $R/L_{Ti}(0) = 7$ (squares) or $\langle R/L_{Ti} \rangle = 7$ (circles).

6.4 Nonlinear results

Considering first the circular equilibrium ($\kappa = 1.01, \delta = 0$) as well as the most elongated equilibrium ($\kappa = 1.52, \delta = 0$), nonlinear simulations are carried out and the resulting electrostatic heat fluxes are shown in Fig. 6.11 as a function of $R/L_{Ti}(0)$ or $\langle R/L_{Ti} \rangle$. For these nonlinear simulations, which have physical parameters close to the standard Cyclone base case, the simulation domain is $l_x \times l_y \times l_z \times l_{v_\parallel} \times l_\mu = 110\,\rho_s \times 90\,\rho_s \times 2\,\pi \times 3\,v_{th,i} \times 9\,T_i/B_{\text{ref}}$ and the grid resolution $n_x \times n_y \times n_z \times n_{v_\parallel} \times n_\mu = 128 \times 48 \times 32 \times 32 \times 8$.

As expected from the linear simulations, we first notice that for a constant $R/L_{Ti}(0)$ the turbulent heat flux is significantly decreased when increasing the elongation. This

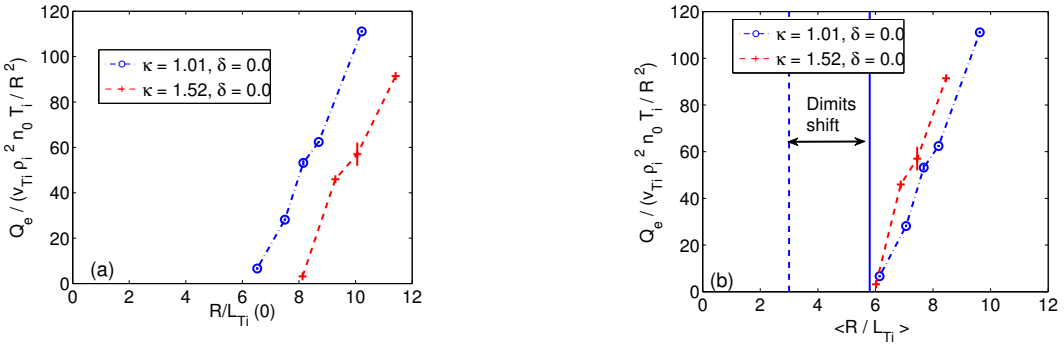

Figure 6.11: Elongation scan : Nonlinear electrostatic heat flux as a function of (a) the temperature gradient at $\chi = 0$, $R/L_{Ti}(0)$, and (b) flux-surface averaged gradient, $\langle R/L_{Ti} \rangle$ for the two equilibria with elongations $\kappa = 1$ and $\kappa = 1.52$ at constant triangularity $\delta = 0$.

can be interpreted, as already discussed in section 6.2, as a favorable effect of elongation for fusion plasmas since a similar inner and outer temperature difference would lead to a lower level of turbulent fluxes in a more elongated plasma. The effect of elongation can here again be essentially accounted for by considering a constant $\langle R/L_{Ti} \rangle$. In particular, by comparing results shown in Figs. 6.2 and 6.11 for the two equilibria with $\kappa = 1.01$ and $\kappa = 1.52$, one observes the same nonlinear 'Dimits' up-shift for the effective critical inverse temperature gradient length from the linear value $R/L_{\text{eff,crit}} =< R/L_{Ti} >_{\text{crit}} \simeq 3$ to the non-linear value $R/L_{\text{eff,crit}} =< R/L_{Ti} >_{\text{crit}} \sim 6$. The observation that there exists a unique effective critical temperature gradient for different elongations are in agreement with nonlinear global simulations presented in [84]. We note that the present simulations were carried out with essentially the same physical parameters as in [84] apart from the density gradient, which is here taken as $R/L_n = 0$, so as to limit the number of parameters that would have to be interpreted in terms of effective gradient or gradient on the equatorial mid-plane, while a finite R/L_n was used in [84]. We finally notice that, since for a constant $\langle R/L_{Ti} \rangle$ the linear growth rates are similar, the remaining differences observed in Fig. 6.11 can be interpreted as additional geometrical effect on the nonlinear fluxes.

Considering now the triangularity scan, the electrostatic heat flux is shown in Fig. 6.11 for $\delta = -0.16, 0.0, 0.16$ at essentially constant elongation. Although the differences between the three curves are not as significant as for the non-linear elongation scan and

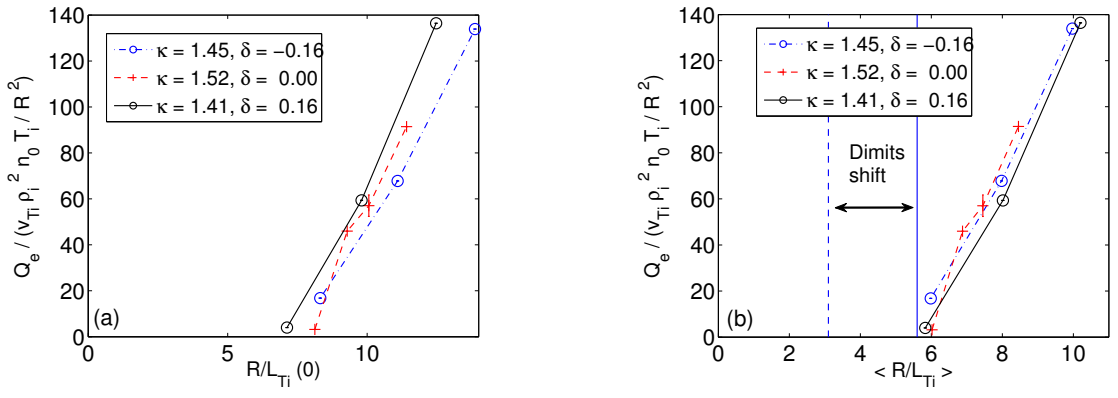

Figure 6.12: Triangularity scan : Nonlinear electrostatic heat flux as a function of (a) the temperature gradient at $\chi = 0$, $R/L_{Ti}(0)$, and (b) flux-surface averaged gradient, $\langle R/L_{Ti} \rangle$ for different triangularities and constant elongation.

also less marked than in the linear triangularity scan, one can still conclude that the turbulent transport is decreased when going from positive to negative triangularity at constant $R/L_{Ti}(0)$. Similar to the linear study, the dominant effect of triangularity can be accounted for in terms of the effective spatial gradient, as the heat flux dependence over the triangularity parameter δ is essentially reduced at constant $< R/L_{Ti} >$. One can furthermore extract an effective nonlinear critical inverse temperature gradient length $R/L_{\text{eff,crit}} =< R/L_{Ti} >_{crit} \simeq [5.7 \pm 0.5]$.

6.5 Summary

In this chapter the effect of flux surface shaping on ITG modes was investigated with flux-tube simulations considering different elongations κ and triangularities δ. Assuming a flat density profile, a decrease of the linear growth rate was observed when increasing the elongation at constant ion temperature gradient on the equatorial midplane, $R/L_{Ti}(0)$, as well as when going from positive to negative triangularity. It was shown that these shaping dependencies could be essentially reduced by keeping the flux surface averaged gradient $\langle R/L_{Ti} \rangle$ constant. In order to further understand how the modifications of the flux surface average gradient could account for these shaping effects, a study with a local dispersion relation was carried out, which suggested that at constant $\langle R/L_{Ti} \rangle$ the linear drive resulting from the temperature gradient and magnetic field curvature essentially compensate each

other. Finally, a series of nonlinear simulations were considered, showing, in line with the linear results, a decrease of the electrostatic heat flux with increasing elongation and when going from positive to negative triangularity at constant $R/L_{Ti}(0)$. We note that since the minor radius on the equatorial plane was kept constant for the different plasma shapes, the observed decrease of the electrostatic heat flux can be interpreted as a favorable effect of elongation and negative triangularity for fusion plasmas. As for the linear case, the main dependence on elongation and triangularity could be reduced by keeping a constant $\langle R/L_{Ti} \rangle$. Finally, in agreement with [84], an important observation is the existence of a unique effective critical inverse temperature gradient length which could be determined accurately for the elongation scan, $R/L_{eff,crit} =< R/L_{Ti} >_{crit} \simeq 6$, and within a given interval for the triangularity scan, $R/L_{eff,crit} =< R/L_{Ti} >_{crit} \simeq [5.7 \pm 0.5]$.

7 Modeling of electron internal transport barriers in the TCV Tokamak

Internal Transport Barriers (ITB) are regions of reduced radial particle and energy transport within the core plasma. The presence of an ITB is usually identified when, for a constant heating power, the temperature or density gradients exceed those of standard discharges. Depending on the heating method, internal transport barriers on ions, electrons, or both can be generated. Although the exact mechanism underlying the transport barrier creation is not yet fully understood, several experiments on different machines have shown that ITB formation is most of the time associated with plasmas rotation and/or the presence of a reversed magnetic shear profile [88]. Because of their enhanced confinement properties, transport barriers are viewed as a promising way to achieve high performance regime in future fusion reactor and are thus actively studied from the theoretical and experimental point of view [89, 90, 91, 92, 93].

In this chapter, turbulent heat and particle transport are investigated with the local version of the GENE code considering a TCV discharge where an electron Internal Transport Barrier (eITB) was obtained in the presence of a reversed shear profile [94]. We note that no measurement of the background plasma rotation was available for this experiment. However, other experimental rotation measurements in TCV suggest that typical shear flow velocities are not significant in the core of the machine, and background $E \times B$ and parallel rotation effects are thus not considered in the present work. A previous study [40], based on similar TCV discharges and using quasi-linear estimates computed with the local code GS2 [11], has shown that for a given electron temperature gradient, one can

find pairs of density and ion temperature gradients values $(R/L_n, R/L_{Ti})$ for which ion temperature gradient (ITG) and Trapped Electron Mode (TEM) contributions to electron particle transport are equal and of opposite sign, thus leading to a net cancellation of the total particle transport. This finding is of particular importance, since in the absence of any particle source and neglecting the neoclassical contributions one indeed expects that in the steady state the turbulent particle flux should be zero. The present work is thus motivated by these quasi-linear results and intends to investigate whether such particle flux cancellation can also be observed for realistic eITB parameters in nonlinear simulations. To this end, scans in the ion temperature gradient shall be carried out while keeping the other reference physical parameters constant until reaching a regime where both TEM and ITG instabilities are present and their respective contributions to the electron flux cancel each other. In addition one is interested in comparing the obtained nonlinear electron heat diffusivity with experimental values and thus to determine whether the obtained regime, for which the particle transport would cancel, is realistic from this point of view as well. Some further simulations are then presented to investigate the sensitivity of the heat diffusivity with respect to the density gradient, the electron temperature gradient and the radial position at which simulations are carried out. Finally some first global nonlinear simulations are carried out for reduced parameters, in order to provide some first estimate concerning the importance of relevant ρ^* effects.

7.1 Physical parameters

The physical parameters considered here are derived from the TCV discharge #29866, which corresponds to a typical eITB scenario in a deuterium plasma. The experimental temperature and density profiles of electrons are plotted in Fig. 7.1, showing a steep gradient in the transport barrier region which is ranging from $\rho_t \simeq 0.28 - 0.46$, where $\rho_t = \sqrt{\phi_\mathrm{t}/\phi_\mathrm{t,edge}}$, ϕ_t being the toroidal flux. The inverse temperature gradient length in this region varies between $R/L_{Te} = 10$ and 30, and the inverse density gradient length R/L_{ne} between 3 and 10. Note that all temperature and density gradients are here defined as $R/L_g = R < |\nabla \ln g| >= (R/a) < |\nabla \rho_t| > d\ln d/d\rho_t$, with $g = T, n$ and $< . >$ stands for the flux-surface average. The ion temperature was not measured in

this experiment, and can only be estimated from the electron profile by considering a fixed ion to electron temperature ratio. The safety factor profile q, computed with the equilibrium code CHEASE is shown in Fig. 7.2, where one observes that the shear $\hat{s} = (\rho_t/q)\,(dq/d\rho_t)$ cancels around $\rho_t = 0.4$, i.e. close to the transport barrier localization. A detailed description of the procedure used for the reconstruction, with CHEASE, of a magnetic equilibrium from experimental and calculated quantities, is given in [95]. Using the interface with the CHEASE code, see Chap.4, local GENE simulations are

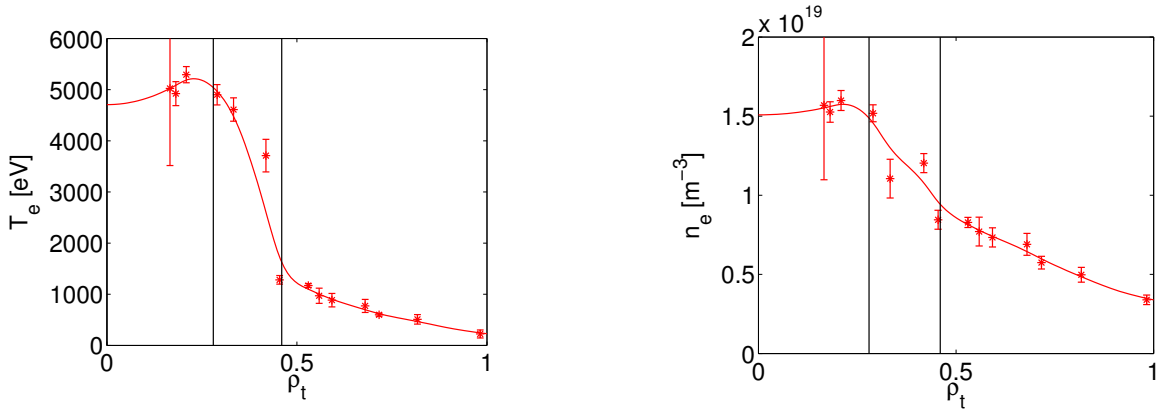

Figure 7.1: Experimental temperature (left) and density (right) profiles of electrons for TCV discharge #29866, obtained from Thomson scattering diagnostic. The vertical solid lines indicate the Internal Transport Barrier region $\rho_t \simeq 0.28 - 0.46$.

carried out at radial position $\rho_t = 0.3$, which corresponds to a local safety factor $q = 3.2$, shear $\hat{s} = -1.17$, and inverse aspect ratio $r/R = 0.09$. Note that this particular radial position is chosen as a first test case, as the corresponding electron temperature and density gradient are not too strong and numerical requirement are thus reduced. A variability investigation, questionning this particular choice will be presented in a latter section. Although using a realistic equilibrium, the present study will only focus on electrostatic modes and an independent small $\beta = 10^{-4}$ value is set, i.e. a β value inconsistent with the actual density and temperature profile considered. Note that one could have used $\beta = 0$, however in this limit some electrostatic modes with very high real frequencies are present in the system, which strongly restrict the time step, and a finite β is thus required for practical reasons. The temperature ratio $\tau = T_e/T_i$ and effective charge $Z_{eff} = \sum_i n_i Z_i^2 / \sum_i n_i Z_i$ are set, consistent with experimental measurements,

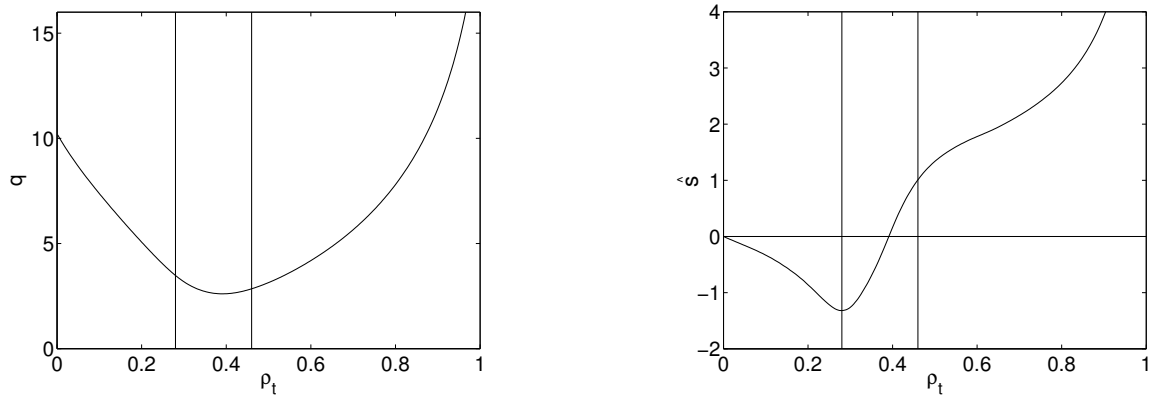

Figure 7.2: Safety factor profile q (left) and shear $\hat{s}$ (right) reconstructed with the equilibrium code CHEASE, for TCV discharge (#29866).

respectively to $\tau = 3.5$ and $Z_{eff} = 2$. Although more demanding from the computational point of view as it requires to add a third species, it is essential to account for this $Z_{eff} > 1$ value, since together with the retained T_e/T_i ratio it has a stabilizing effect on electron temperature gradient (ETG) instabilities thus allowing to consider only ion scales for the nonlinear simulations. The reader is invited to consult Refs. [96] and [97] for issues related to multiscale simulations. Carbon was chosen for the additional ion species as it is the dominant impurity observed in the experimental discharge. The three kinetic species, electrons, deuterium and carbon, are thus considered with normalized densities $n_e/n_{\rm ref} = 1$, $n_D/n_{\rm ref} = 0.8$, and $n_C/n_{\rm ref} = 0.03$ so as to verify $Z_{eff} = 2$, and real mass ratios are taken into account. The choice of retaining a real mass ratio is motivated in particular by a Trapped Electron Mode study in Ref. [27], where some quantitative differences of up to a factor two were observed in the particle flux between a reduced ($m_i/m_e = 400$) and real mass ratio simulations. The electron temperature and density gradients are taken as $R/L_{Te} = 12$ and $R/L_{ne} = 3$. The ion temperature gradients for the two species are assumed to be equal, $R/L_{T,D} = R/L_{T,C} = R/L_{Ti}$, and will be varied between 2 and 10 in the following study. As it is not measured in this particular experiment, the inverse normalized gradient length of carbon is arbitrarily taken as half the electron value, $R/L_{n,C} = 0.5\, R/L_{n,e}$. Note that this choice is based on results in [40] for which a cancellation of both the electron and carbon particle fluxes was observed at a given R/L_{Ti} when $R/L_{n,C} \simeq 0.5\, R/L_{n,e}$, and should not have a strong impact on

the following study since a low carbon density is considered here. For consistency, the deuterium density gradient is then obtained by taking the radial derivative of the quasi-neutrality equation:

$$\frac{dn_D}{dx} + Z_C \frac{dn_C}{dx} = \frac{dn_e}{dx} \,, \tag{7.1}$$

leading to:

$$\frac{R}{L_{n,D}} = \frac{1}{n_D} \left(n_e \frac{R}{L_{ne}} - Z_C \, n_c \frac{R}{L_{n,C}} \right) . \tag{7.2}$$

Finally, a realistic collision frequency is considered, and the normalized collision coefficient $\nu_c = 2.3\,10^{-5} \ln\Lambda \, R[m] \, n_e \, [10^{19}\, m^{-3}]/(T_i[keV])^2$, see Ref. [51], is therefore set to $\nu_c = 5\,10^{-4}$, where $\ln\Lambda$ is the Coulomb logarithm, and considering $R = 0.88m$, $T_i = 1\,keV$, $n_e = 1.2 \times 10^{19}\, m^{-3}$ and $\ln\Lambda = 20$.

To summarize, the considered physical parameters at $\rho_t = 0.3$ are:

- realistic magnetic geometry with: $q = 3.2$, $\hat{s} = -1.17$, $r/R = 0.09$.
- three kinetic species, electron, deuterium, carbon with: $\tau = T_e/T_C = T_e/T_D = T_e/T_i = 3.5$, $n_D/n_e = 0.8$, $n_C/n_e = 0.03$, $R/L_{Te} = 12$, $R/L_{ne} = 3$, $R/L_{T,D} = R/L_{T,C} = R/L_{Ti} = 2 - 10$ $R/L_{n,D} = 3.4$, $R/L_{n,C} = 1.5$.
- normalized collision frequency $\hat{\nu}_c = 5 \cdot 10^{-4}$ and $\beta = 10^{-4}$.

7.2 Linear results

With the above considered parameters, linear computations are first carried out with the eigensolver version of GENE for two different values of the ion temperature gradient $R/L_{Ti} = 5$ and $R/L_{Ti} = 6$. This linear investigation focuses on the growth rate and real frequency of the two most unstable modes for each toroidal mode number $k_y \rho_i$ between 0 and 2.2. The corresponding results are shown in Fig. 7.3. Considering first the case $R/L_{Ti} = 5$, one observes two distinct local maxima in the growth rate spectra. The largest one is found around $k_y \rho_i \simeq 0.5$ and corresponds to a mode with negative real frequency, i.e. propagating in the electron diamagnetic direction, which can thus be identified as a Trapped Electron Mode. The second maximum, at $k_y \rho_i \simeq 1$, is linked to a positive frequency and can be identified as an Ion Temperature Gradient mode. When increasing the ion temperature gradient from $R/L_{Ti} = 5$ to $R/L_{Ti} = 6$ the local maximum around

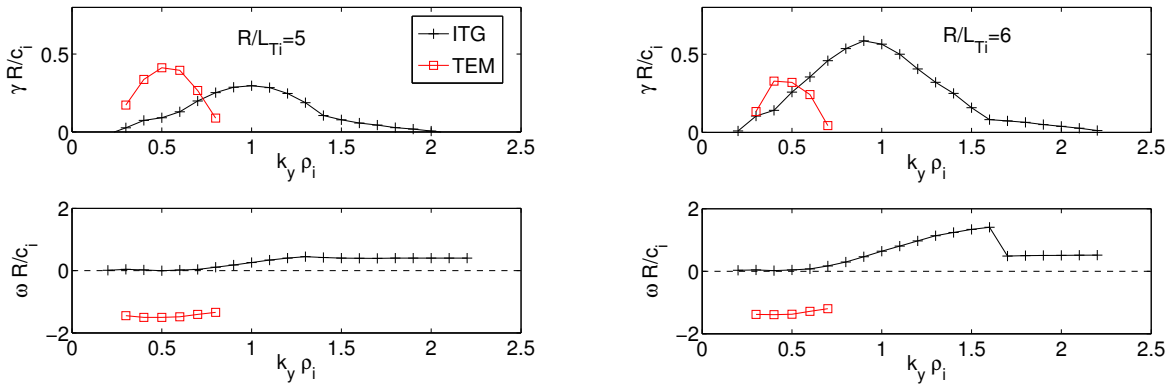

Figure 7.3: Linear spectra for the two most unstable modes for $R/L_{Ti} = 5$ and $R/L_{Ti} = 6$. The TEM (squares) and ITG (crosses) are identified considering the sign of their real frequency.

$k_y \rho_i \simeq 0.5$ remains essentially constant while the local maximum around $k_y \rho_i \simeq 1$ is strongly increased and becomes the largest, thus further confirming the respective nature of the corresponding modes. From these linear results, one expects that the coresponding turbulence will evolve from a TEM dominated regime to an ITG dominated regime, when increasing the ion temperature gradient from $R/L_{Ti} = 5$ to $R/L_{Ti} = 6$. Such behavior will be further investigated in the following by means of nonlinear simulations.

The GENE results shown here have been carried out with a high resolution, considering a velocity box $l_{v_\parallel} \times l_\mu = 3\, v_{th,i} \times 9\, T_i/B_{\rm ref}$ and a grid size $n_x \times n_z \times n_{v_\parallel} \times n_\mu = 24 \times 24 \times 64 \times 16$, for which the growth rate of each individual k_y mode is converged within approximatively 1%. In view of the nonlinear simulations, where a somewhat lower resolution might be used to decrease the computational cost, we shall now discuss how a reduced grid would affect these linear results. As explained in section 3.2.3, each individual ($k_y = 2\,\pi\, k/l_y, k_x = 2\, l\pi\, /l_x$) mode is coupled to different ($k_y, k'_x = k_x + p\, \delta k_x$) modes as a result of the parallel boundary condition, where $\delta k_x = 2\,\pi n_c\, k/l_x$. The radial grid resolution is therefore determined by the number of required connections to correctly describe the parallel structure of the mode. The length l_x, which can only have quantized values [see (3.30)]:

$$l_x = n_c \, \frac{l_y}{|2\,\pi \hat{s}|} \, , \tag{7.3}$$

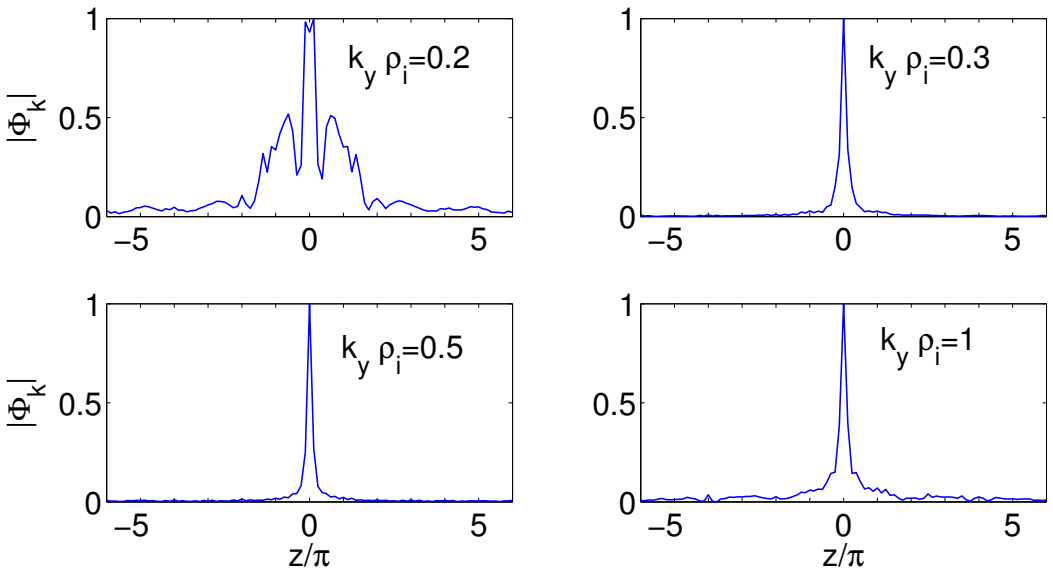

Figure 7.4: Absolute value of the electrostatic potential of several k_y Fourier modes as a function of the parallel coordinate z. This plot is obtained by connecting each individual (k_x, k_y) mode, defined over $z = [-\pi, \pi]$, to an other (k'_x, k_y) according to the parallel boundary condition (3.32). The grid resolution is $n_x = 24$, such that 11 positive and negative connections are considered, and the first 6 connections are shown here.

is adapted in a linear simulation for each individual k_y mode so that $n_c = 1$. In this case, all k_x modes are connected and the number of $p_{\max}$ connections is therefore $p_{\max} = [(n_x - 1)/2]$, where [ ] stands for integer part. The parallel structure of several k_y Fourrier components of the electrostatic modes are shown in Fig. 7.4 for $n_x = 24$. One observes that modes $k_y > 0.2$ have a strongly ballooned structure, which suggests that only a few connections are required for correct numerical resolution. In fact, simulations with no connections, i.e. $n_x = 1$ have already shown a good agreement with the higher resolved results. Considering now the other phase-space directions, convergence tests have shown that a reasonably good agreement with the reference high resolution results, in the order of 10%, is reached by using a parallel resolution $n_z = 16$, as well as velocity resolutions $n_{v_\parallel} = 48$ and $n_\mu = 8$. To summarize this convergence study, the growth rate and real frequency of the most unstable mode for each individual mode number k_y are plotted in Fig. 7.5 for both resolutions $n_x \times n_z \times n_{v_\parallel} \times n_\mu = 24 \times 24 \times 64 \times 16$ and $1 \times 16 \times 48 \times 8$, indeed showing maximum differences on the linear growth rates of the order of 10%.

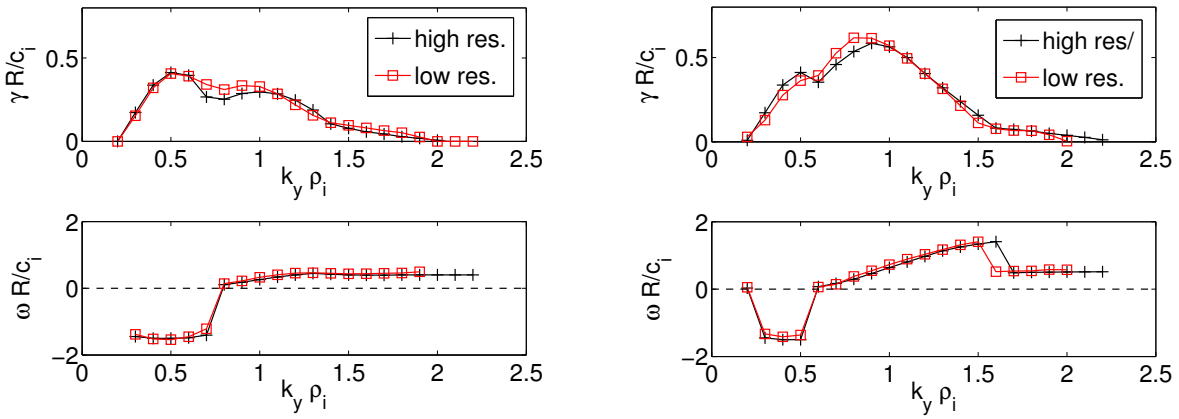

Figure 7.5: Linear spectra for the most unstable modes considering two different resolutions: $n_x \times n_z \times n_{v_\parallel} \times n_\mu = 24 \times 24 \times 64 \times 16$ and $1 \times 16 \times 48 \times 8$, for $R/L_{Ti} = 5$ (left) and $R/L_{Ti} = 6$ (right).

7.3 Nonlinear simulations

7.3.1 Choice of numerical parameters

As we are here considering physical parameters which are far away from the usual Cyclone base case, we shall start by further discussing the choice of the different numerical parameters used in these nonlinear simulations. The linear results in Fig. 7.3 show that

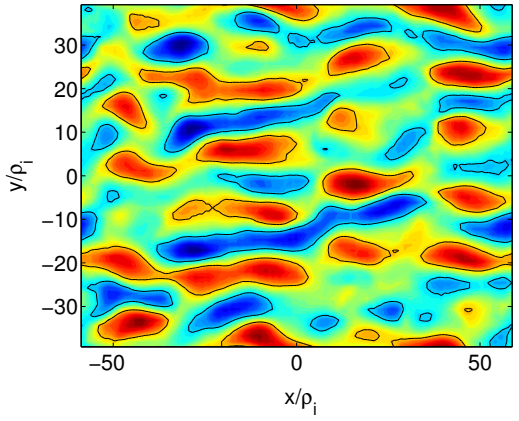

Figure 7.6: Contour plot of the electrostatic potential in the perpendicular (x,y) plane at $tR/c_i = 160$.

the linear modes are typically unstable in the region $k_y\,\rho_i \in [0.2\,,\ 2]$ for the considered physical parameters. Based on this observation, the box size in the y-direction is set such that $k_{y,min}\ \rho_i = 2\,\pi\,\rho_i/l_y = 0.08$ and the number of considered modes is $n_{ky} = 32$,

leading to a maximal resolved mode $k_{y,max}\ \rho_i = 2\,\pi\,n_{ky}\,\rho_i/l_y = 2.6$. Considering now the system size in the x direction, the length l_x should be large enough to contain the turbulent eddies, whose dimensions are characteristic of the radial decorrelation length, so that the periodic boundary condition in the radial direction can be well justified. For the considered physical parameters, where TEMs are present, elongated structures, often referred to as streamers, develop. The radial length of some of these streamers can be near $100\,\rho_i$ long as illustrated in Fig. 7.6. A radial box length of approximately $l_x = 120\,\rho_i$ should thus be appropriate. As already discussed in the previous section, the radial box length l_x needs to take on one of the quantized values $l_x = n_c\,l_y/|2\,\pi\hat{s}|$, where n_c is an integer. For the present shear value $\hat{s} = -1.17$, one obtains for $n_c = 11$ a box length of $l_x = 117.5\rho_i$, which will be used in the following. The required radial resolution is then determined by the size of the smallest turbulent eddies, which are typically of the order of a few ρ_i, as well as by the number of connexions that are required in the parallel direction, as already discussed in section 7.2. In order to connect each $(k_y, k_x = 0)$ mode to at least one other (k_y, k_x') mode, the number of points in the radial x-direction would need to be $n_x = 2 \cdot n_c \cdot n_{k_y} + 1 = 2 \cdot 11 \cdot 32 + 1 = 705$. The linear convergence studies have shown,

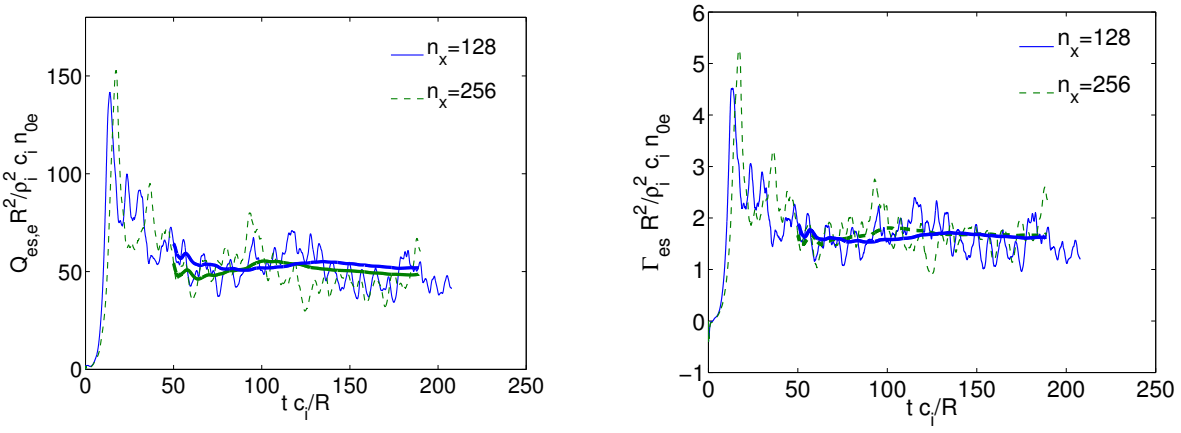

Figure 7.7: Time evolution of the electron heat and particle fluxes, for $R/L_{Ti} = 5$, and resolutions $n_x \times n_y \times n_z \times n_{v_\parallel} \times n_\mu = 128\times64\times16\times48\times8$ and $256\times64\times16\times48\times8$. The running average, see Eq. (7.4), is represented by the thicker lines.

however, that modes $k_y\rho_i > 0.2$ have a strongly ballooned structure, so that even when taking no connection, the main physics is still correctly described. In order to further determine whether a lower x-resolution could be envisaged, two nonlinear simulations with resolution $n_x = 128$ and $n_x = 256$ are compared. Note that for these two resolutions,

the last modes with at least one connexion are respectively $k_y\rho_i = 0.40$ and $k_y\rho_i = 0.88$. In real space, these two resolutions would thus correspond to a radial grid spacing of $\Delta x = l_x/n_x = 0.92\,\rho_i$ and $\Delta x = 0.46\,\rho_i$ respectively. For the z-direction the resolution $n_z = 16$ and for the velocity space resolution the parameters $l_{v_\parallel} \times l_\mu = 3\,v_{th,i} \times 9\,T_i/B_{\mathrm{ref}}$ and $n_{v_\parallel} \times n_\mu = 48 \times 8$, which had proven appropriate for the linear runs, were kept for the nonlinear simulations. The time trace of the electron heat and particle fluxes and their respective k_y spectra obtained from the nonlinear GENE runs are shown in Figs. 7.7 and 7.8 for the case $R/L_{Ti} = 5$. As can be observed, the running average heat fluxes for the two radial resolutions, defined as:

$$\langle Q \rangle(t) = \frac{1}{t - t_0} \int_{t_0}^{t} Q(t)\, dt\ , \qquad \text{for} \qquad t > 0\ , \tag{7.4}$$

having chosen $t_0 = 50 c_i/R$, differ by less then 10% at $t = 190 R/c_i$. The corresponding running average of the particle fluxes vary only by a few percent as well. In Fig. 7.8, one remarks in addition that the k_y spectra of the turbulent fluxes are not significantly changed. From these results we conclude that a radial resolution of $n_x = 128$ is sufficient for the present study. This grid resolution enables to reduce the computational effort thus allowing us to investigate the influence of several physical parameters on the nonlinear simulations.

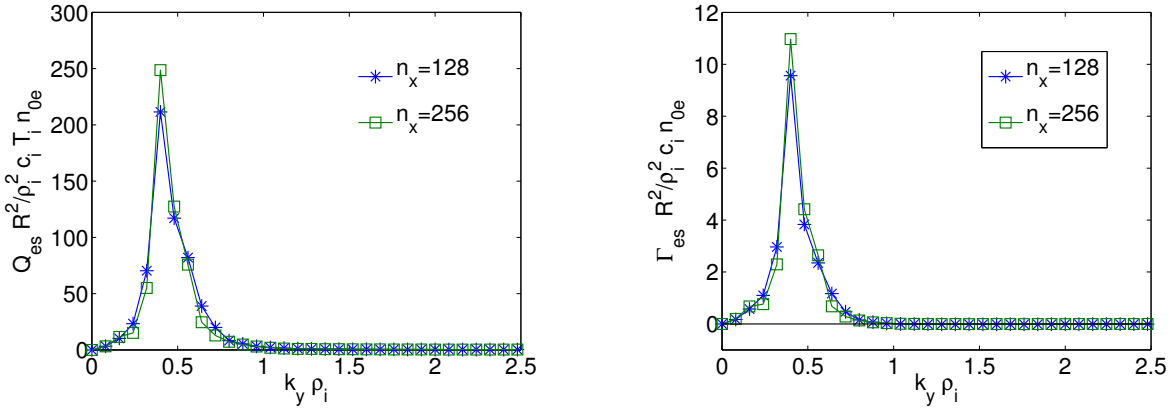

Figure 7.8: Electron particle flux spectra for $R/L_{Ti} = 5$ and considering different radial resolutions $n_x = 128$ and $n_x = 256$.

To summarize, a resolution of $n_x \times n_y \times n_z \times n_{v_\parallel} \times n_\mu = 128 \times 64 \times 16 \times 48 \times 8$ shall be used in the following, for which we estimate that the nonlinear simulation results are converged within about 10% to 20%.

7.3.2 Nonlinear results

Using the physical and numerical parameters described previously, a series of nonlinear simulations are carried out for various values of the ion temperature gradient. Considering first the case $R/L_{Ti} = 5$, the time evolution of electrostatic heat and particle fluxes for the different kinetic species are shown in Fig. 7.9. One observes, as could be expected from the linear physics where TEMs were the most unstable modes, that the electron heat flux is dominant. In addition, as carbon is only a trace species, $n_c/n_e = 0.03$, we also notice that its contribution to the heat flux is negligible. Concerning the particle fluxes, the electron and deuterium particle fluxes are very close, while the remaining small carbon particle flux is such that the ambipolarity relation is satisfied:

$$\Gamma_{es,D} + Z_C \, \Gamma_{es,C} = \Gamma_{es,e} \ , \tag{7.5}$$

as can also be observed in Fig. 7.10.

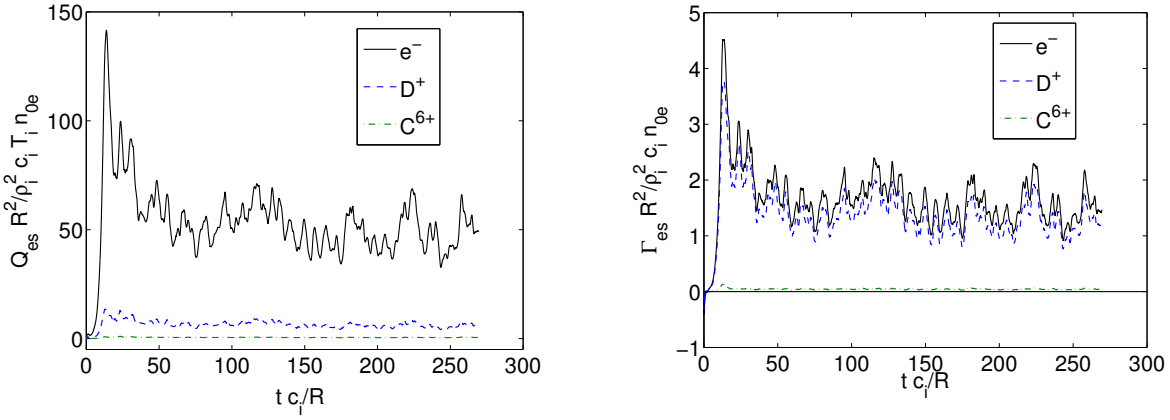

Figure 7.9: Time evolution of the electrostatic heat and particle fluxes of electrons, deuterium and carbon for $R/L_{Ti} = 5$.

In the following, we will concentrate on electron transport and try to compare simulation results with some experimental measurements.

Considering now the actual scan in the ion temperature gradient, the time-averaged electron particle fluxes are shown in Fig. 7.11 as a function of R/L_{Ti}. One observes that the particle flux is continuously changed from a positive to a negative value when increasing R/L_{Ti} and crosses the zero axis around $R/L_{Ti} \simeq 6$. One notices, in particular, that this ion temperature gradient value for which the electron particle flux drops to zero corre-

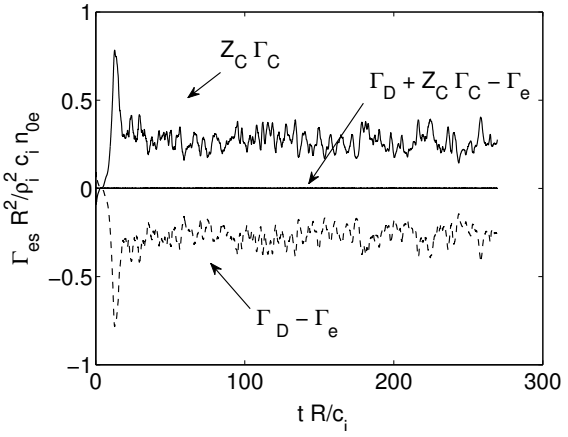

Figure 7.10: Comparison between the electrostatic particle fluxes. The cancellation of time traces $\Gamma_{es,D} - \Gamma_{es,e}$ and $Z_C\Gamma_{es,C}$ show that the ambipolarity relation is verified.

sponds to the transition from TEM to ITG dominated linear drive, as pointed out in Fig 7.3. A more detailed analysis of the particle flux spectra, shown in Fig. 7.12, reveals that the flux cancellation results from positive contributions at low $k_y\,\rho_i$ (where TEMs are the most unstable linear modes) which are compensated by negative contributions at higher $k_y\,\rho_i$ (where ITG modes are most unstable). This observation is in agreement with similar results in Ref. [51] which have been obtained for different physical parameters, as well as with a quasi-linear study in Ref. [40]. This latter comparison with quasi-linear results will be further investigated in the following section.

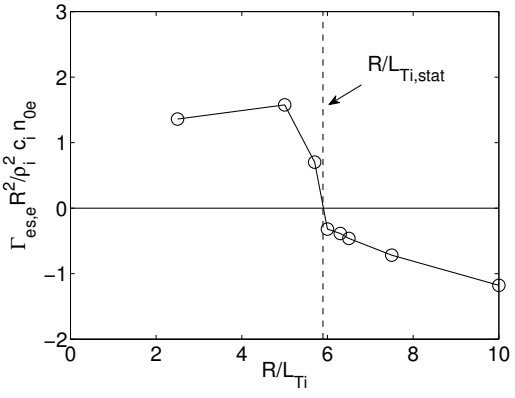

Figure 7.11: Electron particle flux as a function of R/L_{Ti}.

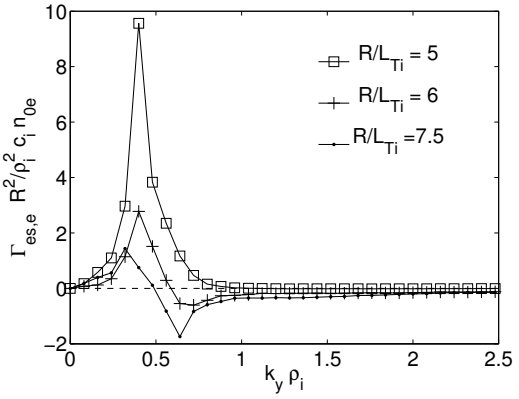

Figure 7.12: Electron particle flux spectra for different R/L_{Ti}.

Since the observed particle spectra for different k_y modes seems to reflect features of the linear physics, one may obtain some useful information by investigating whether some characteristic frequencies are present in the turbulence. To this end, a time-windowed Fourier transform of the electrostatic potential is employed, see Ref. [28], which provides for each k_y value a frequency spectra. The time interval and window width considered here are respectively $t\, c_i/R = [100\,,\ \ 250]$ and $\Delta t_{\rm w}\, c_i/R = 37.5$. The resulting normalized frequency spectra obtained for different ion temperature gradient values are shown in Fig. 7.13. Most of the linear physics characteristics are still observed in the nonlinear simulations. Indeed for the $R/L_{Ti} = 5$ case, the dominant frequencies are negative for $k_y\, \rho_i \in [0.2\,,\ \ 0.7]$ and positive for $k_y\, \rho_i \in [0.8\,,\ \ 1]$ in good agreement with result in Fig. 7.3. Note that no dominant frequency can be determine for $k_y\, \rho_i > 1$. Considering now $R/L_{Ti} = 6$, a clear transition from negative to positive frequency is observed at $k_y\, \rho_s = 0.5$, as for the linear simulation results of Fig. 7.3. Finally, for $R/L_{Ti} = 7.5$, the regime is, as expected, ITG dominated with essentially positive frequencies.

These results show that the negative and positive contributions observed at different $k_y\, \rho_i$ in the particle flux spectra in Fig. 7.12 can be clearly associated respectively to dominant TEM and ITG modes which still persist in the nonlinear regime.

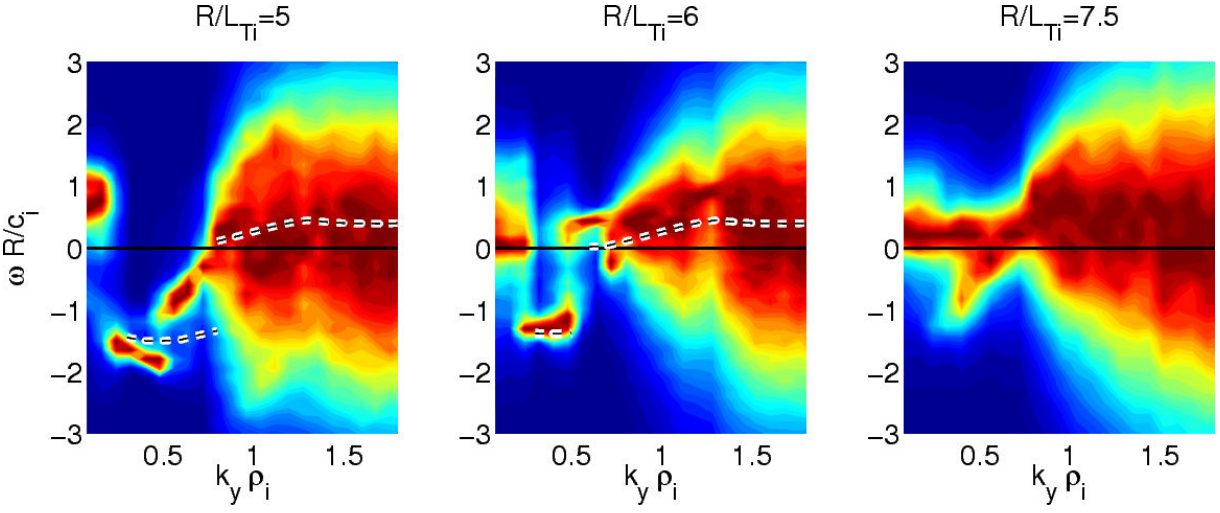

Figure 7.13: Frequency and k_y spectra of the electrostatic potential Φ. For each k_y mode the frequency spectra has been normalized to its maximal value. The frequency of the most unstable linear mode of Fig. 7.3 are reported here in dashed line.

As already discussed, the point in parameter space for which the particle flux goes to zero, $\Gamma \simeq 0$, is remarkable as it corresponds, in the absence of particle sources, to a stationary state situation. In particular, when considering experimental temperature and density profiles for carrying out gyrokinetic simulations, one could investigate whether the condition for such a stationary state are met within the experimental uncertainties. Assuming that the physical parameters are indeed such that the constraint $\Gamma \simeq 0$ on the particle fluxes is fulfilled, *i.e.* $R/L_{Ti} = R/L_{Ti,stat}$, we shall now focus our attention on the heat transport, and in particular compare the corresponding electrostatic electron heat diffusivity $\chi_{es,e}$ with the observed experimental value. The electron heat diffusivity obtained from the nonlinear simulations, defined as:

$$\chi_{es,e} = \frac{Q_{es,e}}{n_e < |\vec{\nabla} T_e| >} , \tag{7.6}$$

is shown in Fig. 7.14 for the different ion temperature gradient values. In view of comparing with the experiment, the different results obtained in normalized units have been here converted to SI units ($m^2\, s^{-1}$) using TCV parameters: $T_e = 4\, keV$, $B_{\rm ref} = 1.44\, T$ and $R_0 = 0.88\, m$. A remarkable feature observed in Fig. 7.14 is that the ion temperature gradient value for which the particle flux cancels $R/L_{Ti} \simeq 6$ corresponds to a minimum of the heat diffusivity, for which it is equal to $\chi_{e,stat} \simeq 2\, m^2\, s^{-1}$. This observation is in agreement with results in [51]. From the Fourier decomposition of the heat flux in Fig. 7.14, one observes that the peak related to TEM modes at $k_y\, \rho_i \simeq 0.5$ is removed when going from $R/L_{Ti} = 5$ to $R/L_{Ti} = 6$. The heat flux spectra peaks then in the ITG part of the spectrum around $k_y\, \rho_i \sim 0.7$, and this new peak increases with increasing temperature gradient from $R/L_{Ti} = 6$ to $R/L_{Ti} = 7.5$. The local minimum of the electron heat flux around $R/L_{Ti} = 6$ can therefore be interpreted as a nonlinear interaction between ITG and TEM modes in the $k_y\, \rho_i \simeq 0.5$ region. The value obtained from these nonlinear simulations for $\chi_{e,stat}$ can be compared with the experimental electron heat diffusivity, which is computed from the measured temperature and density profiles, as well as the magnetic equilibrium and the absorbed power defined as follows:

$$\chi_{exp,e} = -\frac{1}{V'\, T_e'\, n_e\, \langle |\nabla \rho_t| \rangle^2} \int_0^{\rho_t} P_e\, dV , \tag{7.7}$$

where the prime superscript denotes the partial derivative with respect to the flux label ρ_t,

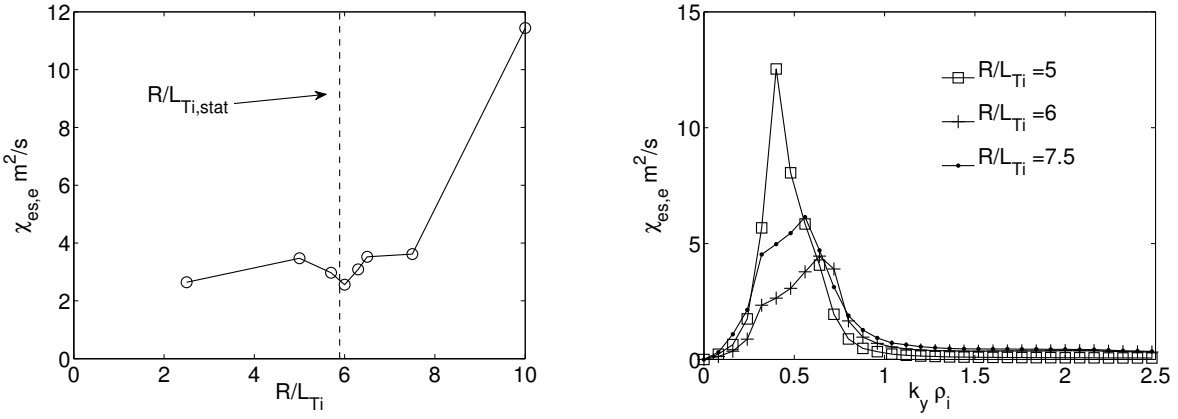

Figure 7.14: Electron heat diffusivity $\chi_{es,e}$ as a function of R/L_{Ti} (left). Note the local reduction of $\chi_{es,e}$ for $R/L_{Ti} = R/L_{Ti,stat}$. On the right, the electron heat diffusivity spectra is shown for different R/L_{Ti} values.

and P_e is the power absorbed by electrons, calculated as the sum of the ohmic power, the absorbed ECH power and the equipartition power loss (collisional equilibration between electrons and ions):

$$P_e = P_{ECH} + P_{OH} - P_{EQ} \; . \tag{7.8}$$

For the present case, the experimental electron heat diffusivity is estimated to be about $1\, m^2\; s^{-1}$ in the region $\rho_t = 0.3 - 0.4$. The simulation results are thus within a factor two of these experimental values. Let us point out however, that the flux tube computations were not carried out for the radial position with the steepest electron temperature and density gradient. A discussion concerning the sensitivity of the obtained heat diffusivity with respect to some of the physical parameters will be thus provided in section 7.5 to address this particular issue.

7.4 Comparison with quasi-linear estimates

Concerning particle flux cancellation the nonlinear results discussed in the previous section show a good qualitative agreement with the quasi-linear results in Ref. [40]. In order to further validate the quasi-linear approach, we have carried out some direct quantitative comparisons, for our physical parameters, with quasi-linear particle fluxes obtained from GENE simulations.

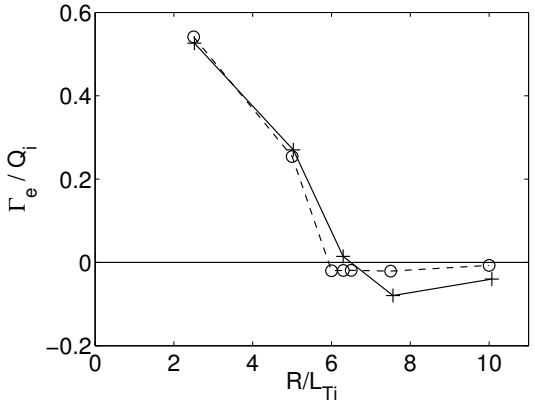

Figure 7.15: Quasi-linear estimate of the electron particle flux as a function of R/L_{Ti}.

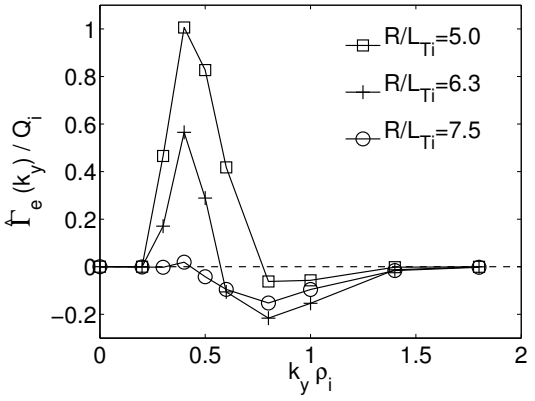

Figure 7.16: Quasi-linear estimate of the electron particle flux spectra for $R/L_{Ti} = 5$ and $R/L_{Ti} = 6$.

For the eITB study in Ref. [40] the quasi-linear rule was only retaining the mode $k_y\rho_i$ corresponding to the highest value of $\gamma/ < k_\perp^2 >$. Considering however that the particle flux cancellation observed for the nonlinear simulations in Fig. 7.12 had resulted from positive and negative contributions at different k_y values, it appears essential to keep all k_y modes in the quasi-linear approach. We therefore adopt here the more suited rule proposed in Ref. [98], for which the quasi-linear flux is given by:

$$F^{\,q.l.} = \sum_{k_y} \hat{F}_{k_y}^{q.l.}\, \Delta k_y \ , \tag{7.9}$$

where F stands for the heat Q or particle fluxes Γ. The single k_y mode contribution is defined as:

$$F_{k_y}^{q.l.} = A_0 \left(\frac{\gamma_{k_y}}{\langle k_\perp^2 \rangle} \right)^{\xi} \frac{\hat{F}_{k_y}}{|\hat{\Phi}_{0,k_y}(0)|^2} \ . \tag{7.10}$$

The quantities $\hat{F}_{k_y}$ and $\hat{\Phi}_{0,k_y}(0)$ are obtained from the linear simulations and the flux-surface averaged perpendicular wave number is computed as:

$$\langle k_\perp^2 \rangle = \frac{\sum_{k_x} \int \left(k_y^2\, g^{yy} + k_x^2\, g^{xx} + k_x\, k_y g^{xy} \right) |\hat{\Phi}_{k_x,k}(z)|^2 \, dz}{\sum_{k_x} \int |\hat{\Phi}_{k_x,k}(z)|^2 \, dz} \ . \tag{7.11}$$

Note that the k_x sum is running over all connected k_x for a given k_y ($n_x = 24$ here). The value of the constant A_0 needs only to be determined if one needs to obtain absolute quantities. We are however only interested here in finding physical parameters for which the particle flux goes to zero which can be determined by looking at the ratio Γ/Q between

the particle and heat fluxes since the heat flux is always positive. Finally, the parameter ξ is first set to $\xi = 2$, as suggested in [98].

The quasi-linear flux ratio Γ_e/Q_i, where Q_i is the deuterium heat flux, is shown in Fig. 7.15. As for the nonlinear simulations (see Fig. 7.12), the particle flux changes from a positive to a negative value when increasing the ion temperature gradient while keeping all the other physical parameters constant. We furthermore notice that the temperature gradient $R/L_{Ti,stat}$ for which $\Gamma_e = 0$ is in good agreement with the nonlinear results. Considering now each individual k_y contribution, which are shown in Fig. 7.16, it is clear that the observed flux cancellations results from positive and negative contributions at different k_y values. This is also in very good agreement with the observed spectra in the nonlinear simulations, see Fig. 7.12, and stresses the importance of keeping several k_y modes in the quasi-linear approach.

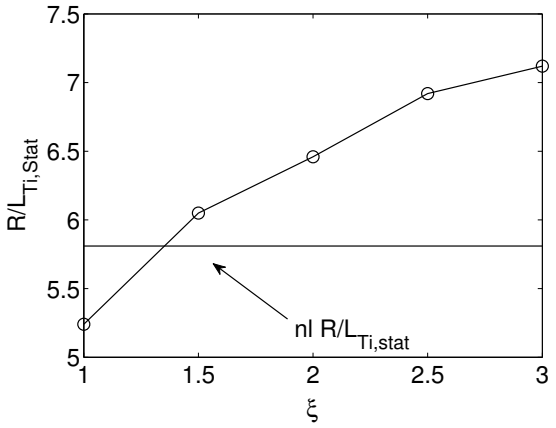

Figure 7.17: Stationary R/L_{Ti} obtained from quasi-linear estimates for different values of the ad-hoc parameter ξ. Also shown is the stationary gradient obtained from the nonlinear simulations.

When computing the quasi-linear flux, the relative importance of the different k_y contributions will in principle be influenced by the choice of the ξ exponent in Eq. (7.10). For instance, a higher value of ξ will increase the relative weight in Eq. (7.9) of the low k_y modes (where $\gamma/ < k_\perp^2 >$ peaks) with respect to the higher k_y modes. In order to investigate this effect, a scan in ξ is carried out in the range $\xi \in [1\ 4]$ and the stationary ion temperature gradient $R/L_{Ti,stat}$ is reported in Fig. 7.17 as a function of the parameter

ξ. The dependence with respect to ξ is relatively weak and an agreement within 20% with the non-linear results is reached for ξ between 2 and 3. The choice of $\xi = 2$ seems therefore appropriate.

7.5 Sensitivity of the computed heat diffusivity

The nonlinear flux-tube computations of the electron heat diffusivity presented in section 7.3 have shown that a reasonable agreement can be reached with the experimental results. The simulations discussed previously were however carried out considering relatively low density and electron temperature gradients compared to the maximal values that can be reached in typical TCV eITBs. In this section, we shall address the issue of the sensitivity of the computed heat diffusivity with respect to some of the key physical parameters. For this study, we consider a slightly different equilibrium profile, for which the safety factor profile q is shown in Fig. 7.18. Although this equilibrium does not exactly correspond to the TCV discharge #29866, it is still representative of some other TCV experimental eITB scenarios, see [95]. For this safety factor profile, the cancellation of the shear $\hat{s}$ is shifted to higher ρ_t values, thus allowing to compare simulations at $\rho_t = 0.3$ and $\rho_t = 0.4$. Note that with the previously considered equilibrium the $\hat{s} = 0$ was located around $\rho_t = 0.4$, which prevented us from running flux tube simulations at this position. The flux tube model is indeed inappropriate for handling zero shear regions. We remark in particular that the radial simulation length $l_x \to +\infty$ for $\hat{s} \to 0$, see Eq. 7.3, which reflects this problem.

In the following, the dependence of the electron heat diffusivity with respect to the density gradient, the electron temperature gradient and the flux-tube position is investigated by varying these parameters one by one while holding all the other ones constant. The considered ranges for varied parameters and fixed values for the constant parameters are as follows:

- realistic magnetic geometry with local values:
  - at $\rho_t = 0.3$ $q = 9$, $\hat{s} = -0.55$, $\epsilon = 0.09$.
  - at $\rho_t = 0.4$ $q = 7$, $\hat{s} = -1.22$, $\epsilon = 0.12$.
- three kinetic species, electron, deuterium, carbon with: $\tau = T_e/T_C = T_e/T_D =$

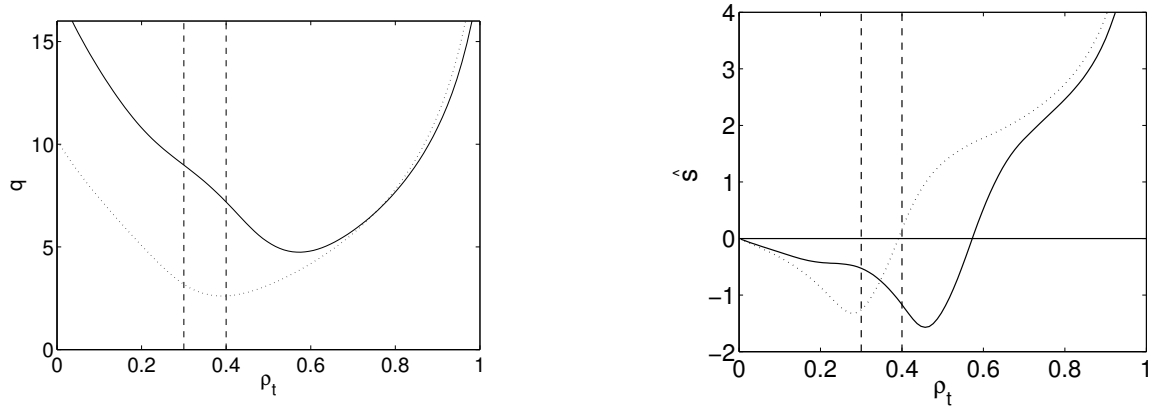

Figure 7.18: Safety factor profile q (solid line) for alternative equilibrium to the one of TCV discharge #29866. Safety factor for shot # 29866 is shown for reference with dotted line. The corresponding shear profiles are shown on the left plot.

$T_e/T_i = 3.5$, $n_D/n_e = 0.8$, $n_C/n_e = 0.03$, $R/L_{Te} = 12$, $R/L_{ne} = 2, 3$, $R/L_{T,D} = R/L_{T,C} = R/L_{Ti} = 2 - 10$ $R/L_{n,D} = 2.3, 3.4$, $R/L_{n,C} = 1$.

- normalized collision frequency $\nu_c = 5 \cdot 10^{-4}$ and $\beta = 10^{-4}$.

The values $R/L_{Te} = 12$, $R/L_{ne} = 3$ and $\rho_t = 0.4$ define the reference point from which these parameters are varied. The same numerical parameters as in section 7.3 are used. In Fig. 7.19, the electron particle fluxes and heat diffusivities are shown for the different cases, as a function of the ion temperature gradient. The heat diffusivity at $R/L_{Ti} = R/L_{Ti,stat}$, i.e. corresponding to $\Gamma_e = 0$, is also summarized in Fig. 7.20 as a function of the flux tube position, density gradient and electron temperature gradient.

We first notice in 7.19 that for the reference case $R/L_{Te} = 12$, $R/L_{ne} = 3$, $\rho_t = 0.4$ the heat diffusivity presents a local minimum in the vicinity of $R/L_{Ti,stat}$ as in Fig. 7.14. For the case $R/L_{Te} = 12$, $R/L_{ne} = 3$, $\rho_t = 0.4$, a first scan in R/L_{Ti} did not reveal any clear minimum. By carrying out two additional nonlinear simulations, around the expected $R/L_{Ti,stat}$, it appears however that the heat diffusivity for $R/L_{Ti} = R/L_{Ti,stat}$ is slightly smaller (about 7%) than the two neighboring points. These differences are however not important, and the same exercise which consists in carrying out further nonlinear simulations in the vicinity of $R/L_{Ti,stat}$ was thus not carried out for the two other physical cases for which no clear minimum are observed.

Focusing now on the sensitivity of the stationary heat diffusivity with respect to phys-

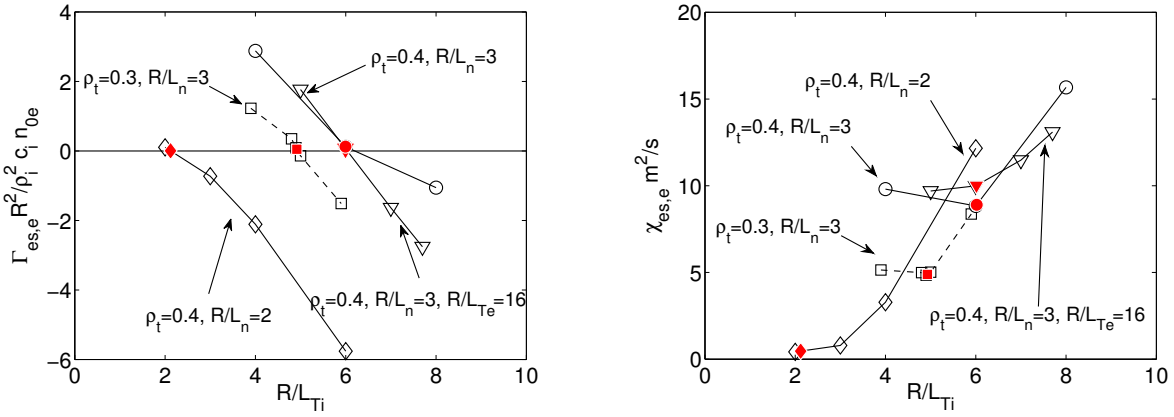

Figure 7.19: Electron particle flux $\Gamma_{es,e}$ and heat diffusivity $\chi_{es,e}$ for different radial positions, density gradients, and electron temperature gradients as a function of R/L_{Ti}. The ion temperature gradient value $R/L_{Ti,stat}$ for which the electron particle flux goes to zero is represented by a filled symbol for each case.

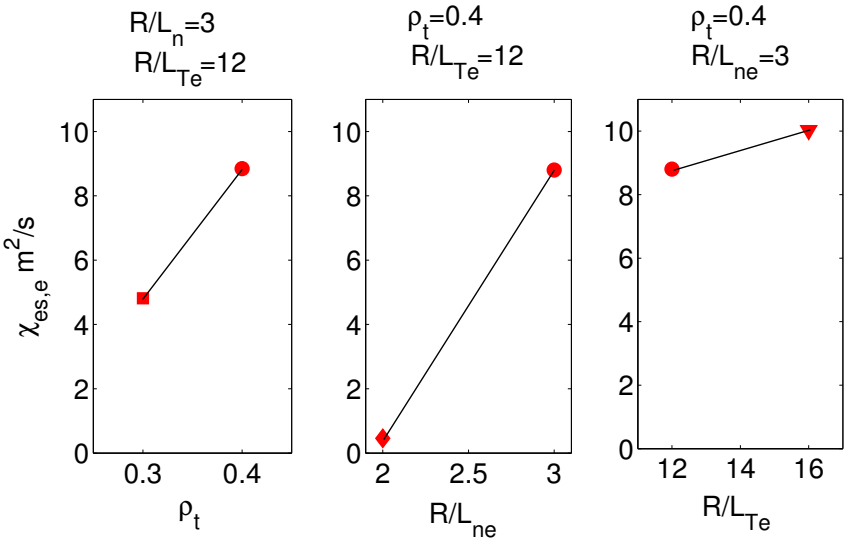

Figure 7.20: Electron heat diffusivity corresponding to $\Gamma_e = 0$ as a function of the flux tube position, electron density gradient and electron temperature gradient.

ical parameters in Fig. 7.20, one observes that when changing the flux tube position from $\rho_t = 0.4$ to $\rho = 0.3$ the heat diffusivity is decreased from $\chi_{e,stat} = 8.8\ m^2\,s^{-1}$ to $\chi_{e,stat} = 4.8\ m^2\,s^{-1}$. This dependence is not going in the expected direction as the shear is increased from $\hat{s} = -1.22$ at $\rho = 0.4$ to $\hat{s} = -0.55$ at $\rho_t = 0.3$ and a more negative shear is usually attributed to have a stabilizing effect on TEM instabilities [7]. One notes however that the local aspect ratio varied from $\epsilon = 0.12$ at $\rho = 0.4$ to $\epsilon = 0.09$ at $\rho_t = 0.3$ which could account for the difference as the trapped particle fraction directly depends on this parameter. Considering the relative variations of the shear and local aspect ratio we

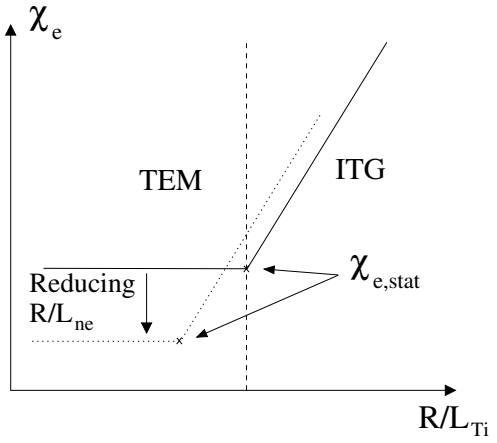

Figure 7.21: Schematic view of the L shaped electron diffusivity dependence with respect to the ion temperature gradient.

conclude however that the dependence of the heat flux over the position is still moderate. When changing the electron temperature gradient from $R/L_{Te} = 12$ to $R/L_{Te} = 16$, only a small change of approximately 10% is observed on the stationary heat diffusivity $\chi_{e,stat}$. The choice of the electron temperature gradient is thus not a critical parameter.

Considering finally the influence of the density gradient, a very strong dependence is observed. The heat diffusivity varies from $\chi_{e,stat} = 8.8\ m^2\,s^{-1}$ for $R/L_n = 3$ to $\chi_{e,stat} = 0.5\ m^2\,s^{-1}$ for $R/L_n = 2$ to , *i.e.* by one order of magnitude. From Fig. 7.19, one also notices that the ion temperature gradient $R/L_{Ti,stat}$ for which $\Gamma_e = 0$ is lower in the low density gradient case ($R/L_{Ti,stat} \simeq 2$ for $R/L_{ne} = 2$ instead of $R/L_{Ti,stat} \simeq 6$ for $R/L_{ne} = 3$.

As already discussed in the previous section, the temperature gradient $R/L_{Ti,stat}$ is obtained close to the transition between TEM and ITG dominated turbulent regime. A

schematic view of the general L-shaped R/L_{Ti} dependence of the electron heat diffusivity is shown in Fig. 7.21. For small values of R/L_{Ti} where turbulence is TEM dominated, $\chi_{es,e}$ only weakly depends on R/L_{Ti}. A strong increase is then observed in ITG dominated regime. If one neglects local minimum of χ_e around $R/L_{Ti,stat}$, the $\chi_{e,stat}$ is then close to the value obtained in the pure TEM regime. The modification of the density gradient has a strong influence on the TEM instabilities, such that when reducing the R/L_{ne} the heat flux in pure TEM regime is reduced, thus explaining the overall reduction of $\chi_{e,stat}$.

7.6 Global effects

As shown in the previous section and as a result of the strong dependence of the stationnary heat diffusivity with respect to the density gradient, nonlinear local simulations with $R/L_{ne} = 6 - 10$, which are typical values in the center of the barrier, result in overestimating the electron heat flux. The $\rho^* = \rho_s/a$ value in TCV being typically of the order of $1/\rho^* = 80$, one possible explanation for the discrepancy between the simulation and experimental results is that global effects play here an important role which need to be accounted for. This hypothesis is in particular supported by the ρ^* scan in Fig. 5.20, which shows that a strong decrease, *i.e.* by one order of magnitude, of the heat diffusivity is observed for this ρ^* value with respect to local simulations. One notes however that these results were obtained for the ion heat diffusivity considering adiabatic electrons, and one may wonder whether a similar decrease would be observed with full kinetic electrons for the electron heat diffusivity.

So as to address this issue, one would ideally have carried out nonlinear global simulations with full kinetic electron dynamics considering the realistic TCV parameters. Because of the increased computational cost of global simulations, it was however not feasible to use the parameters considered previously for the local simulations, *i.e.* in particular three kinetic species and high gradients. Furthermore, issues related with the radial resolution of the non-adiabatic electron response regions near mode rational surfaces, as discussed for linear results in section 5.3, still need to be addressed in nonlinear global simulations using kinetic electrons.

In order to nonetheless provide some first estimates of non-local effects, a reduced pa-

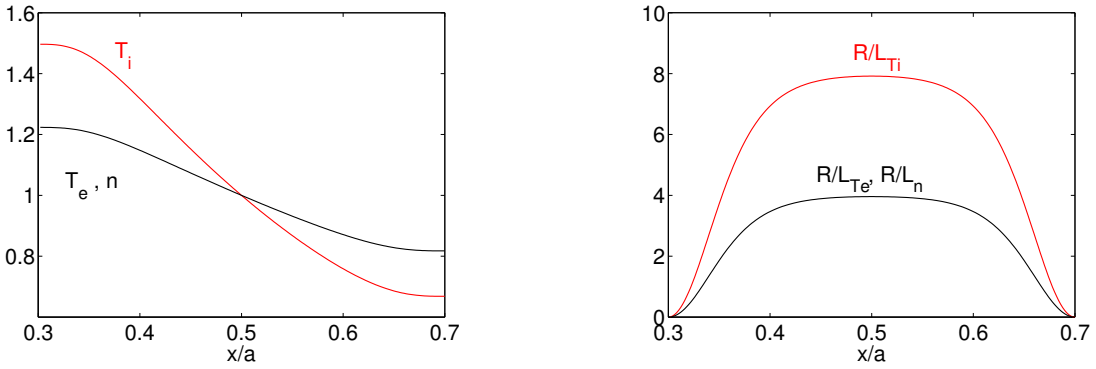

Figure 7.22: Initial temperature and density profiles and the corresponding gradients considered for the global TCV-relevant GENE simulations.

rameter case is investigated and compared with local results. Note that by reduced one understand here that the gradients are low enough so that only a small $k_y\,\rho_i$ region is unstable, thus diminishing the computational requirements. Furthermore, carbon impurities are neglected so that only the distributions of deuterium ions and electrons are evolved. So as to reduce the time scale separation between ion and electron dynamics, the mass ratio is reduced from the realistic value $m_i/m_e = 3672$ to $m_i/m_e = 800$. According to Eq. (5.11), this reduced mass ratio also increases the radial scale of the non-adiabatic electron response regions around mode rational surfaces and thus relaxes the requirements on radial resolution.

The TCV-relevant value for ρ^* is chosen as $\rho^* = 1/80$. In addition, one considers the ad-hoc circular model, with similar parameters as in the Cyclone base case. The considered aspect ratio is thus $a/R = 0.36$ and the safety factor profile is given by:

$$q(x) = 0.95 + 2.22\,(x/a)^2\ . \tag{7.12}$$

and $\rho^* = 1/80$. Note that this q profile slightly differs from the one used in the standard Cyclone base case as considered in Sec. 5.2. These values were indeed adapted as a numerical instability was observed when a mode rational surface is located in the vicinity of the radial boundaries. This issue, only observed when carrying out global simulations with kinetic electron dynamics, is not yet fully understood and is still under investigation. As a result of this problem, we have not been able to obtain stable nonlinear simulations with full kinetic electrons in the case of a reversed magnetic shear, although this would have been more suited in view of studying a transport barrier.

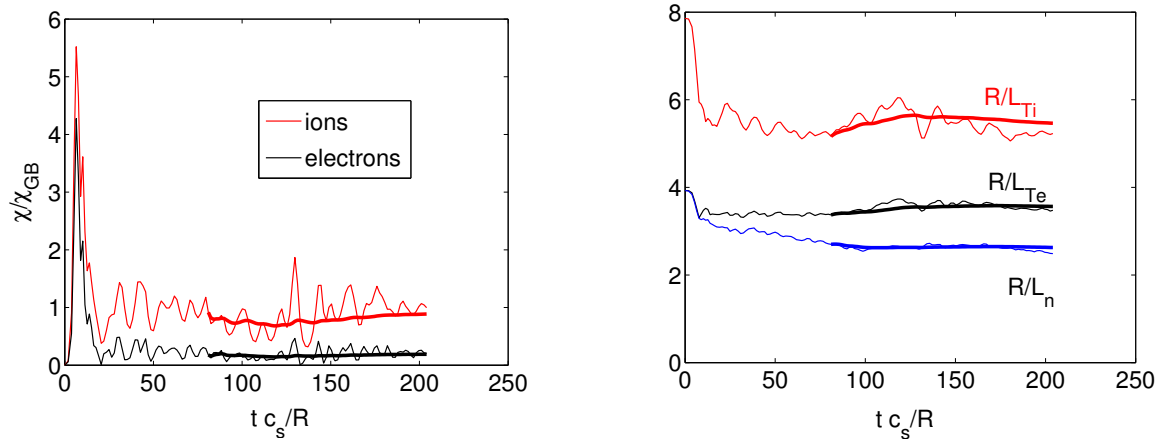

Figure 7.23: Global TCV-relevant GENE simulations. Time evolution of the heat diffusivities (units $\chi_{GB} = c_s\,\rho_s/a^2$) and of the normalized logarithmic gradients of the total temperatures $T = T_0 + T_1$. These quantities have been obtained by radial averaging in the range $x/a = 0.45 - 0.55$. The bold lines represent the running time average starting from $t_0\,c_s/R = 80$.

Two kinetic species are considered, electrons and ions, with flat gradient profiles as defined in Eq. (5.16) and parameter values $\kappa_{Ti} = 8$, $\kappa_{Te} = 4$, $\kappa_{ni} = \kappa_{ne} = \kappa_n = 4$, $\Delta x = 0.4\,a$ and $\Delta T = \Delta n = 0.06$. The different ion and electron profiles are illustrated in Fig. 7.22. We note that a narrow flat gradient region, of about $0.2\,a$ radial width, is considered here, consistently with the size of the eITB barrier previously discussed. For such parameters, ITG instabilities are the most unstable modes.

For these preliminary results, the simulation and grid domain are $l_x \times l_y \times l_z \times l_{v_\parallel} \times l_\mu = 30\,\rho_s \times 84\,\rho_s \times 2\,\pi \times 3.5\,v_{th,i} \times 12.3\,T_i/B_{\rm ref}$ with grid resolution $n_x \times n_{ky} \times n_z \times n_{v_\parallel} \times n_\mu = 40 \times 16 \times 48 \times 48 \times 12$. The box size in the y-direction is chosen so that the smallest mode number in the system is:

$$k_{y,min}\,\rho_s = 2\,\pi\,\rho_s/l_y = 0.075\,. \tag{7.13}$$

This corresponds to $n_0 = 2$ in Eq. (3.4), i.e. the simulation domain only covers one half of each flux surface. An hyperdiffusion $h_x = 4$, $h_z = 4$, and $h_v = 0.5$ is used to ensure numerical stability and buffer regions at the edge of the system which represent 5% of the simulation box on each side are considered. The Krook-type heat source described in section 3.5 is used, with $\gamma_h = 0.03$. It should still be mentioned that for these parameters the radial resolution is insufficient for resolving all the non-adiabatic electron response regions, and that convergence in x should be carried out. This was yet not possible as a numerical instability was again observed when attempting to further increase the radial

resolution and is still under investigation.

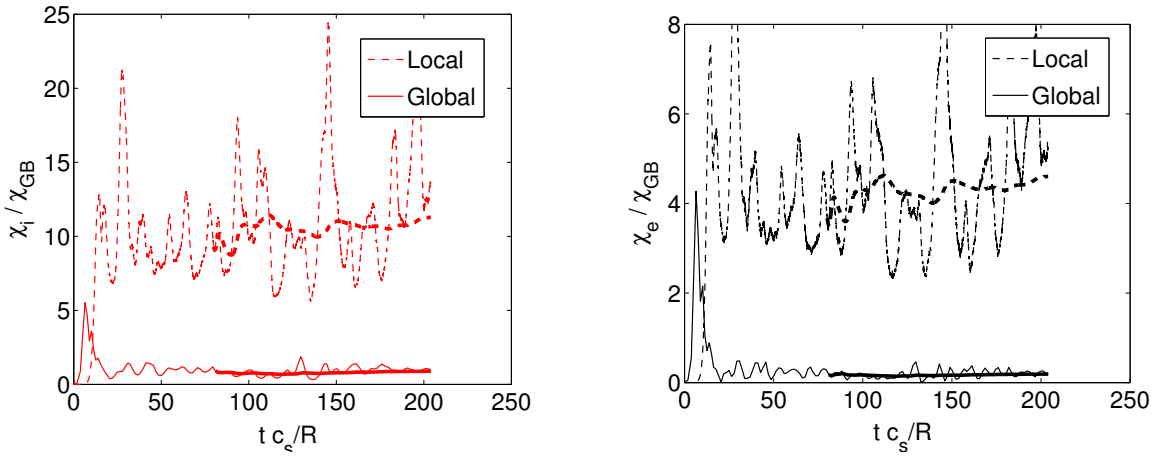

Figure 7.24: Comparison between heat diffusivities using either the global or local version of the GENE code for both ions (left) and electrons (right).

Using these parameters, the time evolution of the heat diffusivity and normalized logarithmic gradients of the total temperature and density are shown in Fig. 5.16 for both ions and electrons, together with their running average starting at $t_0\, c_s/R = 80$. The time-averaged diffusivities $\chi_i = 0.9$ and $\chi_e = 0.2$ for the effective gradients $R/L_{Ti} = 5.5$, $R/L_{Te} = 3.6$, $R/L_n = 2.6$ were obtained in this way. These different quantities have been obtained by radial averaging over the interval $x/a = 0.45 - 0.55$. Note that despite the reduced parameter set, the simulation still required about 40 000 CPU hours on the HPC-FF linux cluster at Jülich, Germany.

The global results, showing $\chi_i/\chi_{GB} = 0.9$ and $\chi_e/\chi_{GB} = 0.2$, are then compared with a local simulation carried out for $R/L_{Ti} = 5.5$, $R/L_{Te} = 3.6$ and $R/L_n = 2.6$. The different heat diffusivities are shown in Fig. 7.24. One observes, in agreement with the ρ^* scan with adiabatic electrons shown in Fig. 5.20, that for this particular ρ^* value, the heat diffusivities obtained with the local code, $\chi_i/\chi_{GB} = 11.3$ and $\chi_e/\chi_{GB} = 4.6$, differ from the global results by an order of magnitude.

These preliminary results thus strongly suggest that a global description would be required for quantitative comparison with experimental results in a small device such as TCV. They however need to be further confirmed. In particular the issue of the radial resolution needs to be addressed. The influence of the size of the prescribed flat gradient

region, clearly a finite ρ^* effect, needs also to be investigated.

7.7 Summary and discussion

In this chapter, we have investigated nonlinear turbulent heat and particle transport using realistic parameters derived from a TCV discharge presenting an electron internal transport barrier. It was shown, in agreement with quasi-linear results presented in [40], that a cancellation of the electron particle flux can be observed by choosing an appropriate value of the ion temperature gradient, $R/L_{Ti} = R/L_{Ti,stat}$. Such cancellation corresponds to a realistic stationnary state situation, and a spectral decomposition of the particle flux reveals that it results from positive and negative contributions at different toroidal wave numbers k_y. In fact, positive contributions from low k_y modes correspond to TEM instabilities and negative contributions from higher k_y modes correspond to ITG instabilities which still persist in the nonlinear regime. A quantitative comparison between the stationary ion temperature gradient obtained with the quasi-linear estimates as proposed in [98] and the nonlinear simulations have shown a remarkable agreement, confirming the interest of this approach to predict critical $R/L_{Ti,stat}$ gradient value. Concerning the nonlinear electron heat diffusivity χ_e, the value obtained for $R/L_{Ti} = R/L_{Ti,stat}$ corresponds to a local minimum, which seems to result from nonlinear interaction between TEM and ITG modes.

A sensitivy study on various parameters has shown that the stationary electron heat diffusivity is very stiff with respect to the density gradient R/L_{ne}. A strong dependence of χ_e on R/L_{Ti} was also shown when ITG modes are destabilized, as illustrated in Fig. 7.14. One should therefore handle the two parameters R/L_{ne} and R/L_{Ti} with great care when computing nonlinear gyrokinetic simulations for eITB relevant parameters if one intends to obtain realistic heat diffusivities. In particular, small uncertainties in the experimental data could lead to strong variations in the resulting heat fluxes. For further efficient eITB investigations, we therefore propose the following scheme, based on the particle and heat diffusivity constraints:

1) Determine maximal and minimal density gradients within experimental uncertainties.

2) For these two limiting R/L_{ne} values, evaluate the corresponding $R/L_{Ti,stat}$ using the quasi-linear approach.

3) Compute the resulting electron heat diffusivity in both cases by means of nonlinear simulations, which can then be compared with experimental values.

However, for the present TCV study a reasonable electron heat diffusivity was only obtained for a density gradient R/L_{ne} which is below the experimental values, even when taking experimental errors into account. The turbulence level resulting from the TEM instabilities seems therefore overestimated in these local flux tube simulations. One possible explanation could be related to the large $\rho^* = \rho_i/a \simeq 1/80$ value, characteristic of TCV eITB experiments, so that global effects could well play a significant role here. In particular, we note that the required box size for the flux tube simulations was here $l_x = 118\,\rho_i$ which is in fact larger then the machine size, suggesting that the local approximation is not appropriate in this case for quantitative comparisons. This is indeed strongly supported by some preliminary global nonlinear results obtained with kinetic electrons and considering reduced parameters, showing much lower heat diffusivities (approximately one order of magnitude) for an appropriate $\rho^* = 1/80$ value than obtained from local flux-tube simulations. Further investigations using the global code are thus required in the future.

8 Conclusions

During the course of this thesis project the local gyrokinetic code GENE has been extended to a global version, thus allowing for the investigation of nonlocal effects. This has required to make important modifications to the code, which have been described in this work, and some first investigations of non-local effects have been presented. In addition to the global code development, the local version of the code has been used to study the effect of shaping on ITG turbulence as well as particle and heat transport in a TCV discharge presenting an electron Internal Transport Barrier. In the following, a brief review of the most important results is provided and an outlook on possible future research topics is given.

8.1 Summary

In view of their implementation in the new version of the GENE code, the gyrokinetic and field equations have been expressed in the field aligned coordinate system considering a general Tokamak geometry and keeping radial variations of equilibrium quantities. Although some remaining ρ^* terms are still neglected, these equations in particular capture the dominant non-local effects associated with the radial variations of the temperature and density gradient profiles.

In order to account for radial variations of equilibrium quantities, the treatment of the radial direction has been modified from Fourier space to a real space representation. In particular, radial boundary conditions were modified from periodic to Dirichlet, both for the distributions and potential fields. Among the different modifications of the code that were thus required, the present work has focused on the implementation of a real space anti-aliasing treatment for the nonlinearity and a Krook-type heat source enabling to carry out steady state global simulations. A detailed analysis of the gyro-averaging operator

was also carried out and corrections to the previous scheme were proposed.

Particular effort was devoted on the magnetic equilibrium description and two different models have been implemented for both the local and global versions of the code: an interface with the MHD equilibrium code CHEASE and an analytic circular concentric flux surface model. A detailed study of the different geometrical terms has furthermore underlined inconsistencies in a previously considered model, the so-called $s - \alpha$ model. It was in particular shown that these inconsistencies had resulted in misinterpreted agreement between local and global results at large $\rho^* = \rho_s/a$ values. True convergence between local and global simulations was finally obtained by correct treatment of the geometry in both cases, and considering the appropriate $\rho^* \to 0$ limit in the latter case.

In order to validate the newly developed global-GENE code, extensive tests and benchmarks were carried out. Considering first adiabatic electrons, very good agreements with various codes were obtained in both the cylindrical limit and for Cyclone base case parameters. Linear simulations with kinetic electrons have shown some first promising results, in particular concerning the ITG/TEM transition. Some discrepancies with other code results on the growth rates are however still to be further investigated. After having shown correct predictions of the zonal flow residual by means of the Rosenbluth Hinton test, nonlinear comparisons with the ORB5 code have shown good agreement in quasi-steady state conditions. Finally, a ρ^* scan was carried out considering Cyclone parameters, showing the expected convergence towards the flux tube results in the limit $\rho^* \to 0$ as well as an excellent agreement with ORB5 code results. This scan also showed that for these parameters global effects become important for $1/\rho^* \lesssim 280$. Finally, these results may provide interesting insight concerning a long lasting disagreement between the GYRO and GTC codes considering a similar ρ^* scan.

Using the interface with the MHD equilibrium code, the effects of plasma shaping on ITG microinstabilities and associated microturbulence were investigated. A favorable effect of elongation and negative triangularity was observed in both linear and nonlinear simulations when considering a constant ion temperature gradient on the equatorial mid-plane. It was shown that most of the shaping effects could be accounted for by the modification of the flux-surface averaged ion temperature gradient. More importantly, a unique effective nonlinear critical ion temperature gradient was observed around

$R/L_{\mathrm{eff,crit}} =< R/L_{Ti} >_{\mathrm{crit}} \simeq 6$ for different elongations and triangularities, considering Cyclone base case-type parameters with flat density profile.

A study of turbulent particle and heat transport for TCV discharges presenting an electron internal transport barrier was finally presented. Confirming some previous quasi-linear estimates, local nonlinear simulations have shown that the electron particle flux goes to zero for a gradient value $R/L_{Ti} = R/L_{\mathrm{Ti,stat}}$ corresponding to the transition between TEM and ITG dominated regimes. This cancellation results from positive and negative contributions associated respectively with the TEM and ITG modes of the linear spectrum which still persist in the nonlinear evolution. By choosing the quasi-linear rule proposed in Ref. [98], which accounts for all unstable linear modes, a good quantitative agreement with the nonlinear results was achieved concerning the particle flux cancellation. Beyond the electron particle flux, this nonlinear study also focused on the electron heat diffusivity. A remarkable minimum of this quantity was observed in the vicinity of $R/L_{Ti} = R/L_{Ti,stat}$, which results from nonlinear destructive interactions between ITG and TEM modes [51]. Some parameter sensitivity study has furthermore shown that the predicted stationary heat diffusivity was very stiff with respect to the electron density gradient. Comparisons with experimental results revealed that a reasonable agreement could only be reached in regions where the density gradient is relatively small, *i.e.* $R/L_{ne} \simeq 3$, whereas the flux tube simulations seem to overestimate the heat transport if one accounts for density gradient values of order $R/L_{ne} \sim 6 - 10$ found in the center of the transport barrier. Some preliminary nonlinear global results, including kinetic electrons, finally suggest that non-local effects may play an essential role for these TCV eITB cases. A global approach therefore seems required if one intends to obtain quantitative predictions of the heat diffusivity in these conditions.

8.2 Outlook

Global simulations with adiabatic electrons have been thoroughly validated in both the linear and nonlinear regimes, and the new version of the GENE code thus opens wide possibilities for investigating the influence of nonlocal effects. Some further efforts are however still required concerning kinetic electron dynamics in global simulations, in par-

ticular, further benchmarks of linear runs should be carried out both in the TEM and KBM regimes. A better understanding of some numerical instabilities observed when trying to run nonlinear simulations with kinetic electrons is also necessary, and further modifications may be introduced in order to obtain a more robust code in this limit. We note that some recent investigations of an alternative treatment of the $\vec{E} \times \vec{B}$ nonlinearity using the so-called Arakawa scheme [99, 13] by D. Told have already provided interesting perspectives, although numerical instabilities are still observed in some cases. Concerning the model, one could also envisage to introduce in the implemented gyrokinetic equation some of the remaining missing finite ρ^* terms, in particular those scaling as $1/r$, in view of extending the domain of validity of the code. Finally, to facilitate the investigation of the TEM regime, one should enable the option of considering only trapped kinetic electrons while passing electrons are still assumed adiabatic (similar to the kinetic electron model in the ORB5 code for instance). This would indeed avoid the necessity of resolving the fine radial structures generated by the non-adiabatic response of passing electrons on mode rational surfaces, which lead to computationally heavy simulations. In fact, validating such a reduced kinetic electron model for the TEM regime is in itself an issue of physical interest, *i.e.* determining whether the fine radial structures in linear modes due to non-adiabatic passing electrons have a significant effect on the associated non-linear turbulent transport.

The global GENE code should be used to further address the general issue of transport barriers, in particular once the functionality of running global simulations in the TEM regime using either full or only trapped kinetic electrons has been implemented. This would enable to pursue the investigation of TCV eITBs presented in this work. One could then verify whether a cancellation of the electron particle flux still occurs in global simulations for relevant physical parameters at the transition between ITG and TEM dominated regime. As a first attempt in this direction, the quasi-linear approach described in [98] could be used and extended to the global case by introducing some radial averaging. Considering nonlinear simulations, a first investigation could be carried out with the gradient driven approach, *i.e.* using the Krook-type heat source, and comparison with experimental heat diffusivity could thus be envisaged for realistic temperature gradient values. In addition, one could verify whether destructive interaction between TEM and

ITG modes still leads to a reduction of the heat diffusivity in the vicinity of $R/L_{Ti,stat}$. Such gradient driven simulations are however not completely satisfactory as an artificial heat source is used to pin the temperature profile to a prescribe value. In this case, the transport barrier formation is thus not addressed. A more physical approach consist in considering flux driven simulations using a realistic heat source. Simulations using such a heat source, and considering realistic experimental input power, could be carried out and one could investigate whether the steep electron temperature gradient could be maintained. In this respect, the interface with the MHD equilibrium should be used, to account for the combined effects related to the magnetic geometry such as the reversed shear and the Shafranov shift.

Global simulations with kinetic electrons could also be carried out to further study the beneficial effect of negative triangularity observed in the TCV experiment and in particular to extend the flux-tube study by A. Marinoni published in Ref. [85].

Finally, the problem of global nonlinear simulations in the high β regime has not yet been extensively addressed, and the new version of the GENE code could thus be used to provide a better understanding of microturbulence in this regime.

A CHEASE output for gyrokinetic codes

The CHEASE code for computing axisymmetric MHD plasma equilibria [36] has been adapted to provide a specific output file, containing appropriate magnetic equilibrium data for the gyrokinetic codes GENE and ORB5. This output is calculated when the input parameter NIDEAL is set to 9 (see [36] for more information on the CHEASE input parameters). In this case, a file in HDF5 format [100] named ogyropsi.h5 is written.
The input parameters NEGP and NER, used to defined the Jacobian in CHEASE :

$$J = C(\Psi) R^{\mathrm{NER}} |\nabla \Psi|^{\mathrm{NEGP}}$$

should be set to NER=2 and NEGP=0. In this case the (Ψ, χ, Φ) coordinates, where Ψ is the poloidal magnetic flux function, χ the generalized poloidal angle and Φ the toroidal angle, define a strait field line coordinate system.
The ogyropsi.h5 HDF5 file is structured as follows:

- The hierarchy of the file is organized into one main group /data itself subdivided into groups /data/grids, /data/var1d, and /data/var2d. The input file is in addition stored in the group /inputs.
- As attributes of /data are the scalars:

NPSI	number of points in the Ψ direction
NCHI	number of points in the χ direction
R0EXP	major radius
B0EXP	magnetic field on magnetic axis

- In /data/grids, the radial and poloidal grids:

PSI(NPSI)	PSI grid
CHI(NCHI)	CHI grid, going from 0 to $2\pi - \Delta\chi$

- In /data/var1d, the 1-dimensional fields:

Rgeom(NPSI)	major radius, $R_{\text{geom}} = (R_{\max} + R_{\min})/2$
ageom(NPSI)	minor radius, $a_{\text{geom}} = (R_{\max} - R_{\min})/2$
q(NPSI)	safety factor
dqdpsi(NPSI)	$dq/d\Psi$
d2qdpsi2(NPSI)	$d^2q/d\Psi^2$
shear(NPSI)	$\hat{s} = (\Psi/q)\, dq/d\Psi$
dshdpsi(NPSI)	$d\hat{s}/d\Psi$
p(NPSI)	pressure
dpdpsi(NPSI)	$dp/d\Psi$
f(NPSI)	$F = R\, B_\phi$
fdfdpsi(NPSI)	$F\ dF/d\Psi$
ρ_t(NPSI)	$\sqrt{\Phi_t/\Phi_{t,\text{edge}}}$, where Φ_t is the toroidal flux
kappa(NPSI)	elongation
delta(NPSI)	triangularity
V(NPSI)	volume inside Ψ = cst $/2\pi$
dVdpsi(NPSI)	$dV/d\Psi$
drho_tdpsi(NPSI)	$d\rho_t/d\Psi$
GDPSI_av(NPSI)	$\langle\lvert\nabla\Psi\rvert\rangle$ where $\langle\ \rangle$ is the flux-surface average
rad_av(NPSI)	flux-surface averaged minor radius
R_av(NPSI)	flux-surface averaged major radius

- In /data/var2d, the 2-dimensional fields:

g11(NPSI,NCHI)	$g^{11} = \lvert\vec{\nabla}\Psi\rvert^2$
g12(NPSI,NCHI)	$g^{12} = \vec{\nabla}\Psi \cdot \vec{\nabla}\chi$
g22(NPSI,NCHI)	$g^{22} = \lvert\vec{\nabla}\chi\rvert^2$
g33(NPSI,NCHI)	$g^{22} = \lvert\vec{\nabla}\Phi\rvert^2$
B(NPSI,NCHI)	norm of the magnetic field
dBdpsi(NPSI,NCHI)	$\partial B/\partial\Psi$
dBdchi(NPSI,NCHI)	$\partial B/\partial\chi$
J(NPSI,NCHI)	Jacobian $J = [(\vec{\nabla}\Psi \times \vec{\nabla}\chi) \cdot \vec{\nabla}\Phi]^{-1}$
R(NPSI,NCHI)	cylindrical coordinates (R, Z, Φ)

Z(NPSI,NCHI)	cylindrical coordinates (R, Z, Φ)
dChidr(NPSI,NCHI)	$\partial\chi/\partial R$
dChidz(NPSI,NCHI)	$\partial\chi/\partial Z$
dPsidr(NPSI,NCHI)	$\partial\Psi/\partial R$
dPsidz(NPSI,NCHI)	$\partial\Psi/\partial Z$

The CHEASE code can be run in many different ways, as described in Ref. [36], using analytical or experimental pressure and current profiles. The most straighforward way however to obtain a suitable ogyropsi.h5 file for gyrokinetic investigation is to start from an exisiting EQDSK equilibrium file [69]. To this end, an EQDSK file renamed EXPEQ needs to be copied in the folder where the CHEASE code is run, and the following chease_namelist input file can be used:

```
*** Standard input to run with EQDSK file
*** Create h5 output for gyrokinetic codes
***

 &EQDATA
 NIDEAL=9,
 NEGP=0, NER=2,
 NS=60, NT=60, NPSI=180, NCHI=16, NISO=180, NDIFPS=1,
 NEQDSK=1, NSURF=6, NPPFUN=4, NFUNC=4,
 EPSLON=1.0E-11, GAMMA=1.6666666667,
 /
```

Note that, the variable NDIFPS=1 in this example ensures that the Ψ grid is such that $\rho_v(\Psi) = \sqrt{V/V_{edge}}$ is equidistant which is appropriate for the global version of GENE. Detailed information describing how to run the GENE code using such a geometrical file are provided in the user manual [101].

B A local dispersion relation for toroidal-ITG modes

In the following a derivation of the local dispersion relation (6.7) based on Refs. [87] and considering a slab geometry is presented. Although one could have used the gyrokinetic equation (2.51) to obtained this dispersion relation, it is in fact possible in the present simple local geometry to integrate directly the particle trajectories, without going through the Lie transform formalism. The gyrokinetic limit is then simply recovered in the final expression by assuming $\omega \ll \Omega$.

In this local approach, the effect of curvature and gradient of the magnetic field is introduced through an external force (assuming a low pressure plasma):

$$\vec{F} = -m \left(\frac{v_\perp^2}{2} + v_\parallel^2 \right) \vec{\nabla} \ln B \,. \tag{B.1}$$

An $(\vec{e}_x, \vec{e}_y, \vec{e}_z)$ orthogonal cartesian coordinate system is considered, with a uniform magnetic field $\vec{B} = B\,\vec{e}_z$. A temperature gradient is assumed in the x-direction, opposite to the magnetic field gradient, while the density n is assumed to be flat.

Considering electrostatic perturbations, the Vlasov equation for the particle distribution $f(\vec{r}, \vec{v}, t)$ reads :

$$\frac{df}{dt} = \left[\frac{\partial}{\partial t} + \vec{v} \cdot \frac{\partial}{\partial \vec{r}} + \frac{1}{m} \left(q\,\vec{v} \times \vec{B} + \vec{F} - q\vec{\nabla}\Phi \right) \cdot \frac{\partial}{\partial v} \right] f = 0 \tag{B.2}$$

where m and q are the mass and charge of the particle, and Φ is the electrostatic potential of the perturbation. In order to linearize the Vlasov equation, the particle distribution is split into an equilibrium and perturbed part $f = f_0 + \delta f$. The particle distribution $f_0 \neq f_0(t)$ is a stationary solution of the unperturbed Vlasov Equation and is a function

of the constants of motion,

$$X = x + \frac{v_y}{\Omega} = \text{cst} \,, \tag{B.3}$$

$$K = \frac{1}{2} m\, v^2 = \text{cst} \,, \tag{B.4}$$

where $\Omega = qB/m$ is the gyro-frequency, X is the guiding center position along x, and K is the kinetic energy. Assuming a near thermodynamic equilibrium, one considers:

$$f_0(X,K) = \left(\frac{m}{2\,\pi\, T(X)} \right)^{3/2} n \, \exp\left(-\frac{K}{T(X)} \right) \,, \tag{B.5}$$

where $T(x)$ is the local temperature, and n the density. Assuming that the Larmor radius $\rho_L = c_{th}/\omega$, with $c_{th} = \sqrt{T/m}$, is small compared to the equilibrium characteristic length L, f_0 is expanded in the small parameter $\varepsilon = \rho_L/L$:

$$f_0(X,K) = f_0(x,K) + \frac{v_y}{\Omega} \frac{\partial f_0}{\partial x}(x,K) + \mathcal{O}(\varepsilon^2) \tag{B.6}$$

$$= f_0 + \frac{v_y}{\Omega} \frac{d\ln T}{dx} \left(\frac{K}{T} - \frac{3}{2} \right) f_0 \,. \tag{B.7}$$

Having defined the equilibrium state, one notices that the unperturbed system is homogeneous in the y and z directions, as well as in time. One can thus consider an electrostatic perturbation of the form:

$$\Phi = \hat{\Phi}(x) \exp i(\vec{k}\cdot\vec{r} - \omega t) = \hat{\Phi}(x) \exp i(k_y\, y + k_z\, z - \omega t) \,, \tag{B.8}$$

where k_y and k_z are wave numbers in the y- and z-directions respectively, and ω is the frequency of the linear perturbation. The x-dependence of $\hat{\Phi}$ is furthermore neglected, and only local perturbations to $x = 0$ surface are considered. The perturbed particle distribution function has a similar dependence:

$$\delta f = \delta \hat{f} \exp i(k_y\, y + k_z\, z - \omega t) \,, \tag{B.9}$$

and is solution of the linearized Vlasov equation:

$$\left.\frac{d}{dt}\right|_{u.t.} \delta\hat{f} = \left[\frac{\partial}{\partial t} + \vec{v}\cdot\frac{\partial}{\partial \vec{r}} + \frac{1}{m}\left(q\,\vec{v}\times\vec{B} + \vec{F}\right)\cdot\frac{\partial}{\partial v} \right] \delta\hat{f} = \frac{q}{m}\,\vec{\nabla}\Phi\cdot\frac{\partial f_0}{d\vec{v}} \,, \tag{B.10}$$

where $u.t.$ stands for the total time derivative along the unperturbed trajectories.
By integrating Eq. (B.10) along the unperturbed trajectories one obtains:

$$\delta\hat{f}(\vec{r},\vec{v},t) = \frac{q}{m}\int_{-\infty}^{t} dt'\,\vec{\nabla}\Phi\cdot\left.\frac{\partial f_0}{d\vec{v}}\right|_{\vec{r}'(t'),\vec{v}'(t'),t'} \tag{B.11}$$

assuming $\delta\hat{f}(\vec{r},\vec{v},-\infty)=0$, which is consistent with the condition of causality.
The unperturbed particle trajectories $[\vec{r}'(t'),\vec{v}'(t')]$ are defined by:

$$\frac{d\vec{r}'}{dt'} = \vec{v}'\,, \tag{B.12}$$

$$\frac{d\vec{v}'}{dt'} = \frac{1}{m}(q\,\vec{v}'\times\vec{B}+\vec{F})\,, \tag{B.13}$$

with initial conditions:

$$\vec{r}'(t'=t) = \vec{r}\,, \tag{B.14}$$

$$\vec{v}'(t'=t) = \vec{v}\,. \tag{B.15}$$

These trajectories can be straightforwardly integrated as follows:

$$\vec{r}'(t') = \vec{r}+\frac{1}{\Omega}\mathbf{M}_1(t'-t)\,(\vec{v}-\vec{v}_F)+\vec{v}_F\,, \tag{B.16}$$

$$\vec{v}'(t') = \mathbf{M}_2(t'-t)(\vec{v}-\vec{v}_F)+\vec{v}_F\,, \tag{B.17}$$

where

$$\vec{v}_F = \frac{\vec{F}\times\vec{B}}{q\,B^2} \tag{B.18}$$

and the matrices $\mathbf{M}_1$ and $\mathbf{M}_2$ are defined in the $(\vec{e}_x,\vec{e}_y,\vec{e}_z)$ coordinate system by:

$$\mathbf{M}_1(t) = \begin{pmatrix} \sin(\Omega t) & 1-\cos(\Omega t) & 0 \\ \cos(\Omega t)-1 & \sin(\Omega t) & 0 \\ 0 & 0 & \Omega t \end{pmatrix}\,, \tag{B.19}$$

$$\mathbf{M}_2(t) = \begin{pmatrix} \cos(\Omega t) & \sin(\Omega t) & 0 \\ -\sin(\Omega t) & \cos(\Omega t) & 0 \\ 0 & 0 & 1 \end{pmatrix}\,. \tag{B.20}$$

After having made explicit the unperturbed particle trajectories, we now expand the integrand of Eq. (B.11):

$$\vec{\nabla}\Phi \cdot \frac{\partial f_0}{\partial \vec{v}} = \frac{i}{c_{th}^2}[\omega_T - \vec{k}\cdot\vec{v}]\, f_0\, \Phi\,, \tag{B.21}$$

where

$$\omega_T = \frac{T}{q\,B}\, k_y\, \frac{d\ln T}{dx}\left(\frac{K}{T} - \frac{3}{2}\right) \tag{B.22}$$

$$= \vec{k}\cdot\frac{(-\vec{\nabla}T)\times\vec{B}}{q\;B^2}\,\mathcal{E}\,, \tag{B.23}$$

having defined $\mathcal{E}(v) = K(v)/T - 3/2$. We note that ω_T has been expressed in Eq. (B.23) as a vector relation in order to be replaced later on by the corresponding effective value in the toroidal system.

Since f_0 is a stationary state, *i.e.* $df_0/dt' = 0$, one can write:

$$\frac{d}{dt'}[f_0\,\Phi] = \frac{d}{dt'}[f_0\,\hat{\Phi}\,\exp i(\vec{k}\cdot\vec{r}\,' - \omega t')] = i(\vec{k}\cdot\vec{v} - \omega) f_0\,\hat{\Phi}\,\exp i(\vec{k}\cdot\vec{r}\,' - \omega t')\,. \tag{B.24}$$

Using this last relation, the integrand (B.21) of Eq. (B.11) can be express as:

$$\vec{\nabla}\Phi\cdot\left.\frac{\partial f_0}{d\vec{v}}\right|_{\vec{r}\,'(t'),\vec{v}\,'(t'),t'} = \frac{1}{c_{th}^2}\left[i(\omega_T-\omega) - \frac{d}{dt'}\right]\, f_0\,\Phi\,. \tag{B.25}$$

Using this last form, and integrating Eq. (B.11) by parts, $\delta\hat{f}$ becomes:

$$\delta\hat{f} = \delta f\,\exp -i(\vec{k}\cdot\vec{r} - \omega t)$$

$$= -\frac{q\hat{\Phi}}{T}\left\{1 - i(\omega_T-\omega)\int_{-\infty}^{t} dt'\exp i[\vec{k}\cdot(\vec{r}\,' - \vec{r}) - \omega(t'-t)]\right\} f_0\,. \tag{B.26}$$

The time integral is now evaluated using Eq.(B.16) for $\vec{r}\,'$, and after some algebra can be written as:

$$\delta\hat{f} = -\frac{q\hat{\Phi}}{T}\left[1 - (\omega_T-\omega)\sum_{n,n'=-\infty}^{\infty}\frac{J_n(\frac{k_y v_\perp}{\Omega})\; J_{n'}(\frac{k_y v_\perp}{\Omega})\; e^{i(n-n')\alpha}}{k_z v_\parallel + n\,\Omega + \omega_F - \omega}\right] f_0\,, \tag{B.27}$$

where $\omega_F = \vec{k}\cdot\vec{v}_F$, $J_n(z)$ are Bessel functions of the first kind, and $v_\perp$ and α are defined by:

$$v_x = v_\perp\,\sin\alpha\,, \quad v_y - v_F = v_\perp\,\cos\alpha\,. \tag{B.28}$$

Equation (B.27) provides a relation between $\delta\hat{f}$ and $\hat{\Phi}$. In order to close the system and to obtain a dispersion relation for (k_y, k_z, ω), one invokes quasi-neutrality of the plasma:

$$\sum_j q_j\, \delta n_j = 0 \qquad \Rightarrow \qquad \sum_j q_j\, \delta\hat{n}_j = 0\ . \tag{B.29}$$

Where $\delta\hat{n}_j$ is the amplitude of the perturbed density of species j. In the following we consider only one kinetic ion species and assume adiabatic electrons. The amplitude of the linear electron density perturbation is thus given by:

$$\delta\hat{n}_e = n_0 \frac{e\hat{\Phi}}{T_e}\ , \tag{B.30}$$

and the amplitude of the ion density perturbation is obtained using Eq. (B.27):

$$\begin{aligned} \delta\hat{n}_i &= \int d\vec{v}\, \delta\hat{f}_i \\ &= -n_{0i}\frac{q_i\hat{\Phi}}{T_i}\left[1 - \sum_{n,n'=-\infty}^{\infty} \int d\vec{v}\, (\omega_{Ti} - \omega)\, \frac{f_{0i}}{n_{0i}}\, \frac{J_n(\frac{k_y v_\perp}{\Omega_i})\, J'_n(\frac{k_y v_\perp}{\Omega_i})\, e^{i(n-n')\alpha}}{k_z v_\parallel + n\,\Omega_i + \omega_{Fi} - \omega}\right] \end{aligned} \tag{B.31}$$

In the limit $\omega << \Omega$, only the $n = 0$ contribution needs to be considered in the sum over n. The velocity element is express as $d\vec{v} = dv_\parallel\, v_\perp\, dv_\perp\, d\alpha$, and carrying out the integral over α, only the $n' = 0$ contribution of the $\exp(-i\, n'\, \alpha)$ term is non zero, leading to the following dispersion relation for ω:

$$\frac{1}{Z_i\,\tau} + 1 - \int d\vec{v}\, (\omega_{Ti} - \omega)\, \frac{f_{0i}}{n_{0i}}\, \frac{J_0^2(\frac{k_y v_\perp}{\Omega_i})}{k_z v_\parallel + \omega_{Fi} - \omega} = 0\ , \tag{B.32}$$

where $\tau = T_e/T_i$, $Z_i = q_i/e$, and with the notation $d\vec{v} = 2\,\pi dv_\parallel\, v_\perp\, dv_\perp$.

Bibliography

[1] *Key World Energy Statistics 2009*, International Energy Agency, 2009.

[2] D. Meadows, J. Randers, and D. Meadows, *Limits to growth : the 30 years Update*, Eathcan, 2005.

[3] J. Wesson, *Tokamaks, 2nd Edition*, Oxford University Press, Claredon Press, 1997.

[4] J. Wendell Horton, D.-I. Choi, and W. M. Tang, Phys. Fluids, **24**(6), 1077, 1981.

[5] F. Romanelli and S. Briguglio, Phys. Fluids B, **2**, 754, 1990.

[6] W. Horton, Rev. Mod. Phys., **71**(3), 735, 1999.

[7] J. Li and Y. Kishimoto, Plasma Phys. Control. Fusion, **44**(5A), A479, 2002.

[8] G. Rewoldt, W. Tang, and R. Hastie, Phys. Fluids, **30**, 807, 1987.

[9] M. A. Beer, S. C. Cowley, and G. W. Hammett, Phys. Plasmas, **2**, 2687, 1995.

[10] M. Kotschenreuther, G. Rewoldt, and W. Tang, Comput. Phys. Comm., **88**, 128, 1995.

[11] W. Dorland, F. Jenko, *et al.*, Phys. Rev. Lett., **85**, 5579, 2000.

[12] F. Jenko, W. Dorland, *et al.*, Phys. Plasmas, **7**, 1904, 2000.

[13] J. Candy and R. Waltz, J. Comput. Phys., **186**, 545, 2003.

[14] Y. Idomura, M. Ida, *et al.*, Comput. Phys. Comm., **179**, 391, 2008.

[15] M. Kotschenreuther, Bull. Am. Phys. Soc., **34**, 2107, 1988.

[16] S. E. Parker and W. W. Lee, Phys. Fluids, **B 5**, 77, 1993.

[17] R. Sydora, Phys. Scripta, **52**, 474, 1995.

[18] A. M. Dimits, T. J. Williams, *et al.*, Phys. Rev. Lett., **77**, 71, 1996.

[19] Z. Lin, T. Hahm, *et al.*, Science, **281**, 1835, 1998.

[20] T. M. Tran *et al.*, in *Joint Varenna-Lausanne Int. Workshop on Theory of Fusion Plasmas*, page 45, 1998, italy.

[21] Y. Idomura, S. Tokuda, and Y. Kishimoto, Nucl. Fusion, **43**, 234, 2003.

[22] C. Z. Cheng and G. Knorr, J. Comput. Phys., **22**, 330, 1976.

[23] F. Filbet and E. Sonnendrücker, Comput. Phys. Comm., **150**, 247, 2003.

[24] M. Brunetti, V. Grangirard, *et al.*, Comput. Phys. Comm., **163**(1), 1, 2004.

[25] V. Grangirard *et al.*, J. Comput. Phys., **217**(2), 395, 2006.

[26] V. Grandgirard, Y. Sarazin, *et al.*, Plasma Phys. Control. Fusion, **49**(12B), B173, 2007.

[27] T. Dannert and F. Jenko, Phys. Plasmas, **12**, 072309, 2005.

[28] T. Görler, *Multiscale effects in plasma microturbulence*, Ph.D. thesis, Universität Ulm, 2009.

[29] J.-M. Moret, S. Franke, *et al.*, Phys. Rev. Lett., **79**(11), 2057, 1997.

[30] H. Weisen, J.-M. Moret, *et al.*, Nucl. Fusion, **37**(12), 1741, 1997.

[31] F. Hofmann, R. Behn, *et al.*, Plasma Phys. Control. Fusion, **43**(12A), A161, 2001.

[32] A. Pochelon, T. Goodman, *et al.*, Nucl. Fusion, **39**(11Y), 1807, 1999.

[33] Y. Camenen *et al.*, Plasma Phys. Control. Fusion, **47**(11), 1971, 2005.

[34] E. A. Lazarus, M. S. Chu, *et al.*, Physics of Fluids B: Plasma Physics, **3**(8), 2220, 1991.

[35] J. Ongena, W. Suttrop, *et al.*, Plasma Phys. Control. Fusion, **43**(12A), A11, 2001.

[36] H. Lütjens, A. Bondeson, and O. Sauter, Comput. Phys. Comm., **97**(3), 219, 1996.

[37] J. W. Connor, R. J. Hastie, and J. B. Taylor, Phys. Rev. Lett., **40**, 396, 1978.

[38] X. Litaudon, E. Barbato, *et al.*, Plasma Phys. Control. Fusion, **46**(5A), A19, 2004.

[39] T. P. Goodman, R. Behn, *et al.*, Plasma Phys. Control. Fusion, **47**(12B), B107, 2005.

[40] E. Fable, *Experimental and theoretical study of particle transport in the TCV tokamak*, Ph.D. thesis, EPFL, Switzerland, 2009.

[41] M. A. Beer, *Gyrofluids models of turbulent transport in tokamaks*, Ph.D. thesis, Princeton University, 1994.

[42] A. J. Wootton, B. A. Carreras, *et al.*, Phys. Fluids B, **2**(12), 2879, 1990.

[43] E. A. Frieman and L. Chen, Phys. Fluids, **25**, 502, 1982.

[44] R. G. Littlejohn, J. Plasma Phys., **29**, 111, 1983.

[45] T. S. Hahm, Phys. Fluids, **31**, 2670, 1988.

[46] T. Hahm, W. Lee, and A. Brizard, Phys. Fluids, **31**, 1940, 1988.

[47] A. J. Brizard and T. S. Hahm, Rev. Mod. Phys., **79**(2), 421, 2007.

[48] J. Cary and A. J. Brizard, Rev. Mod. Phys., **81**, 693, 2009.

[49] T. Dannert, *Gyrokinetische Simulation von Plasmaturbulenz mit gefangenen Teilchen und elektromagnetischen Effekten*, Ph.D. thesis, Technische Universität München, 2005.

[50] Y. Idomura, M. Ida, *et al.*, J. Comput. Phys., **226**(1), 244, 2007.

[51] F. Merz, *Gyrokinetic simulation of multimode plasma turbulence*, Ph.D. thesis, Universität Münster, 2008.

[52] P. Xanthopoulos and F. Jenko, Phys. Plasmas, **13**(9), 092301, 2006.

[53] W. D. D'Haeseleer, W. N. G. Hitchon, *et al.*, *Flux Coordinates and Magnetic Field Structure*, Springer, Berlin, 1991.

[54] S. Jolliet, A. Bottino, *et al.*, Comput. Phys. Comm., **177**, 409, 2007.

[55] M. A. Barnes, *Trinity: A unified treatment of turbulence, transport, and heating in magnetized plasmas*, Ph.D. thesis, University of Maryland, USA, 2008.

[56] X. Garbet and R. E. Waltz, Phys. Plasmas, **3**(5), 1898, 1996.

[57] A. Gallice, Master's thesis, 4th year semester work, Ecole Polytechnique Fédérale de Lausanne, CRPP internal report, 2009.

[58] http://www.grycap.upv.es/slepc.

[59] J. L. Mead and R. A. Renaut, J. Comput. Phys., **152**(1), 404, 1999.

[60] H. Lederer, R. Tisma, *et al.*, Adv. Parallel Comput., **15**, 713, 2008.

[61] T. Dannert, private communication, 2008.

[62] B. F. McMillan, S. Jolliet, *et al.*, Phys. Plasmas, **15**(5), 052308, 2008.

[63] V. Shafranov, in *Reviews of Plasma Physics*, M.A. Leontovich, Consultants Bureau, New York, Vol. 1, p. 1, 1966.

[64] A. J. Redd, A. H. Kritz, *et al.*, Phys. Plasmas, **6**(4), 1162, 1999.

[65] J. E. Kinsey, R. E. Waltz, and J. Candy, Phys. Plasmas, **14**(10), 102306, 2007.

[66] R. L. Miller, M. S. Chu, *et al.*, Phys. Plasmas, **5**(4), 973, 1998.

[67] X. Lapillonne, S. Brunner, *et al.*, Phys. Plasmas, **16**(3), 032308, 2009.

[68] A. M. Dimits, G. Bateman, *et al.*, Phys. Plasmas, **7**, 969, 2000.

[69] L. L. Lao, J. R. Ferron, *et al.*, Nucl. Fusion, **30**, 1035, 1990.

[70] A. Peeters and D. Strintzi, Phys. Plasmas, **11**, 3748, 2004.

[71] X. Garbet, Plasma Phys. Control. Fusion, **43**(12A), A251, 2001.

[72] M. Fivaz, S. Brunner, *et al.*, Comput. Phys. Comm., **111**, 27, 1998.

[73] M. N. Rosenbluth and F. L. Hinton, Phys. Rev. Lett., **80**(4), 724, 1998.

[74] S. Brunner, *Global approach to the spectral problem of microinstabilities in Tokamak plasmas using a gyrokinetic model*, Ph.D. thesis, EPFL, 1997.

[75] G. L. Falchetto, J. Vaclavik, and L. Villard, Phys. Plasmas, **10**(5), 1424, 2003.

[76] R. Ganesh, P. Angelino, *et al.*, Phys. Plasmas, **11**(6), 3106, 2004.

[77] B. F. McMillan, S. Jolliet, *et al.*, Phys. Plasmas, **16**(2), 022310, 2009.

[78] P. H. Diamond, S.-I. Itoh, *et al.*, Plasma Phys. Control. Fusion, **47**(5), R35, 2005.

[79] Z. Lin, S. Ethier, *et al.*, Phys. Rev. Lett., **88**(19), 195004, 2002.

[80] J. Candy, R. E. Waltz, and W. Dorland, Phys. Plasmas, **11**(5), L25, 2004.

[81] G. Rewoldt, W. M. Tang, and M. S. Chance, Phys. Fluids, **25**(3), 480, 1982.

[82] D. D. Hua, X. Q. Xu, and T. K. Fowler, Phys. Fluids B, **4**(10), 3216, 1992.

[83] E. A. Belli, G. W. Hammett, and W. Dorland, Phys. Plasmas, **15**(9), 092303, 2008.

[84] P. Angelino, X. Garbet, *et al.*, Phys. Rev. Lett., **102**(19), 195002, 2009.

[85] A. Marinoni, S. Brunner, *et al.*, Plasma Phys. Control. Fusion, **51**(5), 055016, 2009.

[86] R. E. Waltz and R. L. Miller, Phys. Plasmas, **6**(11), 4265, 1999.

[87] S. Ishimaru, *Basic Principles of Plasma Physics, A statistical approach*, W.A. Benjamin, Frontiers in Physics, 1973.

[88] R. C. Wolf, Plasma Phys. Control. Fusion, **45**(1), R1, 2003.

[89] X. Garbet, C. Bourdelle, *et al.*, Phys. Plasmas, **8**(6), 2793, 2001.

[90] J. Candy, R. E. Waltz, and M. N. Rosenbluth, Phys. Plasmas, **11**(5), 1879, 2004.

[91] J. Connor, T. Fukuda, *et al.*, Nucl. Fusion, **44**(4), R1, 2004.

[92] M. A. Henderson, Y. Camenen, *et al.*, Phys. Rev. Lett., **93**(21), 215001, 2004.

[93] S. Coda, E. Asp, *et al.*, Nucl. Fusion, **47**(7), 714, 2007.

[94] E. Fable, O. Sauter, *et al.*, Plasma Phys. Control. Fusion, **48**(9), 1271, 2006.

[95] C. Zucca, *Modeling and control of the current density profile in tokamaks and its relation to electron transport*, Ph.D. thesis, EPFL, 2009.

[96] T. Görler and F. Jenko, Phys. Rev. Lett., **100**(18), 185002, 2008.

[97] T. Görler and F. Jenko, Phys. Plasmas, **15**(10), 102508, 2008.

[98] E. Fable, C. Angioni, and O. Sauter, Plasma Phys. Control. Fusion, **52**(1), 015007, 2010.

[99] A. Arakawa, J. Comput. Phys., **1**, 119, 1966.

[100] http://www.hdfgroup.org/HDF5.

[101] F. Jenko and the GENE development team, http://www.ipp.mpg.de/~fsj/gene/.

Acknowledgments

I am extremely grateful to the numerous people who help me all along this thesis.

Foremost, I owe my gratitude to my thesis supervisor Stephan Brunner who has led me through this work with great enthusiasm. During these years, he was always available, and ready to spend time explaining various aspects of plasma physics and numerical methods. It was a very privileged position to be his thesis student and I shall not forget his patience answering all my questions in the clearest possible way. I am furthermore very much in debt to Laurent Villard who also accepted to guide and supervise this work. I greatly benefited from his valuable idea and suggestions to carry on with my project.

I am deeply grateful to Frank Jenko from IPP Garching, who was very enthusiast from the beginning to start our collaboration, in the perspective of developing a global version of the GENE code. This work could not have been carried out without his idea and precious help. A special thanks goes to all those who participated to this project at IPP. I particularly would like to thank Tobias Görler who has also devoted a large part of his PHD to the development the global code. I appreciated very much that we could work together, sharing the difficulties, especially when the code was not working as planed, and the great moments when we finally obtained our first encouraging results. I also would like to thank Tilman Dannert who initiated me to the GENE code and Florian Merz for valuable discussions on various numerical aspects and for showing me around in Munich.

I greatly benefited from T. Minh Tran who help me with HDF5 and Fortran issues, as well as Olivier Sauter who introduced me to the CHEASE code.

I also would like to thanks E. Fable and O. Sauter for valuable discussions and advice concerning Transport Barriers in TCV.

I am particularly thankful to Ben McMillan for many ideas and suggestions during my work, and for the time and efforts he devoted to carry out our codes comparisons.

I would like to acknowledge Jugal Chowdury for his participation to the global code validation during his visit at CRPP.

A special thanks goes to all the post-doc and PhD students at CRPP, for all the great moments we had there, and to all the people and friends I have met here during these years in Lausanne.

I also would like to thanks my family for their encouragements, and Dorothee who was always of great support, especially during the last months of the thesis.

Curriculum Vitae

Personnal Data

Name:	Xavier Lapillonne
Date of birth:	February 25th, 1982
Nationality:	French

Educational background and academic experiences

2005-2009	Centre de Recherches en Physique des Plasmas, Ecole Polytechnique Fédérale de Lausanne, Switzerland. PHD student.
2004-2005	Imperial College, London, United Kingdom. Final master year in physics and master project: Linear Delta Expansion applied to the quantum anharmonic oscillator.
Jun-Aug 2004	Internship, CRPP, EPFL, Switzerland. Study of the efficiency of electron cyclotron current drive in fusion devices.
2002-2005	Institut Polytechnique de Grenoble, France. Master in Physical Engineering.
2000-2002	Classes Préparatoires aux Grandes Ecoles, Lycée Champollion, Grenoble, France.
2000	Baccalauréat Scientifique, Grenoble, France.

List of publications

Publications in peer-reviewed journals

- M. Albergante, J. P. Graves, A. Fasoli, X. Lapillonne, and the TCV Team,
  Microturbulence driven transport of energetic ions in the ITER steady-state scenario,
  accepted in Nuclear Fusion.

- X. Lapillonne, S. Brunner, T. Dannert, S. Jolliet, A. Marinoni, L. Villard, T. Görler, F. Jenko, and F. Merz,
  Clarifications to the limitations of the $s - \alpha$ equilibrium model for gyrokinetic computations of turbulence,
  Physics of Plasmas, **16**, 032308, 2009.

- A. Marinoni, S. Brunner, Y. Camenen, S. Coda, J. P. Graves, X. Lapillonne, A. Pochelon, O. Sauter, and L. Villard,
  The effect of plasma triangularity on turbulent transport: modeling TCV experiments by linear and non-linear gyrokinetic simulations,
  Plasma Physics and Controlled Fusion, **51**, 055016, 2009.

- T. Dannert, S. Günter, T. Hauff, F. Jenko, X. Lapillonne, and P. Lauber,
  Turbulent transport of beam ions,
  Physics of Plasmas, **15**, 062508, 2008.

- X. Garbet, Y. Sarazin, V. Grandgirard, G. Dif-Pradalier, G. Darmet, Ph. Ghendrih, P. Angelino, P. Bertrand, N. Besse, E. Gravier, P. Morel, E. Sonnendrucker, N. Crouseilles, J.-M. Dischler, G. Latu, E. Violard, M. Brunetti, S. Brunner, X. Lapillonne, T.-M. Tran, L. Villard, and M. Boulet,
  Beyond scale separation in gyrokinetic turbulence,
  Nuclear Fusion, **47**, 1206, 2007.

Conference proceedings

- X. Lapillonne, S. Brunner, E. Fable, T. Görler, F. Jenko, B. F. McMillan, F. Merz, O. Sauter, and L. Villard,
  Gyrokinetic simulations of microturbulence in tokamak plasmas presenting an electron internal transport barrier, and development of a global version of the GENE code,
  the 36th Conference on Plasma Physics, Sofia, Bulgaria, 2009.

- X. Lapillonne, T. Dannert, S. Brunner, A. Marinoni, S. Jolliet, L. Villard, F. Jenko, T. Goerler, and F. Merz,
  Effects of geometry on linear and non-linear gyrokinetic simulations, and development of a global version of the GENE code, AIP proceedings, Theory of plasmas, 1069, 289, Varenna Conference, Italy, 2008.

- X. Lapillonne, M. Brunetti, S. Brunner, and T.-M. Tran,
  Development of a grid-based gyro-kinetic simulation code,
  Societa Italiana di Fisica, Theory of plasmas, 289, Varenna Conference, Italy, 2006.